Aix*Marseille université
Socialement engagée

NNT : 2024AIXM0275

THÈSE DE DOCTORAT

Soutenue à Aix-Marseille Université
le 3 octobre 2024 par

Eliott DUBOIS

Utilisation des méthodes de machine learning pour la description des oxydes mixtes à l'échelle atomique

Discipline
Physique et Sciences de la Matière

Spécialité
Matière condensée et Nanosciences

École doctorale
ED 352 : Physique et Sciences de la Matière

Laboratoires
CEA, DEs, IRESNE, DEC, SESC, LM2C
CEA, DAM, DIF

Composition du jury

Matthieu VERSTRAETE Professeur des universités Université de Liège	Rapporteur Président du Jury
Marie-Pierre GAIGEOT Professeure des universités Université d'Evry Val d'Essonne	Rapporteure
David A. ANDERSSON Chercheur Los Alamos National Laboratory	Examinateur
Cosmin-Mihai MARINICA Ingénieur-Chercheur CEA Saclay	Examinateur
Thomas D. SWINBURNE Chargé de recherche CNRS CINAM - Aix-Marseille Université	Examinateur
Michel FREYSS Directeur de recherche CEA Cadarache	Directeur de thèse
Jean-Bernard MAILLET Directeur de recherche CEA, DAM, DIF	Co-encadrant
Johann BOUCHET Ingénieur-Chercheur CEA Cadarache	Co-encadrant
Julien TRANCHIDA Ingénieur-Chercheur CEA Cadarache	Membre invité

cea

Affidavit

I, undersigned, Eliott DUBOIS, hereby declare that the work presented in this manuscript is my own work, carried out under the scientific supervision of Michel FREYSS, Julien TRANCHIDA, Johann BOUCHET and Jean-Bernand MAILLET, in accordance with the principles of honesty, integrity and responsibility inherent to the research mission. The research work and the writing of this manuscript have been carried out in compliance with both the french national charter for Research Integrity and the Aix-Marseille University charter on the fight against plagiarism.

This work has not been submitted previously either in this country or in another country in the same or in a similar version to any other examination body.

Fait à Arpajon, le 12 Juillet 2024

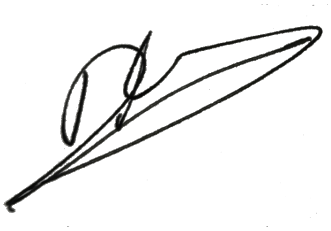

This work is licensed under Creative Commons Attribution-NonCommercial-NoDerivatives 4.0 International Public License

List of publications and Conferences participation

List of publications:

1. **Dubois, E. T.**, Tranchida, J., Bouchet, J. & Maillet, J.-B. Atomistic simulations of nuclear fuel UO_2 with machine learning interatomic potentials. *Phys. Rev. Mater.* 8, 025402 (2024). https://doi.org/10.1103/PhysRevMaterials.8.025402

Conferences participation:

1. GDR IAMAT, May 30 - June 1 2022, Paris, France - **Oral** - url
2. COSIRES 2022 : The 15th conference of COmputer Simulation of IRradiation Effects in Solids, May 22 - 26 2022, Porquerolles, France - **Poster** - url
3. MATÉRIAUX 2022, October 24-28 2022, Lille, France - **Oral** - url
4. Uranium Science 2023, July 5-7 2023, Manchester, UK - **Oral** - url
5. 53rd Journées des Actinides international conference, April 15-18 2024, Lille, France - **Oral** - url
6. PuFutures - The Science 2024, September 8–12 2024, Charleston, USA - **Oral** - url

Résumé

Les pastilles de dioxyde d'uranium (UO_2) constituent le combustible de référence pour la plupart des centrales nucléaires dans le monde. Dans des conditions d'exploitation ou d'accident, ces pastilles sont soumises à des conditions extrêmes qui ont un impact considérable sur leur microstructure. Dans ce contexte, les simulations à l'échelle atomique ont été largement utilisées pour comprendre les phénomènes physiques mis en jeu dans le combustible irradié. Les méthodes dîtes *ab initio*, telle que la théorie de la fonctionnelle de la densité (DFT), sont les méthodes les plus précises et constituent l'une des approches de choix pour la caractérisation à l'échelle atomique du combustible nucléaire. Cependant, en raison des coûts de calcul très élevés, de nombreuses propriétés d'intérêts sont impossibles à simuler en DFT. À plus grande échelle, les potentiels interatomiques semi-empiriques permettent de réaliser des simulations classiques impliquant des milliards d'atomes et sur des durées pouvant aller jusqu'à quelques microsecondes. Néanmoins, ils ne sont pas toujours comparables en termes de précision, aux calculs *ab initio* de référence. Ces dernières années, des outils d'apprentissage automatique ont été utilisés pour apprendre des surfaces d'énergie potentielle complexes à partir d'ensembles de données *ab initio* et se sont avérés efficaces pour décrire avec précision diverses classes de matériaux. L'objectif de ce travail était d'explorer la faisabilité de l'application de ces méthodes pour l'entraînement de potentiels numériques pour les oxydes d'actinides. Malgré la complexité des calculs DFT+U pour décrire les interactions entre électrons $5f$, nécessaires à la construction de la base d'entraînement, les potentiels développés présentent un bon accord avec un large ensemble de métriques *ab initio* et expérimentales. La dépendance à la température des potentiels a notamment été étudiée, en particulier en ce qui concerne l'évolution des constantes élastiques, de l'expansion thermique et de la capacité calorifique. Enfin, ces potentiels numériques ont été utilisés pour étudier les propriétés thermomécaniques du monocristal d'UO_2, en particulier, la dépendance directionnelle de la contrainte macroscopique à l'activation du premier mécanisme de déformation irréversible.

Abstract

Pellets of uranium dioxide (UO_2) are the reference fuel for most nuclear power plants in the world. In operating or accidental conditions, these pellets are facing severe conditions that dramatically impact their microstructure. In this context, atomic scale simulations have been extensively employed to provide insights into the physical phenomena at stake in irradiated fuels. High-accuracy first-principles methods, such as Density Functional Theory (DFT), are the approaches of choice for atomic scale characterisation of nuclear fuel materials. However, due to high computational cost, numerous properties remain out of the reach of DFT. At larger scales, semi-empirical interatomic potentials allow for classical molecular dynamics involving up to billions of atoms and microseconds long simulations, but do not always quantitatively compare to first principles reference calculations. In recent years, machine-learning methods have successfully been employed to learn complex potential energy surfaces from reference *ab initio* datasets, and proved to be effective in accurately describing various classes of materials. The intention of this work was to explore the feasibility of training machine learning interatomic potentials for actinide oxides materials. Despite the complexity of the reference DFT+U calculations to describe the $5f$ electrons interactions, the developed potentials exhibit good agreement with a large and selective set of *ab initio* and experimental metrics. The temperature dependence of the potentials was investigated, specifically regarding the evolution of elastic constants, thermal expansion, and heat capacity. Eventually, the machine learning potentials were used to investigate thermomechanical properties of UO_2 single crystal, in particular, the directional dependence of the macroscopic stress at the onset of the first irreversible deformation mechanism.

Résumé général

Les pastilles de dioxyde d'uranium (UO_2) et d'oxyde mixte $(U,Pu)O_2$, également appelé MOX, constituent le combustible de référence pour la plupart des centrales nucléaires dans le monde. Dans des conditions d'exploitation, incidentelles ou accidentelles, ces pastilles sont confrontées à des conditions extrêmes de gradient thermique ($\simeq$ 500K entre le centre et la périphérie de la pastille de 1 cm de diamètre), à de fortes contraintes mécaniques et à des dommages dus à l'irradiation. Ces conditions ont un impact considérable sur la microstructure des pastilles, avec des phénomènes observés tels que le fluage, des fractures (Figures 1-a), une restructuration importante comme la formation d'une structure dite "High Burn-up" (HBS) (Figures 1-a et 1-c) ou l'accumulation et la précipitation de produits de fission (PF) (Figures 1-b et 1-c).

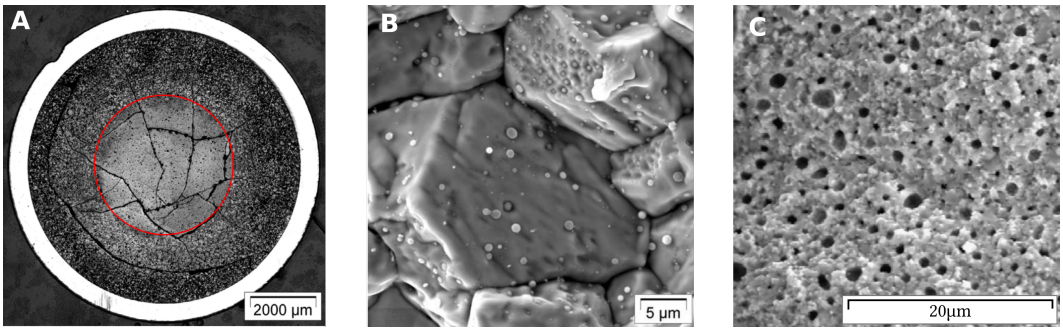

Figure 1 – **A** - Macrographie optique d'un combustible UO_2 hétérogène à 63 GWd/tU après gravure chimique [1]; **B** - Surface de grain de combustible MOX après irradiation. Les taches rondes correspondent à des précipités de produits de fission métalliques, et les cavités sont la signature de bulles de gaz de fission vides [2]; **C**- Fractographies MEB illustrant la structure HBS au bord d'une pastille d'UO_2–M5^{TM} [3].

Cette modification de la miscrostructure des pastilles a plusieurs conséquences pour le matériau combustible, comme une diminution importante de la conductivité thermique déjà faible (UO_2 étant un isolant électronique [4]), ce qui entraîne un gradient thermique d'autant plus important à l'intérieur des pastilles et une modification de leur réponse élastoplastique [5, 6]. L'évolution des propriétés du combustible a également un impact sur les matériaux qui constituent la gaine, avec par exemple le gonflement dû à l'accumulation de gaz de fission ou la fissuration par corrosion sous contrainte de la gaine ductile en zircaloy, face aux produits de fission corrosifs et volatils (Cs, I) susceptibles d'être libérés hors de la pastille [7–10].

Le Commissariat à l'énergie atomique et aux énergies alternatives (CEA) doit impérativement comprendre et être capable de prédire l'évolution de la microstructure des pastilles de combustible nucléaire et des propriétés physiques associées. Cette compréhension est cruciale car elle influence directement les codes de performance du combustible et, en conséquence, pourra avoir un impact significatif sur les marges de sécurité des réacteurs nucléaires.

Pour mieux comprendre ces phénomènes et leurs interconnexions, il est essentiel de procéder à des caractérisations complètes et à des mesures expérimentales du combustible post-irradié. Bien que la réalisation de ces expériences soit entravée par le coût et la complexité associés, l'acquisition de ces informations revêt une importance cruciale pour la construction de modèles précis et l'obtention de données fiables qui seront intégrées dans les codes développés par le CEA: ALCYONE [11] et GERMINAL [12], qui visent à modéliser les éléments combustible dans des conditions d'exploitation, respectivement pour la 3e et la 4e génération de réacteurs.

Pour compléter les études expérimentales, le Département d'étude du combustible nucléaire (DEC) du CEA est fortement investi dans le développement d'un vaste programme de simulation multiéchelle, à travers la plateforme PLEIADES [13], qui intègre des outils de simulation numérique de l'élément combustible lors de ses différentes phases de vie (fabrication, comportement sous irradiation, entreposage). Cette approche multiéchelle consiste à affiner les lois et paramètres et des modèles macroscopiques par une modélisation précise des processus physiques élémentaires se produisant à des échelles plus petites. Ainsi, la plateforme PLEIADES s'appuie sur des données allant des calculs de structure électronique *ab initio* très précis, jusqu'à la modélisation thermomécanique par éléments finis, en passant par des méthodes classiques (dynamique moléculaire, monte carlo), la dynamique d'amas, le champ de phase, la dynamique des dislocations discrète, et bien d'autres encore. La large gamme des données, issues des différentes échelles, permet de garantir la qualité de la représentation physique et permet à terme une description précise du cycle de vie des matériaux combustibles nucléaires.

Dans ce contexte, les simulations à l'échelle atomique, où est étudiée l'interaction entre les atomes, (encadrée en bleue sur la Figure 2) ont été largement utilisées pour fournir, entre autres, des données structurales, élastiques et thermodynamiques aux codes macroscopiques. Ces simulations atomistiques ne se limitent pas à l'alimentation des bases de données thermodynamiques, mais constituent également un outil extrêmement précieux pour mieux comprendre les phénomènes physiques sous-jacents qui se produisent dans des matériaux complexes tels que les combustibles post-irradiés.

Les méthodes dites *ab initio*, telle que la théorie de la fonctionnelle de la densité (DFT), sont des méthodes très précises et constituent l'une des approches de choix pour la caractérisation à l'échelle atomique du combustible nucléaire. Néanmoins, pour UO_2, l'application d'un terme de correction de Hubbard est nécessaire pour tenir compte des fortes corrélations entre les électrons $5f$ de l'uranium [14–17], introduisant une complexité supplémentaire par rapport aux calculs DFT standard [17, 18] pour converger vers l'état fondemental. Grâce à la DFT+U, de nombreuses études on permis de calculer

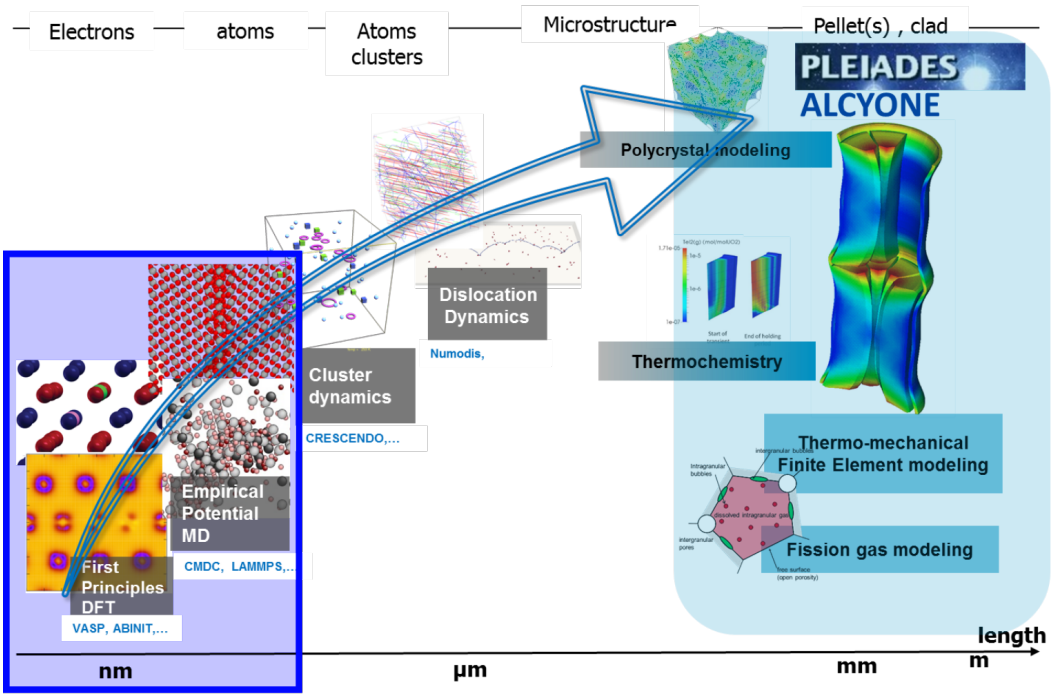

Figure 2 – Illustration de l'approche multiéchelle pour la simulation du combustible nucléaire. Les échelle spatiale charactéristique sont données en abscisses. Le rectangle bleu regroupe les méthodes atomistiques.

avec précision les énergies de formations de défault ponctuels de type interstitiels, lacunaire ou Schottky liés ("bounded Schottky defect" BSD) [17, 19, 20]. Ces énergies de formation peuvent être incorporées dans des modèles thermodynamiques, pour calculer les coefficients de diffusion des défauts [21, 22]. Bien que cela soit plus difficile, de petits groupes de ces défauts peuvent également être étudiés par la DFT+U [23] pour simuler l'accumulation de défaut ponctuels due à l'irradiation. Cependant, en raison des coûts de calcul prohibitifs, de nombreuses propriétés d'interêts sont impossibles à simuler en DFT+U. Des études récentes ont mis en évidence l'importance de considérer des cellules de simulation plus grandes (par exemple des supercellules 3×3×3, correspondant à 324 atomes) pour prédire avec précision les énergies de formation des BSD [24, 25], soulignant la nécessité de réaliser des calculs à une échelle plus grande que les simulations DFT+U typiques. Bien que des progrès récents aient permis des descriptions des propriétés thermophysiques des combustibles nucléaires basées sur les methodes *ab initio* [26], ces méthodes sont toujours limitées à de petites tailles de configurations atomiques, et la modélisation des effets à grande échelle dépendant de la température reste un défi de la DFT+U.

À plus grande échelle, des potentiels empiriques ("semi-empirical interatomic potential" SEIPs) ont été développés et appliqués à UO_2. Ces SEIPs utilisent des fonctions analytiques simples pour définir un paysage d'énergie potentielle à partir duquel les énergies des configurations atomiques et les forces entre atomes peuvent être calculées. Traditionnellement, les SEIPs pour UO_2 combinent des potentiels de paire, tels que

l'interaction coulombienne et le modèle de Buckingham [27], dont les paramètres sont ajustés sur des propriétés expérimentales [28–32]. Une fois les paramètres definis, ces potentiels peuvent être utilisés dans des simulations à grande échelle de dynamique moléculaire classiques ou Monte Carlo [33] pour étudier les structures de défauts étendues, telles que les cascades de déplacements, les dislocations ou les joints de grains [34–36]. Plus récemment, Cooper, Rushton et Grimes ont introduit une contribution à plusieurs corps [37] en addition des termes de paire [38]. Le potentiel ainsi nommé Cooper-Rushton-Grimes (CRG), a nettement amélioré les écarts précédemment observés sur les propriétés élastiques par rapport aux observations expérimentales [39, 40], et permet de prédire avec précision les constantes élastiques et certaines propriétés thermophysiques en excellent accord avec les mesures expérimentales. Le potentiel CRG a notamment été utilisé dans diverses études, y compris la dérivation d'une loi de capacité thermique testée dans les codes de performance des combustibles [41] et le calcul des structures de joints de grains [42]. Cependant, aucun des SEIPs mentionnés ci-dessus n'a été spécifiquement conçu pour reproduire les énergies de formation et de migration des défauts ponctuels, et présentent des désaccord avec les prédictions DFT+U [24, 43–45]. En outre, ces SEIPs présentent des divergences significatives entre eux en ce qui concerne les énergies de formation des défauts ce qui peut avoir des conséquences importantes lors de la simulation par dynamique moléculaire de l'accumulation de defauts d'irradiation [46]. Des différences dans les surfaces d'énergie de fautes d'empilement, cruciales pour la prédiction des structures de dislocation et de joints de grain, ont également été observées dans UO_2 parmi les potentiels disponibles [47]. Ces différences peuvent, entre autre, conduire à des écarts importants sur la formation et la mobilité des dislocations. Enfin, les performances du potentiel CRG ont récemment été examinées pour la prédiction de la conductivité thermique [44, 45] montrant des valeurs largement supérieures aux données expérimentales. Une forte surestimation de la conductivité thermique, peut être considérée comme un inconvénient majeur, étant donné qu'elle est sans doute l'une des propriétés physiques les plus importantes, sinon la plus importante, pour un combustible nucléaire.

Ces différences entre les modèles disponibles (DFT+U et les différents SEIPs) sont sources d'incertitudes pour la prédiction des propriétés simulées à l'échelle atomique, notamment concernant l'accumulation de dommage d'irradiation et le comportement élastoplastique, malgré leur importance fondamentale dans les combustibles nucléaires. De ce constat émerge un besoin d'amélioration des potentiels interatomiques, qui doivent être capables de décrire avec précision toutes les propriétés que l'on pourrait attendre d'un combustible post-irradié : conductivité thermique, dommages causés par l'irradiation (défauts ponctuels et dislocations), comportement thermomécanique, etc. Le tout en faisant le lien d'échelle entre les résultats obtenus par DFT+U, dynamique moléculaire classiques et les observations expérimentales.

Ces dernières années, des outils d'apprentissage automatique (*machine learning*) ont été utilisés avec succès pour apprendre des paysage d'énergie potentielle complexes à partir d'ensembles de données de calcul *ab initio* de référence. Ces potentiels numériques (aussi appelés "machine learning interatomic potentials" MLIPs) se sont

avérés performants pour décrire avec précision de nombreux matériaux [48]. Deux études récentes ont exploité ces approches *machine learning* pour les combustibles nucléaires. Yang *et al.* on developpé un potentiel basé sur des réseaux de neurones pour des calculs de conductivité thermique dépendant spécifiquement de la température dans le dioxyde d'uranium [49]. Kobayashi *et al.* ont appliqué des potentiels réseaux de neurones au dioxyde de thorium ThO_2 [50]. Ces deux études ont permis d'obtenir d'excellentes résultats sur les propriétés thermophysiques, mais n'ont pas étudié les configurations de défauts ponctuels ou étendus. Elles ont également mis en évidence les difficultés liées à l'extension de leur étude aux structures de défauts dans UO_2, notamment en raison de la complexité supplémentaire introduite par les calculs dans le formalisme DFT+U.

L'objectif de ce travail était donc d'explorer la faisabilité de l'application de ces méthodes à des matériaux complexes à base d'oxydes d'actinides et de développer des potentiels numériques qui devrait décrire à la fois les propriétés thermiques, mécaniques, élastiques et les défauts pour simuler avec précision le combustible irradié par le biais de simulations de dynamique moléculaire classique à grande échelle.

La première partie de ce travail de thèse (Chapitre 2) a été consacrée au développement et à la validation de deux potentiels interatomiques numériques pour le dioxyde d'uranium en utilisant les méthodologies SNAP (modèle linéaire) et HDNNP (reseau de neurones). Des méthodes d'apprentissage actif ont été associées aux calculs de DFT+U pour générer des ensembles divers et représentatif de configurations atomiques sur lesquelles les potentiels ont été entraînés. Malgré la complexité des calculs DFT+U de référence, les deux potentiels présentent un bon accord avec un ensemble de métriques *ab initio* et expérimentales. La dépendance à la température des potentiels a notamment été étudiée, en particulier en ce qui concerne l'évolution des constantes élastiques, de l'expansion thermique et de la capacité calorifique. La comparaison avec les données expérimentales existantes montre un accord raisonnable. En outre, les potentiels reproduisent avec succès la transition superionique (transition de Bredig) autour de 2500 K (voir Figure 3), caractérisé par un pic dans l'évolution de la chaleur spécifique en température, et ce malgré les petites configurations de 96 atomes utilisées dans la base de données d'entraînement. Cette transition, associée à une mobilité accrue du sous-réseau d'oxygène, a été discutée théoriquement et expérimentalement et fait toujours l'objet d'intenses recherches [51, 52]. Le potentiel SNAP a ensuite été utilisé pour minimiser des configurations atomiques correspondant à des fautes d'empilement et permis leur évaluation par DFT+U. Les surfaces d'énergie de fautes d'empilement calculées avec cette approche pourraient contribuer de manière significative à la compréhension du comportement plastique du matériau, notamment par l'évaluation des contraintes de nucléation des dislocations. Ces résultats sont fondamentaux pour le domaine des combustibles nucléaires irradiés, ils permettent, en effet, de vérifier la validité et la précision des potentiels interatomiques pour simuler la mobilité et la stabilité des dislocations dans UO_2. Finalement, des applications physiques des potentiels, réalisées en collabora-

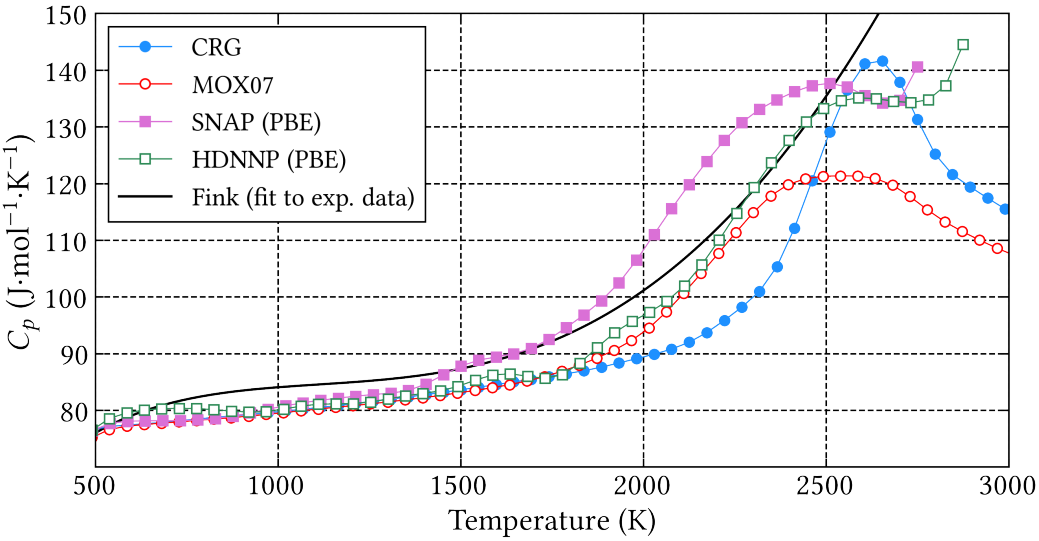

Figure 3 – Évolution de la chaleur spécifique, C_p, en fonction de la température. La ligne noire correspond aux recommandations expérimentales de Fink *et al.* [53].

tion avec d'autres étudiants, ont été brièvement présentées. La première était l'étude de la diffusivité de l'oxygène dans le dioxyde d'uranium hyper-stoechiométrique UO_{2+x}, pour laquelle un SNAP spécifique a été développé sans interactions coulombiennes à longue portée. Ce travail a mis en évidence la corrélation possible entre le volume du matériau et le mouvement collectif de l'oxygène associé à la transition de Bredig. La seconde étude concernait l'utilisation du SNAP dans le cadre de la méthode ART pour le calculs des coefficients de diffusion de défauts ponctuels dans le matériau. Le SNAP a notamment permis de calculer les énergies de migration de trois types de défauts montrant des différence avec le potentiel CRG.

Malgré les résultats très prometteurs obtenus dans la première partie de la thèse, un certain nombre de questions restaient en suspens, en particulier la sous-estimation de la densité prédite par nos MLIPs, en fort désaccord avec les prédictions expérimentales. Bien que le problème soit identifié et lié à la fonctionnelle d'échange-corrélation GGA-PBE utilisé pour la construction de la base de données, dont les potentiels ne sont censés être qu'un reflet, de nombreuses discussions ont soulevé la question de la confiance que l'on peut accorder aux résultats prédits avec ces potentiels par simulations à grande échelle du combustible. C'est pourquoi, dans une deuxième partie (Chapitre 3), nous avons cherché à réconcilier les approximations DFT avec les observations expérimentales. Nous avons choisi d'utiliser la fonctionnelle d'échange-corrélation GGA-PBEsol, qui nous a permis d'améliorer l'accord entre nos prédictions et la densité expérimentale. Afin de reproduire correctement la structure fluorine isotrope du matériau, nous avons également choisi d'utiliser un ordre magnétique 3**k** non colinéaire. À cette fin, il a été nécessaire de prendre en compte le couplage spin-orbite dans les

calculs afin de stabiliser les configurations magnétiques associées, et, comme cela a déjà été discuté dans la littérature, nous a également permis de nous affranchir de la procédure de contrôle des matrices d'occupation électronique. Ce nouveau jeu de paramètre DFT+U a ensuite été utilisée comme base pour le développement et la validation d'un nouveau SNAP qui présente un très bon accord avec la densité expérimentale jusqu'à 2500 K, et corrige donc certaines des principales préoccupations soulevées par les potentiels précédents. Confiants dans ce nouveau potentiel, nous avons ensuite étudié les propriétés thermomécaniques du matériau en calculant la surface d'écoulement du matériau, représentant la dépendance à l'orientation de la contrainte macroscopique à la nucléation du premier mécanisme de déformation irréversible. Les résultats obtenus mettent en évidence un comportement anisotrope d'UO_2 à 300 K en termes de seuils de contrainte mais aussi dans le type de mécanisme accommodant la déformation. Nous avons observé au moins 3 types de mécanisme : le flambage, la fracturation et la nucléation de dislocations (Figure 4-b).

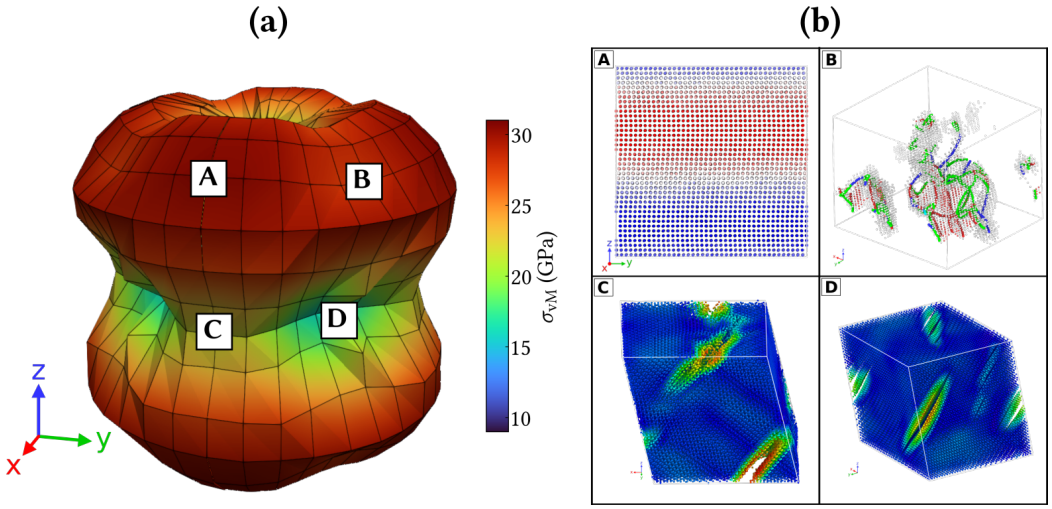

Figure 4 – (a) Surface d'écoulement d'UO_2 à 300 K obtenue pour $\dot{\gamma} = 10^8 s^{-1}$. Les labels A, B, C et D correpondent à des directions particulières retenues pour une examination approfondie des mécanismes activés; (b) Défauts de plasticité nucléés pour les directions A, B, C et D.

L'influence de la température sur la surface d'écoulement a été étudiée, révélant à la fois une forte diminution des contraintes seuil et une isotropisation du matériau. Nous avons également observé une transition entre un comportement fragile à 300 K et un comportement plus ductile à des températures plus élevées. Cette transition fragile-ductile, observée expérimentalement pour UO_2, conforte les capacités de prédiction de ce nouveau SNAP-PBEsol. Enfin, nous avons examiné l'influence de la microstructure, en particulier la présence de défauts d'irradiation (défauts ponctuels et dislocations) préexistants avant la déformation. En particulier, nous avons observé qu'une densité initiale non nulle de dislocations participe fortement à l'abaissement des contraintes critiques et à l'homogénéisation de la réponse plastique. Ces résultats préliminaires,

qui mettent en évidence le comportement mécanique diversifié et complexe du dioxyde d'uranium, ont également été une bonne occasion de démontrer la capacité du potentiel développé à réaliser des simulations de dynamique moléculaire à grande échelle impliquant de multiples phénomènes physiques.

Remerciements

Je remercie en premier lieu les membres du jury, M. Matthieu VERSTRAETE et Mme Marie-Pierre GAIGEOT, rapporteurs, ainsi que David A. ANDERSSON, Thomas D. SWINBURNE et Cosmin-Mihai MARINICA, examinateurs, pour avoir accepté d'évaluer mes travaux.

Cette thèse, réalisée entre le CEA Cadarache et le CEA-DIF, n'aurait pas été possible sans l'accueil et les moyens matériels mis à disposition par les différents laboratoires, dirigés par M. Emeric BOURASSEAU, M. Nicolas PINEAU et M. Jean-Bernard MAILLET, qui m'ont accueilli successivement au cours de la thèse.

Je souhaite également remercier mon directeur de thèse, M. Michel FREYSS, et mes encadrants M. Johann BOUCHET, M. Jean-Bernard MAILLET et M. Julien TRANCHIDA pour m'avoir fait confiance en me confiant la réalisation de cette thèse et pour m'avoir soutenu à chaque étape de ce travail. Un remerciement particulier à M. Paul LAFOURCADE dont l'encadrement non officiel a joué un rôle clé dans la réalisation de ce travail. Je les remercie pour leurs précieux conseils et les nombreuses discussions, qui, pendant ces années d'initiation à la recherche, ont été sources de motivation et d'enrichissement.

Je remercie l'ensemble des membres des laboratoires et services dans lesquels j'ai évolué pendant ces trois ans, d'abord à Cadarache, puis à la DIF. Merci à vous pour votre accueil et pour tous les échanges, scientifiques ou non, sans lesquels ces années auraient été bien différentes.

Je tiens à remercier Mathieu et Baptiste avec qui j'ai partagé cette aventure, d'abord à Cadarache puis à distance, et qui ont toujours été un soutien moral et scientifique (particulièrement en ce qui concerne la DFT sur les actinides). Et bien sûr *la team*, Pauline et Killian, sur lesquels j'ai toujours pu compter dans les bons moments mais aussi dans les plus difficiles.

Enfin, merci à ma famille pour leur soutien sans faille. Merci pour vos encouragements tout au long de mes études, pour l'intérêt que vous avez porté à mon travail, et pour votre présence au quotidien.

Table of contents

Affidavit i

List of publications and conference participations iii

Résumé v

Abstract vii

Résumé général ix

Remerciements xvii

Table of contents xix

List of Acronyms xxi

Introduction 1

1. Atomistic scale modelling: Review and Methodology 9
- 1.1. Molecular Dynamics . . . 10
  - 1.1.1. Derivation of molecular dynamics . . . 10
  - 1.1.2. Numerical integration of equations of motions . . . 11
  - 1.1.3. Control the temperature and pressure of the system . . . 12
- 1.2. First principle methods . . . 12
  - 1.2.1. The many-body problem . . . 12
  - 1.2.2. Density Functional Theory . . . 14
- 1.3. Classical Methods . . . 20
  - 1.3.1. Semi-empirical interatomic potentials . . . 21
  - 1.3.2. Electrostatic interactions . . . 24
  - 1.3.3. Semi-empirical potentials for actinide oxides . . . 25
- 1.4. Machine learning interatomic potentials . . . 28
  - 1.4.1. Local atomic environments . . . 29
  - 1.4.2. Training and Validation . . . 32
  - 1.4.3. Spectral Neighbour Analysis Potential . . . 33
  - 1.4.4. High-Dimensional Neural Network Potential . . . 37
- 1.5. Conclusion . . . 47

2. Machine learning potential for UO_2 **49**
2.1. Density Functional Theory setup . . . 50
2.2. Structure of the potential . . . 52
2.3. Training Procedure . . . 54
2.3.1. Spectral neighbour analysis potential . . . 54
2.3.2. High dimensional neural network potentials . . . 54
2.4. Database description . . . 58
2.4.1. Initial training set . . . 58
2.4.2. Active learning . . . 59
2.5. Assessment of the potentials . . . 62
2.5.1. Numerical errors . . . 62
2.5.2. Equation of state . . . 64
2.5.3. Phonons . . . 66
2.5.4. Thermodynamics properties . . . 67
2.5.5. Thermo-elasticity . . . 70
2.5.6. Point defects formation energy . . . 75
2.5.7. Generalised stacking fault surfaces . . . 75
2.6. Potential use cases . . . 80
2.6.1. Oxygen diffusivity in UO_2 and UO_{2+x} . . . 80
2.6.2. Cationic auto-diffusion in UO_2 . . . 82
2.7. Conclusion . . . 85

3. Mechanical response of UO_2 single crystal at the atomic scale **87**
3.1. Toward a new DFT recipe . . . 88
3.2. A new database, a new potential . . . 92
3.3. Assessment of the SNAP-PBEsol . . . 94
3.4. Application: UO_2 mechanical response at the atomic scale . . . 105
3.4.1. Method . . . 105
3.4.2. UO_2 single crystal at 300K . . . 109
3.4.3. Effect of strain-rate on the flow surface . . . 114
3.4.4. Effect of temperature . . . 116
3.4.5. Effect of irradiation at ambient temperature . . . 122
3.4.6. Irradiation and temperature effects altogether . . . 126
3.5. Conclusion . . . 130

Conclusions and perspectives **133**

Bibliography **137**

A. Elasticity in solids **161**

B. Mechanical study: Supplementary materials **165**

List of Acronyms

ACSF Atom Centred Symmetry Function 31, 39–42, 47, 55
Adam Adaptive Moment Estimation 43, 46
AFM Anti-ferromagnetic 51, 88, 89
AIMD ***Ab Initio*** Molecular Dynamics 11, 20, 68, 98
AL Active Learning 59–61
AMF Around Mean Field 18
ANN Artificial Neural Network 37
ART Activation-relaxation Technique 83, 85, 134

BAL Batch Active Learning 61
BO Born-Oppenheimer 13, 20
BSD Bounded Schottky Defect 4, 75, 83, 84, 92

CEA French Alternative Energies And Atomic Energy Commission 2
CMD Classical Molecular Dynamic 11, 21, 24
COMB Charge-optimized Many-body 27
CRG Cooper-Rushton-Grimes xii, 5, 25–28, 64, 66–68, 70–77, 80, 81, 83, 85, 92–94, 97–100, 104, 134

DDD Discrete Dislocation Dynamics 130
DFT Density Functional Theory 3, 4, 6, 10, 14, 16, 18–20, 28, 36, 39, 50, 52–54, 59, 62–64, 76, 88, 94–96, 103, 130, 134
DFT+*U* Hubbard Corrected DFT 4–6, 18, 19, 47, 50–53, 62, 64–66, 68–72, 75–78, 81, 83, 85, 88, 91, 92, 95, 96, 98, 133
DMFT Dynamical Mean Field Theory 18
dpU Displacement Per Uranium 122–130
DXA Dislocation Extraction Algorithm 113, 120, 122

EAM Embedded Atoms Method 5, 23, 25, 54, 92
EKF Extended Kalman Filter 44–46, 58

FLL Full Focalized Limit 18
FP Fission Product 1–4
FPA Frenkel Pairs Accumulation 122

GAP Gaussian Approximation Potential 31
GGA Generalized Gradient Approximation 17, 18, 50, 87, 88, 92, 134

HBS High Burn-up Structure 1–4
HDNNP High Dimensional Neural Network Potential 6, 10, 31, 32, 37, 39, 40, 44, 46, 47, 50, 55, 57, 58, 62, 64, 66, 76, 85, 133

KF Kalman Filter 44, 45
KineCluE Kinetic Cluster Expansion 83

LDA Local Density Approximation 17, 18, 88
LSE Least Square Estimator 36, 37, 54

MAE Mean Absolute Error 33, 62
MD Molecular Dynamics 5, 6, 10–12, 22, 24, 25, 47, 75, 85, 103, 105, 109, 114, 116, 122–124, 130, 135
MEAM Modified Embedded Atoms Method 23, 54
MEP Minimum Energy Path 76, 77, 101
ML Machine Learning 29, 54, 93
MLACS Machine Learning Assisted Canonical Sampling 58, 72–74, 100
MLIP Machine Learning Interatomic Potential 6, 28, 29, 32, 33, 47, 51, 59–62, 64–69, 71, 72, 75–77, 80, 83, 85, 87, 88, 97, 98, 133–135
MLP Multilayer Perceptron 37–39, 43, 47
MTP Moment Tensor Potential 54

NEB Nudged Elastic Band 6, 50, 83, 85, 134
NN Neural Network 39, 40
NNP Neural Network Potential 54

OMC Occupancy Matrices Control 6, 19, 20, 88, 130

PAW Projected Augmented Wave 50, 92
PBE Perdew, Burke And Ernzerhof 17, 50, 69, 70, 87, 88, 92, 97, 98, 101, 104, 134
PBEsol PBE Revised For Solids 6, 17, 88, 90–92, 96, 97, 99, 101, 130, 134
PDOS Phonon Densities Of States 66
PES Potential Energy Surface 13, 28, 29, 39, 59, 83
pppm Particle-particle-particle-mesh 24, 53, 92, 93

QBC Querry-by-committee 60
QHA Quasi-harmonic Approximation 66, 67

RMSE Root Mean Square Error 33, 54, 60, 62

SEIP Semi-empirical Interatomic Potential 5, 6, 10, 11, 21, 28–30, 33, 47, 50, 59, 65, 71, 83, 133
SGD Stochastic Gradient Descent 43, 46
SMTB-Q Second Moment Tight-binding Qeq 27, 28, 64
SNAP Spectral Neighbour Analysis Potential 6, 10, 31, 32, 34, 36, 37, 47, 50, 54, 58, 62, 66, 76, 80, 81, 85, 92, 97, 105, 116, 130, 133, 134

SOC Spin-orbit Coupling 51, 88, 90–92, 96, 99, 101, 130, 134

TDEP Temperature Dependent Effective Potential 66

ZBL Ziegler-Biersack-Littmark 22, 23, 52, 53, 66, 92

Introduction

I'm sure the universe is full of intelligent life. It's just been too intelligent to come here.

– Arthur C. Clarke

Pellets of uranium dioxide (UO_2) and mixed oxide $(U,Pu)O_2$, also referred to as MOX, are the reference fuel for most nuclear power plants in the world. In operating, incidental or accidental conditions, these pellets are facing severe conditions of radial heat gradient ($\simeq$ 500K between the centre and the periphery of the 1 cm diameter pellet), strong mechanical stress and radiation damages. This dramatically impacts their microstructure, with observed phenomena such as creep, cracking, intense restructuring such as formation of the high burn-up structure (HBS) (Figures 5-a and 5-c) or the accumulation and precipitation of fission products (FPs) (Figures 5-b and 5-c).

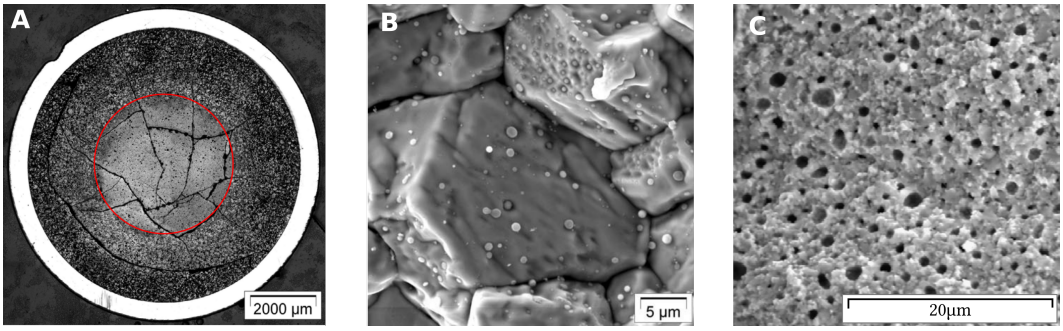

Figure 5 – **A** - Optical macrographs after chemical etching of an heterogeneous UO_2 fuel at 63 GWd/tU [1]; **B** - The surface of MOX fuel grains after irradiation. The round spots are precipitates of metallic fission products, and the cavities the signature of empty fission gas bubbles [2]; **C**- SEM fractographs illustrating a HBS at the rim of a UO_2–M5^{TM} [3].

This restructuring of the fuel pellets implies several consequences for the fuel material itself, such as an important decrease of their already low thermal conductivity (as UO_2 is an electronic insulator) [4], therefore leading to a stronger heat gradient within the pellets, or a modification of the pellet elastoplastic response [5, 6]. The evolution of fuel properties also impacts the cladding materials, for instance swelling of the pellet due to fission gas accumulation or stress corrosion cracking of the ductile zircaloy cladding material, facing corrosive and volatile fission products (Cs, I) that might be

released from the pellet [7, 9, 54, 55]. It is imperative for the French Alternative Energies And Atomic Energy Commission (CEA) to understand and be able to predict such an evolution of the fuel pellet microstructure and associated physical properties, as it will drive the fuel performance codes and strongly impact the safety margins of the reactors.

To gain insights into these phenomena and their interconnections, comprehensive characterisations and experimental measurements of post irradiated fuel are crucial. Although performing those experiments is hindered by the associated cost and complexity, the acquisition of such information holds crucial significance in constructing accurate models and obtaining reliable data that will be fed into fuel performance codes, such as the ALCYONE [11] and GERMINAL [12] codes developed by the CEA, respectively for 3rd and 4th generation of reactors, that aims to model nuclear assembly during operating conditions.

To complete and supplement experimental studies, the CEA's Nuclear Fuel Department is deeply involved in the development of a large multiscale simulation programme, as illustrated in Figure 6, through the PLEIADES platform [13], which embeds tools for numerical simulation of the fuel element during its different lifetime phases (manufacture, behaviour under irradiation, storage). This multiscale approach involves refining the laws and parameters of macroscopic models by accurately modelling the elementary physical processes occurring on smaller scales. The PLEIADES platform draws on data ranging from highly accurate *ab initio* electronic structure calculations to thermomechanical modelling using finite elements, going through classical methods (molecular dynamics, monte carlo), cluster dynamics, phase fields, discrete dislocation dynamics, and many others. The wide range of data, from different scales, guarantees the quality of the physical representation and ultimately enables an accurate description of the life cycle of nuclear fuel materials.

In this context, atomic scale simulations, i.e. where interactions between atoms are investigated, (marked as blue in Figure 6) have been extensively employed to provide, among others, structural, elastic and thermodynamics data to macroscopic codes. Atomistic simulations are not limited to thermodynamics database feeding, but also come as an incredibly valuable tool to gain insights and understanding of underlying physical phenomena that occur in complex materials such as post-irradiated fuels.

A very good example is the formation of the HBS, occurring when the burn-up, i.e., the combustion rate or the irradiation rate, which measures the fraction of nuclear fuel that is consumed in a reactor, reaches a certain level. It is of particular importance for the description of fuel materials as it leads to important restructuring (see Figure 5-c) and impacts thermal properties, hardness, swelling and fission gas release. Such a structure is expected to be formed due to interactions of accumulated : (1) radiation damage, including point defects and dislocations; (2) FPs; and (3) stored energy from inelastic damaging processes. Figure 7 illustrates a proposed series of mechanisms for the formation of the HBS, as discussed by Sonoda *et al.* [56]. At low burn-up, radiation damage leads to the accumulation of point defects and dislocations, although much of this damage is mitigated by recombination and the annealing of fission tracks. Electronic

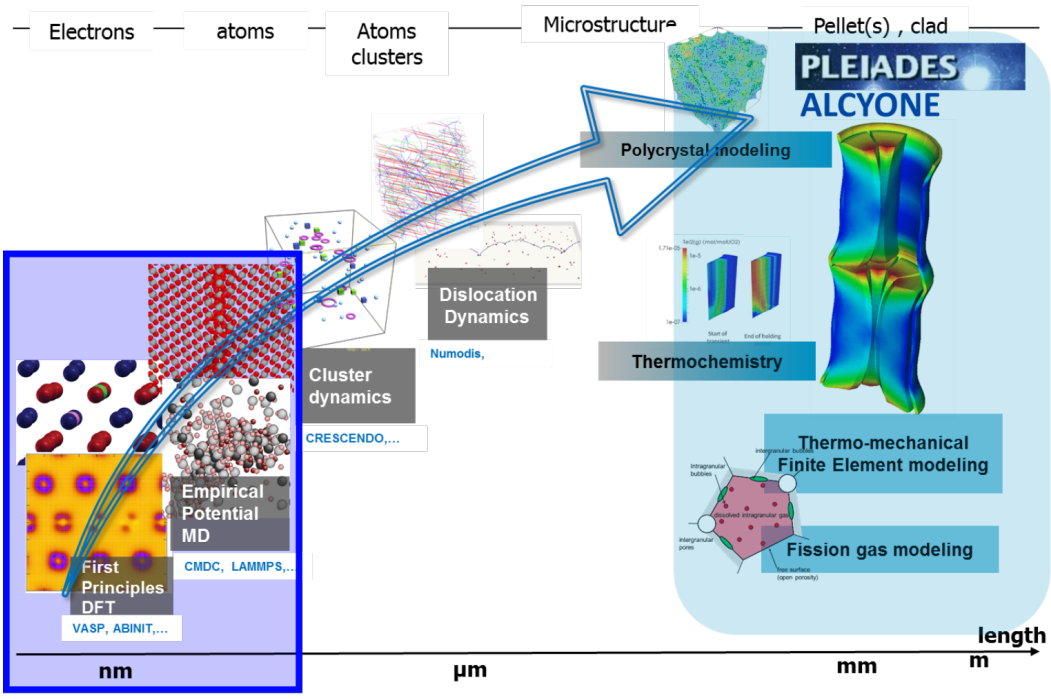

Figure 6 – Illustration of the multiscale approach for the nuclear fuel simulation. The characteristic space scales of the different methods are given by the x-axis. The blue square encompasses the atomistic methods.

excitation not only aids in annealing, but also enhances the diffusion of interstitials and vacancies, contributing to the growth of dislocation loops and possibly increasing their mobility [57]. As burn-up increases, FPs accumulate upon reaching a certain size and density. The FPs precipitates will then start to interact with radiation damage, pinning dislocations at extended defects locations (such as nanometric fission gas bubbles) and causing them to pile up. Further burn-up causes the accumulation of dislocations and FPs precipitates to act as sinks for radiation defects and FPs, leading to significant strain energy within the grains [58]. Eventually, this strain energy is relieved through the formation of low-angle subgrain boundaries heavily decorated with FP bubbles and precipitates. During subgrain formations, FPs may migrate in conjunction with vacancies within these boundaries, potentially leading to the formation of numerous coarsened bubbles and slight rotation of the subgrains.

In this described formation process of the HBS, the steps marked in red in Figure 7 can be simulated at the atomic level in order to investigate fundamental physical processes at stake [42, 59, 60]. This provides valuable insight on complex interacting phenomena that are likely to be found in post irradiated fuel and, therefore, must be accurately described and predicted by macroscopic fuel performance codes. We distinguished two principal methods used at the atomic scale characterised by their respective time and space scales.

First-principles methods, also referred to as *ab initio* methods, such as density functional theory (DFT), have proven to be a reliable tool for predicting energies, atomic

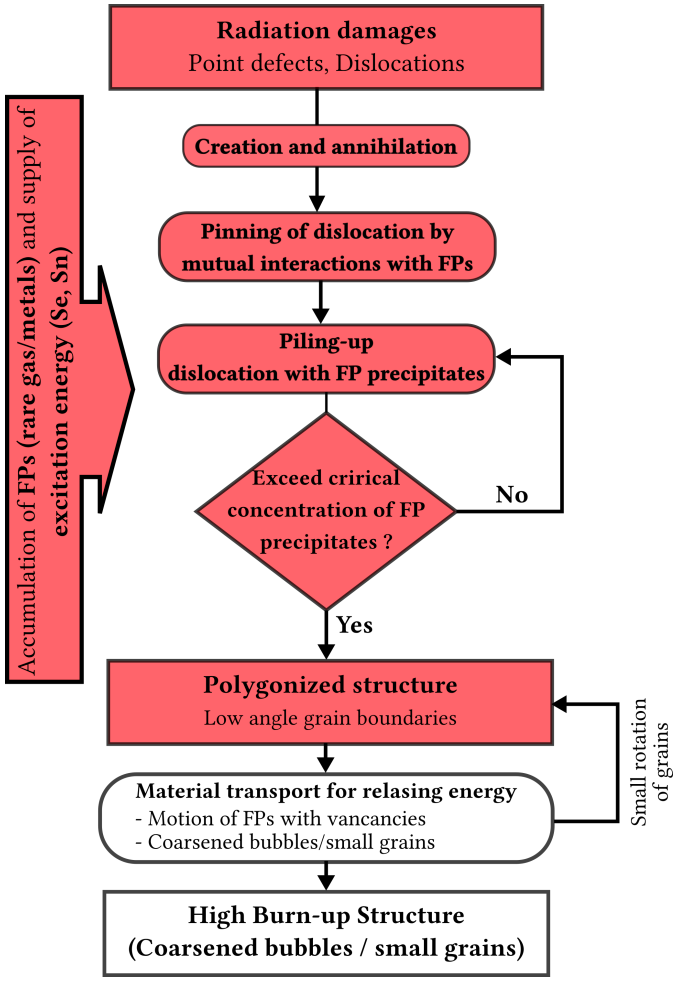

Figure 7 – Diagram of a proposed formation mechanism for the HBS by polygonization, showing the effects associated to the accumulation process of radiation damage, FP and excitation energy. Adapted from [56].

forces, and stress tensors of small atomic configurations. However, for UO_2 , the application of a Hubbard correction term is necessary to account for the strong correlations among uranium $5f$ electrons [14–17], introducing additional complexity compared to standard DFT [17, 18] to converge towards the ground state due to metastable states in the electronic structure. Within this Hubbard corrected DFT (DFT+U) framework, accurate computations of formation energies of interstitial atoms or vacancies, such as the neutral bounded Schottky defects (BSDs), have been extensively performed [17, 19, 20]. These formation energies can be incorporated into thermodynamic models, to calculate diffusion rates of defects [21, 22]. Although more challenging, small clusters of those defects can also be considered at the DFT level [23]. Recent studies have highlighted the importance of considering larger simulation cells (for example 3×3×3 supercells, corresponding to 324 atoms) for accurately predicting bounded Schottky defect (BSD) formation energies [24, 25], emphasising the need for calculations at a larger scale than typical DFT simulations. While recent advances have allowed DFT-based descriptions

of thermophysical properties in nuclear fuels [26], these methods are still limited to small atomic configurations, and modelling temperature-dependent large-scale effects remains challenging within the DFT+U framework.

At larger scales, semi-empirical interatomic potential (SEIP) have been developed and applied to UO_2. Those SEIPs define a potential energy landscape from which energies of atomic configurations and forces between atoms can be computed. Traditionally, SEIPs for UO_2 have combined pair potentials, such as the Coulombic interaction and the Buckingham model [27], fitted to experimental properties [28–32]. Once constructed, those potentials were used in large-scale classical molecular dynamics (MD) or Monte Carlo simulations [33] to investigate extended defective structures, such as displacement cascades, dislocations, or grain boundaries [34–36]. More recently, Cooper, Rushton, and Grimes introduced a many-body embedded atoms method (EAM) contribution [37] to pairwise terms [38]. Referred to as the CRG potential, it improved upon previously observed deviations from experimental elastic properties [39, 40], and accurately predicted elastic constants and thermophysical properties in excellent agreement with experimental measurements. Notably, the CRG potential has been employed in various studies, including the derivation of a heat-capacity law tested in fuel-performance codes [41] and the computation of grain boundary structures with excellent agreement to experimental observations [42]. However, none of the SEIPs mentioned above were specifically designed to reproduce the formation and migration energies of small atomic structures, such as defects, as predicted by DFT+U [24, 25]. Furthermore, these SEIPs exhibit significant discrepancies regarding defect's formation energies, which can critically impact the outcomes of MD simulations of damage accumulation, as recently discussed by Van Brutzel *et al.* [46]. Differences in the calculated stacking-fault energy surfaces, crucial for the prediction of dislocation and grain boundary structures, have also been observed in UO_2 among SEIP [47]. The observed differences can lead to large discrepancies in terms of predicted extended defect configurations, such as dislocation formation and mobility. Eventually, the CRG potential has recently been reviewed for thermal conductivity predictions [44, 45] exhibiting a much higher thermal conductivity values than experimental data. This suggests that empirical potentials for UO_2 should be further optimised for a more robust prediction of the thermal conductivity both in perfect crystals and in the presence of complex defects. This can be seen as a significant drawback of these potentials, given that thermal conductivity is arguably one of the most important physical properties, if not the most important, of a nuclear fuel.

Overall, inconsistencies between available models (DFT+U and different SEIPs) have been hampering down the predictability of damage accumulation and plastic behaviour simulations, despite their fundamental importance in nuclear fuels. This observation highlights the need for interatomic potentials capable of accurately capturing all properties expected to characterise post-irradiated fuel, such as thermal conductivity, radiation damage (including point defects and dislocations), and thermomechanical behaviour, thus enabling large-scale MD simulations that encompass all relevant interacting physical phenomena. Bridging results from DFT+U, classical MD, and experimental observations.

In recent years, machine learning tools have been successfully employed to learn complex potential energy surfaces from reference *ab initio* calculation datasets. These machine learning interatomic potentials (MLIPs) have been proven to be effective in accurately describing various classes of materials [48]. Two recent studies have explored the potential of MLIPs in nuclear fuel materials. Yang *et al.* trained a neural network potential on UO_2 configurations for specifically temperature-dependent calculations of thermal conductivity [49]. Kobayashi *et al.* applied neural network potentials to train three MLIPs for thorium dioxide ThO_2 [50]. Both studies obtained excellent thermophysical properties, but did not investigate point or extended defect configurations. They also highlighted the challenges of extending their study to defect structures in UO_2, particularly due to the additional complexity introduced by DFT+U calculations.

The intention of this work was to explore the feasibility of applying machine learning methods to complex actinide oxides materials in order to train MLIPs that should describe at the same time thermal, mechanical, elastic, defects properties to accurately simulate post irradiated fuel through large-scale classical MD simulations with first principles accuracy at a fragment of its computational cost.

This manuscript is organised in four chapters. The first chapter briefly details the atomistic methods used in this work. In particular DFT and classical methods as well as their applications on actinide oxides. It will be followed by an introduction to machine learning potentials starting from the key concept of local atomic descriptor up to high-dimensional optimisation regression problems. Dedicated section, will be reviewing the spectral neighbour analysis potential (SNAP) and high dimensional neural network potential (HDNNP) formalisms that are used in upcoming chapters.

The second chapter is dedicated to the training and validation of two machine learning interatomic potentials for uranium dioxide using the SNAP and HDNNP methodologies. The first objective was to generate a representative *ab initio* database by DFT+U calculation using the occupancy matrices control (OMC) procedure. In order to reduce the time and cost required to build this database, we combined electronic structure calculations with active learning methods to accelerate the sampling of the high-dimensional configuration space. Eventually, the developed potentials are assessed against reference data and their predictions in molecular dynamics simulation are confronted to other SEIPs and available experimental data. The final section of the chapter is dedicated to the presentation of research applications, performed in collaboration with other students, using the developed MLIPs. In particular concerning the oxygen diffusivity in off-stoichiometric UO_{2+x} fuel and the migration of point type defects using nudged elastic band (NEB) calculations.

The aim of the third chapter is to reconcile DFT+U and experimental observation, in particular concerning the well known problem of the underestimated density predicted by DFT using the GGA-PBE exchange-correlation functional. Based on the PBE revised for solids (PBEsol) functional along with non-collinear 3$\mathbf{k}$ magnetic order and spin-orbit coupling, we modified our DFT+U calculation setup to find the best agreement with experimental observation [61–63]. With this new DFT+U setup, a SNAP potential was

developed and assessed using the methodology described in Chapter 2. In a second step, this newly developed SNAP-PBEsol was used to investigate thermo-mechanical properties of UO_2, in particular, the directional dependence of the macroscopic stress at the onset of the first irreversible deformation mechanism, also referred to as critical shear stress flow surface [64, 65].

In the final section of the manuscript, the results are synthesised and the numerous perspectives opened by this work are discussed.

Chapter 1.

Atomistic scale modelling: Review and Methodology

Product of optimism and knowledge is a constant.

– Lev Landau

Contents

1.1. Molecular Dynamics . . . 10
1.1.1. Derivation of molecular dynamics . . . 10
1.1.2. Numerical integration of equations of motions . . . 11
1.1.3. Control the temperature and pressure of the system . . . 12
1.2. First principle methods . . . 12
1.2.1. The many-body problem . . . 12
1.2.2. Density Functional Theory . . . 14
1.3. Classical Methods . . . 20
1.3.1. Semi-empirical interatomic potentials . . . 21
1.3.2. Electrostatic interactions . . . 24
1.3.3. Semi-empirical potentials for actinide oxides . . . 25
1.4. Machine learning interatomic potentials . . . 28
1.4.1. Local atomic environments . . . 29
1.4.2. Training and Validation . . . 32
1.4.3. Spectral Neighbour Analysis Potential . . . 33
1.4.4. High-Dimensional Neural Network Potential . . . 37
1.5. Conclusion . . . 47

In this chapter, we will briefly review common methods used for atomic-scale modelling of materials, with a focus on condensed matter. We will specifically examine the molecular dynamics method, the DFT, and classical approaches that involve SEIPs. Subsequently, we will delve into the formalism behind two machine learning potentials: namely SNAP and HDNNP. Given the breadth of methods to be discussed, our review will not be exhaustive but will aim to provide a general overview, with particular emphasis on points that are relevant to the present work.

1.1. Molecular Dynamics

1.1.1. Derivation of molecular dynamics

The MD method involves following, in space and time, the evolution of a multi-particulate system. The fundamental equations of MD for a system of N discrete point particles of mass m, can be derived by considering the following Hamiltonian $\mathcal{H}$:

$$\begin{aligned}\mathcal{H}(\boldsymbol{q},\boldsymbol{p}) &= T(\boldsymbol{q},\boldsymbol{p}) + V(\boldsymbol{q}) \\ &= \sum_{i}^{N} \frac{p_i^2}{2m_i} + V(\boldsymbol{q})\end{aligned} \tag{1.1}$$

where T and V are the kinetic energy and potential energy operators respectively. In this case $\mathcal{H}$ represents the total energy of the system. It depends on $\boldsymbol{q}$ and $\boldsymbol{p}$, namely the generalised (i.e. independent of the representation space) positions and momenta. The latter is expressed from generalised velocity $\dot{\boldsymbol{q}}$, such as $\boldsymbol{p} = m\dot{\boldsymbol{q}}$. From the formulation of Hamilton's canonical equations, the Newton's equation of motion can easily be derived:

$$\dot{\boldsymbol{q}} = \frac{\partial \mathcal{H}}{\partial \boldsymbol{p}} = \frac{\boldsymbol{p}}{m}, \tag{1.2}$$

$$\dot{\boldsymbol{p}} = -\frac{\partial \mathcal{H}}{\partial \boldsymbol{q}} = -\frac{\partial V(\boldsymbol{q})}{\partial \boldsymbol{q}} \tag{1.3}$$

Considering the generalised coordinates $\boldsymbol{q}_i$ as the Cartesian coordinate $\boldsymbol{R}_i$ of one particle, one can write:

$$m\ddot{\boldsymbol{r}}_i = -\frac{\partial}{\partial \boldsymbol{R}_i} V(\boldsymbol{R}) = \boldsymbol{f}_i \tag{1.4}$$

where $\boldsymbol{f}_i$ represents the force derived from the total potential energy function $V(\boldsymbol{R})$ applied to the ith particle. In the classical limit, the potential energy function $V(\boldsymbol{r})$, also referred to as interaction potential, describes the interactions between atoms (considered as point particles) at positions $\boldsymbol{R} \equiv \{\boldsymbol{R}_1, \ldots, \boldsymbol{R}_n\}_{n=N}$. The forces $\boldsymbol{f}_i$ acting on the ith atoms can be explicitly computed from the gradient of the potential energy function:

$$\boldsymbol{f}_i = -\boldsymbol{\nabla}_{\boldsymbol{r}_i} V(\boldsymbol{r}) \tag{1.5}$$

where $\boldsymbol{\nabla}$ is the gradient operator.

An absolute keystone of MD is the potential energy function $V(\boldsymbol{R})$, as it describes **all** the physical interactions within the system and every properties predicted by the method (themodynamics, mechanicals, transports, etc.) are solely determined by $V(\boldsymbol{R})$. Ideally, $V(\boldsymbol{R})$ is derived from quantum mechanics through *ab initio* methods, leading to so-called ***ab initio*** molecular dynamics (AIMD). However due to the very high computational cost of those methods, the use of SEIP is often preferred for large-scale classical molecular dynamic (CMD) simulations. Note that in both *ab initio* and classical methods rely on the same classical propagation of the trajectory by integration of (1.4) and only differs by the way $V(\boldsymbol{R})$ is computed. Both methods will be discussed in dedicated Sections 1.2 and 1.3.

1.1.2. Numerical integration of equations of motions

Once the interaction potential $V(\boldsymbol{R})$ is chosen, one could solve the dynamic by integrating the equations of motions (1.4). However, this integration cannot be achieved analytically and is instead discretised on short time intervals Δt. To do so, multiple numerical integration schemes have been employed and tested in the context of MD: Gear predictor-corrector [66], Euler methods, Runge-Kutta methods [67–69], the Simple-Verlet algorithm [70], Leapfrog-Verlet [71] algorithm and the one used in this work, the Velocity-Verlet algorithm [72].

In the Velocity-Verlet algorithm an iteration (going from time t to time $t + \Delta t$) is achieved in four steps:

$$1. \quad \dot{\boldsymbol{R}}\left(t + \frac{\Delta t}{2}\right) = \dot{\boldsymbol{R}}(t) + \frac{\boldsymbol{f}(t)}{2m}\Delta t \tag{1.6}$$

$$2. \quad \boldsymbol{r}(t + \Delta t) = \boldsymbol{R}(t) + \dot{\boldsymbol{R}}\left(t + \frac{\Delta t}{2}\right)\Delta t \tag{1.7}$$

$$3. \quad \boldsymbol{f}(t + \Delta t) = -\frac{\partial V(\boldsymbol{R}(t + \Delta t))}{\partial \boldsymbol{R}(t + \Delta t)} \tag{1.8}$$

$$4. \quad \dot{\boldsymbol{R}}(t + \Delta t) = \dot{\boldsymbol{R}}\left(t + \frac{\Delta t}{2}\right) + \frac{\boldsymbol{f}(t + \Delta t)}{2m}\Delta t \tag{1.9}$$

Advantages of the Velocity-Verlet integrator over other Verlet's variants is that it requires less memory and the velocities are explicitly computed during integration, allowing for the calculation of kinetic energy and temperature at the same timestep. Note also that local errors in terms of positions and velocities of the integrator are $O(\Delta t^4)$ and $O(\Delta t^2)$. The Velocity-Verlet integrator also ensures important properties for physical systems, namely time reversibility and conservation of the symplectic 2-form $(\mathrm{d}\boldsymbol{p} \wedge \mathrm{d}\boldsymbol{q})$ on phase space, along the trajectory propagation (for a suitable chosen Δt). Consequently, the Hamiltonian, and so the total energy, comes as a conserved quantity.

1.1.3. Control the temperature and pressure of the system

Direct application of the Velocity-Verlet integration along with the Hamiltonian defined as in Eq. (1.1), implies that the number of particles N, the volume V, and the total energy E are conserved. Therefore, MD simulations inherently sample the microcanonical (NVE) statistical ensemble. In many applications, it is more convenient to perform simulations with constant temperature and pressure since those are the conditions met in either laboratory experiments or naturally occurring physical phenomena.

Thermostats are algorithms that are used to steer the system's average temperature during the simulation toward a targeted temperature. Several thermostating algorithms have been developed and are widely used in MD simulations, including Andersen [73], Berendsen [74], Velocity-rescaling [75], Langevin [76, 77] and Nosé-Hoover [78, 79] thermostats.

As for thermostats, multiple barostat algorithms were developed to maintain a constant system's pressure (in average). The most widely used are due to Andersen [73], which, however, only allows for isotropic relaxation of the simulation box, and Rahman-Parinello [80], which supports anisotropic scaling of both the shape and size of the box cell vectors.

Thermostats allow for the sampling of the canonical (NVT) ensemble. When coupled with a barostat, simulations can be achieved in the isothermal-isobaric (NPT) ensemble. Note that both thermostats and barostats operate by altering the equations of motion of particles, they should therefore be used with care as they can significantly affect the calculation of particular dynamical properties of particles [81, 82].

Unless specified, in this work we used the Nosé-Hoover thermostat coupled with a Rahman-Parinello barostat as implemented in the `LAMMPS` code [83].

1.2. First principle methods

1.2.1. The many-body problem

A many-body system composed of N_n nucleus and N_e electrons, at respective positions $\boldsymbol{R} \equiv \{\boldsymbol{R}_1, \ldots, \boldsymbol{R}_n\}_{n=N_n}$ and $\boldsymbol{r} \equiv \{\boldsymbol{r}_1, \ldots, \boldsymbol{r}_n\}_{n=N_e}$, can be described at quantum level through a many-body wavefunction $\Psi(\boldsymbol{R}, \boldsymbol{r})$ that satisfies the time-independant Schrödinger equation[1] [84]:

$$\hat{H}\Psi(\boldsymbol{R}, \boldsymbol{r}) = E\Psi(\boldsymbol{R}, \boldsymbol{r}) \tag{1.10}$$

where E denotes the total energy and $\hat{H}$ is the Hamiltonian of the coupled electron-nucleus system. As in its classical formulation, see (1.1), the Hamiltonian operator is built as the sum of kinetic energy $\hat{T}$ and potential energy $\hat{V}$ operators for nucleus-nucleus, electron-electron and nucleus-electron interactions:

$$\hat{H}(\boldsymbol{R}, \boldsymbol{r}) = \hat{T}_{\mathrm{n}}(\boldsymbol{R}) + \hat{T}_{\mathrm{e}}(\boldsymbol{r}) + \hat{V}_{\mathrm{nn}}(\boldsymbol{R}) + \hat{V}_{\mathrm{ee}}(\boldsymbol{r}) + \hat{V}_{\mathrm{ne}}(\boldsymbol{R}, \boldsymbol{r}) \tag{1.11}$$

[1] The dependency of Ψ on the electronic spin variable is omitted.

where subscripts "e" and "n" denote respectively electrons and nuclei.

A first step towards a solution of (1.10) is the Born-Oppenheimer (BO) approximations [85] which suggests a partial decoupling of nuclear and electronic degrees of freedom, since their associated time scale differ by about two orders of magnitude due to significant mass difference between nuclei and electrons. In other words, the electrons are treated as evolving in a field of fixed nuclei and adapt instantly to any nuclear motions. In the classical limit, the nuclei are fully localised about single points that represent classical point particles. Under this approximation, the total wavefunction can be factorised into a nuclear wavefunction ϕ_n and an electronic wavefunction ϕ_e:

$$\Psi(\boldsymbol{R},\boldsymbol{r}) = \phi_\mathrm{n}(\boldsymbol{R})\phi_\mathrm{e}(\boldsymbol{R},\boldsymbol{r}) \tag{1.12}$$

where ϕ_e depends parametrically on nuclear positions. The electronic wavefunction can then be solved for a given set of fixed nuclear coordinates:

$$\hat{H}_\mathrm{e}\phi_\mathrm{e}(\boldsymbol{R},\boldsymbol{r}) = E_\mathrm{e}\phi_\mathrm{e}(\boldsymbol{R},\boldsymbol{r}) \tag{1.13}$$

with a Hamiltonian written as purely electronic terms[2]:

$$\hat{H}_\mathrm{e} = \underbrace{-\frac{1}{2}\sum_{i=1}^{N_e}\nabla_i^2}_{\hat{T}_\mathrm{e}} + \underbrace{\frac{1}{2}\sum_{i,j=1,i\neq j}^{N_e}\frac{1}{|\boldsymbol{r}_i-\boldsymbol{r}_j|}}_{\hat{V}_\mathrm{ee}} + \underbrace{\sum_{i=1}^{N_e} v_\mathrm{ext}(\boldsymbol{r}_i)}_{\hat{V}_\mathrm{ext}}. \tag{1.14}$$

where $\hat{V}_\mathrm{ext}$, the external ionic potential applied to electrons induced by the nuclear field, writes[3]:

$$\hat{V}_\mathrm{ext} = \sum_{i=1}^{N_\mathrm{e}}\sum_{k=1}^{N_\mathrm{n}}\frac{-Z_k}{|\boldsymbol{r}_i-\boldsymbol{R}_k|} + \sum_{k,l=1,k\neq l}^{N_\mathrm{n}}\frac{Z_kZ_l}{|\boldsymbol{R}_k-\boldsymbol{R}_l|} \tag{1.15}$$

with Z denoting nuclear atomic numbers[4].

The eigenvalue $E_{\mathrm{e},0}$ associated to the ground state $\phi_{\mathrm{e},0}$ defines a hypersurface $V_0(\boldsymbol{R})$ commonly known as the adiabatic (or Born-Oppenheimer (BO)) potential energy surface (PES). For the rest of the manuscript, it will be referred to as *interatomic potential* or simply $V(\boldsymbol{R})$. It can be seen as an equivalent to the potential energy function introduced in Section 1.1. This potential includes all the electronic effects and contributes to the nuclear motion described by ϕ_n, satisfying a Schrödinger-type equation for nuclei:

$$\left[\hat{T}_\mathrm{n} + V(\boldsymbol{R})\right]\phi_\mathrm{n} = E\phi_\mathrm{n} \tag{1.16}$$

Note that the BO approximation only applies if the potential energy surfaces $V_\mu(\boldsymbol{r})$, that are solutions of (1.13), are well separated: $V_0(\boldsymbol{R}) \ll V_1(\boldsymbol{R}) \ll \ldots \ll V_\mu(\boldsymbol{R})$.

[2] In reduced units, i.e, $m_\mathrm{e} = 1$, $\hbar = 1$ and $e = 1$.

[3] We chose to include V_nn as it only depends on nuclear coordinates and shift eigenvalues of (1.13) by a constant value

[4] The electric charge of a nucleus k is then equal to eZ_k

As suggested, the primary quantity of interest is the ground-state energy $E_{e,0}$ that, according to the variational principle, can be obtain by the following minimisation:

$$E_{e,0} = \min_{\phi_e} \langle \phi_e | \hat{H}_e | \phi_e \rangle \tag{1.17}$$

the minimum being reached for $\phi_e = \phi_{e,0}$. Even for fixed positions of nuclei, finding a solution to (1.17) is a formidable computational task. *First principle* or *ab initio* methods refer to the diverse set of methods developed in the literature to approximate a solution. For example, Hartree-Fock [86, 87] and post-Hartree-Fock [88, 89] methods are based on the expansion of the wavefunction in Slater determinants [90]. Although often used in the field of quantum chemistry for the study of small molecules [91], they still required a high computational effort (scaling as $O(N_e^5)$) and stay out of reach for many condensed matter systems. Another approach, the DFT, provides an alternative way in which the electronic density $n(\boldsymbol{r})$ is introduced to substitute the electronic wavefunction.

1.2.2. Density Functional Theory

In the context of the Density Functional Theory (DFT), all electrons of the system are treated by a single mean field defined by the electronic density $n(\boldsymbol{r})$:

$$n(\boldsymbol{r}) = N \int \mathrm{d}^3\boldsymbol{r}_2 \ldots \int \mathrm{d}^3\boldsymbol{r}_N \psi^*(\boldsymbol{r}_1, \ldots, \boldsymbol{r}_N)\psi(\boldsymbol{r}_1, \ldots, \boldsymbol{r}_N) \tag{1.18}$$

which satisfies the following condition for a system of N_e electrons:

$$\int_{\mathbb{R}^3} \mathrm{d}\boldsymbol{r}\, n(\boldsymbol{r}) = N_e \tag{1.19}$$

The electronic density is used to substitute the electronic wavefunction in (1.17) and reformulate the variational theorem in term of electronic density. In practice, this reduces the dimensionality of the minimisation problem from $3N_e$ variables (3 variables per electron) to only 3 space variables and allows for a drastic reduction of the computational effort required to approximate a solution of (1.13).

Consider an electronic system bathing in an external potential $v_{ext}(\boldsymbol{r})$ such that the corresponding Hamiltonian is defined as in eq. (1.11). A ground-state wavefunction ϕ can be obtained by solving (1.13), from which an associated ground-state density $n(\boldsymbol{r})$ can be deduced. Therefore, one has a mapping from the potential $v_{ext}(\boldsymbol{r})$ to the electronic density $n(\boldsymbol{r})$:

$$v_{ext}(\boldsymbol{r}) \longrightarrow n(\boldsymbol{r}) \tag{1.20}$$

In 1964, Hohenberg and Kohn [92] showed that the inverse mapping is also true, i.e. a ground-state density $n(\boldsymbol{r})$ determines a potential $v_{ext}(\boldsymbol{r})$ up to an arbitrary additive constant.

$$n(\boldsymbol{r}) \xrightarrow[HK]{} v_{ext}(\boldsymbol{r}) + \text{const.} \tag{1.21}$$

If the ground-state $n(\boldsymbol{r})$ determines the potential $v_{\text{ext}}(\boldsymbol{r})$, then it determines the Hamiltonian, and eventually the ground-state wavefunction and all observables. In other words, the potential $v_{\text{ext}}(\boldsymbol{r})$ is a unique functional of $n(\boldsymbol{r})$, as well as all other properties. This includes the total electronic energy, which can then be written as a functional of the electronic density:

$$E[n(\boldsymbol{r})] = F[n(\boldsymbol{r})] + V_{\text{ext}}[n(\boldsymbol{r})] \tag{1.22}$$

where $F[n(\boldsymbol{r})]$, the universal (i.e. independent from $v_{\text{ext}}(\boldsymbol{r})$) density functional, writes:

$$F[n(\boldsymbol{r})] = T_{\text{e}}[n(\boldsymbol{r})] + V_{\text{ee}}[n(\boldsymbol{r})] \tag{1.23}$$

Hohenberg and Kohn further showed that the energy functional respects a variational property, i.e. a minimisation of this functional with respect to the electronic density leads to the ground-state energy E_0 for $n(\boldsymbol{r}) = n_0(\boldsymbol{r})$, the ground-state density corresponding to $v_{\text{ext}}(\boldsymbol{r})$. This synthetically writes:

$$E_0 = \min_{n(\boldsymbol{r})} E[n(\boldsymbol{r})] \text{ for } n(\boldsymbol{r}) = n_0(\boldsymbol{r}) \tag{1.24}$$

From this point, finding a solution of (1.13) consists in minimising the following density functional:

$$E[n(\boldsymbol{r})] = T_{\text{e}}[n(\boldsymbol{r})] + V_{\text{ee}}[n(\boldsymbol{r})] + \int \mathrm{d}\boldsymbol{r}\, n(\boldsymbol{r}) v_{\text{ext}}(\boldsymbol{r}) \tag{1.25}$$

The existence of a mapping from a ground-state density $n(\boldsymbol{r})$ to a local external potential and the variational property of the energy with respect to the electronic density constitutes the *Hohenberg-Kohn theorems*.

In practice solving (1.25) is not possible because $\hat{T}_{\text{e}}$ and $\hat{V}_{\text{ee}}$, needed to express $F[n(\boldsymbol{r})]$, have no analytical descriptions in terms of electronic density except in the case of non-interacting particles. Kohn and Sham [93], assessed this issue by mapping the N interacting body problem onto a set of N independent problems similar to (1.13) where electrons, described by mono-electronic wavefunctions ϕ_i (also referred to as Kohn-Sham orbitals), are bathing in an effective potential V_{KS}. For one electron, the so-called Kohn-Sham equation reads:

$$\left[-\frac{\nabla_i^2}{2} + V_{KS}[n(\boldsymbol{r})]\right]\phi_i(\boldsymbol{r}) = \epsilon_i \phi_i(\boldsymbol{r}) \tag{1.26}$$

with

$$V_{\text{KS}}[n(\boldsymbol{r})] = V_{\text{ext}}[n(\boldsymbol{r})] + \frac{\delta E_{\text{H}}[n(\boldsymbol{r})]}{\delta n(\boldsymbol{r})} + \frac{\delta E_{\text{xc}}[n(\boldsymbol{r})]}{\delta n(\boldsymbol{r})} \tag{1.27}$$

where E_{H} is the Hartree energy, characterising the coulombic interaction of independent electrons with the mean charge field created by other particles, and E_{xc}, namely the exchange-correlation energy functional, corresponding to all the remaining unknown many-body interactions. For a system of N_{e} electrons, there are N_{e} Kohn-Sham equations. Note that the density of the fictitious system $n_s(\boldsymbol{r})$ is the same as the true one

and can be computed from Kohn-Sham orbitals:

$$n(\boldsymbol{r}) \equiv n_{\mathrm{s}}(\boldsymbol{r}) = \sum_{i}^{N_e} \phi_i^*(\boldsymbol{r})\phi_i(\boldsymbol{r}) \tag{1.28}$$

As Kohn-Sham equations explicitly depend on the electronic density as input, they must be solved through a self-consistent scheme described in fig. 1.1. Although equation (1.26)

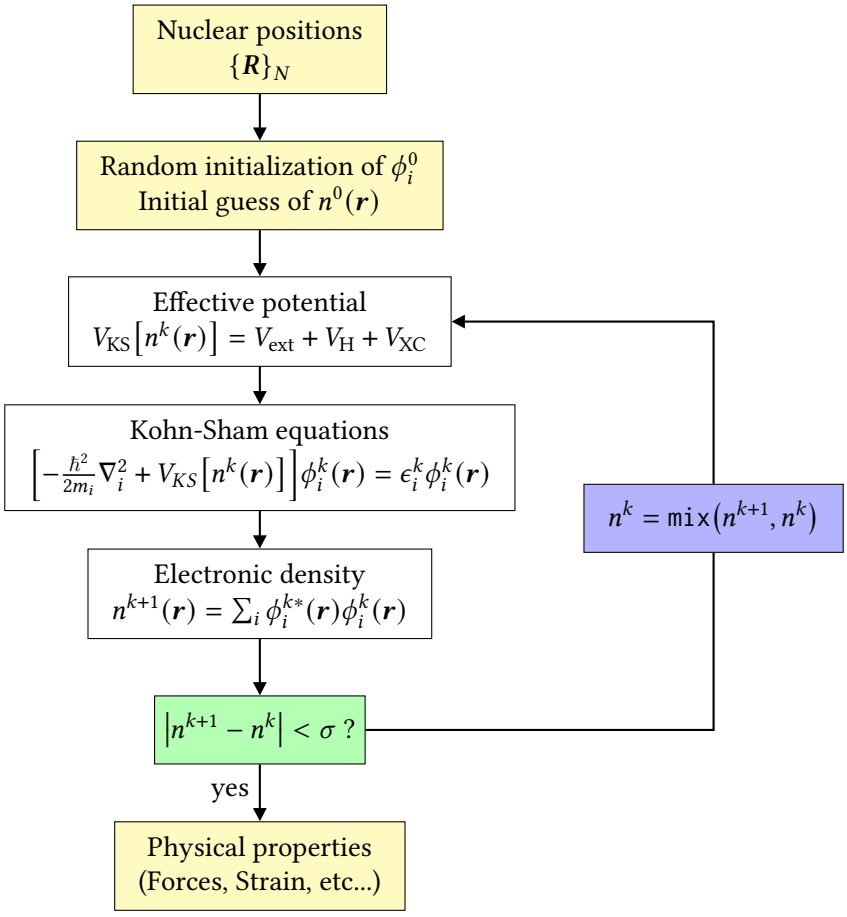

Figure 1.1 – Flowchart of the self-consistent field of a DFT calculation. The subscript k denotes the properties computed at iteration k. In practice, the convergence criterion (here on density) can also be taken on the energy, forces, wavefunctions or the Hamiltonian.

describes only one non-interacting particle, the construction of $E_{\mathrm{xc}}[n(\boldsymbol{r})]$ ensures that the problem is identical to (1.13) where the Hamiltonian is (1.14). Indeed, from Hohenberg and Kohn's expression (1.23) of the universal functional along with Kohn-Sham's reformulation of the same functional:

$$F[n(\boldsymbol{r})] = T_{\mathrm{s}}[n(\boldsymbol{r})] + E_{\mathrm{H}}[n(\boldsymbol{r})] + E_{\mathrm{xc}}[n(\boldsymbol{r})] \tag{1.29}$$

where $T_s[n(\boldsymbol{r})]$ is the kinetic energy of non-interacting electrons, one can write E_{xc} as:

$$E_{\text{xc}}[n(\boldsymbol{r})] = V_{\text{ee}}[n(\boldsymbol{r})] - E_{\text{H}}[n(\boldsymbol{r})] + T_{\text{e}}[n(\boldsymbol{r})] - T_s[n(\boldsymbol{r})] \tag{1.30}$$

and clearly see that it expressed the difference between the interacting system and the fictitious non-interacting one.

Approximation of the exchange-correlation functional

If going from Schrödinger equation to Kohn-Sham equations is done without loss of generality, the exchange-correlation term (E_{xc}) still has no analytical description and must therefore be approximated.

Among several existing approximations, the Local Density Approximation (LDA) [93] and Generalized Gradient Approximation (GGA) [94, 95] are the most popular.

$$E_{\text{xc}}^{\text{LDA}}[n(\boldsymbol{r})] = \int \mathrm{d}\boldsymbol{r}\, \epsilon_{\text{xc}}[n(\boldsymbol{r})] n(\boldsymbol{r}) \tag{1.31}$$

$$E_{\text{xc}}^{\text{GGA}}[n(\boldsymbol{r})] = \int \mathrm{d}\boldsymbol{r}\, \epsilon_{\text{xc}}[n(\boldsymbol{r}), \nabla n(\boldsymbol{r})] n(\boldsymbol{r}) \tag{1.32}$$

The LDA (1.31) corresponds to the solution of an homogeneous electron gas, where the exchange-correlation energy ϵ_{xc} only depends on the the local density $n(\boldsymbol{r})$. Although suitable for many systems, LDA shows its limit when dealing with quick variations of the electronic density, for example, in the case of insulators or semiconductors. The LDA was further extended to operate with spin-polarised electrons [96, 97]. The GGA (1.32) brings non-local corrections to LDA, introducing a dependency of ϵ_{xc} both on the local density $n(\boldsymbol{r})$ and its gradient $\nabla n(\boldsymbol{r})$.

From the formulation of LDA and GGA there are multiple ways to choose and parameterize the expression of ϵ_{xc} [95, 98–110]. In this work, the Perdew, Burke and Ernzerhof (PBE) [111] and the PBEsol [112] parameterisations for GGA will be used and discussed.

Strongly-correlated systems in DFT

Because LDA and GGA are based on the description of a homogeneous electron gas, they tend to overly delocalise the electronic density. Therefore, they both fail to have a correct description of strongly correlated systems which present localised d or f electrons. This is a strong limitation of the method, which is particularly impactful for systems we aim to simulate such as actinide oxides (UO_2, PuO_2, AmO_2, etc.) that are insulators [113–115] but predicted as metals by both LDA and GGA, leading to a qualitatively incorrect description of these materials.

Several methods exist to overcome the limitations of (semi)local functionals to describe strongly correlated electrons. The most straightforward way is to change the local character of the exchange-correlation functional. Hybrid functionals [116], such as PBE0 [117] or HSE [118, 119], introduce a non-local exchange term computed at the

Hartree-Fock level of theory, with the associated additional computational cost and constraints.

Another method is to correct the self-interaction error that arises from the computation of the Hartree energy, E_{H}, where one needs to compute the interaction of an electron with the total density, which already contains this particular electron. Direct correction of this error leads to self-interaction correction methods [98].

Finally, the last kind of methods makes advantage of the localisation of the strongly correlated electrons on specific orbitals of the system. Interactions are treated between electrons inside those orbitals and neglected with the rest of the system. Two of those model are the DFT+Dynamical Mean Field Theory (DMFT) [120, 121] (that will not be discussed in this manuscript, but is restricted to small systems due to its high computational cost) and the DFT+U [14, 122, 123] used in this work. The latter is computationally efficient, making it practical for large-scale simulations and is therefore very popular for dealing with correlated systems [124–129]. The DFT+U was first applied to uranium dioxide by Dudarev *et al.* [16].

In the DFT+U formalism the energy functional is corrected as:

$$E_{\mathrm{DFT}+U}\left[n(\boldsymbol{r}), n_m^\sigma\right] = E_{\mathrm{DFT}}\left[n(\boldsymbol{r})\right] + E_U\left[n_m^\sigma\right] - E_{\mathrm{dc}}\left[n_m^\sigma\right] \tag{1.33}$$

where n_m^σ denotes the occupation, by electrons of spin σ, with the orbital magnetic quantum number m. E_{DFT} is the energy functional obtained through the standard LDA or GGA approximations. The correction, E_U, that describes repulsive coulombic interactions between strongly correlated electrons reads:

$$E_U = \frac{1}{2}\sum_{m\sigma\neq m'\sigma'}(U_{mm'} - J_{mm'}\delta_{\sigma\sigma'})n_m^\sigma n_{m'}^{\sigma'} \tag{1.34}$$

and depends on two empirical parameters, U and J, respectively describing an effective coulombic interaction and an exchange interaction acting on same-spin electrons. The last term in equation (1.33) is a double counting term that aims to suppress redundant correlations already accounted for by E_{DFT}. There are two main expressions for E_{dc}: the full focalized limit (FLL) [15], suitable for systems with localised electrons in particular orbitals, and the around mean field (AMF) [130], that better describes system where electrons are spread in correlated orbitals. In this work only the FLL double counting has been used, as implemented in the `ABINIT` software [131–133]. The repulsive interaction, defined by $E_U - E_{\mathrm{dc}}$, promotes whole orbitals' occupations. Consequently, some orbitals will be filled while other orbitals will be emptied, allowing eventually for a gap opening in the band structure and the recovery of expected behaviour for Mott insulators.

To highlight a major effect of DFT+U we present the example of uranium dioxide, UO_2, where 2 valence electrons are distributed in 7 f-type orbitals. In DFT and in the absence of an effect that would lift the orbitals' degeneracy, each orbital will be occupied by $2/7^{\mathrm{ths}}$ of an electron. This is mainly due to the self-interaction error that tends to electron delocalisation. Using DFT+U with FLL-type double counting, whole occupancy

is promoted, so the electrons will try to fill out 2 of the 7 orbitals. Because these orbitals are no longer degenerate, the different possibilities of occupation no longer correspond to the same energy level. During the calculation, the system can, therefore, find itself trapped in a local minima corresponding to a metastable state of higher energy than the targeted ground state. As depicted in Figure 1.2, the self-consistent process of energy minimisation then becomes a stochastic process where the final energy of the system depends on the initialisation of the electronic local occupancy. Strategies to avoid the issues of metastable states have been described in the literature and briefly described in the following paragraphs.

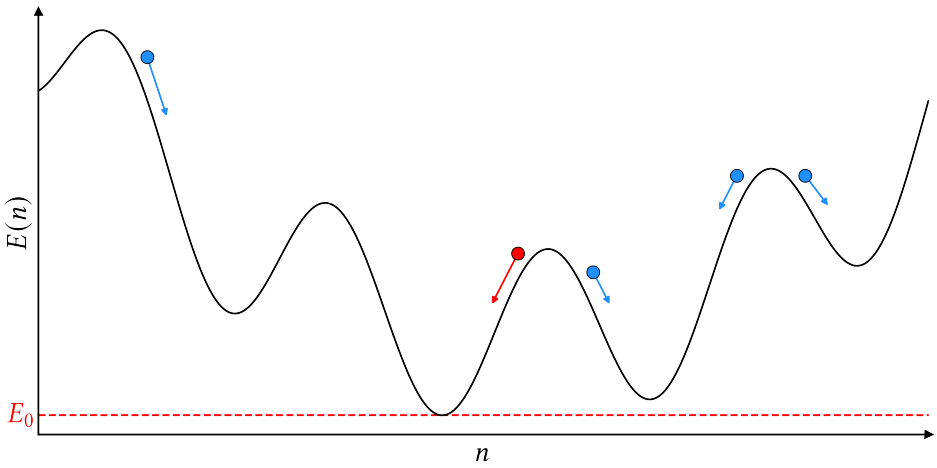

Figure 1.2 – Illustration of the local minima problem introduced by the DFT+U. The energy as a function of occupancy, n, has several barrier-separated minima, so that not all starting points allow the global minimum E_0 to be reached.

The U-ramping method [134] starts from standard DFT ($U = 0$ eV) and iteratively increases U, up to the desired value. At each step, the energy barriers created between local minima are supposed to be sufficiently low to allow the system to relax toward the global minimum.

The quasi-annealing method [135] heats the system with a spurious potential, allowing to cross energy barriers between metastable states and eventually converge to the ground state.

Finally, the OMC method imposes local occupancy matrices ($n^{\sigma}_{mm'}$) during the first iterations of the self-consistent field cycle [18, 136]. Once the constraint is lifted, the system converges to the nearest local minimum. The initial occupancy matrices that lead to the global minimum can be obtained by systematic studies of different possible occupancies [18]. For example, it is possible to test all combinations of diagonal occupancy matrices [137] ($\binom{7}{2} = 21$ for UO_2 [137], $\binom{7}{4} = 35$ for PuO_2 [18], $\binom{7}{5} = 21$ for AmO_2 [138]) and choose the configuration that predicts the lowest energy. This is already a tedious computational task, but if one wants to extend to non-diagonal occupancy matrices [139], the number of possibilities becomes intractable. Therefore, there is no guarantee for the OMC method to reach the true ground state. Nevertheless,

the OMC procedure has proven to be a reliable choice to describe correlated materials [140–146] including actinide oxides [18, 19, 61–63, 137, 138] and is the method used in this manuscript.

Ab initio molecular dynamics

Extension of molecular dynamics has been proposed by Car and Parrinello [147] to first principle calculations. The key idea is to propagate the nuclei as classical particles but with forces computed from *ab initio* methods.

In the context of the BO approximation it is assumed that nuclei propagate following a semiclassical Newton equation of motion where the potential is obtained, following the Ehrenfest theorem, as the expectation of the electronic Hamitonian with respect to the electronic wavefunction. It is also assumed that the electronic wavefunction is in its ground state. Thus, the dynamics is described by the following Lagrangian

$$\mathcal{L} = \frac{1}{2}\sum_{I=1}^{N} M_I \dot{\boldsymbol{R}}_{\boldsymbol{I}}^2 - \left\langle \phi_{\mathrm{e},0} \middle| \hat{H}_{\mathrm{e}} \middle| \phi_{\mathrm{e},0} \right\rangle + \sum_{ij} \Lambda_{ij} \left(\left\langle \psi_i \middle| \psi_j \right\rangle - \delta_{ij} \right) \tag{1.35}$$

defined as the difference between the kinetic energy of nuclei and the potential energy defined by the electrons. The last term is a Lagrange multiplier that enforces orthogonality at all times of the orbitals ψ. The orthogonality criterion is not preserved by the stationary Schrödinger equation, but is a physical requirement in order to compute real observable quantities. From Euler-Lagrange equations on can write the nuclear equation of motion,

$$M_I \ddot{\boldsymbol{R}}_{\boldsymbol{I}} = -\nabla_I \min_{\phi_{\mathrm{e}}} \left\langle \phi_{\mathrm{e}} \middle| \hat{H}_{\mathrm{e}} \middle| \phi_{\mathrm{e}} \right\rangle \tag{1.36}$$

which, in the formalism of DFT, is rewritten as a function of the electronic density

$$M_I \ddot{\boldsymbol{R}}_{\boldsymbol{I}} = -\nabla_I \min_{n(\boldsymbol{r})} E[n(\boldsymbol{r})] \tag{1.37}$$

where ∇_I is the gradient operator with respect to nuclear positions $\boldsymbol{R}_I$.

1.3. Classical Methods

So far, *first principle* methods (with a large focus on DFT) have been used to describe multi-particulate physical systems. Based on the direct quantum description of electrons, they are the most accurate methods to compute a broad spectrum of physical properties (electronic, magnetic, optical, …). However, these calculations can only be performed at a very high computational cost, as they roughly scale in N_{e}^3 at best (with N_{e} the number of valence electrons considered in the computation). This limits AIMD simulations to systems containing at most few hundreds of atoms, and to time scales of about a few hundreds of picoseconds. This is a major limitation as it makes the study of numerous physical processes impossible when the intrinsic length and time scales

greatly exceed the accessible scales with *ab initio* methods. Examples include atomic diffusion properties [148], gas bubble formation and migration [149, 150], liquid phase characterisation [151], mechanical properties such as critical shear stresses [65], irradiation damages [34], extended defects such as dislocations [59] or grain boundaries [42], etc.

Semi-empirical Interatomic Potentials (SEIPs), also referred to as force fields, come as a solution to drastically reduce the computational complexity and, by the direct application of equations from classical mechanic described in Section 1.3, allow for so-called Classical Molecular Dynamic (CMD) simulations involving trillions of atoms [152–154] on microsecond time scale [155].

1.3.1. Semi-empirical interatomic potentials

For a system of N atoms, semi-empirical interatomic potentials parameterise the $3N$-dimensional potential energy surface through "simple" analytical functions instead of the complex many-body wavefunction. The most general form, where only nuclear positions $\boldsymbol{R}$ are considered, writes

$$V(\boldsymbol{R}) = \Phi_{\boldsymbol{\theta}}(\boldsymbol{R}) \tag{1.38}$$

where $\boldsymbol{\theta}$ is a set of adjusted parameters that allows to reproduce particular physical or chemical properties of the materials. The functional forms of Φ are based on physical knowledge of interatomic bonding and should encompass a qualitative description of the electron shell. They are chosen to ensure the invariance of the potential energy by rotation, translation, and permutation. Without loss of generality, $V(\boldsymbol{R})$ can be expressed as a series expansion:

$$V(\boldsymbol{R}) = V_0 + \sum_i \phi_1(\boldsymbol{R}_i) + \sum_{i,j} \phi_2(\boldsymbol{R}_i, \boldsymbol{R}_j) + \cdots + \sum_{i,j,\ldots,n} \phi_n(\boldsymbol{R}_i, \boldsymbol{R}_j, \ldots, \boldsymbol{R}_n) \tag{1.39}$$

where $\phi_1, \phi_2, \ldots, \phi_n$ are functions describing $1, 2, \ldots, N$-body interactions. As long as enough terms are included, the development of (1.39) does not assume any approximation. However, taking into account all the N-body interactions is mathematically intractable, and therefore approximations are necessary. This results in a truncation of Eq. (1.39) beyond a certain order, although this is justified because, for most systems, the contributions decrease with the interaction order.

Pair potentials

The simplest approximation is to truncate (1.39) at the second order, keeping only pairwise interactions. Thus, the potential is only a function of pairwise distances between atoms. One of the first introduced pair potentials, that describes the short repulsion and attraction between atoms, is the Lennard-Jones potential [156] which is still very common for the description of noble gases, but is limited for almost all other classes of materials. Various functions have been developed from the early stage of

MD simulations to reflect the variety of physical phenomena that drive interactions between particles in different classes of materials. Here, we restrict ourselves to the presentation of the *Buckingham*, *Morse*, and *ZBL* pair potential functions that are often encountered for the simulation of actinide oxides.

The ***Buckingham*** potential [27], is the sum of a Born-Mayer potential [157] $A\exp(-r/B)$ and a dispersive term $-C/r^6$:

$$V(r_{ij}) = A\exp\left(\frac{-r_{ij}}{B}\right) - \frac{C}{r_{ij}^6} \tag{1.40}$$

with A, B and C adjustable parameters. The Buckingham potential can be found in two forms: the "Full Ionic Model" variation, corresponding to (1.40), which describes purely ionic bonding, and the "Partial Ionic Model" which accounts for both ionic and covalent bounding. Extensions of the Buckingham potential include the "Buckingham-4-ranges" which suppresses the non-physical attractive behaviour for very short distances due to the $1/r^6$ terms.

The ***Morse*** [158] potential describes covalent bonding, and can be written as

$$V(r_{ij}) = D\left[e^{-2\gamma(r_{ij}-r_0)} - 2e^{\gamma(r_{ij}-r_0)}\right] \tag{1.41}$$

where D, the depth of the potential well, γ, its curvature, and r_0, the equilibrium distance, are adjustable parameters. It is often mixed with the *Buckingham* potential to better describe the covalent bonding in ionocovalent materials, which is only partially accounted for by the *Buckingham* potential.

The ***Ziegler-Biersack-Littmark (ZBL)*** [159] potential describes the screened nuclear repulsion between atoms occurring at very short distances.

$$V_{ij,\mathrm{ZBL}}(r_{ij}) = \frac{Z_i Z_j e^2}{4\pi\epsilon_0 r_{ij}}\phi\left(\frac{r_{ij}}{a}\right) + S(r_{ij}) \tag{1.42}$$

with a and ϕ defined as follow:

$$a = \frac{0.46850}{Z_i^{0.23} + Z_j^{0.23}} \tag{1.43}$$

$$\begin{aligned}\phi(x) = {} & 0.18175e^{-3.19980x} + 0.50986e^{-0.94229x} \\ & + 0.28022e^{-0.40290x} + 0.02817e^{-0.20162x}\end{aligned} \tag{1.44}$$

In preceding equations, Z_i and Z_j are the atomic numbers of atoms i and j, r_{ij} the distance between them, e the elementary charge and ϵ_0 the vacuum permittivity. The switching function $S(r_{ij})$ ensures a smooth decay of the energy and first derivative (i.e. forces) to zero between an inner and outer cutoff radius. Those radii are the only

parameters for the adjustment of a ZBL potential.

Many-body potentials

A 2-body description of interatomic interactions is not always sufficient to properly model metals, semiconductors, or any system where higher-body interactions are non-negligeable. The aim of many-body potentials is to explicitly include such interactions. A very popular formalism, initially designed by Baskes *et al.* [37] for metallic systems, is the embedded atoms method (EAM). In the EAM formalism, the potential energy is expressed as:

$$V_{i,\mathrm{EAM}} = \frac{1}{2}\sum_{j}\phi_2\left(r_{ij}\right) + F(\bar{\rho}_i) \tag{1.45}$$

combining pairwise, $\phi\left(r_{ij}\right)$, and embedding, $F(\bar{\rho}_i)$, contributions. The embedding terms account for the electronic density $\bar{\rho}_i$ at site i, expressed as a sum over neighbouring atoms of a pairwise function:

$$\bar{\rho}_i = \sum_{i\neq j}\rho\left(r_{ij}\right) \tag{1.46}$$

The embedding function F ensures the many-body behaviour of the potential energy function, translating the non-linearity of the atomic density. If F is a linear function, the potential reduces to a pair potential. Note that EAM only includes 2-body interactions for the description of local densities. The modified embedded atoms method (MEAM), also introduced by Baskes [160–162] extends the EAM formalism, including 3-body terms through a screening term.

Other formalisms exist for higher-body potentials; one could, for example, involve the explicit calculation of 3-body or higher terms. Such potentials, including, for example, *Tersoff* [163], *Axilrod-Teller-Muto* [164, 165] potentials, or (M)GPT potentials developed by Moriarty *et al.*. [166–168], will not be detailed in the context of this work.

Short-range potentials and energy partitioning

For most of the potential energy functions presented above, the contribution to the interaction decreases quickly with distance. The potentials then reflect only short-range interactions between atoms. With that in mind, the search of interacting atoms can be truncated at a certain cutoff distance. This distance defines, for each atom, a cutoff sphere of radius r_c outside of which the interactions are not considered

$$V\left(r_{ij}\right) = 0 \ \text{ for } \ r_{ij} \geq r_c \tag{1.47}$$

To avoid potential discontinuity at r_c (energy jump when a particle moves inside or outside the cutoff sphere) the potential and first derivative are usually shifted to zero at r_c, by splines or using a smooth cutoff function. This energy localisation around each

atom allows for a partitioning of the total energy

$$E = \sum_{i}^{N} E_i(\boldsymbol{R}_i) \tag{1.48}$$

where E_i are atomic energies that depends on $\boldsymbol{R}_i = \{\boldsymbol{R}_{i1}, \boldsymbol{R}_{i2}, \ldots, \boldsymbol{R}_{in}\}$ the positions of atoms inside the cutoff sphere. Those atoms are also referred to as *neighbours* of atom i. The concept of energy locality is fundamental for semi-empirical potentials and CMD, as this partitioning enables an efficient and easily parallelizable computation of energy and forces as a linear $O(N)$ process, where N is the number of atoms. Consequently, it has been a fundamental aspect in the development of MD softwares [83, 169]. Note that such an approximation is only valid with short-range potentials. Long-range interactions such as electrostatic interactions should be treated through separated terms and computed with specific numerical methods. Those are described in the next section.

1.3.2. Electrostatic interactions

Accounting for description of electrostatic interactions is of particular importance when dealing with systems where charge transfers are important and where atoms are not neutral anymore. Such systems are, for example, molecular systems or ionocovalent solids such as carbides [170], borides [171], nitrides [172], or in the context of this work, actinide oxides. As opposed to *first principles* methods, where such interactions are implicitly encompassed by the electronic structure's treatment, classical methods require an explicit description without considering the electrons. Proposed by Coulomb in 1785, the eponym pair potential:

$$V_{\mathrm{C}}(r_{ij}) = \frac{q_i q_j}{4\pi\epsilon_0 r_{ij}} \quad , \tag{1.49}$$

allows for such description and is at the core of many interatomic potential development for above mentioned systems. Despite the very simple 2-body form of eq. (1.49), evaluation of long-range electrostatic interactions can be the most time-consuming parts of a simulation for periodic systems. Indeed, the long-range interactions are slowly decreasing as $1/r$, while the number of particles to be considered increases as $4\pi r^3/3$. Thus, truncating such interactions during the simulation might be an excessive approximation, the energy evaluation forming a conditional convergent series. To avoid this issue, two techniques have been developed and widely used in MD: the Ewald summation method and the particle-particle-particle-mesh (pppm) method [173, 174]. Both allow for a drastic acceleration of the calculation but are still very computationally expensive compared to 2, 3 or N-body interactions and remain a huge limitation both in resources and scaling ($O(N^{3/2})$ and $O(N \log N)$, respectively). For that reason, for very large systems, compromises between accuracy and cost can be found by only focusing on a short-range description of electrostatic interactions [175, 176].

In Eq. (1.49), the only free parameters are the charge values and the way they are described. The most straightforward manner is the *rigid-ion* model, which describes particles as point charges whose values are kept constant throughout the simulation.

The *core-shell* method [177] has been developed to account for the ion's polarisability which is not possible with the *rigid-ion* model. Ions are then represented by a "core" point mass, containing nucleus and core electrons, and a massless shell standing for the valence electrons. When they belong to the same ion, species interact by a harmonic potential, $V(r_{ij}) = kr_{ij}^2$. Although it presents some advantages over the *rigid-ion* model, the *core-shell* model is, however, much less efficient for MD simulations, as the motion of massless shells, whose frequency modes are higher than those for the cores, imposes the use of simulation timesteps around one order of magnitude smaller, typically, 0.1 fs instead of 1 fs [178].

Finally, the *variable-charge* model allows one to account for the charge variations of an atom as a function of its environment, for example, when a system should be compensating charge defects to conserve electroneutrality or during charge transfer in molecular systems. A popular strategy for charge computations is the QEq method [179–181], which consists in the minimisation of the system's electrostatic energy by adjusting the partial charge on individual atoms, the minimisation being constrained by electroneutrality. Force fields based on the *variable-charge* model, such as ReaxFF [182], have been widely used for simulations of chemical reactions, but are far less developed for non-reactive systems in condensed phase. Nevertheless, such potentials have been developed for UO_2 [183–187] and will be discussed in section 1.3.3.

1.3.3. Semi-empirical potentials for actinide oxides

Several semi-empirical pair potentials are available in the literature for atomistic simulations of actinide oxides. Some popular ones include: Morelon [29], Yamada [188], Arima [189], Potashnikov (referred to as MOX-07) [28, 190], Tiwari [191], Basak [31], Yakub [192] and Cooper14 [38] (mainly refereed as the CRG potential). All are based on the *rigid-ion* model, where short-range interactions are described by a single *Buckingham*-type potential or by a mixture of *Buckingham* and *Morse* potentials. All potentials, except Arima, use partial charges proportional to formal ionic charges on cations and anions, such as $Q^{\text{eff}} = \zeta Q$, where the coefficient ζ is usually determined by *ab initio* calculations. Only CRG includes, within the EAM formalism, many-body contributions. We briefly remind its formalism:

$$V_{i,\text{CRG}} = \frac{1}{2}\sum_j \phi_{\alpha\beta}(r_{ij}) - G_\alpha \sqrt{\sum_{i\neq j} \frac{\eta_\beta}{r_{ij}^8} \frac{1}{2}\left[1 + \text{erf}\left(20 r_{ij} - 30\right)\right]}, \tag{1.50}$$

where α and β denote the chemical species. The 2-body term $\phi_{\alpha\beta}$ is the sum of a long-range Coulomb potential and a short-range *Morse-Buckingham* mixed potential. The erf function in the density calculation acts as a lower short-range cutoff to prevent many-body interactions to overcome pair repulsion [38]. Due to the many-body interaction

term, it is the only potential from the list to capture the Cauchy violation ($C_{12} \neq C_{44}$) observed in actinide oxides with the fluorite structure [193].

Since all of the previously mentioned force fields are based on the rigid-ion model, it is not possible to study hyper- or hypo-stoichiometric compounds. A popular workaround strategy is to extend the potential to include different oxidation states that are treated as different chemical species during the simulation. This has been extensively done for the CRG potential, in order to include terms for Pu^{3+} [194], U^{5+} and Am^{3+} by Labonne *et al.* [195] and more recently U^{3+} by Porto *et al.* [196].

Along with the variety of available potentials, multiple studies were conducted to assess the potentials' performances in various conditions for diverse physical properties [39, 43–45, 47, 197]. For the sake of conciseness , we limit the discussion to the results of the two leading potentials for the simulation of UO_2: (i) the CRG potential and (ii) the MOX-07 potential.

Both potentials have a good description of the thermal expansion and heat-capacity with a λ-peak appearing in the heat-capacity curve associated with a super-ionic transition (also named Bredig transition) experimentally observed below of the melting point in UO_2 [52]. Concerning elastic properties, the CRG potential, which has been fitted to single-crystal experimental elastic constants, shows the best agreement with experimental data, while MOX-07, which has been fitted to polycrystalline elasticity data, shows a poorer agreement. The difference in the fitting strategies also translates in terms of material anisotropy. The CRG predicts an anisotropic behaviour at low temperature, whereas MOX-07 is fully isotropic. Furthermore, both potentials exhibit a brittle-to-ductile transition with transition temperature in good agreement with experimental data [43]. Balboa *et al.* [43] also highlights an unexpected plastic-like behaviour along crack propagation with a 'rutile'-type phase ahead of the crack tips for CRG (see fig. 1.3). On the other hand, MOX-07 predicts a cleavage-propagating crack as expected for brittle materials. Since there are no available experimental observations, these predictions remain inconclusive. Eventually, the CRG potential has recently been reviewed for thermal conductivity predictions [45] and compared to experimental neutron scattering experiments from Pang *et al.* [198, 199]. The authors conclude that CRG reasonably captures acoustic branches' dispersion; those are directly linked to elastic properties that are included in the potential training set. However, it exhibits significant discrepancies for the optical branches (see fig. 1.5), leading to an overestimation of phonon lifetimes and to much higher thermal conductivity values than experimental data, for which results are presented Figure 1.4. Similar conclusions were recently drawn by Torres *et al.* [44] suggesting that the discrepancies of thermal properties predicted by CRG and MOX-07 are likely due to inaccuracies in the phonon optical modes' description. The authors' findings suggest that the empirical potentials for UO_2 should be further optimised for a more robust prediction of the thermal conductivity both in perfect crystals and in the presence of complex defects. This can be seen as a significant drawback of these potentials, given that thermal conductivity is arguably one of the most important physical properties for a nuclear fuel.

In addition to CRG, only two other many-body potentials have been parameterised for

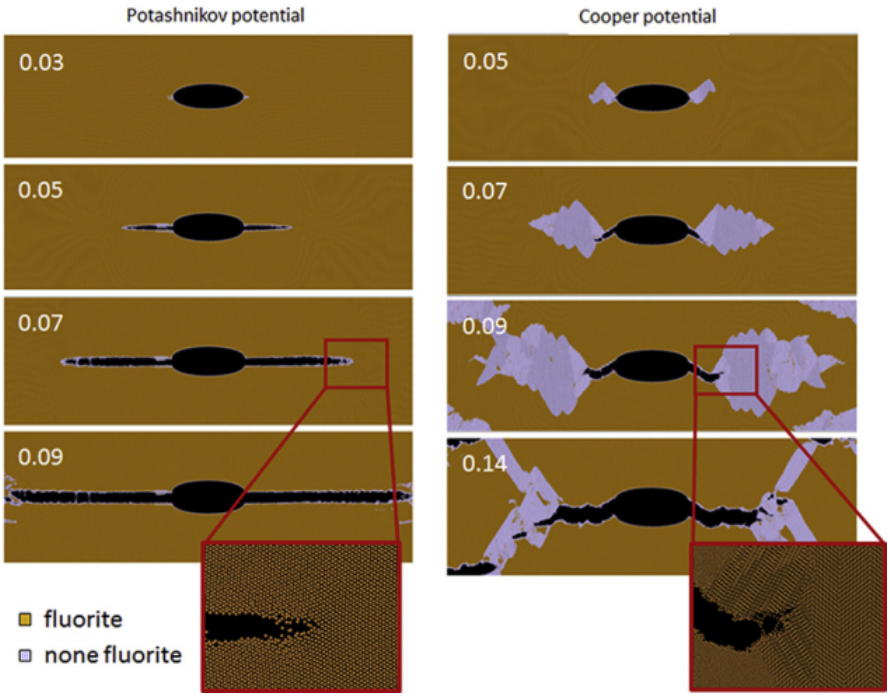

Figure 1.3 – Snapshots during crack propagation in (U,Pu)O_2 system with 25 at.% of Pu at 300 K for Potashnikov (MOX-07) Cooper (CRG) potentials. The load is applied along the ⟨111⟩ crystallographic direction in the fluorite structure. The inserts in each figure depict a close up of the crack front. Figure extracted from [43].

UO_2: the charge-optimized many-body (COMB) potential and the second moment tight-binding qeq (SMTB-Q) potential. Both are *variable-charge* potentials (see 1.3.2). We also mention for completeness ReaxFF (not detailed here) which proposes a parameterisation for CeO_2 that is close to UO_2 from an electronic point of view [202]. The COMB [183, 185] potential is based on a *Tersoff* potential adapted to include short-range electrostatic interactions. Coulombic interactions are described using a formalism close to the *core-shell* model with a Streitz-Mintmire [203] charge equilibration scheme. We will not detail the COMB potential here as it failed at several points to have an accurate description of the material [185, 204].

The SMTB-Q [186] potential integrates many-body interactions through a second-moment tight-binding approach for the cation-oxygen U-O interactions along with a *Buckingham* term for the O-O bonding. The U-U short-range repulsions are treated solely by Coulombic interactions. In bulk UO_2, this approximation is justified by the absence of short-range U-U interaction, but can be a strong limitation for the description of defects such as uranium interstitials. Atomic charges are equilibrated in the QEq formalism (see 1.3.2). Because of the variable charges, the SMTB-Q allows for the study of non-stoichiometric systems without any workaround on the atomic species, as opposed to CRG, where the oxidation states of cationic atoms are altered. Nevertheless, the SMTB-Q potential has been extensively assessed and shows its relevance for the

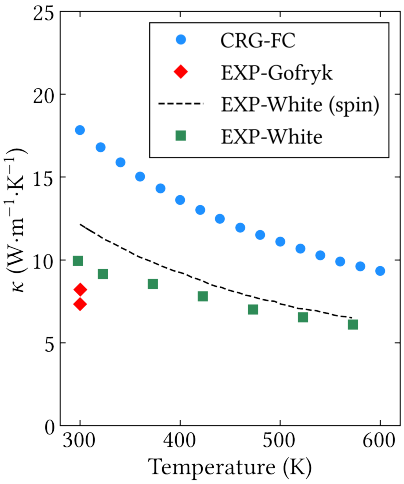

Figure 1.4 – Thermal conductivity with respect to temperature in UO_2 from CRG and experiments [200, 201]. The dashed line is modelling the conductivity without spin scattering using [200] data.

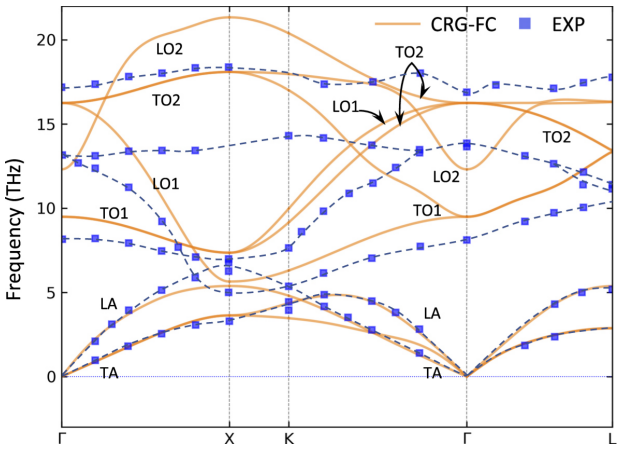

Figure 1.5 – Dispersion curve in UO_2 from CRG. The experimental measurements [198] (blue squares) are overlapped for comparison. The dashed line is to guide view. Figure extracted from [45].

study of UO_2, UO_{2+x} and U_4O_9 compounds [205, 206]. However, advantages of the SMTB-Q potential are very little compared to its high computational cost due to the charge equilibration step along with the long-range treatment of electrostatic interactions, making the SMTB-Q potential almost two orders of magnitude slower than CRG or MOX-07. Furthermore, the energy convergence criterion for charge equilibration should be chosen with care; otherwise, the SMTB-Q potential does not conserve energy in the microcanonical ensemble and a linear decrease of the total energy over the simulation time is observed [207]. This criterion should be as small as possible, further increasing the computational cost of the potential.

1.4. Machine learning interatomic potentials

Unlike SEIPs described in Section 1.3.1, that target a particular set of properties to fit their parameters, machine learning interatomic potentials (MLIPs) aim at performing a direct mapping of the $3N$-configurational space onto the system's PES. This is achieved through a numerical interpolation (regression) where the training set is a discrete representation of the PES consisting in a set of atomic configurations for which energy, forces, and stress have been computed with DFT. During the regression process, a large number of parameters are optimised to obtain a smooth PES that best interpolates between training points. Due to the extensive size of the reference database and

the high dimensionality of the parameter space, solving this optimisation problem is challenging and greatly benefits from the application of machine learning (ML) techniques. This large number of parameters is one of the strengths of ML models, allowing a finer adjustment of complex energy landscape that would not be possible with simple functions used as in SEIPs.

Most of MLIPs rely on the same locality principle as SEIPs and express the total energy as a sum of local atomic energies. Therefore, the mapping is achieved between local atomic environments $\boldsymbol{R}_i = \{\boldsymbol{R}_{i1}, \ldots, \boldsymbol{R}_{1n}\}$ and atomic energies E_i. The summation of such local maps allows in principle for the reconstruction of the total PES.

$$E = \sum_{i=1}^{N} E_i = \sum_{i=1}^{N} \mathcal{R}_{\boldsymbol{\theta}}(G_i(\boldsymbol{R}_i)) \tag{1.51}$$

where $\mathcal{R}$ is the regression model, parameterised by $\boldsymbol{\theta}$, that maps local atomic environments to atomic energies. Note that the mapping is achieved through a set of functions G_i which will ensure adequate representation of the atomic environments. Those functions are referred to as atomic descriptors and will be the topic of Section 1.4.1.

1.4.1. Local atomic environments

As with SEIPs, a crucial requirement of MLIPs is the invariance of the potential energy under coordinate axes' rotation and translation and equivalent atoms' permutation. This is achieved as long as the chosen representation of local atomic environments itself respect those invariants, which is not the case for Cartesian atomic positions vector $\boldsymbol{R}_i$. Therefore, before any regression model is applied, $\boldsymbol{R}_i$ should be substituted by a vector of local structural parameters (commonly referred to as local atomic descriptors or atomic fingerprints) $\boldsymbol{G}_i$, that are functions of neighbours' positions $\boldsymbol{R}_i$. Those functions must be:

(i) invariant by *rototranslation*:

$$\boldsymbol{G}_i(\mathcal{Q}\boldsymbol{R}_i + \mathcal{T}) = \boldsymbol{G}_i(\boldsymbol{R}_i) \tag{1.52}$$

where $\mathcal{Q}$ and $\mathcal{T}$ are rigid rotation and translation. Additionally, it is possible to ensure that the gradients of the PES will behave in the correct equivariant way with a constrain on the outer derivative,

$$\frac{\partial}{\partial \boldsymbol{R}_i}\boldsymbol{G}_i(\mathcal{Q}\boldsymbol{R}_i + \mathcal{T}) = \mathcal{Q}\frac{\partial}{\partial \boldsymbol{R}_i}\boldsymbol{G}_i(\boldsymbol{R}_i) \tag{1.53}$$

(ii) invariant by *permutation* of two same-species atoms:

$$\boldsymbol{G}(\boldsymbol{r}_{i1}, \ldots, \boldsymbol{r}_{in}) = \boldsymbol{G}\big(\boldsymbol{r}_{i\sigma_1}, \ldots, \boldsymbol{r}_{i\sigma_n}\big) \tag{1.54}$$

for any $\sigma \in \boldsymbol{S}_n$ a set of permutation $(1, \ldots, n)$,

(iii) *smooth* with respect to the number of atoms in the considered interaction neighbourhood sphere of radius r_{cut} :

$$\boldsymbol{G}_i(\boldsymbol{r}_{i1}, \ldots, \boldsymbol{r}_{in}) \simeq \boldsymbol{G}(\boldsymbol{r}_{i1}, \ldots, \boldsymbol{r}_{in+1}) \tag{1.55}$$

whenever $|\boldsymbol{r}_{in+1}| \leq r_{cut}$.

Another benefit of such representation is that it also replaces the variable-size positions vector $\boldsymbol{R}_i$ (whose length n depends on the number of neighbours of the atom i within the cutoff radius) by a *features* vector of fixed length K. This is of crucial importance because otherwise, it would be required to train a regression model $\mathcal{R}_i^n$ for each possible number of neighbours. With K being fixed, a *single* pre-trained regression model $\mathcal{R}$, mapping the K-dimensional descriptor space onto the 1D space of atomic energies, is needed for the total energy calculation. Eventually, the local mapping can be represented by the following formula.

$$\boldsymbol{R}_i \in \mathbb{R}^{3n} \longrightarrow \boldsymbol{G}_i \in \mathbb{R}^K \xrightarrow{\mathcal{R}} E_i \in \mathbb{R} \tag{1.56}$$

Choosing suitable descriptors is important and can strongly impact the accuracy of the resulting potential. Some general requirements are:

1. **Resolution**, different local atomic environments must be sufficiently discriminated by the descriptors.
2. **Completeness**, the set of descriptors is capable of exactly reconstructing the local environment.
3. **Computational cost**, the computational efficiency of machine learning potentials is often limited by the computation of the descriptors, as forward applications of regression models are usually cheap. Furthermore, the computational cost of the descriptor is linked to **the descriptor size K** which should be kept as small as possible.

Although a simple example of such descriptor can be relative pairwise distances (which are commonly used with SEIPs), they lack the above requirements, and more sophisticated functions are necessary. The following paragraphs describe some commonly used descriptors. Further theoretical details and benchmarks for different descriptors can be found in the literature [48, 208, 209].

Coulomb Matrix [210]. As part of the first introduced descriptor models, the coulomb matrix describes an atomic configuration of N atoms through a matrix $M_{ij} \in \mathbb{R}^{N\times N}$ whose coefficients are weighted nuclear Coulombic interactions.

$$M_{ij} = \begin{cases} 0.5 \times Z_i^{2.4} & \text{for } i = j \\ \frac{Z_i Z_j}{|\boldsymbol{r}_i - \boldsymbol{r}_j|} & \text{for } i \neq j \end{cases} \tag{1.57}$$

While working reasonably well to evaluate the similarity between molecules, it has been generalised to periodic systems [211]. However, such representations suffer from two

major flaws: (i) two different systems can result in the same Coulomb matrix [212]; (ii) it is not a smooth function of system's coordinates; i.e., a smooth change of coordinate vectors does not result in a smooth modification of the descriptor coefficients.

Atom Centred Symmetry Functions (ACSFs), proposed by Behler [213, 214], are combinations of two-body and three-body Gaussian functions mapping interatomic distances and bond angles, multiplied by a smooth cutoff function.

$$G_i^2(\boldsymbol{R}_i) = \sum_{j \neq i} g^k(r_{ij}) f_c(r_{ij}) \tag{1.58}$$

$$G_i^3(\boldsymbol{R}_i) = \sum_{j,k \neq i} g^k(\theta_{ijk}) f_c(r_{ij}) f_c(r_{ik}) f_c(r_{jk}) \tag{1.59}$$

More theoretical details on ACSFs are provided in Section 1.4.4, where their use as input for HDNNP training is discussed.

Moment tensor polynomials [215]. Moment tensors of different ranks are formed as follow with $\mu, \nu \geq 0$:

$$M_{\mu,\nu}(\boldsymbol{R}) = \sum_{j=1}^{n} |r_j|^{2\mu} r_j^{\otimes \nu}, \tag{1.60}$$

where $r_j^{\otimes \nu} = r_j \otimes \ldots \otimes r_j$ is the Kronecker product of μ copies of r_j. For $\mu > 0$, $M_{\mu,\nu}$ can be interpreted as weighted moments of inertia with $|r_j|^{2\mu}$ the weight of the j-th atom. Rotationally and permutationally invariant scalars are obtained from contractions of these tensors.

Smooth overlap of atomic positions (SOAP) [216, 217] use a local expansion of the Gaussian smeared atomic density on the basis of spherical harmonics. Invariant descriptors are obtained from the expansion coefficients. Initially designed to be used with gaussian approximation potential (GAP), they proved to be very powerful descriptors, working also fine with other regression models such as neural networks [218]. Although, they showed to be computationally slower than some mentioned alternatives.

The bispectrum SO(4) are used in tandem with SNAP. They are very similar to SOAP, except that density peaks are expanded on the basis of 4D hyper-spherical harmonics. Theoretical and computational details can be found in the dedicated Section 1.4.3, where the training of linear potentials in the SNAP framework is discussed.

Atomic cluster expansion (ACE) descriptors are based on the same principle of density projection as SOAP and SO(4) descriptors. Atomic environments are represented by a set of invariant polynomials forming a completed orthogonal basis. Each basis being a function of a radial basis with spherical harmonics that correspond to angular com-

ponents. ACE can be seen as a direct generalisation of some of the above descriptors, providing features of arbitrary correlation order [208].

1.4.2. Training and Validation

In previous paragraphs, the mapping of Cartesian coordinates $\boldsymbol{R}_i$ onto a descriptor space $\boldsymbol{G}_i$ has been discussed. We are now describing the finding of the regression model, $\mathcal{R}_\theta$ that maps the descriptor space onto atomic energies. This is referred to as the training step.

Training step

Given a unknown function f that relate two observed variables x and y such as

$$y = f_\theta(x, \epsilon) \tag{1.61}$$

where θ is a set of parameters to be adjusted and ϵ is an unobserved noise term, referred to as *noise* or *error*, accounting either for inaccuracy of the model or for the natural variability of y. The purpose of regression is to be able to predict the value of an outcome y for any new values of x. Regression methods are parts of supervised methods in the sense that they start by a *learning* or *training* phase on a dataset of paired value samples $(x_1, y_1), \ldots, (x_n, y_n)$. In most cases, x is multivariate and its coordinates, $x^1, x^2, \ldots, x^p$, are named explanatory variables or features. The variable y is the explained variable or label. In the case of MLIPs, $x \equiv G_i \in \mathbb{R}^K$ and $y \equiv E_i \in \mathbb{R}$.

The regression process aims to: (i) find the vector of parameters $\boldsymbol{\theta}$ that allow reconstructing f; (ii) estimate the distribution law parameters for ϵ. Therefore, one need to solve the optimisation problem

$$\hat{\boldsymbol{\theta}} = \underset{\boldsymbol{\theta}}{\operatorname{argmin}}\, J[y, f(x, \theta)]\,, \tag{1.62}$$

where J is a loss function that characterises the quality of the parameters applied to the regression model with respect to observed samples. A simple form for the loss function is the mean quadratic error of each sample

$$J = \frac{1}{N}\sum_{i=1}^{N}\left\| y_i - \hat{f}(\theta, x_i)\right\|_2^2\,. \tag{1.63}$$

Due to the high-dimensionality of the parameters space (especially true for neural networks that involve several thousands of parameters), finding a global minimum to the optimisation problem (1.62) is impossible. Still, there are a large number of high-quality local minima which represent the training dataset with accuracy.

The distinction between the methods used for regression lies in the functional form chosen for f, which can be linear (e.g. SNAP) or nonlinear (e.g. HDNNP), and the definition of the cost function J, which can, for instance, include physically informed

penalty terms [219, 220] or regularisation terms to numerically constrain the solution $\hat{\boldsymbol{\theta}}$. Concerning the development of MLIPs, the most used regression models include: neural networks, kernel methods and linear regression. In this work the kernel methods will not be discussed, but interested readers are referred to [216]. Neural networks optimisation and linear regression will be detailed in respective sections 1.4.3 and 1.4.4.

Note that depending on the machine learning potential, hyperparameters should be adjusted in addition to the parameter optimisation. Such hyperparameters are for example the architecture of a neural network, penalty introduced in the cost function, choice of the descriptors parameters, etc.

Validation Step

Once training is achieved with the desired degree of accuracy, as for SEIP, the parameters are fixed and become an integrant part of the potential. At this point, the MLIP is expected to make accurate predictions of energy and forces for new configurations that interpolate the training dataset; this, however, should be assessed. The most straightforward method to evaluate the quality of the potential is to compare the numerical error between the potential predictions and the values of a test set excluded from the training set. Common error metrics include the root mean square error (RMSE) and the mean absolute error (MAE),

$$\mathrm{RMSE} = \left[\frac{1}{N}\sum_{i=1}^{N}(y_i - \hat{y}_i)^2\right]^{\frac{1}{2}} \tag{1.64}$$

$$\mathrm{MAE} = \frac{1}{N}\sum_{i=1}^{N}|y_i - \hat{y}_i| \tag{1.65}$$

Additionally, for non linear regression methods as the neural networks, the divergence between errors on training and testing sets can indicate the onset of overfitting which is especially detrimental as it results in oscillations between reference points and degrades the predictive capability of potentials.

We emphasise that a second validation step must be performed on a set of particular physical properties of interest (lattice parameter a_0, elastic constants and modulii, defect formation energies, melting temperature, generalised stacking fault surfaces, etc.) as potentials which exhibit low numerical errors can still produce non-physical behaviour with respect to targeted properties, especially when the potentials are in extrapolation. Depending on the regression model, MLIP are more or less robust with respect to extrapolation, linear models tend to be more robust than neural networks. This should be considered with care during potential assessment and use in production simulations.

1.4.3. Spectral Neighbour Analysis Potential

In this section, we review the SNAP framework as described in previous studies [221, 222]. Following the work of Bartók *et al.*, the method is based on the expansion

of the density of neighbours on the basis of 4D hyperspherical harmonics [217]. The corresponding bispectrum components, which are real valued and rotationally invariant, can be constructed as the scalar triple product of the expansion coefficients of the neighbour density in this basis [216]. The SNAP contribution to the potential energy of an atom i can then be expressed as a linear combination of these bispectrum components:

$$E_i^{\text{SNAP}} = \beta_0 + \sum_{k=1}^{K} \beta_k (B_k^i - B_{k0}^i) = \beta_0 + \boldsymbol{\beta} \cdot \boldsymbol{B}^i \tag{1.66}$$

where B_k^i represents the kth bispectrum component of atom i, and β_k its associated linear coefficient. $\boldsymbol{B}^i$ is the vector of bispectrum components of atom i. The terms $\beta_k B_{k0}^i$ shift the contribution of each bispectrum component, ensuring that the SNAP energy of an isolated atom is equal to β_0.

From Eq. 1.66, we can derive the SNAP contribution to the forces acting on atom j:

$$\boldsymbol{F}_j^{\text{SNAP}} = -\nabla_j \sum_{i=1}^{N} E_i^{\text{SNAP}} = -\boldsymbol{\beta} \cdot \sum_{i=1}^{N} \frac{\partial \boldsymbol{B}^i}{\partial \boldsymbol{R}_j} \tag{1.67}$$

where $\boldsymbol{R}_j$ represents the position of atom j. Similarly, the contributions to the stress tensor can be obtained as follows:

$$\boldsymbol{W}^{SNAP} = -\sum_{j=1}^{N} \boldsymbol{R}_j \otimes \boldsymbol{F}_j = -\boldsymbol{\beta} \cdot \sum_{j=1}^{N} \boldsymbol{R}_j \otimes \sum_{i=1}^{N} \frac{\partial \boldsymbol{B}^i}{\partial \boldsymbol{R}_j} \tag{1.68}$$

where $\otimes$ denotes the Cartesian outer product operator. It is important to note that the SNAP contribution to the energy, forces, and stress tensor components (as expressed in Eqs. 1.66, 1.67 and 1.68) are all obtained as linear combinations β_k coefficients.

1.4.3.1. The *Bispectrum* SO(4)

To compute the bispectrum coefficients $\boldsymbol{B}^i$ for a given atom at position $\boldsymbol{R_i}$ of environment $\boldsymbol{R}_i \equiv (\boldsymbol{R}_{i1}, \ldots, \boldsymbol{R}_{in})$ within a sphere of radius r_{cut}, the starting quantity to consider is the local atomic density expressed as a sum of δ-functions located in a 3D-space:

$$\rho_i(\boldsymbol{R}_i) = \delta(\boldsymbol{R}_i) + \sum_{k}^{n} w_k \delta(\boldsymbol{R}_i - \boldsymbol{R}_{ik}) f_c(r_{ik}) \tag{1.69}$$

where w_k are unitless weights arbitrarily chosen to distinguish atoms of different types.

Density points defined in a 3D ball (r, θ, ϕ) are then projected to a subset of the 3-sphere (θ_0, ϕ, θ) by mapping the radial distance r to a polar angle θ_0 defined as:

$$\theta_0 = \theta_0^{\max} \frac{r}{r_{cut}} \tag{1.70}$$

where points below $\theta_0^{\max}$ are excluded. The 3-sphere density is then expanded in

terms of 4D hyper-spherical harmonics $U^j_{m,m'}(\theta_0, \phi, \theta)$ defined for $j = 0, \frac{1}{2}, 1, \ldots$ and $m, m' \in \mathbb{Z} : -j \leq m, m' \leq j$, resulting in:

$$\rho(r) = \sum_{j=0}^{j_{\max}} \sum_{m=-j}^{j} \sum_{m'=-j}^{j} \alpha^j_{m,m'} U^j_{m,m'}(\theta_0, \phi, \theta) \tag{1.71}$$

where the expansion coefficients $\alpha^j_{m,m'}$ can be written as a weighted sum of discrete values of corresponding basis function:

$$\alpha^j_{m,m'} = U^j_{m,m'}(0,0,0) + \sum_{r_{ij} < r_{cut}} w_j U^j_{m,m'}(\theta_0, \phi, \theta) f_c\left(r_{ij}\right) \tag{1.72}$$

The coefficients of the bispectrum descriptor $\boldsymbol{B}^i$ are real-valued and rotationally invariant quantities derived from the $\alpha^j_{m,m'}$ coefficients:

$$B_{j_1,j_2,j_3} = \sum_{m_1,m_1'=-j_1}^{j_1} \sum_{m_2,m_2'=-j_2}^{j_2} \sum_{m_3,m_3'=-j_3}^{j_3} \left(\alpha^{j_3}_{m_3,m_3'}\right)^* C^{\substack{m_1,m_1',j_1,\\ m_2,m_2',j_2,\\ m_3,m_3',j_3}} \alpha^{j_1}_{m_1,m_1'} \alpha^{j_2}_{m_2,m_2'} \tag{1.73}$$

with C some coupling coefficients. As summation in (1.73) must be finite, a truncation at $j = j_{\max}$ is introduced. In addition, equivalence properties [221] of the bispectrum coefficients can be used to restrict $j_2 \leq j_1 \leq j_3 \leq j_{\max}$ resulting in $(j_{\max}+1)(j_{\max}+2)\left(j_{\max}+\frac{3}{2}\right)/3$ distinct non-zero elements in $\boldsymbol{B}^i$. Eventually, the third-rank matrices $\boldsymbol{B}^i$ are reorganised into a single K-dimensional vector $\boldsymbol{B}^i \in \mathbb{R}^K$, where K is the number of distinct non-zero elements.

1.4.3.2. Linear regression

In the context of *linear regression*, the function f of Eq. (1.61) is assumed to be affine and writes,

$$f(x, \epsilon) = \beta_0 + \sum_{j=1}^{p} \beta_j x_j + \epsilon \tag{1.74}$$

with $x = \left(x_1, \ldots, x_p\right) \in \mathbb{R}^p$ and $\beta = \left(\beta_0, \ldots, \beta_p\right) \in \mathbb{R}^{p+1}$. The parameterisation of the function f reduces the task of estimating f to finding an estimate of the vector β. For a sample of n pairs of observation $(x_i, y_i)_{1 \leq i \leq n}$ we introduce the notation

$$\boldsymbol{Y}_n = \begin{pmatrix} y_1 \\ \vdots \\ y_n \end{pmatrix} \in \mathbb{R}^n, \qquad \boldsymbol{X}_n = \begin{pmatrix} 1 & x_1^1 & \ldots & x_1^p \\ \vdots & \vdots & \ddots & \vdots \\ 1 & x_n^1 & \ldots & x_n^p \end{pmatrix} \in \mathbb{R}^{n \times (p+1)}, \qquad \boldsymbol{\epsilon}_n = \begin{pmatrix} \epsilon_1 \\ \vdots \\ \epsilon_n \end{pmatrix} \in \mathbb{R}^n,$$

so that

$$\boldsymbol{Y}_n = \boldsymbol{X}_n \boldsymbol{\beta} + \boldsymbol{\epsilon}_n \tag{1.75}$$

A straightforward approach consists in finding the coefficients such that the distances between the observable values and the predicted values are minimised. A convenient distance definition is the Euclidean norm in $\mathbb{R}^n$

$$\|Y_n - X_n\boldsymbol{\beta}\|^2 = \boldsymbol{\epsilon}_n^{\mathsf{T}}\boldsymbol{\epsilon}_n \tag{1.76}$$

so that minimising the distances is equivalent to minimising the sum of the squared errors ϵ_i. This leads to the least square estimator (LSE) problem

$$\hat{\boldsymbol{\beta}} = \underset{\boldsymbol{\beta}}{\operatorname{argmin}} \|Y_n - X_n\boldsymbol{\beta}\|^2 , \tag{1.77}$$

where the solution $\hat{\boldsymbol{\beta}}$ is the LSE of $\boldsymbol{\beta}$. Geometrically, the LSE problem involves finding the orthogonal projection of Y_n onto the linear subspace spanned by X_n, thereby minimising the Euclidean distance between Y_n and X_n in the vector space $\mathbb{R}^n$. Let $\hat{Y}_n$ be the orthogonal projection of Y_n on the range of X_n, any vector $\hat{\boldsymbol{\beta}} \in \mathbb{R}^{p+1}$ that satisfies

$$\widehat{Y}_n = X_n\widehat{\boldsymbol{\beta}} \tag{1.78}$$

is a LSE for $\boldsymbol{\beta}$. Now assuming that $p \leq n-1$ and that X_n has full rank[5],

$$\widehat{\boldsymbol{\beta}} = \left(X_n^{\mathsf{T}}X_n\right)^{-1} X_n^{\mathsf{T}}Y_n \tag{1.79}$$

is the unique vector in $\mathbb{R}^{p+1}$ that satisfies (1.78). In practice, we do not explicitly compute the inverse, but instead use a QR factorisation to solve for $\widehat{\boldsymbol{\beta}}$.

Thus, training a SNAP consists in finding the optimum $\boldsymbol{\beta}$ coefficients to minimise the error on energy, forces, and stress with respect to the reference DFT values. For a particular atomic configuration c, containing N_c atoms, electronic structure calculations typically yield $3N_c + 7$ data: the total energy of the configuration E_c, $3N_c$ forces components $F_{i,\alpha}$ and the stress tensor $W_{\alpha,\beta}$ with 6 independent components. Because of the affine forms of (1.66), (1.67) and (1.68), the problem formulation for the configuration c is the same as (1.75) with

$$Y_c = \begin{pmatrix} E_c^{\mathrm{DFT}} \\ F_{i,\alpha}^{\mathrm{DFT}} \\ \vdots \\ W_{\alpha,\beta}^{\mathrm{DFT}} \\ \vdots \end{pmatrix} \in \mathbb{R}^{3N_c+7}, \quad X_c = \begin{pmatrix} N_c & \boldsymbol{B} \\ 0 & -\sum_{j=1}^{N_c} \frac{\partial \boldsymbol{B}^i}{\partial r_{i,\alpha}} \\ \vdots & \vdots \\ 0 & -\sum_{j=1}^{N_c} r_{j,\alpha} \otimes \sum_{i=1}^{N_c} \frac{\partial \boldsymbol{B}^i}{\partial r_{j,\beta}} \end{pmatrix} \in \mathbb{R}^{(3N_c+7)\times(K+1)},$$

where $\boldsymbol{B}^i = (B_1, \ldots, B_k) \in \mathbb{R}^K$ is the bispectrum descriptor vector for atom i as defined in 1.4.3.1. Note that, because only the total energy E_c is available from electronic

[5]Therefore the matrix $X_n^{\mathsf{T}}X_n \in \mathbb{R}^{(p+1)\times(p+1)}$ is invertible.

structure calculations, in the first line of matrix $\boldsymbol{X}_c$ only $\boldsymbol{B} = \sum_{i=1}^{N_c} \boldsymbol{B}^i$ is considered.[6]

Now suppose a training dataset of C configurations, the LSE of $\boldsymbol{\beta}$ is obtained by solving the following weighted LSE problem

$$\hat{\boldsymbol{\beta}} = \underset{\boldsymbol{\beta}}{\operatorname{argmin}} \|\boldsymbol{W}(\boldsymbol{\mathcal{Y}} - \boldsymbol{\mathcal{X}}\boldsymbol{\beta})\|^2 , \tag{1.80}$$

where

$$\boldsymbol{\mathcal{Y}} = \begin{pmatrix} Y_1 \\ \vdots \\ Y_c \end{pmatrix} \in \mathbb{R}^{C(3N_c+7)} \qquad \text{and} \qquad \boldsymbol{\mathcal{X}} = \begin{pmatrix} \boldsymbol{X}_1 \\ \vdots \\ \boldsymbol{X}_c \end{pmatrix} \in \mathbb{R}^{C(3N_c+7)\times(K+1)}$$

are obtained by stacking vertically the matrices $\boldsymbol{X}_c$ and vectors Y_c for the C configurations in the training set. The definition of the LSE problem differs from Eq. (1.77) by the addition of the diagonal matrix

$$\boldsymbol{W} = \begin{pmatrix} w_1^{(1)} & 0 & \dots & 0 \\ 0 & w_2^{(1)} & \dots & 0 \\ \vdots & \vdots & \ddots & \vdots \\ 0 & 0 & \dots & w_{3N_c+7}^{(C)} \end{pmatrix} \in \mathbb{R}^{C(3N_c+7)\times C(3N_c+7)}$$

whose coefficients weight the rows of $\boldsymbol{\mathcal{X}}$ and $\boldsymbol{\mathcal{Y}}$. This allows for specifying a fitting weight for each quantity (energy, forces, and stress), addressing the substantial differences in their relative magnitudes due to the units they are expressed in. Additionally, this approach enables control over the relative importance of different configuration types in the training set, in order to increase the accuracy for particular physical properties that depend on the desired applicability domain of the SNAP. Thompson *et al.* [221] also highlight the benefit in preventing overweighting of configurations with a larger number of atoms, converting all extensive quantities to intensive quantities. Thus, the rows corresponding to energy and stress tensor components for a configuration c are typically normalised by the number of atoms N_c and the volume V_c, respectively.

1.4.4. High-Dimensional Neural Network Potential

Artificial Neural Networks

In the case of HDNNP, the functional form of the regression model $\mathcal{R}_\theta(G_i)$ is a multilayer perceptron (MLP). A MLP is a particular type of Artificial Neural Network (ANN) consisting of feed-forward fully connected layers. It essentially means, that each node in each layer is connected by weights, w_{ij}^{kl}, to all the nodes in the previous and subsequent layers (with exception to the last layer) and connections can only go from one layer to another layer with larger index. A small MLP is represented schematically

[6] $E_c = N_c\beta_0 + \sum_{i=1}^{N_c}\sum_{k=1}^{K}\beta_k B_k^i = N_c\beta_0 + \sum_{k=1}^{K}\beta_k \sum_{i=1}^{N_c} B_k^i = N_c\beta_0 + \sum_{k=1}^{K}\beta_k B_k = (N_c, \boldsymbol{B})(\beta_0, \boldsymbol{\beta})^\intercal$

in Figure 1.6. Weight notation is that w_{ij}^{kl} is connecting node i in layer k with node j in layer l, with the input layer corresponding to the layer subscript -1. Additionally, except for the input layer, a bias node of value 1 is connected to each node i in layer k (not shown in 1.6) by the bias weight, b_i^l, that is used as an adjustable offset to shift the input of the nodes. The process of computing a L-layer network output for a given

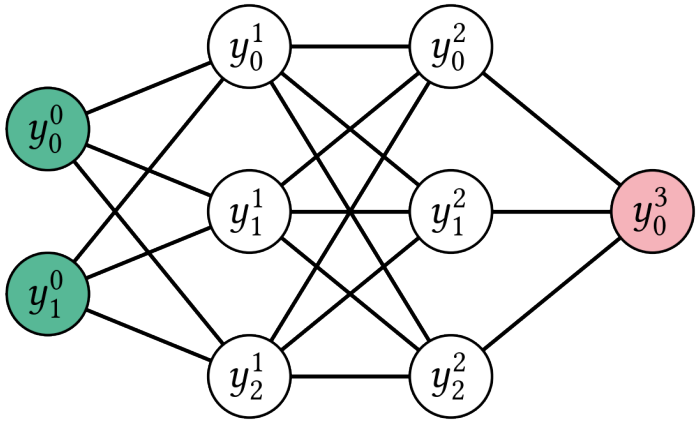

Figure 1.6 – Illustration of a MLP with 2 hidden layers of 3 neurons each (white nodes). The green and pink nodes denotes respectively the input and output layers. Biases are not displayed for visibility.

input x consists in assigning each coordinate of x to one of the input nodes, and then propagating the input through the neural network. For each layer l consisting of N^l nodes, the values can be packed into vectors such as $\{y_i\}^l = \boldsymbol{y}^l \in \mathbb{R}^{N^l}$, $\{b_i\}^l = \boldsymbol{b}^l \in \mathbb{R}^{N^l}$ and $\{W_{ij}\}^l = \boldsymbol{W}^l \in \mathbb{R}^{N^l \times N^{l-1}}$. Therefore, for $1 \leq l \leq L$, $\boldsymbol{y}^l$ writes:

$$\boldsymbol{y}^l = f^l\left(\boldsymbol{W}^l \boldsymbol{y}^{l-1} + \boldsymbol{b}^l\right) \tag{1.81}$$

The function f^l, called *activation* function, is non-linear and provides the capability to the neural network to fit arbitrary functions. Without the activation function, the output would simply reduce to a linear combination of the inputs. Popular activation functions are hyperbolic tangent, sigmoid, and reLu. With this notation, the function represented by the neural network in fig. 1.6 has for fully analytic form:

$$\hat{\boldsymbol{y}} = f^3\left(\boldsymbol{W}^3 f^2\left(\boldsymbol{W}^2 f^1\left(\boldsymbol{W}^1 \boldsymbol{x} + b^1\right) + b^2\right) + b^3\right) \tag{1.82}$$

where input y^0 and output y^3 were noted x and $\hat{y}$ and respectively.

The universal approximation theorem makes MLPs particularly attractive among machine learning models. This theorem states that feed-forward networks can approximate any continuous function between two Euclidean spaces to any desired accuracy,

given a sufficiently large number of neurons. In other words, even the simplest MLP can approximate any regular function $f : \mathbb{R}^n \rightarrow \mathbb{R}^m$ if it has enough neurons. Therefore, it should be possible to approximate any PES using MLPs.

High-dimensional PES representation

At this point, standard neural networks face limitations in representing PESs in a high-dimensional space. Firstly, each degree of freedom is assigned to an input node such that the size of neural networks must vary with the number of atoms. Secondly, once trained, the number of input nodes cannot be altered, necessitating separate neural networks for each system size. Since typical system sizes in DFT are around hundreds of atoms, transferability to large-scale simulations would be compromised. Eventually, neural networks do not inherently maintain permutation invariance of input nodes, thus not guaranteeing invariance of the potential energy when permuting atoms of the same species. Addressing the last point can be achieved by replicating the training dataset to cover all possible permutations of a system, which is impractical for large systems.

To assess these issues, Behler *et al.* [213] proposed describing the total PES using a set of atomic neural networks, each providing the atomic energy contribution E_i so that $E = \sum_i E_i$. A schematic representation of such atom-based neural networks is presented in Figure 1.7 where each line represents a single atom of a N-atom configuration. Atomic neural networks provide the functional relation between the descriptor vectors $\boldsymbol{G}_i$ and the atomic energies. As mentioned in the previous section, the descriptors are functions of the Cartesian coordinates of all neighbouring atoms within a given cutoff radius. They encode the geometrical environments of atoms into a fixed K-dimensional vector, corresponding to the size of the input layer. The descriptors ensure the invariance of the potential energy under roto-translation, while the permutation invariance is maintained by the atom-based architecture of the potential[7]. Finally, this representation is independent of the number of atoms, as adding or removing atoms simply corresponds to adding or deleting rows in the figure, for which a unique atomic neural network is trained. For multispecies systems, such as UO_2, one atomic neural network is trained for each chemical species. This approach allows for the different species to have distinct architectures. Although, in theory, any descriptor could be used with neural networks, we chose to retain only the ACSFs introduced by Behler *et al.* [213, 214] along with HDNNP. This decision was primarily motivated because these are the only descriptors available in the `n2p2` package [223, 224] used to fit such potentials. Detailed descriptions of ACSFs are given in Section 1.4.4.1.

The training of HDNNP, consisting in the optimisation of the weights associated with atomic NNs, is achieved through supervised learning procedures and algorithms, which are described in Section 1.4.4.2.

[7] Permuting the coordinates of two atoms results in a corresponding permutation of rows in the Figure 1.7, which does not affect the total energy

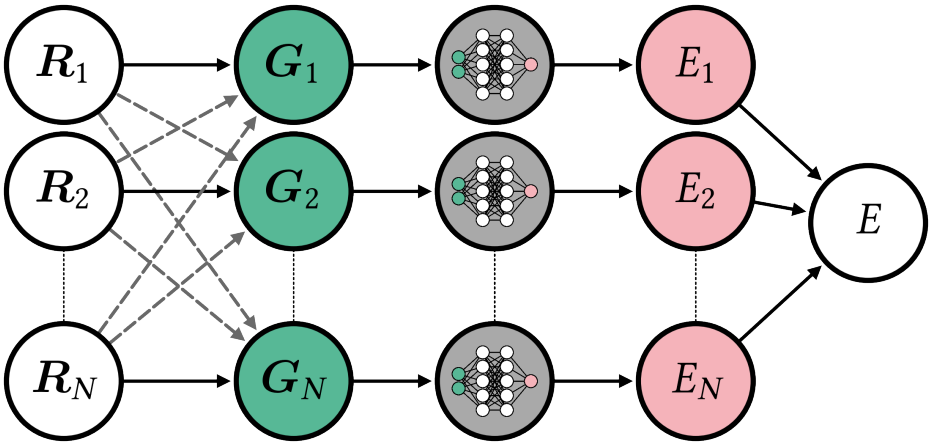

Figure 1.7 – Graph representation of HDNNP. Each line correspond to one atom whose Cartesian position are $\boldsymbol{R}_i$. The Cartesian coordinates are first transformed into a set of descriptors $\boldsymbol{G}_i$ accounting for all atoms in the vicinity of a particular atom. Those descriptors vectors are then used as the input layer for atomic neural networks (NNs) which outputs the atomic energy E_i for each atom. The total energy is recovered by summing all the atomic energy contributions.

1.4.4.1. Atom centred symmetry functions

There are two main classes of ACSFs that map radial, 2-body and angular (3-body) contributions, which can be used as descriptor functions to encode local atomic environments. The most common radial symmetry function, denoted G^2, consists in the sum of Gaussian functions evaluated at the radial distance of all neighbours of an atom i:

$$G_i^2 = \sum_{i \neq j} e^{-\eta(r_{ij}-\mu)^2} f_c(r_{ij}) \tag{1.83}$$

where $\mu, \eta \in \mathbb{R}$ are free parameters. The Gaussian shift μ allows one to increase the sensitivity of the function in particular spherical shells by shifting the centre of the Gaussian functions. Examples of ACSFs with varying η and μ are represented in Figure 1.8. The cutoff function $f_c(r) : \mathbb{R} \to \mathbb{R}$ allows for a smooth decay of the symmetry function to zero at a given cutoff radius r_c. Popular cutoff functions include, but are not restricted to, the monotonously decreasing part of the cosine function:

$$f_c(r) = \begin{cases} \frac{1}{2}[\cos(\pi r / r_c) + 1] & \text{for } r \leq r_c \\ 0 & \text{for } r_c < r \end{cases} \tag{1.84}$$

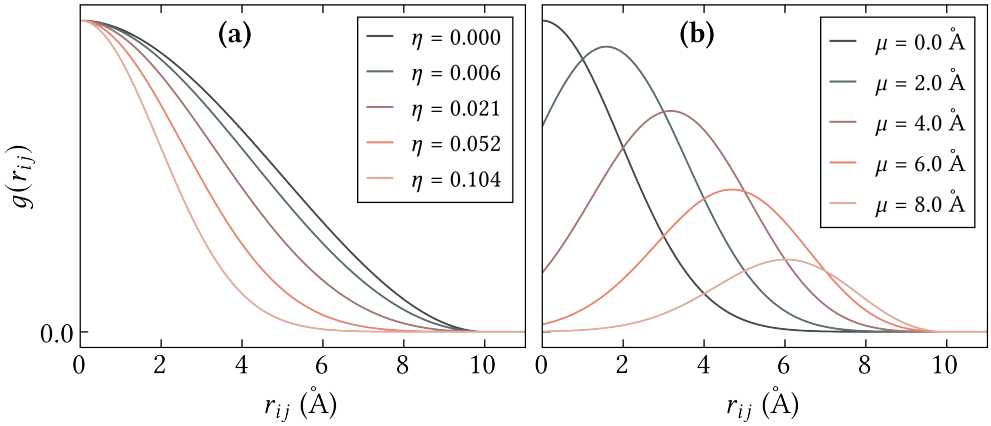

Figure 1.8 – (a) Centred radial symmetry functions for varying η and (b) shifted radial symmetry functions for varying μ with $\eta = 0.104$ and $r_c = 10$ Å.

For an atom i, angular ACSFs sum over atom triplets ijk, where the radial contributions, ij and ik, are weighted according to angle θ_{ijk}. There are two variations of such angular functions, denoted G^4 and G^5, that are commonly used:

$$G_i^4 = 2^{1-\zeta} \sum_{\substack{j,k\neq i \\ j<k}} (1 + \lambda \cos\theta_{ijk})^\zeta e^{-\eta(r_{ij}^2+r_{ik}^2+r_{jk}^2)} f_c(r_{ij}) f_c(r_{ik}) f_c(r_{jk}) \tag{1.85}$$

$$G_i^5 = 2^{1-\zeta} \sum_{\substack{j,k\neq i \\ j<k}} (1 + \lambda \cos\theta_{ijk})^\zeta e^{-\eta(r_{ij}^2+r_{ik}^2)} f_c(r_{ij}) f_c(r_{ik}) \tag{1.86}$$

where $\eta, \zeta \in R$ and $\lambda \in \{-1, 1\}$ are free parameters. The purpose of λ is to centre the maxima of the cosine function at angle 0 or π. The parameter ζ controls the angular resolution of the function. Figure 1.9 highlights the role of λ and ζ parameters in the case of G^5. The cutoff function f_c is the same as Eq. (1.84). The multiplication by the 2 or 3 cutoff functions of pairwise distance ensures that only atom triplets that are close to each other contribute to the summation.

Unlike bispectrum descriptors detailed in Section 1.4.3.1, there is no need for the ACSF values to be linear with respect to the potential energy since neural networks are able to approximate any functional forms.

To construct the input layer of atomic neural networks, a K-dimensional descriptor vector $\boldsymbol{G}_i$ (similar to $\boldsymbol{B}_i$ in Section 1.4.3.1) is built for each atom by computing the values for a given set of K ACSFs with varying parameters $\boldsymbol{\gamma}$ that are specific to a given atom type.

$$\boldsymbol{G}_i = \begin{pmatrix} G_{i,1}(\boldsymbol{\gamma}_1) & G_{i,2}(\boldsymbol{\gamma}_2) & G_{i,3}(\boldsymbol{\gamma}_3) & \dots & G_{i,k}(\boldsymbol{\gamma}_k) \end{pmatrix} \tag{1.87}$$

The construction of the set of symmetry functions and choice of their parameters is at the user's responsibility. Multiple methods to generate and select appropriate sets of symmetry functions are documented in the literature [225, 226]. In this work, functions were selected using a *CUR* decomposition [227] from large pools of candidates as

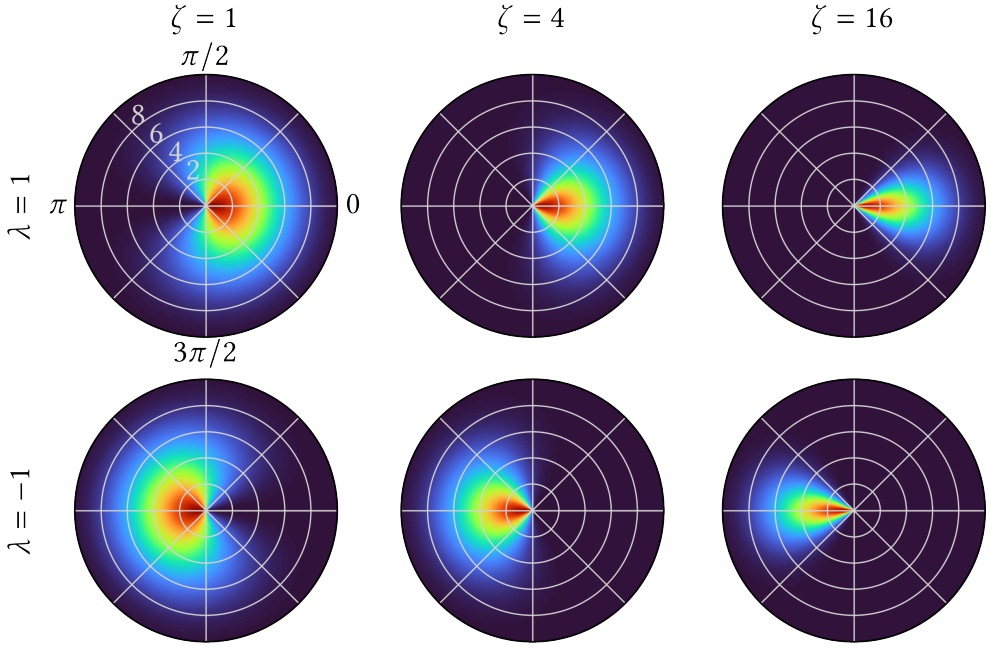

Figure 1.9 – Polar plots of angular G^5 symmetry functions with different values of λ and ζ. The cutoff radius and Gaussian witdh are set to $r_c = 12$ Å and $\eta = 0$ respectively. The radial axis corresponds to both neighbour distances r_{ij} and r_{ik}.

generated by Imabalzano *et al.*; more details are provided in the Section 2.3.

One extension to the original ACSFs involves weighting the contribution of neighbours by their atomic numbers Z [225] such as, for example,

$$G_i = \sum_{i \neq j} Z_j e^{-\eta(r_{ij}-\mu)^2} f_c(r_{ij}) \,, \tag{1.88}$$

in the case of radial functions. We also remind for completeness, alternatives where computationally expensive Gaussian functions are substituted by cheaper polynomial functions with compact support [228] or Legendre polynomials [219, 229, 230].

Although ACSFs consist of atomic distances and angles, i.e., 2- and 3-body interactions, they are formally N-body functions, as they simultaneously depend on all atomic positions within the cutoff sphere.

1.4.4.2. Neural Network optimisation

The process of finding the best parameters that satisfies an accuracy criterion is called the *learning* or *training* phase. As already mentioned, the learning phase of any regression model reduces to an optimisation problem where the parameters of the model are optimised to minimise a cost function $J(\theta)$.

The backbone of neural network training is the backpropagation algorithm, that computes the gradient of the loss function with respect to the network parameters $\nabla_{\boldsymbol{\theta}} J$. If a forward evaluation of a neural network consists in propagating the input layer x to the output layer y, the backpropagation consists in propagating the gradient of the last layer back to the input layer. This can be achieved due to the particular architecture of MLP and the derivative chain rule. The direct application of the backpropagation algorithm leads to gradient descent-based optimisers, the most straightforward being the stochastic gradient descent.

The ***stochastic gradient descent (SGD)*** optimiser updates parameters as follow

$$\boldsymbol{\theta}_{k+1} = \boldsymbol{\theta}_k - \eta \nabla_{\boldsymbol{\theta}_k} J \tag{1.89}$$

where k is the training iteration and η is called the *learning rate*. The choice of a suitable learning rate has a great impact on the success of the learning process. Improper learning rate can lead either to slow convergence, numerical instability, or suboptimal solutions. A way to avoid those issues is to makes the learning rate varying as the optimisation progresses, a common update procedure is given by a decreasing exponential function

$$\eta_k = \eta_0 e^{-\gamma k} \tag{1.90}$$

which motivates the use of large learning rate during the first iterations for fast convergence and smaller learning rate at the end of training to refine final convergence and avoid oscillation between multiple local minima.

The SGD has been extensively used as a base for many variants. A popular of these variants is the ***adaptive moment estimation (Adam)*** [231] which attempts to solve most of the SGD flaws. The parameters are updated as

$$\boldsymbol{\theta}_{k+1} = \boldsymbol{\theta}_k - \frac{\eta}{\sqrt{\hat{n}_k} + \epsilon} \hat{m}_k \tag{1.91}$$

where m and n measure the decaying average of past gradients and squared gradients

$$\begin{cases} m_{k+1} = \beta_m m_k + (1 - \beta_m) \nabla J(\boldsymbol{\theta}_k) \\ n_{k+1} = \beta_n n_k + (1 - \beta_n) \nabla J(\boldsymbol{\theta}_k)^2 \end{cases} \tag{1.92}$$

where β_m and β_n are typically taken between 0.9 and 1. Both m and n are corrected to be unbiased

$$\begin{cases} \hat{m}_k = m_k / (1 - \beta_m^k) \\ \hat{n}_k = n_k / (1 - \beta_n^k) \end{cases} \tag{1.93}$$

In Eq. (1.91) the $\epsilon \simeq 10^{-8}$ is added to prevent zero division and instability due to small values of $\tilde{n}_k$ that might occur in the first iterations. The Adam optimiser has be found to be one of the most sable and efficient SGD-based optimisers, with limited dependency towards the parameters β_m, β_n and ϵ.

Another approach, not based on gradient descent, is the Kalman Filter (KF) algorithm. The KF is an algorithm which, given a dynamical system governed by a linear process and a temporal series of noisy measurements, produces estimates of the state of the system over time. Its success stems from its recursive nature, where only estimates of the previous state and the previous error covariance matrix are required to compute the estimates of the current time step. Originally introduced by R.E. Kalman [232, 233], it has since been adapted to a wide range of problems. Its non-linear extension, the Extended Kalman Filter (EKF), has notably become a standard for navigation systems and GPS [234]. In 1988, Singhal and Wu showed that EKF could be used to train neural networks [235]. Although computationally expensive, its fast convergence makes it a good alternative to standard gradient descent algorithms. Because this is the method we used in this work for HDNNP training, following paragraphs focus on KF and EKF as described in [236] and implemented in the n2p2 software [223, 224].

Standard Kalman Filter

Consider a dynamic system governed by the following linear process:

$$x_k = A_k x_{k-1} + B_k u_k + w_k \tag{1.94}$$

where x_k denotes the state of the system at time k, A_k and B_k are the state-transition and control-input matrices, u_k is an optional parameter of control and $w_k \sim \mathcal{N}(0, Q_k)$ is the process noise. The goal of KF is to compute *a posteriori* estimates $\hat{x}_{k|k}$ that minimise the expected value of squared errors $\mathbb{E}(\left\|x_k - \hat{x}_{k|k}\right\|_2^2)$. The $i|j$ subscript denotes a quantity at time i given observations up to and including time j.

The KF algorithm is split into a prediction step and a correction step. The prediction step computes *a priori* estimates of the state $\hat{x}_{k|k-1}$ and its error covariance matrix $P_{k|k-1}$ by application of the dynamic (1.94):

$$\hat{x}_{k|k-1} = A_k \hat{x}_{k-1|k-1} + B_k u_k + w_k \tag{1.95}$$

$$\begin{aligned} P_{k|k-1} &= \mathbb{E}\left[\left(x_k - \hat{x}_{k|k-1}\right) \left(x_k - \hat{x}_{k|k-1}\right)^\mathsf{T} \right] \\ &= A_k P_{k-1|k-1} A_k^\mathsf{T} + Q_k \end{aligned} \tag{1.96}$$

The correction step accounts for the fact that true state values x_k are never known and only accessed through noisy measurements z_k:

$$z_k = H_k x_k + v_k \tag{1.97}$$

with H_k the measurement matrix and $v_k \sim \mathcal{N}(0, R_k)$ the measurement noise. Random noises w_k and v_k are assumed to be Gaussian distributed with zero mean and known covariance matrices Q_k and R_k. The estimate $\hat{x}_{k|k-1}$ is updated according to:

$$\hat{x}_{k|k} = \hat{x}_{k|k-1} + K_k \left(z_k - H_k \hat{x}_{k|k-1}\right) \tag{1.98}$$

where K_k is the Kalman gain matrix. It can be shown that the optimal Kalman gain writes:

$$K_k^* = P_{k|k-1} H_k^\mathsf{T} \left(H_k P_{k|k-1} H_k^\mathsf{T} + R_k \right)^{-1} \tag{1.99}$$

from which *a posteriori* error covariance writes:

$$P_{k|k} = P_{k|k-1} \left(I - H_k^\mathsf{T} K_k^{*\mathsf{T}} \right) \tag{1.100}$$

Note that the initial values $\hat{x}_{0|0}$, P_0, Q_0 and R_0, as well as the update rule for the noise covariance matrices, are problem-specific and should be chosen with care.

Extended Kalman Filter

The EKF is a generalisation of standard KF to non-linear systems. Consider the following state and measurement models:

$$x_k = f_k(x_{k-1}, u_k) + w_k \tag{1.101}$$

$$z_k = h_k(x_k) + v_k \tag{1.102}$$

where f_k and h_k are differentiable functions which may be non-linear. A linear approximation of (1.101) is obtained by truncating first-order Taylor expansions of f and h in the vicinity of x_{k-1} and x_k:

$$x_k \simeq \hat{x}_{k|k-1} + A_k (x_{k-1} - \hat{x}_{k-1|k-1}) + w_k \tag{1.103}$$

$$z_k \simeq h\left(\hat{x}_{k|k-1}\right) + H_k \left(x_k - \hat{x}_{k|k-1}\right) + v_k \tag{1.104}$$

where

$$[A_k]_{i,j} = \frac{\partial [f_k]_i}{\partial x_j} \left(\hat{x}_{k-1|k-1}, u_k\right), \qquad [H_k]_{i,j} = \frac{\partial [h_k]_i}{\partial x_j} \left(\hat{x}_{k|k-1}\right) \tag{1.105}$$

As for the standard KF, the *a priori* state estimator $\hat{x}_{k|k-1}$ is obtained by applying (1.101) to $\hat{x}_{k-1|k-1}$. By substituting $x_k - \hat{x}_{k|k-1}$ with (1.103) the definition of $P_{k|k-1}$ is left unchanged:

$$P_{k|k-1} = A_k P_{k-1|k-1} A_k^\mathsf{T} + Q_k \tag{1.106}$$

The correction step is also the same as for standard KF:

$$\hat{x}_{k|k} = \hat{x}_{k|k-1} + K_k \left(z_k - h_k\left(\hat{x}_{k|k-1}\right)\right) \tag{1.107}$$

Minimising $\mathbb{E}(\left\|x_k - \hat{x}_{k|k}\right\|_2^2)$ using linearised equations (1.103) and (1.104) leads to the same expressions as those obtained for the optimal Kalman gain (1.99) and *a posteriori* error covariance (1.100) matrices as for the standard case. Note that the linearisation is a significant approximation and may lead to non-optimal results.

Training neural networks with the EKF

Consider a training dataset made up of N inputs and reference outputs (x_i, y_i). The key is to use the reference outputs as an artificial time series of measurements of a supposedly ideal set of network parameters. The state and measurement update models are the following:

$$\theta_k = \theta_{k-1} + w_k \tag{1.108}$$

$$y_k^{\text{ref}} = \hat{f}(\theta_k, x_k) + v_k \tag{1.109}$$

where $\hat{f}$ is the non-linear function mapping the network input layer to the output layer. Note that up to a noise term, the state is stationary, since it was assumed to be optimal.

The current implementation [224] skips the update of the a priori error covariance matrix and instead adds the process noise covariance matrix to the a posteriori error covariance matrix estimate. Eventually, the training iteration writes:

$$K_k = P_{k-1} H_k^{\mathsf{T}} \left(H_k P_{k-1} H_{k-1}^T + R_k \right)^{-1} \tag{1.110}$$

$$\theta_k = \theta_{k-1} + K_k \left(y_k^{\text{ref}} - \hat{f}(\theta_{k-1}, x_k) \right) \tag{1.111}$$

$$P_k = P_{k-1} \left(I - H_k^{\mathsf{T}} K_k^{\mathsf{T}} \right) + Q_k \tag{1.112}$$

where

$$[H_k]_{i,j} = \frac{\partial \hat{f}_i}{\partial \theta_j}(\theta_{k-1}, x_k) \tag{1.113}$$

Singraber *et al.* found a net increase in accuracy after each update, as well as improved computational efficiency compared to traditional neural networks optimisation schemes (SGD, Adam) [224]. Several improvements are considered for training neural networks with EKF: for instance,[237] suggested to gather network parameters in groups and ignoring the covariance terms corresponding to weights belonging to different groups. In another work [238], they study a so-called multi-stream EKF which performs batch updates, each measurement vector being the concatenation of a subset of reference outputs.

High dimensional neural network potentials

For HDNNP training we introduce the following cost function

$$J(\boldsymbol{\theta}) = \sum_{c=1}^{N} \left| E_c - \hat{f}(\boldsymbol{\theta}, \{\boldsymbol{R}\}_c) \right|^2 + \lambda^2 \sum_{c=1}^{N} \sum_{i=1}^{N_c} \sum_{\alpha=1}^{3} \left| F_{i,\alpha}^c + \frac{\partial}{\partial r_{i,\alpha}} \hat{f}(\boldsymbol{\theta}, \{\boldsymbol{R}\}_c) \right|^2 \tag{1.114}$$

where forces are included as available from *ab initio* calculations. Comparison of force components $F_{j,\alpha}$ to $\partial \hat{f} / \partial r_{i,\alpha}$ comes naturally, as forces are the negative gradient of the total energy with respect to atomic positions. Because the output of the neural network

represents the total energy, forces can be expressed as the negative gradient of the output layer with respect to atomic coordinates

$$F_{j,\alpha} = -\frac{\partial \hat{f}_\theta}{\partial R_{j,\alpha}} = -\sum_{i=1}^{N_c} \frac{\partial E_i}{\partial R_{j,\alpha}} = -\sum_{i=1}^{N_c} \sum_{k=1}^{K} \frac{\partial E_i}{\partial G_{i,k}} \frac{\partial G_{i,k}}{\partial R_{j,\alpha}} \tag{1.115}$$

where K is number of descriptor functions used for atom i. The term $\partial E_i / \partial G_{i,k}$ is fixed by the neural network architecture, while $\partial G_{i,k} / \partial R_{j,\alpha}$ is obtained from the definition of employed ACSF. Note that analytic gradients are ensured by the mathematical formulation of MLPs, most of them being already computed as required for backpropagation. In theory, because backpropagation can be used on gradients themselves, higher derivatives, such as stress tensor, could be included in the loss function [214]. Accounting for forces and stress is always beneficial, as it leads to better accuracy, reduces the risk of overfitting, and a lowers the number of required training samples [239].

1.5. Conclusion

In summary, this chapter provides an overview of various methods for atomic-scale modelling of materials and in particular actinide oxides, focusing on DFT+U and SEIPs and their use along with MD method. We also discussed the formalism of SNAP and HDNNP machine learning potentials and evoked key points to account and the particular difficulties that we expect for the MLIPs training on UO_2 material. Although not exhaustive, the review highlights the fundamental principles and relevant aspects of each method, setting the stage for their application in the following chapters.

Chapter 2.

Machine learning potential for UO_2

Be you, be proud of you because you can be do what we want to do.

– François Hollande

Contents

2.1. Density Functional Theory setup . . . 50
2.2. Structure of the potential . . . 52
2.3. Training Procedure . . . 54
2.3.1. Spectral neighbour analysis potential . . . 54
2.3.2. High dimensional neural network potentials . . . 54
2.4. Database description . . . 58
2.4.1. Initial training set . . . 58
2.4.2. Active learning . . . 59
2.5. Assessment of the potentials . . . 62
2.5.1. Numerical errors . . . 62
2.5.2. Equation of state . . . 64
2.5.3. Phonons . . . 66
2.5.4. Thermodynamics properties . . . 67
2.5.5. Thermo-elasticity . . . 70
2.5.6. Point defects formation energy . . . 75
2.5.7. Generalised stacking fault surfaces . . . 75
2.6. Potential use cases . . . 80
2.6.1. Oxygen diffusivity in UO_2 and UO_{2+x} . . . 80
2.6.2. Cationic auto-diffusion in UO_2 . . . 82
2.7. Conclusion . . . 85

In this chapter, we describe the development and validation of two machine learning interatomic potentials (MLIPs) for uranium dioxide (UO_2) using the SNAP and HDNNP methodologies. We first review the DFT+U setup used for the construction of the training dataset. This includes the choice of exchange-correlation functional and other computational details relevant to the generation of accurate reference data. In the following, we describe the construction of an initial dataset generated from DFT+U calculations and its extension using active learning methods to ensure a comprehensive sampling of the potential energy surface. Subsequently, we present the assessment of trained potentials using various metrics, both numerical and physical, confronting predicted results to other SEIPs and available experimental data. Eventually we present two applications of the SNAP potential, performed in collaboration with other students, concerning the oxygen diffusivity in off-stoichiometric UO_{2+x} fuel and the migration of defects using NEB calculations.

Most of the results in this chapter have already been published [240], and can be directly cited as:
Dubois, E. T., Tranchida, J., Bouchet, J. & Maillet, J.-B. Atomistic simulations of nuclear fuel UO_2 with machine learning interatomic potentials. *Phys. Rev. Mater.* 8, 025402 (2024). https://doi.org/10.1103/PhysRevMaterials.8.025402

2.1. Density Functional Theory setup

In this chapter all the DFT calculations were performed with the ABINIT package [131–133] using the projected augmented wave (PAW) method [241, 242]. The PBE parameterisation of the GGA was used to describe the exchange-correlation energy and potential [111], with a cutoff energy of 25 Ha. In order to account for strong correlation between f electrons, we use the DFT+U formalism as described in Chapter 1.2. We chose the Liechtenstein scheme [15] with parameters U and J for uranium cations similar to previous DFT+U calculations, i.e., $U = 4.5$ eV and $J = 0.54$ eV, that were estimated based on x-ray photoemission spectra analysis by Kotani and Yamazaki [19, 243]. An occupation matrix control procedure was applied to f-orbitals of uranium atoms in order to search for the ground state of the DFT+U calculations [18, 137]. The occupation matrices imposed for spin up, $S^{\uparrow}$, and spin down, $S^{\downarrow}$, given by Eqs. (2.1) and (2.2), were imposed during the first 30 iterations of the self-consistent cycle and then allowed to fully relax.

$$S^{\uparrow} = \begin{pmatrix} 0.962 & 0.000 & 0.049 & 0.000 & 0.000 & 0.000 & 0.000 \\ 0.000 & 0.128 & 0.000 & 0.000 & 0.000 & 0.000 & 0.000 \\ 0.049 & 0.000 & 0.032 & 0.000 & 0.000 & 0.000 & 0.000 \\ 0.000 & 0.000 & 0.000 & 0.964 & 0.000 & -0.019 & 0.000 \\ 0.000 & 0.000 & 0.000 & 0.000 & 0.030 & 0.000 & -0.005 \\ 0.000 & 0.000 & 0.000 & -0.019 & 0.000 & 0.030 & 0.000 \\ 0.000 & 0.000 & 0.000 & 0.000 & -0.005 & 0.000 & 0.028 \end{pmatrix} \tag{2.1}$$

$$S^{\downarrow} = \begin{pmatrix} 0.026 & 0.000 & 0.004 & 0.000 & 0.000 & 0.000 & 0.000 \\ 0.000 & 0.099 & 0.000 & 0.000 & 0.000 & 0.000 & 0.000 \\ 0.004 & 0.000 & 0.028 & 0.000 & 0.000 & 0.000 & 0.000 \\ 0.000 & 0.000 & 0.000 & 0.031 & 0.000 & -0.001 & 0.000 \\ 0.000 & 0.000 & 0.000 & 0.000 & 0.026 & 0.000 & -0.004 \\ 0.000 & 0.000 & 0.000 & -0.001 & 0.000 & 0.025 & 0.000 \\ 0.000 & 0.000 & 0.000 & 0.000 & -0.004 & 0.000 & 0.029 \end{pmatrix} \tag{2.2}$$

Settings for the magnetic configuration of uranium atoms reproduce a longitudinal 1**k** anti-ferromagnetic (AFM) order (depicted in Figure 2.1) which, without including the spin-orbit coupling (SOC), is shown to be more stable than the experimentally observed 3**k** AFM order [19].

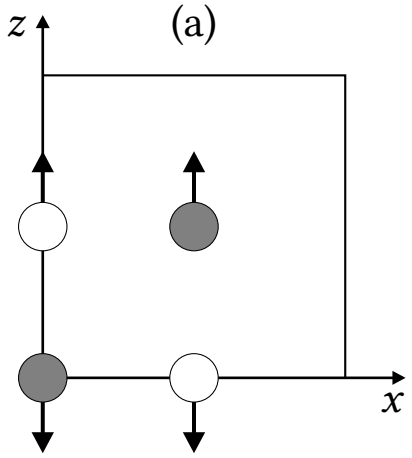

Figure 2.1 – Schematic representation of the longitudinal 1**k** ordering. Circles represents uranium atoms at $y = 0$ (grey) and $y = 0.5$ (white) positions. Oxygen are omitted for visibility.

In agreement with previous studies [49, 244] the SOC was neglected. Including SOC would significantly increase the computational complexity of DFT+U calculations, although it has been shown to have negligible impact on ground state and defect formation energies [20, 245]. Furthermore, the energy differences resulting from the inclusion of SOC are expected to be very close to, if not less than, the precision achievable with MLIPs (a few meVs per UO_2) [246] and would therefore offer practically no

improvement in terms of accuracy. A recent study by Zhou *et al.* confirmed these hypotheses, showing that the magnetic configuration used for the DFT+U calculations has an overall small impact on the phonon spectrum in UO_2 [63]. All calculations were performed using Monkhorst-Pack-generated k-point meshes [247]. Table 2.1 summarises the corresponding k-point meshes for the different training configuration groups for all DFT+U calculations.

Table 2.1 – Training dataset

group label	N Config.	At/cell	N data	k-mesh
$fm\bar{3}m$	130	12	5590	$4\times4\times4$
Polymorphs	300	12	12900	$4\times4\times4$
Hot bulk 1 (300 to 2000 K)	409	96	120655	$2\times2\times2$
Hot bulk 2 (2200 to 2500 K)	145	96	42775	$2\times2\times2$
Hot bulk 3 (2800 to 3200 K)	223	96	65785	$2\times2\times2$
Defects	375	96, 144	124692	$2\times2\times2$
γ-Surfaces	262	96, 144	73978	$2\times2\times2$
Total	1844	-	446375	-

2.2. Structure of the potential

We chose to express the total potential energy of the system, E_p as a sum three distinct contributions:

$$E_p = E_r + E_c + E_{\mathrm{ML}} \tag{2.3}$$

where E_r is a short-range and pair-wise repulsive interaction, E_c a coulombic contribution and E_{ML} is the machine learned contribution. Both E_r and E_c can be referred to as reference potentials that will be subtracted to the learning dataset energies before the training procedure. The contributions of these reference potentials to atomic forces and total stress will also be subtracted to the DFT values before optimisation of the machine learning part.

The short-range E_r contribution aims at representing a screened nuclear repulsion, and is accounted for through the ZBL pair potential [159]:

$$E_r = \sum_{i,j} \frac{1}{4\pi\epsilon_0} \frac{Z_i Z_j e^2}{r_{ij}} \phi(r_{ij}/a) + S(r_{ij}) \tag{2.4}$$

with Z_i and Z_j the atomic numbers of atoms i and j, e the elementary charge, r_{ij} the distance between atoms i and j, ϵ_0 the vacuum permittivity, and a, $\phi(x)$, and $S(r_{ij})$ are defined following the work of Ziegler *et al.* [159] (with more details given in section 1.3). The ZBL potential depends on two parameters: an inner cutoff radius (r_i) and an outer cutoff radius (r_o), ensuring that the energy and forces smoothly decay to zero between

r_i and r_o. These parameters were adjusted to approximately match highly-compressed (in the range [-25%;-10%] of volumetric deformation) DFT+U calculations of the UO_2 primitive cell. The obtained values are r_i = 1.2 Åand r_o = 2.5 Å. The resulting fit on compressive energy-volume and pressure-volume curves are displayed in figure 2.2.

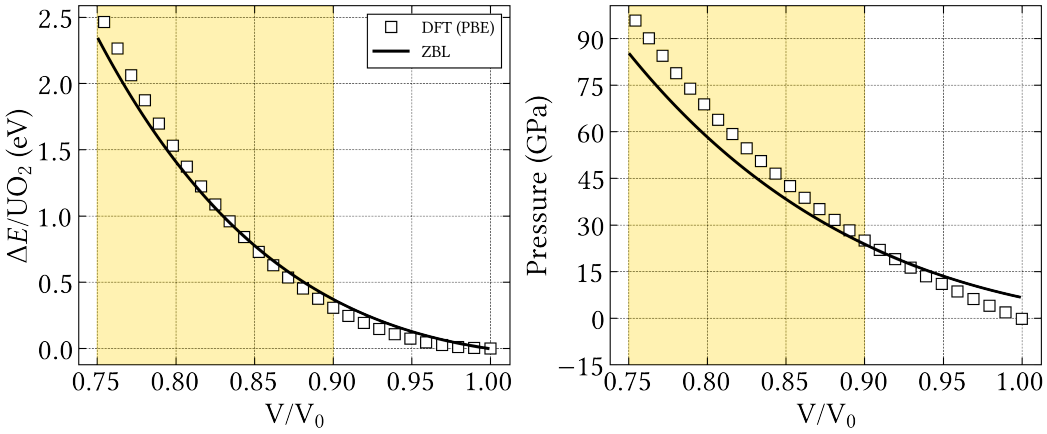

Figure 2.2 – Equation of states at 0 K in the compressive regime. Open symbols correspond to DFT calculation, the solid black line the ZBL potential. The yellow zone correspond the fitting domain of the ZBL potential.

The second contribution E_c accounts for the electrostatic interactions:

$$E_c = \sum_{i,j} \frac{q_i q_j}{4\pi\epsilon_0 r_{ij}} \tag{2.5}$$

with q_i and q_j the charges of two atoms i and j. For this work, we only considered constant partial charge values optimised by Yakub et al. for actinide oxides by applying an ionicity coefficient ζ = 0.05552 to the formal charges [192]. The electrostatic interaction term was computed either using the Ewald or `pppm` summation methods, both of which were tested and found to yield equivalent results, accounting for long-range contributions. Note that the constant charge approximation primarily affects long-range interactions, as the short-range interactions will be corrected by the ML contribution. The underlying assumption is that local variations in charges (such as those due to defects) have a limited impact on long-range interactions. Therefore, only the mean field resulting from constant atomic charges is computed. It is important to note that the use of constant atomic charges limits the potential's applicability to non-reactive simulations, where the chemical nature of the atomic environment remains weakly perturbed. To address the significant evolution of atomic charges during simulations, specific strategies integrated into machine learning frameworks have been developed. For more details, see the recent review on the performance and cost assessment of machine learning interatomic potentials [48].

2.3. Training Procedure

2.3.1. Spectral neighbour analysis potential

The training procedure for SNAPs is a direct application of Section 1.4.3. Bispectrum $SO(4)$ descriptors were computed using the `LAMMPS` software package [83]. The LSE problem

$$\hat{\boldsymbol{\beta}} = \underset{\boldsymbol{\beta}}{\operatorname{argmin}} \|\boldsymbol{W}(\boldsymbol{\mathcal{Y}} - \boldsymbol{\mathcal{X}}\boldsymbol{\beta})\|^2 , \tag{2.6}$$

was solve for $\boldsymbol{\beta}$ using the `numpy` implementation of QR decomposition [248]. Remaining hyperparameters are the coefficients of the weight matrix $\boldsymbol{W}$, which controls the contributions of each quantity (energy, forces, and stress) for each configuration groups, and the cut-off radius, r_c, that determines the size of the local atomic environments considered around each atom, and the effective radius r_α and weight w_α, which allows weighting of the SNAP energy contribution for each atom based on its chemical type. Those remaining were optimised altogether using an evolutionary algorithm controlled by the `Dakota` software [249] in order to solve the optimisation problem

$$\boldsymbol{\beta}_{opt} = \underset{\boldsymbol{W}, r_c, r_\alpha, w_\alpha, \ldots}{\operatorname{argmin}} \; O(\boldsymbol{W}, r_c, r_\alpha, w_\alpha, \ldots) , \tag{2.7}$$

where the objective function, O, for the evolutionary algorithm consists in a weighted sum of RMSEs on energies, forces, and stress. We also include a penalty term on the non-zero components of the elastic tensor with respect to the value obtained from DFT calculations.

$$O(\boldsymbol{W}, r_c, r_\alpha, w_\alpha, \ldots) = \tau_1 \mathrm{RMSE}(E) + \tau_2 \mathrm{RMSE}(F) + \tau_3 \mathrm{RMSE}(W) + \tau_4 \mathrm{RMSE}(\boldsymbol{C}) \tag{2.8}$$

Using this optimisation framework, illustrated in Figure 2.3, we identify the five "best" potentials according to the objective function. The final SNAP is chosen among selected candidates after further assessment. According to [221] the choice of the objective function is not trivial as SNAP can exhibit high sensitivity to the weight of each error measure in the objective function.

2.3.2. High dimensional neural network potentials

In a recent benchmark, the effectiveness of physics-based interatomic potentials, such as EAM [37] and MEAM [161], was compared to state-of-the-art ML methods [48] using a shared training set. The results revealed that moment tensor potentials (MTPs) with the highest accuracy and computational efficiency occupy the optimal point on the Pareto front. Although neural network potentials (NNPs) require more computational resources compared to MTPs or SNAP, they still offer a satisfactory balance between computational cost and accuracy, making them suitable for materials exploration purposes, especially for complex systems [250].

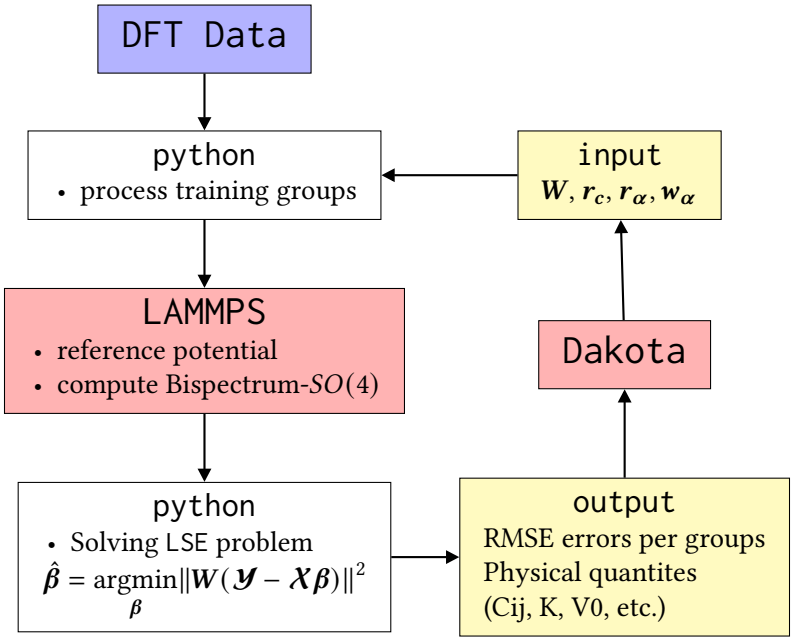

Figure 2.3 – Flowchart illustration of a SNAP optimisation loop LAMMPS [83] and Dakota [249]. The python-marked steps correspond to hand-made scripts.

Feature selections

Descriptors used for HDNNP were restricted to type-2 (radial), type-4 and type-5 (angular) ACSFs described in Section 1.4.4. We recall their formulation

$$G_i^2 = \sum_{i \neq j} e^{-\eta(r_{ij}-\mu)^2} f_c(r_{ij}) \tag{2.9}$$

$$G_i^4 = 2^{1-\zeta} \sum_{\substack{j,k \neq i \\ j<k}} (1 + \lambda \cos\theta_{ijk})^\zeta e^{-\eta(r_{ij}^2 + r_{ik}^2 + r_{jk}^2)} f_c(r_{ij}) f_c(r_{ik}) f_c(r_{jk}) \tag{2.10}$$

$$G_i^5 = 2^{1-\zeta} \sum_{\substack{j,k \neq i \\ j<k}} (1 + \lambda \cos\theta_{ijk})^\zeta e^{-\eta(r_{ij}^2 + r_{ik}^2)} f_c(r_{ij}) f_c(r_{ik}) \tag{2.11}$$

To select the most relevant set of symmetry functions for our case study, given a database of m atomic environments, we first generated a large pool of n function according to the systematic procedure proposed by Imbalzano *et al.* [226]. For the radial parts two groups of functions were considered, a centered group ($\mu = 0$) and a shifted group ($0 \leq \mu \leq r_c$), denoted by superscripts c and s. The parameters' grids are given by

$$\eta_i^c = \left(\frac{n^{\frac{i}{n}}}{r_c}\right)^2 \qquad \mu_i^s = \frac{rc}{(n+1)^{\frac{n+1-i}{n+1}}} \qquad \eta_i^s = \frac{1}{\left(\mu_{i+1}^s - \mu_i^s\right)^2} \tag{2.12}$$

where $0 \leq i \leq n-1$ and $\mu_n^s = r_c$. For the radial part, both (2.10) and (2.11) can be broken into a Gaussian part identical to (2.9). The angular part depending on $\lambda \in \{-1, 1\}$ and $\zeta \in \{1, 4, 16\}$, for which the effects have been shown in Section 1.4.4. The final set of symmetry functions is then obtained by the Cartesian product of the radial grid, λ and ζ. Note that for multispecies systems, a function set is generated for each pair or triplet of atoms for radial and angular function, respectively.

Let $G_1, \ldots, G_n$ denote the n candidate symmetry functions and $G_i(\Omega_p)$ be the scalar value of the ith symmetry function for the local environment of atom p. The feature matrix $\widetilde{\boldsymbol{A}} \in \mathbb{R}^{m \times n}$ is constructed over the full dataset as

$$\widetilde{A}_{i,j} = G_j(\Omega_i) \tag{2.13}$$

and then immediately pruned by discarding the l functions (i.e. columns of $\widetilde{\boldsymbol{A}}$) that do not satisfy

$$\left| \max_{\Omega} G_i(\Omega) - \min_{\Omega} G_i(\Omega) \right| > 10^{-4} \tag{2.14}$$

where $\boldsymbol{\Omega}$ represent the ensemble of the m atomic environments. This step allows for the disposal of symmetry functions that do not discriminate atomic environments and those whose absolute values are close. The resulting matrix $\boldsymbol{A} \in \mathbb{R}^{m \times (n-l)}$ is then sparsified to select the most representative and uncorrelated symmetry functions for the particular training set. As proposed in [226] we used a *CUR* decomposition [227], which consists in the following approximation

$$\boldsymbol{A} \simeq \boldsymbol{CUR} \tag{2.15}$$

where $\boldsymbol{C} \in \mathbb{R}^{m \times k}$ is a subset of $\boldsymbol{A}$'s columns, $\boldsymbol{R} \in \mathbb{R}^{k \times (n-l)}$ is a subset of $\boldsymbol{A}$'s rows, and $\boldsymbol{U} \in \mathbb{R}^{k \times k}$ optimises the approximation. An schematic illustration of the *CUR* decomposition is displayed in Figure 2.4. Note that each column of $\boldsymbol{A}$ corresponds to a particular

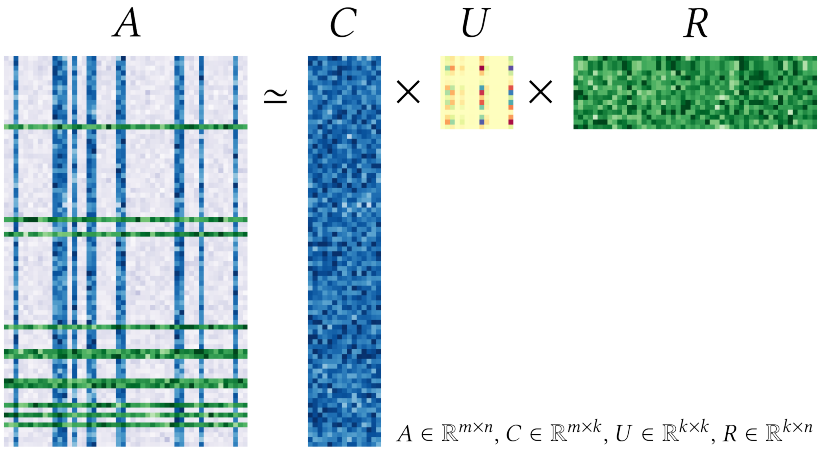

Figure 2.4 – Schematic representation of the CUR approximation [227].

symmetry function. Since we are only interested in reducing the number of symmetry functions (i.e. the number of column of A), the problem consist in constructing the

matrix C such that both the size of C and the error ϵ of the approximation

$$\epsilon = \frac{\|\boldsymbol{A} - \boldsymbol{CUR}\|_{\mathrm{F}}}{\|\boldsymbol{A}\|_{\mathrm{F}}} \tag{2.16}$$

remain low. The $\|\cdot\|_{\mathrm{F}}$ denotes the Frobenius norm. In practice, the size of C is usually fixed by the user and corresponds to the size of the input layer of the HDNNP. An illustration of the feature selection process for radial functions is displayed Figure 2.5. For the particular cases of UO_2 a set of symmetry functions was selected for each element,

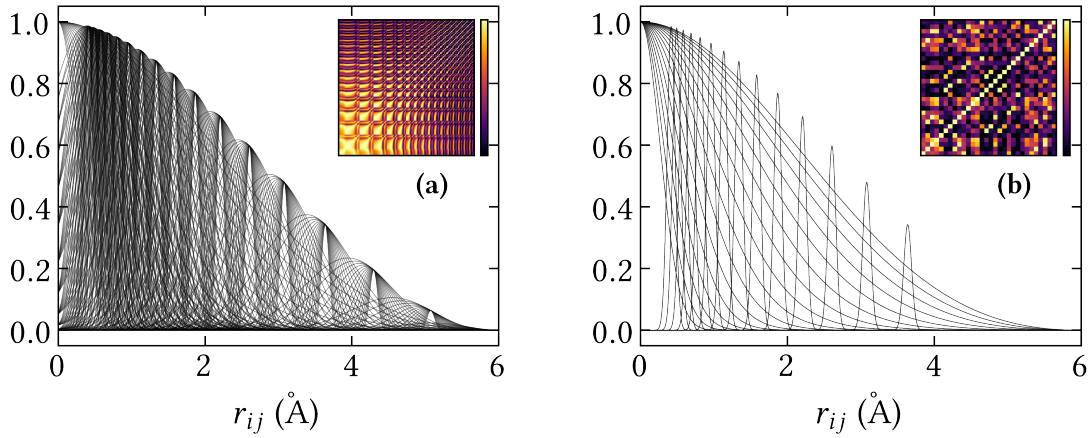

Figure 2.5 – Illustration of the feature selection process using the CUR approximation before (a) and after (b) sparsification. The inset represent the Pearson correlation matrix.

O and U, independently. Both have the same size, but as mentioned in Section 1.4.4 this is not mandatory. We chose to perform the sparsification on the complete feature matrix, containing both radial and angular descriptors, but note that independent selections could have been performed for each.

Neural network training

All HDNNPs have been trained using the `n2p2` neural network package [223, 235]. They are trained solely on energy and forces by minimising the following function introduced in 1.4.4.

$$J(\boldsymbol{\theta}) = \sum_{c=1}^{N} \left| E_c - \hat{f}(\boldsymbol{\theta}, \{\boldsymbol{r}\}_c) \right|^2 + \lambda^2 \sum_{c=1}^{N} \sum_{i=1}^{N_c} \sum_{\alpha=1}^{3} \left| F_{i,\alpha}^c + \frac{\partial}{\partial r_{i,\alpha}} \hat{f}(\boldsymbol{\theta}, \{\boldsymbol{r}\}_c) \right|^2 \tag{2.17}$$

where the forces weight λ is user-defined and chosen such that the normalised error on the testing set is minimum (here $\lambda = 2$). The fit on stress tensor components was not implemented in `n2p2` at the time the manuscript was written. An architecture consisting of $60 \times 45 \times 45 \times 1$ has been chosen by trial and error to best reproduce the UO_2 system, keeping in mind a trade-off between accuracy and computational cost.

The optimisation of neural networks' parameters was performed using a multi-stream EKF as implemented in [224, 232, 233]. The parameters for the EKF are summarised in Table 2.2. Those are the recommended parameters, but we observed that in some cases the optimisation might be sensitive to certain parameters. Further investigations and optimisations of these parameters might lead to better HDNNPs.

Table 2.2 – Extended Kalman filter parameters for HDNNP training.

Parameters	Values
ϵ	0.01
q_0	0.01
q_τ	2.302
q_{min}	10^{-6}
η	0.3
η_τ	2.304
η_{max}	1.0

As mentioned in Section 1.4.4, the vector of neural networks' parameters $\boldsymbol{\theta}$ lies in a high-dimensional space. Due to the local character of the optimisation process, the final set of parameters corresponds to local minima and strongly depends on the randomly initialised parameter vector $\boldsymbol{\theta}_0$.

In other words, given a training dataset and set of hyper-parameters, both fixed, the parameter optimisation is a stochastic process which results in different potentials with varying numerical accuracy. Therefore, in the following, we systematically consider several neural networks at each optimisation step and retain only the best one for subsequent evaluation and computing unless specified.

2.4. Database description

2.4.1. Initial training set

The initial database was constructed based on physical intuition, containing representative configurations of the cold curves of the stable structure $fm\bar{3}m$ as well as small deformations corresponding to elastic deformation (in the xx and xy directions, the other directions being equivalent by symmetry) and isochoric traction. Those configurations are regrouped under the label "$fm\bar{3}m$" in Table 2.1. We also include under the group "polymorphs" (see 2.1) cold curves of UO_2 polymorphic phases, namely $p4_2mnm$, $pnma$, and $pbcn$. From this very small training set we generated uncorrelated atomic configurations by performing several sets of calculations using the recently developed machine learning assisted canonical sampling (MLACS) [26]. From this expanded database, a first SNAP potential was optimised and used to perform NVT/NPT trajectories of a 96-atom supercell using the `LAMMPS` [83] code at several temperatures in the hot solid phase to create an ensemble of candidate configurations for subsequent *ab initio* calculations.

These configurations correspond to the "hot bulk 1" and "hot bulk 2" configurations in Table 2.1. To achieve more efficient sampling of the high-dimensional configuration space (especially at high temperature), an active learning procedure described in the following section was employed to select the most appropriate configurations, which are subsequently computed using single-point DFT calculations. The active learning scheme was mainly used to generate the "hot bulk 3" group of configurations. Finally, the database was expanded with configurations targeting specific properties such as the γ-surface and specific defects.

2.4.2. Active learning

MLIPs only reflect the knowledge they have acquired; i.e., their capabilities are determined by the extent of the training database and the density of available data points, which can be limiting factors in the training process since each point corresponds to an *ab initio* calculation. Unlike SEIPs that ensure a certain degree of transferability through their physics-based functional forms, MLIPs have limited extrapolation capabilities, i.e. there is no guarantee concerning the accuracy of potentials in unseen regions of the configuration space. Therefore, one of the major challenges is to build a comprehensive training dataset that encompasses various configurations representative of the entire accessible space associated with targeted applications in order to construct accurate and versatile models that can effectively handle a wide range of situations.

Although it is impossible to exhaustively sample the entire PES, classical statistical mechanics indicates that thermally accessible and physically relevant regions are confined to a relatively small subset of the configuration space. Significant efforts have been devoted to sampling this specific subspace.

In recent years, active learning (AL) strategies have gained popularity in the field of materials science to efficiently build training sets at a reduced CPU cost [251–261]. Considering that extrapolation should be avoided, AL methods emphasise sampling of unseen parts of the configuration space, i.e. in extrapolation, extending the original training set to improve the transferability of the potential.

Consider an initial set of labelled instances $\mathcal{L}_1$ of size $|\mathcal{L}_1| = l_1$. It corresponds to the initial training set used to train a first model $M_1(\mathcal{L}_1)$. This model is used to generate at low cost, through classical molecular dynamics simulations, a pool of p_1 unlabelled candidate configurations $\mathcal{P}_1$. From the set $\mathcal{P}_1$, are selected $p_1 \geq q_1 \geq 1$ instances, denoted $\mathcal{Q}_1$. Only those queried instances are then labelled by *ab initio* calculations and the set $\mathcal{Q}_1^{\mathsf{C}} \cap \mathcal{L}_1$, i.e. the relative complement of $\mathcal{Q}_1$ in $\mathcal{L}_1$, is discarded. The labelled ensemble for the next generation is then updated as $\mathcal{L}_2 = \mathcal{L}_1 \cup \mathcal{Q}_1$. Note that the size of the new training set is therefore $|\mathcal{L}_2| = l_1 + q_1$.

Without loss of generality, at each generation k, the model $M_k(\mathcal{L}_k)$ is used to produce $\mathcal{P}_k$ from which is queried $\mathcal{Q}_k$. The latter is used to update $\mathcal{L}_{k+1} = \mathcal{L}_k \cup \mathcal{Q}_k$. The process is repeated until a given termination condition is reached. This condition could be, for example, that there are no new configurations to be selected ($q = 0$) or the error with respect to a testing set, representative of the desired sampled region, is below a given

threshold.

Most of AL methods proposed in the literature share a common requirement which appears to be a cornerstone: the metric used to decide whether or not a new unseen configuration needs to be labelled, i.e. which configuration is to be queried.

Query by committee

One popular uncertainty-based query strategy is called the querry-by-committee (QBC) [251, 262, 263]. This approach involves training a committee of multiple learners rather than a single one. Committees of neural networks, for example, could be composed of networks of different architectures or/and trained with different subsets of the whole training database (bootstrap method). The committee disagreement, i.e. the variance of the predicted values among the committee for the same input instance, is associated with the uncertainty of the model. If the variance is comparable to the learners' error metrics (e.g RMSE) , the prediction is deemed reliable. In contrast, if the variance is much larger, the instance should be added to the training data in order to improve the model in the corresponding region of the input space.

In the context of material science, the learners are any MLIPs and the instances to be queried are atomic structures. For a configuration $\boldsymbol{r} \equiv \{r_i\}_{i=1}^{n}$ consisting in n atoms, both energy and forces can be used to compute a disagreement metric by a committee of c learners,

$$\sigma_E(\boldsymbol{r}) = \left[\frac{1}{c}\sum_{k=1}^{c}\left(E^k - \langle E\rangle_c\right)^2\right]^{\frac{1}{2}}, \tag{2.18}$$

$$\sigma_F\left(r_{i,\zeta}\right) = \left[\frac{1}{c}\sum_{k=1}^{c}\left(F_{i,\zeta}^k - \left\langle F_{i,\zeta}\right\rangle_n\right)^2\right]^{\frac{1}{2}}, \tag{2.19}$$

where i represents an atom of the configuration $\boldsymbol{r}$, and ζ the x, y or z direction. The disagreement on total energy $\sigma_E(\boldsymbol{r})$ serves as a global indicator for a structure while the second disagreement on forces $\sigma_F\left(r_{i,\alpha}\right)$ accounts for per-atom informations. In the general case, the variance over forces should be preferred since the total energy is prone to error compensation from the atomic energy contributions. Nevertheless, we decided to use both to define an uncertainty criterion as

$$u(\boldsymbol{r}) = \frac{\sigma_E(\boldsymbol{r})}{\sigma_{\mathcal{P}}\left[\sigma_E(\boldsymbol{r})\right]} + \lambda\frac{\sigma_F(\boldsymbol{r})}{\sigma_{\mathcal{P}}\left[\sigma_F(\boldsymbol{r})\right]} \tag{2.20}$$

where

$$\sigma_F(\boldsymbol{r}) = \langle\sigma_F(\boldsymbol{r})\rangle_{i,\zeta} = \frac{1}{3n}\sum_{i=1}^{n}\sum_{\zeta}^{3}\sigma_F\left(r_{i,\zeta}\right) \tag{2.21}$$

is the average force disagreement over all atoms and directions for configuration $\boldsymbol{r}$, and λ is a parameter to weight each contribution. Both terms are divided by their respective

variance $\sigma_{\mathcal{P}}$ over the pool of unlabelled instances $\mathcal{P}$.

In a sampling scenario, considering the $|\mathcal{P}|$ unlabelled candidate structures, generated by a MLIP, the $q \ll |\mathcal{P}|$ selected structure for subsequent labelling are those with the largest $u(\boldsymbol{r})$.

Adding diversity

In the case of serial AL, where $q = 1$, a single structure is labelled using *ab initio* calculations and added to the training set at each generation of the AL process. Because these *ab initio* calculations are the most time-consuming part of the overall AL process, it is often preferred to query multiple structures at once, i.e. $q > 1$, to be labelled in parallel. This approach, known as pool-based batch active learning (BAL), nowadays becomes a common AL scenario where large volumes of data are available with little or no cost. However, selecting multiple instances ($q > 1$) based solely on uncertainty measures can cause redundant queries. This redundancy arises because instances that are close to each other in the input space are likely to share prediction results. Consequently, the neighbours of the most uncertain instance are also likely to exhibit high uncertainty and thus be queried. Querying these neighbours should be avoided because it does not provide much additional information, leading to an inefficient sampling.

To address this issue of selecting close or correlated configurations, we introduced a diversity measure $d(\boldsymbol{r})$ [264] derived from a distance metrics in the input (descriptor) space

$$d(\boldsymbol{r}) = \sum_{\alpha} \min_{i} D\left(\boldsymbol{G}_i^{\alpha}, \mathcal{K}^{\alpha}\right) \tag{2.22}$$

where D is a distance function between the descriptor vector $\boldsymbol{G}_i^{\alpha}$ of atom i belonging to the structure $\boldsymbol{r}$, and all descriptor vectors corresponding to atomic environments of species α in the current ensemble of labelled and queried structure $\mathcal{K}^{\alpha} = \mathcal{L}^{\alpha} \cup \mathcal{Q}^{\alpha}$. Diversity is achieved when $d(\boldsymbol{r})$ is maximum, that is, when the pairwise distances of query instances are as large as possible in the input space. We defined the distance metric as the Mahalanobis distance

$$D_{MAH}\left(\boldsymbol{G}_i^{\alpha}, \mathcal{K}^{\alpha}\right) = \sqrt{\left(\boldsymbol{G}_i^{\alpha} - \langle \mathcal{K}^{\alpha} \rangle\right)^{\mathsf{T}} S^{+}_{\mathcal{K}^{\alpha}} \left(\boldsymbol{G}_i^{\alpha} - \langle \mathcal{K}^{\alpha} \rangle\right)} \tag{2.23}$$

where the usual inverse of the $\mathcal{K}^{\alpha}$ ensemble covariance matrix has been replaced by the pseudo-inverse ($S^{+}_{\mathcal{K}^{\alpha}}$) for numerical stability. We choose the Mahalanobis distance for its robustness and simplicity, but others distance measures for diversity are widely used in AL [265–268].

The final selected instances should maximise a convex combination of uncertainty and diversity

$$s(\boldsymbol{r}) = (1 - \gamma)u(\boldsymbol{r}) + \gamma d(\boldsymbol{r}) \tag{2.24}$$

where $\gamma \in [0; 1]$ is a user-defined parameter. In this work, we use $\gamma = 0.5$ to balance the diversity and uncertainty criteria.

Note that instance selection is conducted sequentially. Indeed, each time a structure is queried, the ensemble $\mathcal{K}^\alpha$ is updated, so do are $S^+_{\mathcal{K}^\alpha}$ and $\langle\mathcal{K}^\alpha\rangle$. Thus, diversity measure $d(\boldsymbol{r})$, should be recomputed each time a new configuration is selected and added to $\boldsymbol{Q}$.

Kee *et al.* [264] also emphasise that queries should also account for a density criterion to prevent outliers in queries and further improve uncertainty sampling by selecting instances that are more representative. This, however, has not been tested in the context of this work.

2.5. Assessment of the potentials

2.5.1. Numerical errors

In order to assess the performances of the SNAP and HDNNP potentials, we first evaluate their numerical error against reference DFT data. For this purpose, a subset of the database, around 10%, was randomly isolated only for testing purposes and not considered for training. The results in terms of RMSE and MAE are presented in Table 2.3. The energy RMSE of the SNAP and HDNNP potentials on the whole database are 5.26 and 3.38 meV/atom, respectively. These results are satisfactory, especially considering the diversity of configurations in the database, including different polymorphic phases, deformations of the fluorite phase, point defects, and disordered configurations corresponding to varying temperatures. Very good agreement was also observed for the stresses predictions, as indicated in detail in Table 2.3 even for the HDNNP potential for which stress is not included in the training process. The force RMSEs of the two potentials can be considered to be slightly less satisfactory. The potentials yield total values of 308 and 139 meV/Å, respectively. It should be noted that, typically, RMSEs below 100 meV/Å are commonly expected for similar MLIPs [269]. Nevertheless, an examination of Table 2.3 reveals that the average values are significantly influenced by the scores on the hot bulk 2 and 3 configuration groups, which correspond to ionic temperatures above 2000 K and defective structures. This deviation from the standard values may be attributed to the corresponding DFT+U calculations, particularly the complexity involved in operating the occupation matrix control procedure (as discussed in Section 2.1) far from equilibrium configurations. In summary, the overall agreement is satisfactory and correlation plots depicting this agreement on the total database are given Figures 2.6 and 2.6 for SNAP and HDNNP respectively.

Table 2.3 – Errors for SNAP and HDNNP potential.

		E (RMSE) (meV/atom)	E(MAE) (meV/atom)	F (RMSE) (meV/Å)	F (MAE) (meV/Å)	W (RMSE) (meV/Å^3)	W (MAE) (meV/Å^3)
SNAP	$fm\bar{3}m$	1.60	1.27	3.10	0.73	5.69	3.01
	Polymorphs	0.64	0.49	156.74	115.22	3.93	1.89
	Hot bulk 1 (300 to 2000 K)	3.39	2.25	221.11	159.65	5.67	3.65
	Hot bulk 2 (2200 to 2500 K)	5.70	4.47	385.19	295.84	6.00	4.19
	Hot bulk 3 (2800 to 3200 K)	8.45	7.04	493.72	377.91	7.45	5.27
	Defects	6.16	4.57	300.68	211.02	6.66	4.15
	γ-surfaces	6.42	4.97	163.15	82.47	6.67	3.41
	Total	5.26	3.52	308.81	206.00	6.07	3.62
HDNNP	$fm\bar{3}m$	2.71	2.33	11.72	2.30	10.53	4.01
	Polymorphs	3.47	2.81	63.17	46.95	14.37	5.13
	Hot bulk 1 (300 to 2000 K)	2.53	2.10	99.49	72.13	3.91	2.14
	Hot bulk 2 (2200 to 2500 K)	3.59	3.68	175.46	130.76	2.24	1.52
	Hot bulk 3 (2800 to 3200 K)	4.51	2.14	246.58	177.47	2.80	1.96
	Defects	2.53	3.68	115.77	85.07	3.67	2.15
	γ-surfaces	4.33	3.31	64.75	35.49	5.82	3.02
	Total	3.38	2.67	139.63	90.48	7.32	2.82

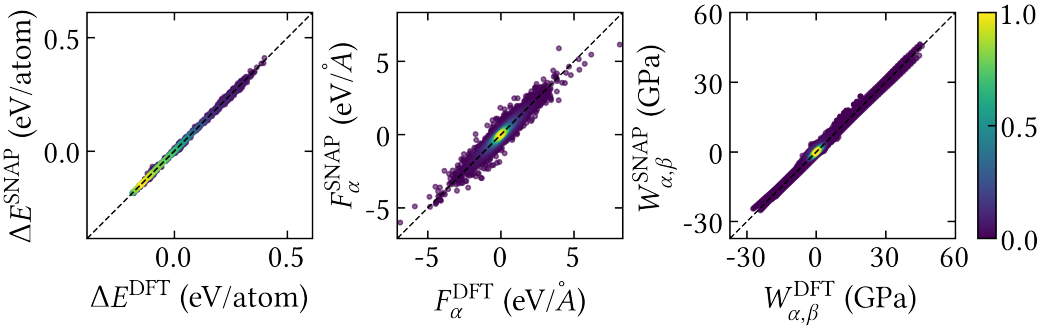

Figure 2.6 – Parity plot for energy, forces and stresses between DFT values (x-axis) and predicted values by the SNAP (y-axis). Points are coloured by the estimated point density using a kernel estimator.

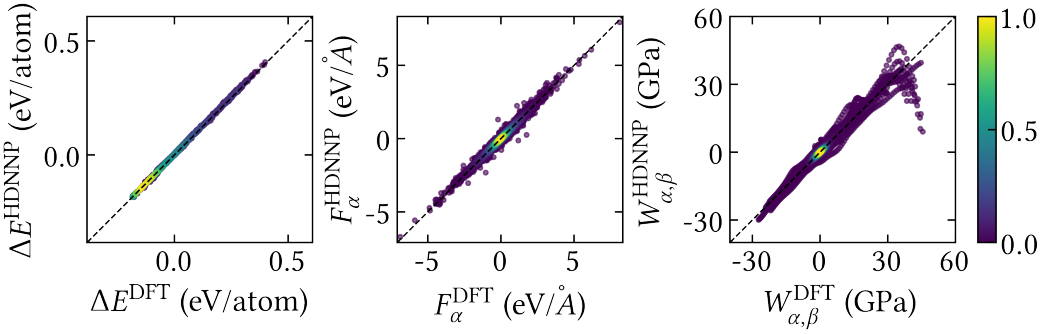

Figure 2.7 – Parity plot for energy, forces and stresses between DFT values (x-axis) and predicted values by the HDNNP (y-axis). Points are coloured by the estimated point density using a kernel estimator.

2.5.2. Equation of state

We computed the Energy-Volume and Pressure-Volume curves for different UO_2 polymorphs (namely $fm\bar{3}m$, *pnma*, *pbcn* and $P4_2mnm$) for volumetric deformations in the range [-10%; 10%]. These curves are displayed in Figure 2.8. We achieved excellent agreement between DFT results and both MLIPs for the considered polymorphs. It should be noted that the HDNNP was not explicitly trained on stresses, which explains the observed inflection points in the P-V curves.

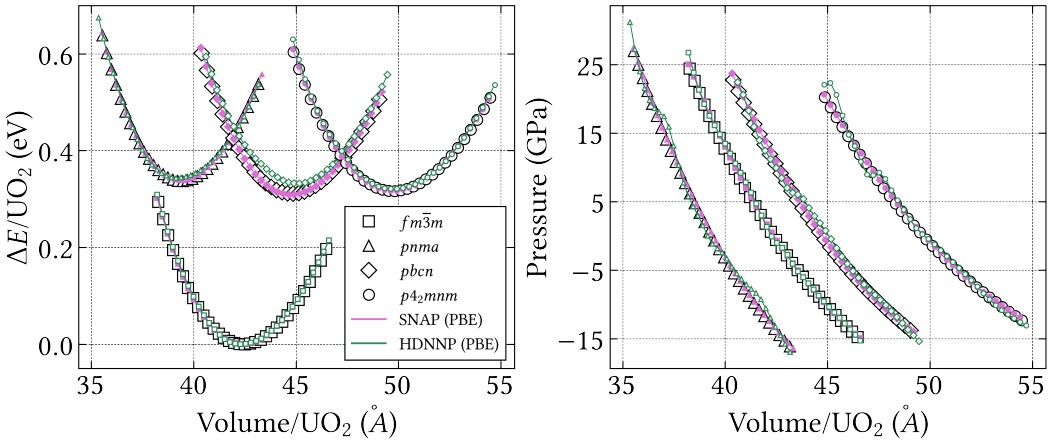

Figure 2.8 – Equation of state at 0 K of four different UO_2 polymorphs: $fm\bar{3}$,*pnma*, *pbcn* and $P4_2mnm$. DFT+U results are represented with white symbols, whereas the SNAP and HDNNP results are displayed as purple and green respectively.

For the fluorite $fm\bar{3}m$ phase, energy-volume data were fitted to a Vinet equation of state (2.25) to extract V_0, K_0 and K_0'. A similar procedure is applied to the results that come from the CRG, MOX-07 and SMTB-Q potentials. Table 2.4 summarises those

results.

$$P = 3K_0\left(\frac{1-\sqrt[3]{\frac{V}{V_0}}}{\left(\sqrt[3]{\frac{V}{V_0}}\right)^2}\exp\left[\frac{3}{2}\left(K_0^{'}-1\right)\left(1-\sqrt[3]{\frac{V}{V_0}}\right)\right]\right) \tag{2.25}$$

Table 2.4 – Extracted values of V_0, K_0 and K_0' from a fit to a Vinet equation of state to the $fm\bar{3}$ fluorine phase for PBE+U and various potentials.

	V_0 (Å^3/UO_2)	K_0 (GPa)	K_0' -
PBE+U	42.43	192.66	4.21
SNAP (PBE+U)	42.39	195.57	4.34
HDNNP (PBE+U)	42.42	197.68	4.25
CRG	40.54	218.10	4.86
MOX07	40.27	121.44	3.46
SMTB-Q	40.53	211.17	3.88

To compare MLIPs with other available potentials, we normalised the volume by the equilibrium volume, V_0, and shifted the energy by E_0 (i.e. the energy at V_0). Results are shown in Figure (2.9). We can observe that almost all potentials share the same trend for energy-volume curvature except for the MOX-07 potential, which exhibits a softer behaviour both in traction and compression, in agreement with the computed value of the compressibility modulus K_0.

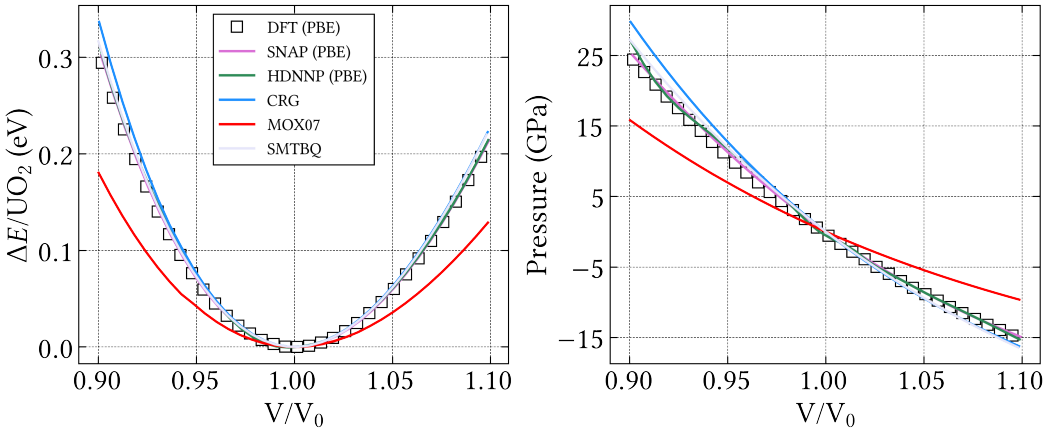

Figure 2.9 – Equation of state at 0 K with normalised volume and shifted E_0 for DFT+U, MLIPs and various SEIPs.

We were finally interested in the extrapolating behaviour of the MLIPs in compression, above the 10% in volume. For that we extend the $[-10\%; 0\%]$ range with new points

calculated in the range $[-25\%; -10\%]$ on which the potentials were not fitted, although those points were used to fit the repulsive ZBL contribution (see Section 2.2). Results plotted in Figure 2.10 show a very good agreement of the SNAP for both energy and pressure curves over the whole compression range. However, HDNNP shows quickly its limit when dealing with compression above the training range, resulting in non-physical behaviour. These results clearly highlight the higher extrapolation capability of SNAP compared to HDNNP due to its linear functional form.

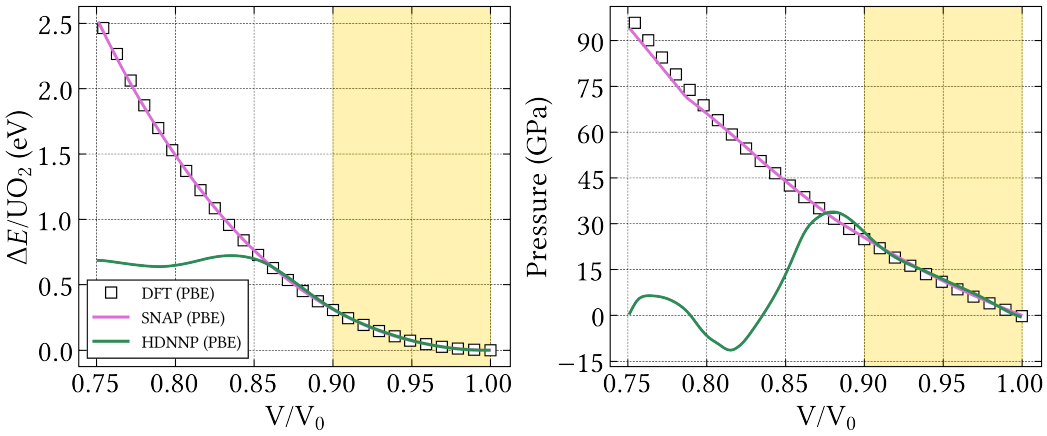

Figure 2.10 – Equation of state at 0 K in compressive regime. The yellow zone, correspond to the training domains of the SNAP (solid purple line) and HDNNP (solid green line) potentials.

2.5.3. Phonons

The phonon densities of states (PDOS) at 300 K were computed using the temperature dependent effective potential (TDEP) method [270] and 5×5×5 supercells equilibrated in the *NVT* ensemble. Results are presented in Figure 2.11 for our MLIPs, the CRG and the MOX-07 potentials, with a comparison to the experimental data of Pang *et al.* [198, 199] and their results using quasi-harmonic approximation (QHA) with GGA+U. The CRG and MOX-07 potentials reproduce correctly the acoustic region (0-25 meV), but the optical modes are strongly overestimated with CRG, as discussed in the work of Jin *et al.* [45], while MOX-07 underestimates them. GGA+U [199] is also in good agreement for the acoustic region, but to a lesser extent for the optical region, particularly the dispersion of the highest branch, between 70 and 80 meV, which is strongly underestimated. The HDNNP shows excellent agreement with the QHA results, with a better comparison to the experimental data for lower optical energies (25 to 55 meV). This can be attributed to the inclusion of anharmonic effects in the TDEP method, which are not accounted for in the QHA. The SNAP exhibits a stronger energy softening compared to QHA, but shows better agreement with DFT+U results and experimental data than the CRG and MOX-07 potentials. This is particularly important since quantities relevant to nuclear fuels, such as thermal conductivity, are related to PDOS. In particular, the CRG

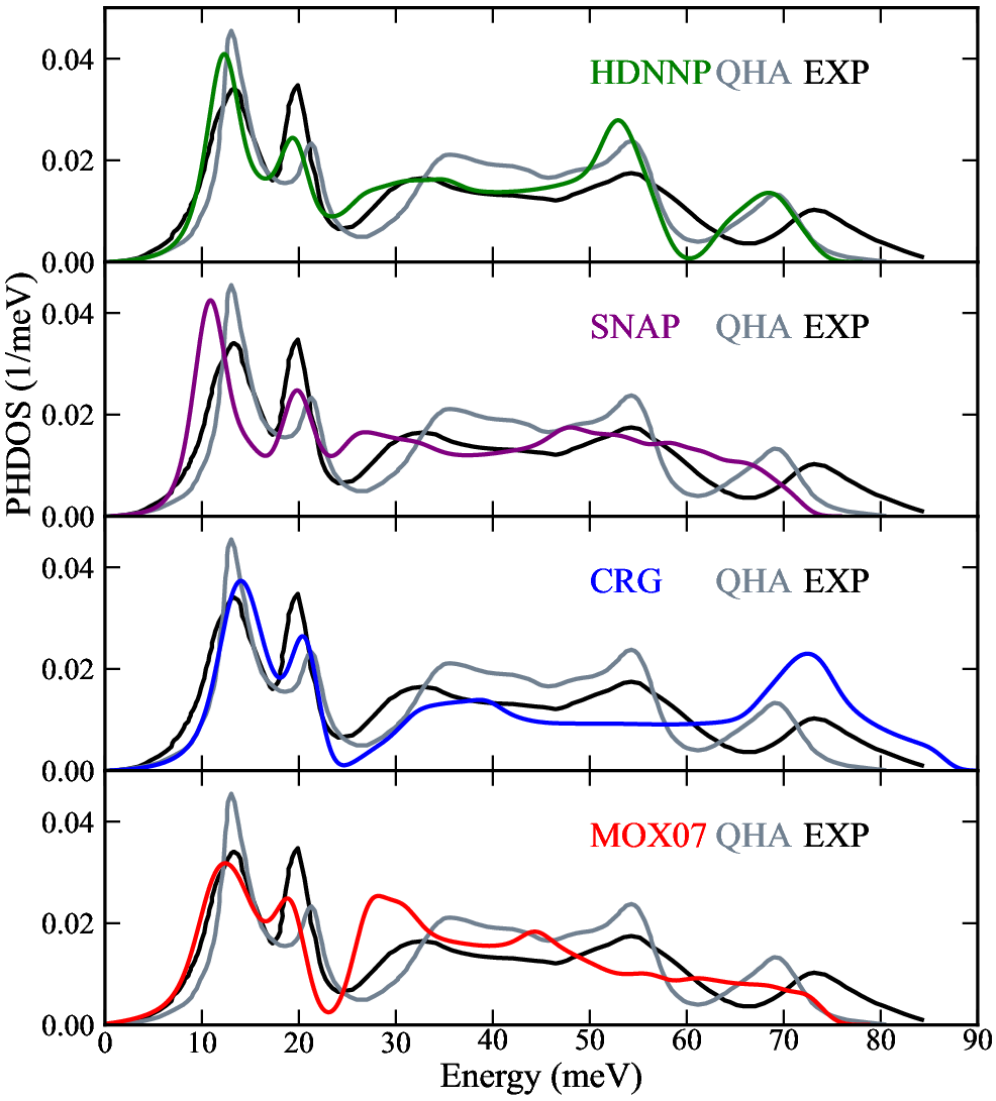

Figure 2.11 – Comparison of the phonon density of states of UO_2 at 300 K obtained with our MLIPs, CRG and MOX-07 with the experimental data [271] and the result of QHA [199].

potential is known to overestimate the phonon lifetime and consequently the thermal conductivity of the nuclear fuel [45].

2.5.4. Thermodynamics properties

The influence of temperature on a set of thermodynamic properties was computed in the isobaric-isothermal (NPT) ensemble. A 6×6×6 supercell (2592 atoms) was equilibrated at P = 1.0 bar at each target temperature for 80 ps. The observables of interest (lattice paremeter, enthalpy, etc.) were averaged over the last 30 ps. This procedure was repeated for temperatures ranging from 300 to 5000 K with a step of 25 K. All calculations were

performed using a 1 fs timestep, with damping parameters set to 0.1 ps and 1 ps for the thermostat and barostat, respectively. The lattice parameter, a, was directly extracted from the simulation, and used to compute the following thermal expansion ratio:

$$\Delta a/a_{300} = \frac{a(T) - a_{300}}{a_{300}} \tag{2.26}$$

The specific heat capacity, Cp, was computed by numerical differentiation of the enthalpy curve.

$$C_p = \left(\frac{\partial H(T)}{\partial T}\right)_P \tag{2.27}$$

The differentiation was performed by convolving the data with the first derivative of a Gaussian kernel of variance $\sigma = 3.8\Delta T$; this directly yields the derivative convolved with a Gaussian kernel of same variance[1]. To further increase the quality of the differentiation, we resampled the raw data using a cubic spline before the convolution step. The results are presented in Figures 2.12 and 2.13.

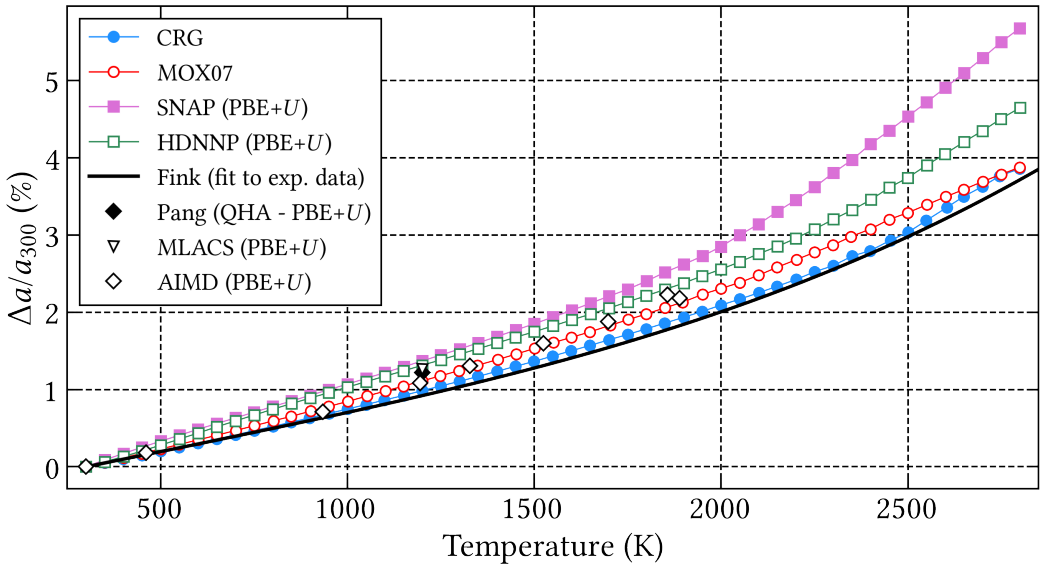

Figure 2.12 – Evolution of the ratio $\Delta a/a_{300}$ with respect to temperature. The black line displays the experimental recommendation from Martin [272]. The black diamond was extracted from the *ab initio* work of Pang *et al.* [199]. Open diamonds correspond to AIMD results extracted from [273]. Open triangles are results obtained by the MLACS method [274].

Concerning the evolution of thermal expansion, the CRG potential provides the best agreement compared to the experimental recommendation [53]. The trends exhibited by the two MLIPs present a slight overestimation of the thermal coefficient. However, these trends seem to be consistent with the existing DFT+U data. This slight overestimation

[1] $\partial(f * G^\sigma) = f * \partial G^\sigma$, where f is an arbitrary function and G^σ is a Gaussian kernel of variance σ.

of the thermal expansion at the first principle level of theory has been previously highlighted in the literature [275, 276]. While the origin of this deviation has not been clearly explained, Nakamura *et al.* [277] suggested box size effects and the choice of the PBE functional, known to overestimate interatomic distances. Thus, as the lattice expands, the binding energy might be underestimated.

Concerning the C_p evolution displayed in Figure 2.13 we notice that MLIPs successfully reproduce the Bredig transition around $T = 2500$ K. The existence of this transition, also referred to as a 'pre-melting' transition, is supported by experimental evidence [52]. It is associated with the emergence of a superionic state and a sudden increase in oxygen mobility within a stable uranium sublattice. As depicted in Figure 2.13, this second-order transition is characterised by a peak in the specific heat capacity. The onset of the transition appears earlier with the SNAP potential than with the other potentials, whereas the HDNNP shows better agreement with the experimental recommendation. We suggest that the early onset of the transition with MLIPs is due to the higher thermal expansion (Figure 2.12), as tendency of oxygen atoms to move to other sites and start a collective motion increases as the lattice expands. We can also anticipate that this larger expansion coefficient can play an important role in oxygen diffusivity after the Bredig transition. Additional work is presented in the Chapter 2.6.1 concerning the diffusivity of oxygen and the role of the lattice parameter at the onset of this superionic transition.

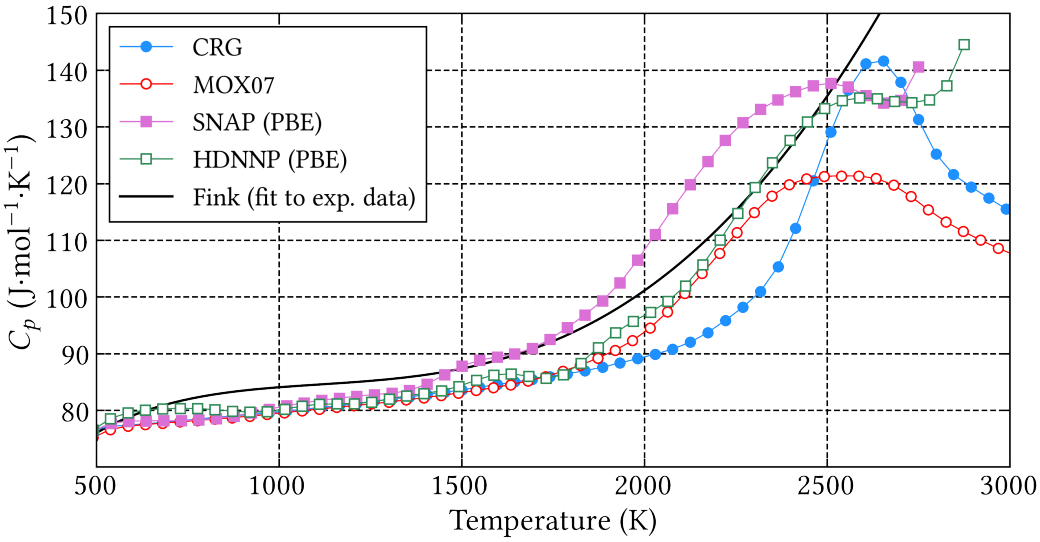

Figure 2.13 – Evolution of the specific heat-capacity, C_p, with respect to temperature. The black line display the experimental recommendation from Fink [53].

As expected from the difference in lattice parameter between DFT+U results and experimental observations, the density of the material evaluated by our MLIPs is underestimated by about 0.6 g·cm^{-3} ($\simeq -5.5\%$) compared to traditional potentials over the range 300 - 2100 K. This difference further increases with temperature, consistently

with the results of the thermal coefficient expansion (see 2.12). This shift of density is fully explained by the choice of the PBE functional that overestimates the volume of the unit cell by about 3.5%. A noticeable result is that, above melting, the density computed by the SNAP potential seems to stay stable with the same linearly decreasing trends. This is not the case with HDNNP, which presents a higher drop at melting and a rather constant density afterward. This is not associated with a physical behaviour; the potential is clearly in extrapolation within the liquid regime. Both potentials have been trained on the same database (see 2.1) that does not include any liquid configuration. This result highlights the stronger extrapolation capability of the SNAP due to its linear formalism compared to HDNNP.

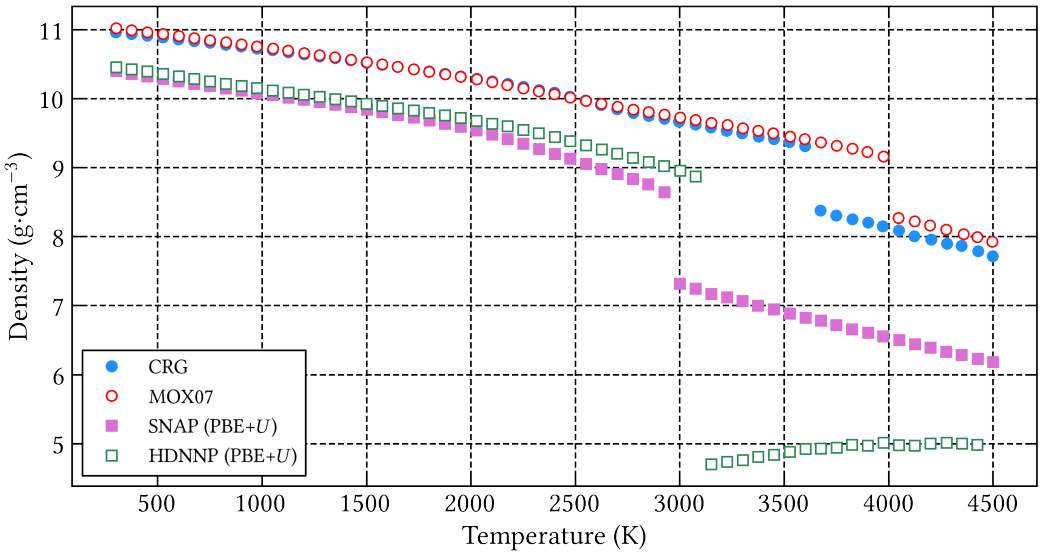

Figure 2.14 – Evolution of the density with respect to temperature.

2.5.5. Thermo-elasticity

Elasticity at 0 K

The stiffness tensor $\boldsymbol{C}$ at 0 K was obtained by direct application of the elasticity theory (see Appendix A for more details). The C_{ij} coefficients were obtained by a linear fit of the stress response to small strain (ranging from -1% to 1%) of the unit cell lattice parameter in each direction (xx, yy, zz, yz, xz, xy). The bulk (B), shear (G) and Young (E) modulii as well as Poisson ratio (ν) and universal anisotropy index (A^U) were computed through usual relationships derived from the stiffness and compliance tensor. Results at 0 K, displayed in Table 2.5, show that the SNAP predictions are in very good agreement with the PBE+U result whereas the HDNNP potential slightly overestimates the elastic tensor. As expected, the CRG potential leads to a better comparison with experimental data as its parameters were optimised to reproduced the experimental elastic tensor. The MOX-07 show the worst agreement; both with experiments and DFT+U results, as

it has been fitted on polycrystalline elasticity data.

Table 2.5 – Elastic constant, bulk modulus (K), shear modulus (G), Young modulus (E), Poisson ratio (ν) and universal anisotropy (A^U) from experiments, DFT+U, SNAP and HDNNP MLIPs potentials and CRG and MOX-07 SEIPs.

	C_{11} (GPa)	C_{12} (GPa)	C_{12} (GPa)	B (GPa)	G (GPa)	E (GPa)	ν -	A^U -
Brandt *et al.* [278]	400	125	59	217	83	222	0.33	0.91
Wachtman *et al.* [279][2]	396	121	64	213	87	231	0.32	0.74
PBE+U	**364**	**112**	**58**	**196**	**80**	**210**	**0.32**	**0.76**
CRG	**406**	**124**	**64**	**218**	**88**	**233**	**0.32**	**0.79**
MOX07	**215**	**74**	**73**	**121**	**72**	**181**	**0.25**	**0.00**
SNAP	**363**	**114**	**60**	**197**	**80**	**212**	**0.32**	**0.68**
HDNNP	**383**	**129**	**67**	**214**	**87**	**229**	**0.32**	**0.52**

Effect of temperature

Computing elastic constants at finite temperature is more challenging because it requires to run simulations that perform time averages of differential properties. The most common method is to perform direct deformation simulations: an equilibrated NPT simulation undergoes a series of finite small deformations. For each deformation, additional NVT or NVE simulations are performed, and the averaged stress tensor is extracted and linearly fitted to the applied strain tensor. While being very effective, it requires a lot of computational effort as well as convergence tests on applied strain and system size. We choose to follow another approach, proposed by Clavier *et al.* [280], exploiting the relationship between stiffness tensor, stress fluctuations, and the Born matrix, i.e. the second derivative of energy w.r.t. strain.

$$C^B_{ijkl} = \frac{1}{V}\frac{\partial^2 U}{\partial\epsilon_{ij}\partial\epsilon_{kl}} \tag{2.28}$$

The 4th order stiffness tensor is eventually obtained by the following relation:

$$C_{ijkl} = \left\langle C^B_{ijkl}\right\rangle + \frac{V}{k_B T}\left(\left\langle\sigma_{ij}\sigma_{kl}\right\rangle - \left\langle\sigma_{ij}\right\rangle\left\langle\sigma_{kl}\right\rangle\right) + \frac{Nk_B T}{V}\left(\delta_{ik}\delta_{jl} + \delta_{il}\delta_{jl}\right) \tag{2.29}$$

where N, T and V are the usual notation for number of particles, temperature and volume respectively. σ stands for the virial stress tensor, δ is the Kronecker delta function, and k_B is the Boltzmann constant. The method has the advantage of requiring only a single NVT simulation at the desired volume and temperature to fully reconstruct

[2] at 298.15K

$\boldsymbol{C}$. In this work, all calculations were performed on 12×12×12 supercells scaled to the equilibrium volume extracted from section 2.5.4's *NPT* simulations, with a timestep of 1 fs and a temperature damping parameter equal to 0.1 ps. Stress fluctuations and Born matrix terms were sampled every 100 timesteps. The final values of C_{ij} were obtained by a post-process Python script and averaged over 5 realisations with different initial velocity distributions.

The temperature dependencies of the three elastic constants (C_{11}, C_{12} and C_{44}) are displayed in Figure 2.15. The evolution of C_{11} for two MLIPs exhibits a similar trend to that calculated with the CRG potential, although with a shift towards lower values (consistent with 0 K DFT+U predictions, see Table 2.5). A continuous decrease is observed up to approximately 2000 K, followed by a stronger non-linear decrease attributed to the onset of the Bredig transition. Similar observations are made for C_{44}, except that the SNAP potential predicts an almost constant value until 1600 K. More significant differences are observed for C_{12}, with HDNNP predicting a rapid softening between 300 and 800 K, while SNAP leads to a constant value and CRG shows a linear decrease. However, the experimental data within the considered range of temperature are very noisy, making it hard to extract a general trend and, therefore, difficult to assess the agreement of the different tested potentials. The highlighted low-temperature behaviour of MLIPs might be associated with extrapolation due to the absence of relevant configurations in the training database, which mainly consist of isotropically deformed *NPT* simulations within the considered range of temperatures.

Figure 2.16 shows the evolution of bulk, shear and Young's moduli with temperature. For every property the two MLIPs show a similar trend and a good agreement with available experimental data for bulk modulus and *ab intio* extracted from MLACS calculations for shear and Young moduli. As these values are obtained directly from the stiffness tensor, they also show the discussed differences in the low temperature range for SNAP and HDNNP, albeit attenuated due to the averaging scheme.

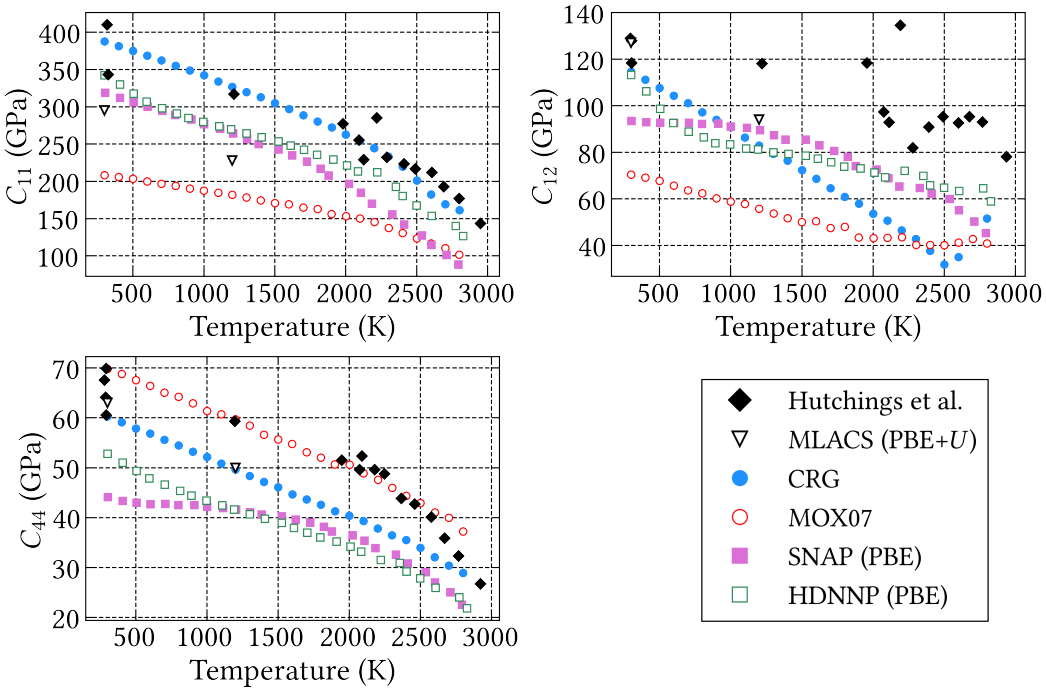

Figure 2.15 – Evolution of elastic constants (C_{11}, C_{12} and C_{44}) with respect to temperature, for four potentials (CRG in filled blue circles, MOX-07 in open red circles, SNAP in purple squares and HDNNP in open green squares). The black diamonds display the existing experimental data, extracted from [281]. The open black triangles refer to *ab initio* values obtained through the MLACS method [26, 274].

Finally, we were interested in the evolution of the Poisson ratio and universal anisotropy index. This is displayed in Figure 2.17. The first thing to note is that all tested potentials lead to different results. The MOX-07 potential exhibits a constant value of 0, which characterises its complete isotropy over the entire temperature range in agreement with the previous section. On the other hand the universal anisotropy ratio computed using the CRG potential exhibits a linear increase with temperature and then drops sharply around the Bredig transition. This decrease is associated with the isotropization of the material after the Bredig transition. A similar pattern is observed with HDNNP, except that the values of A^U before the drop are rather constant instead of increasing. Finally, results obtained by the SNAP potential show a monotonic, almost linear, decrease in A^U with temperature. An interesting observation common to all potentials is that the Bredig transition, and so the oxygen behaviour in the lattice, seems to be linked somehow to an isotropization of the material within this superionic state.

Overall, both SNAP and HDNNP show reasonably good agreement with respect to the evolution of elastic properties with temperature.

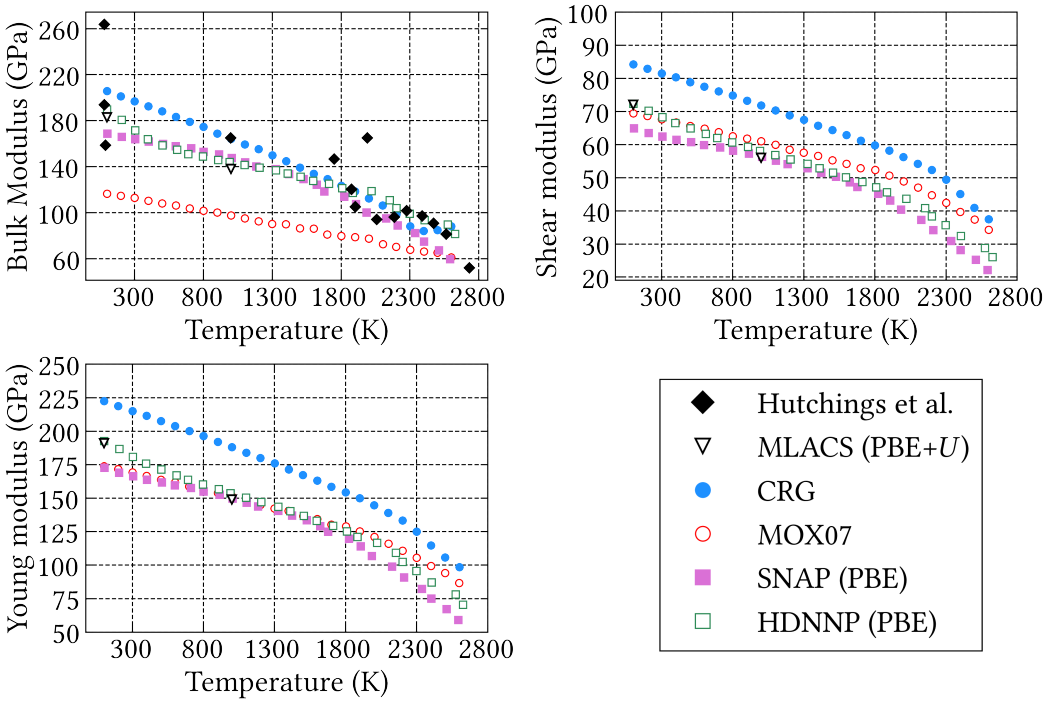

Figure 2.16 – Evolution of bulk, shear and Young moduli with respect to temperature, for four potentials (CRG in filled blue circles, MOX-07 in open red circles, SNAP in purple squares and HDNNP in open green squares). The black diamonds display the existing experimental data, extracted from [281]. The open black triangles refer to *ab initio* values obtained through the MLACS method [26, 274].

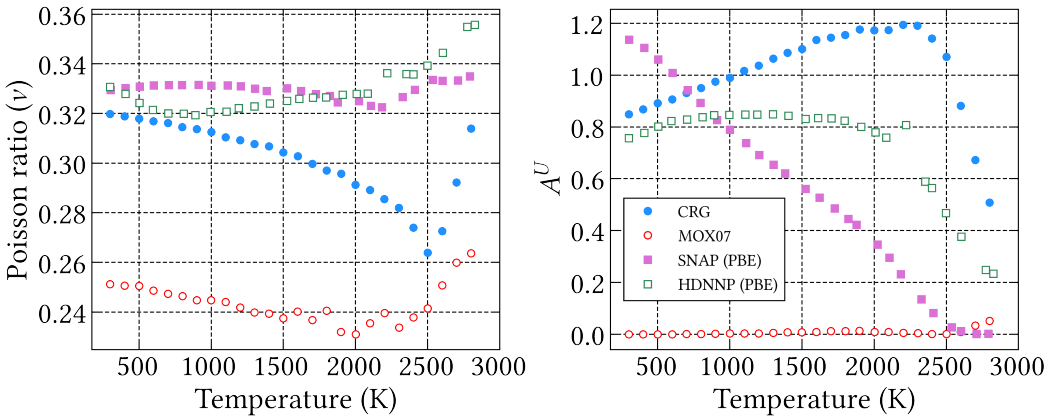

Figure 2.17 – Evolution of the Poisson ration ν, and universal anisotropy index A^U with respect to temperature, for four potentials (CRG in filled blue circles, MOX-07 in open red circles, SNAP in purple squares and HDNNP in open green squares).

2.5.6. Point defects formation energy

When considering the effect of irradiation on UO_2, it is important to account for the presence and creation of defects in the crystalline material. These defects significantly alter the thermomechanical properties of the material [43]. The most common types of defects encountered in UO_2 are the neutral BSD, with 3 different configurations depending of the location of the oxygen vacancies around the uranium vacancy, and the oxygen Frenkel pair (FP_O). For each type of defect, we conducted classical MD simulations to relax the structure around the defect and compute its formation energy at 0 K. Results are presented in Table 2.6 and compared to reference values of the literature. We found that both MLIPs show good agreement with the DFT+U results, with an average error of less than 10 meV/atom.

Table 2.6 – Defect formation energies

	BSD_1 (eV)	BSD_2 (eV)	BSD_3 (eV)	FP_O (eV)
at/cell	96	96	96	144
CRG	6.39	5.06	5.17	5.66
MOX-07	5.59	4.88	4.82	3.58
PBE+U [282]	3.32	2.54	2.82	4.96
SNAP	4.06	3.08	3.20	4.66
HDNNP	4.03	3.55	3.75	4.08

In order to compare the results with reference DFT+U calculations, 96-atom boxes were used in the calculation, although, in [24], the authors highlighted important size effects on the computation of BSDs formation energies and an inversion in the relative stability of BSD-2 and BSD-3 with the cell size. This will be the subject of further research.

2.5.7. Generalised stacking fault surfaces

Generalized Stacking Fault (GSF) energy surfaces, also referred to as γ-surfaces, are a crucial ingredient at the atomic scale for the characterisation of dislocations. To date, several empirical potentials have been used to simulate plasticity and dislocation motion in UO_2, but the γ-surfaces predictions of these potentials were never tested versus reference first-principles data [35, 47, 283]. Indeed, the γ-surfaces have never been computed within the complex DFT+U setup necessary for an accurate first-principles description of UO_2. Therefore, it remains a missing step in previous studies.

The γ-surfaces were computed in the {100}, {110} and {111} slip planes, which correspond to the main dislocations observed in UO_2 [284, 285]. Using suitable oriented supercells with slip planes orthogonal to the z-axis, the excess energy was obtained by translating the upper half of the supercell along a 50×50 (respectively 10×10 for

DFT+U calculations) grid of displacement vectors in the x and y directions. To prevent the system from returning to its original state, relaxation of atomic positions was only allowed along the z-axis, that is, orthogonal to the slip plane. Due to periodic boundary conditions, this setup results in the existence of two stacking faults localised at $l_z^{\max}/2$ and $l_z^{\max}$, where $l_z^{\max}$ is the length of the supercell along the z-axis. The supercells were constructed in such a way that the two planes associated with the stacking faults are equivalent. The periodic image of the stacking fault at the box boundary was taken into account by correcting the excess energy by a factor of 0.5. The resulting stacking fault energy S_α for the slip plane α is given by:

$$S_\alpha(\mathbf{\Delta}) = \frac{1}{2} \cdot \frac{E(\mathbf{\Delta}) - E(0)}{A_\alpha}, \tag{2.30}$$

where $E(\mathbf{\Delta})$ is the energy of the configuration shifted by the vector $\mathbf{\Delta} = \begin{pmatrix} \delta x & \delta y \end{pmatrix}$, and A_α is the area of the slip plane α. The same methodology was applied to compute first-principle γ-surfaces. However, a direct application of the procedure led to convergence issues in our DFT+U calculations. To overcome this difficulty, we leveraged the SNAP (the HDNNP could well have yielded equivalent results although it was less robust in extrapolation). The supercells corresponding to γ-surfaces, were first relaxed using an initial SNAP (initially not trained on) and then computed using single-point DFT+U calculations. These new labelled DFT+U results were added to the database and an updated SNAP was trained. This procedure was repeated until the configurations, relaxed using the surrogate SNAP, were minimised within the DFT+U framework. The obtained DFT+U results for the γ-surfaces along the three mentioned slip planes are displayed in Figure 2.18 and compared with the results obtained with our MLIPs (SNAP & HDNNP) and the CRG and MOX-07 potentials.

Along the {100} slip plane, the glide directions ⟨100⟩, ⟨110⟩, and ⟨100⟩ restore the lattice upon unit slip. The γ-surface suggests that the ⟨100⟩ and ⟨100⟩ directions have a lower energetic barrier for glide compared to the ⟨110⟩ direction which, however, corresponds to the experimentally observed Burger vector. This behaviour is quantitatively recovered by our SNAP and HDNNP potentials, as well as by CRG, whereas the MOX-07 potential exhibits a lower energy barrier in the **a-b** direction. Minimum Energy Path (MEP) along the ⟨100⟩ and ⟨110⟩ directions were extracted from the γ-surfaces and are shown in Figures 2.20-a and 2.20-b. Both SNAP and HDNNP exhibit excellent agreement with the DFT results in the ⟨100⟩ and ⟨110⟩ directions. Surprisingly, the CRG potential exhibits a marked minimum along ⟨100⟩, suggesting the possible stabilisation of partial dislocations with a stacking fault.

For the {110} plane, the glide directions ⟨001⟩ and ⟨110⟩ restore the lattice upon unit slip. The first principles γ-surface reveals that results obtained with our SNAP, HDNNP and MOX-07 potentials are in very good agreement with the DFT results and reproduce accurately the minimum energy path (MEP) along the ⟨110⟩ direction (see Figure 2.20-c). The CRG potential reproduces the shape of the MEP but overestimates the energy barrier by about 30%.

For the {111} slip plane, the glide directions ⟨112⟩, ⟨110⟩ and ⟨011⟩ restore the lattice

upon unit slip. Glide is expected to occur along any of the degenerate ⟨110⟩ and ⟨011⟩ directions, with the dislocation eventually splitting into partials. Both MLIPs reproduce the shape and energy of the γ-surface, whereas CRG and MOX-07 exhibit slightly higher energy barriers along the MEP (see Figure 2.20-d). Note that the results for the {111} slip plane differ from those in [47, 283] because they placed the slip plane between two oxygen layer (Figure 2.19-A), whereas we decided to place the slip plane between U and O layers (Figure 2.19-B). In case B, the layers are closely spaced, so that atoms pass close to one another, resulting in higher GSF energies.

The overall agreement between first principles calculations and SNAP or HDNNP is very satisfactory for the γ-surfaces of the three slip planes considered here. In contrast, CRG and MOX-07 exhibit some discrepancies compared to the DFT+U data, particularly with regard to energy barriers along the minimum energy path. Because these energy barriers control the ease of glide, the elastic-plastic threshold, and the material's behaviour under deformation, we anticipate that those results can have significant consequences in predicting the plastic behaviour and dislocation mobility, which is crucial for irradiated fuel materials. A detailed investigation of these properties will be the subject of future work.

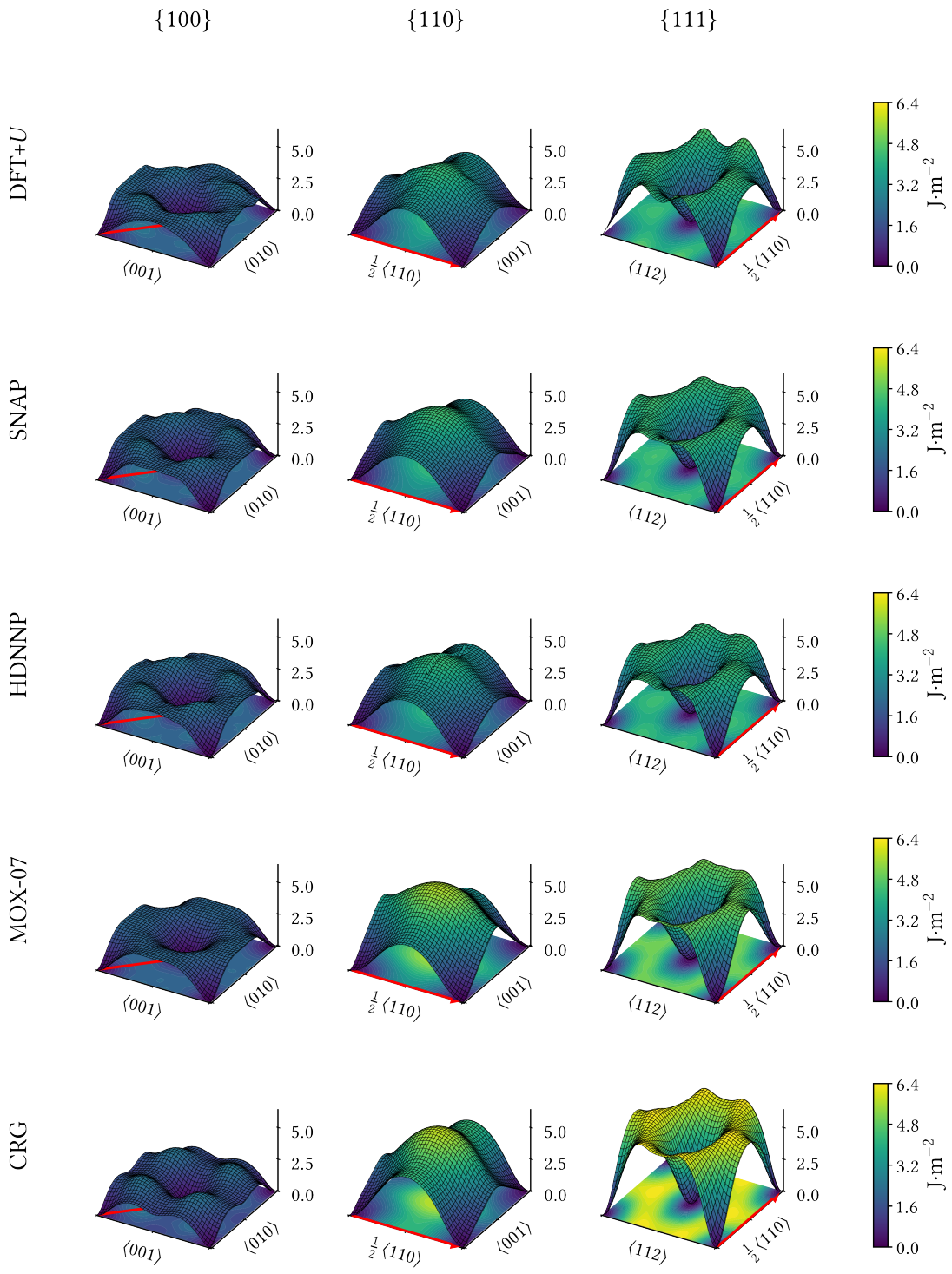

Figure 2.18 – Generalised stacking fault energy surfaces (γ-surfaces) for the {100}, {110} and {111} slip planes in UO_2 computed with DFT+U and different interatomic potentials. For each plane, the Burgers vector $1/2\langle 110\rangle$ is represented by a red arrow. For ease of comparison, all γ-surfaces are plotted on the same energy scale.

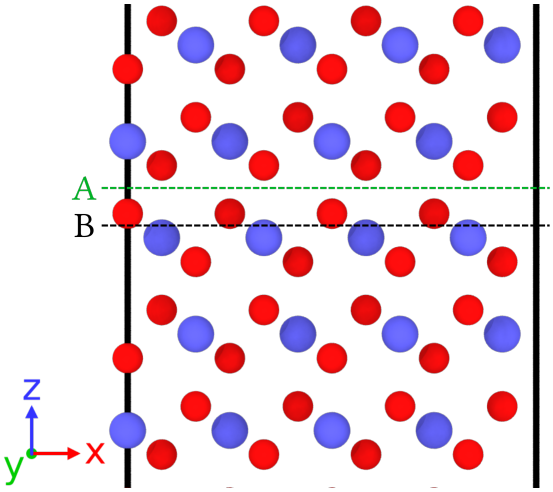

Figure 2.19 – Side view of the {111} supercell. The green and black dashed lines represent the two possible positions for the slip plane.

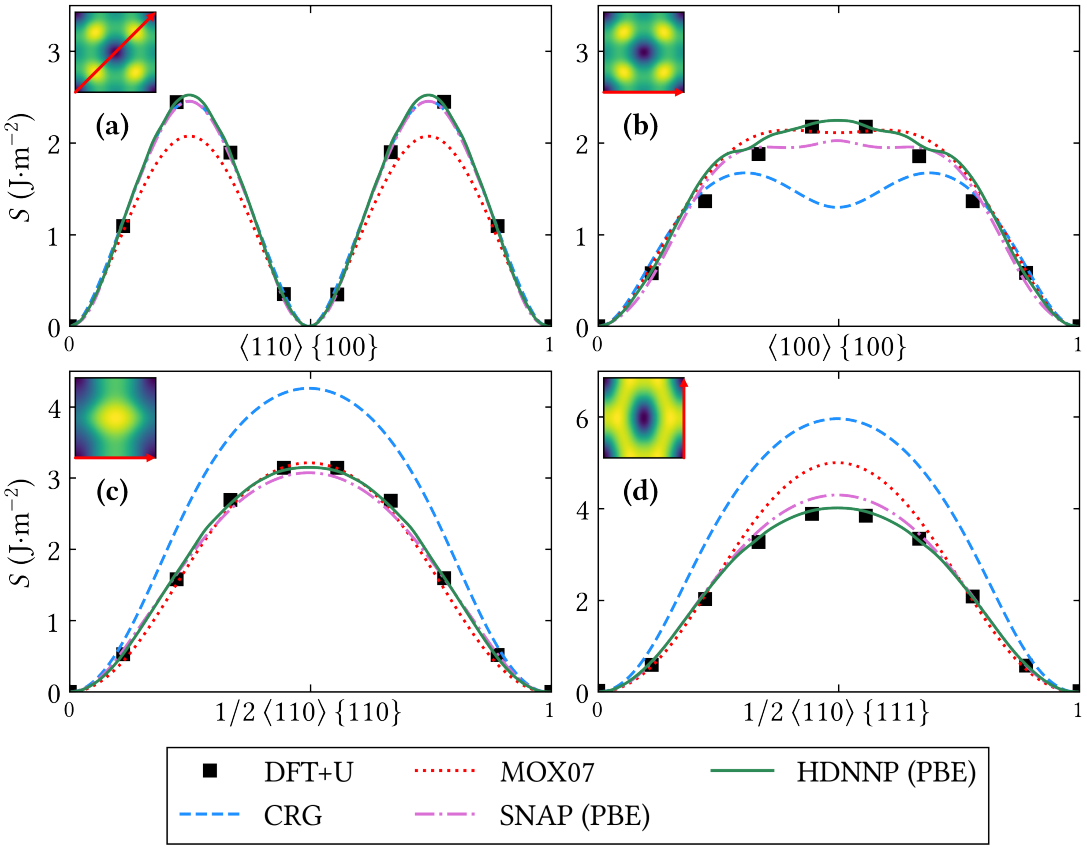

Figure 2.20 – (a) ⟨110⟩{100}; (b) ⟨100⟩{100}; (c) 1/2⟨110⟩{110}; (d) 1/2⟨110⟩{100} γ-lines in UO_2.

2.6. Potential use cases

In this section, we introduce some practical uses of MLIPs developed in the previous sections and how they were used in physical applications in the context of active research on nuclear fuel materials. This collaborative work with other students was really beneficial in terms of feedback for the potential development, either to highlight their possible weaknesses or to adapt them to specific needs. Within those collaborative investigations, I was in charge of developing and testing the MLIP models, and most of the computations were performed by Edoardo Brando (Section 2.6.1) and Petra Ospital (Section 2.6.2) currently PhD students at the DEC/SESC in Cadarache.

2.6.1. Oxygen diffusivity in UO_2 and UO_{2+x}

The SNAP developed in the previous section has been used by Edoardo Brando during his internship at the LM2C to investigate the oxygen diffusivity in both stoichiometric and hyperstoichiometric uranium dioxide (UO_2 and UO_{2+x}). The potential was compared with two other interatomic potentials, the CRG and SMTB-Q potentials. The objective of this work was to gain deeper insight and discern similarities and disparities between the three potentials, radically different by construction and fitting. The original version of the SNAP, where energy is given as follows (see more detail in Chapter 2.2):

$$E = E_r + E_C + E_{\mathrm{ML}} \tag{2.31}$$

was not compatible with hyperstoichiometric conditions. This was mainly related to long-range Coulombic interactions, requiring an Ewald summation scheme and thus formally imposing the electric charge neutrality across the simulation box. After discussions, it was realised that removing this Coulombic interaction could help to solve these problems. Therefore, a modified version of the SNAP was trained on the same training set but with the long-range Coulomb interactions removed.

$$E = E_r + E_{\mathrm{ML}} \tag{2.32}$$

In this case, all the charge effects are implicitly covered by the E_{ML} term. The resulting potential only accounts for local contributions and is therefore a purely short-range potential. The two SNAPs were denoted SNAP-C for the original one (accounting for the long-range Coulombic interactions) and SNAP-NC for the modified one (NC standing for for Non-Coulombic).

As depicted in Figure 2.21, both SNAPs exhibit similar results for oxygen diffusivity in stoichiometric UO_2 but the SNAP-NC yields a much higher peak in the heat capacity curves. The same observation will also discussed when comparing the SNAP from Chapter 2 and 3; where the latter, as the SNAP-NC, does not have explicit description of long range Coulombic interactions. All tested potentials share the same trends for oxygen diffusion except that the sudden increase in oxygen diffusivity for CRG and SMTB-Q occurs around 2100 K, whereas for both SNAPs similar behaviour is observed

at lower temperature, around 1800 K. It was noticed that a possible contribution to the temperature shift could be the differences in volume yielded by the different potentials: CRG and SMTB-Q are fitted to reproduce experimental data, while both SNAPs were trained on DFT+U dataset that, as discussed in 2.5.4, appear to sightly overestimate the volume. To verify this assumption, NVE simulations were conducted on rescaled boxes to ensure comparable volumes. The lattice parameter for SNAP-C and SNAP-NC was scaled by a factor of 0.98 while for the CRG potential it was increased by a factor of 1.02. In this case, the diffusivity increase occurs at comparable temperatures suggesting a possible correlation between the Bredig transition's temperature and the volume of the material.

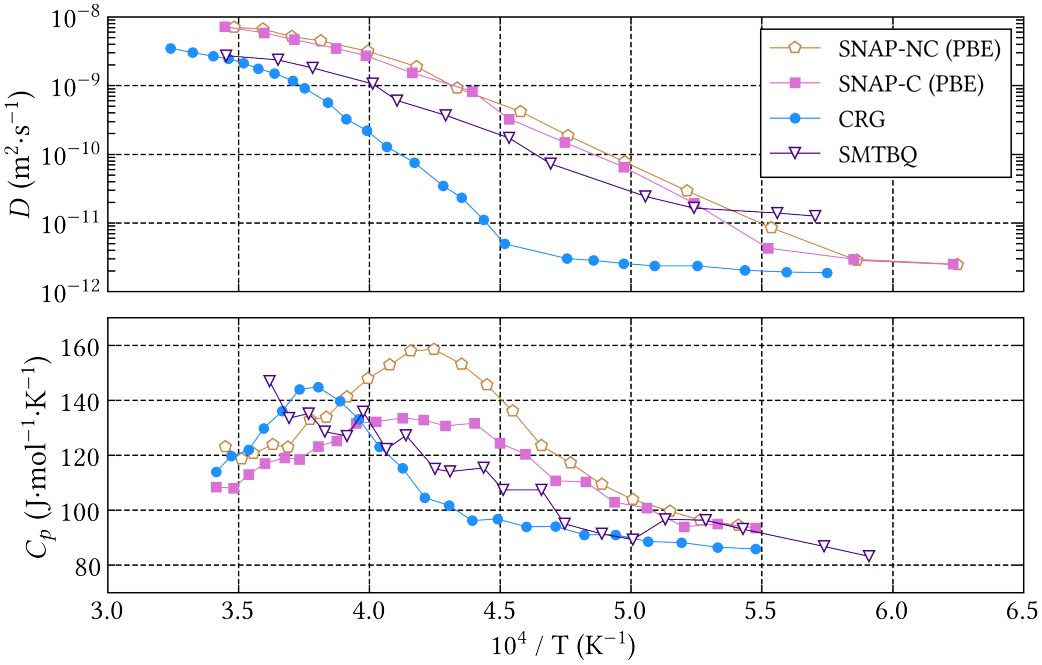

Figure 2.21 – On top, evolution of the oxygen diffusion coefficient as a function of the inverse of the temperature for our four different interatomic potentials for stoichiometric UO_2. At the bottom, heat-capacity of the sample as a function the inverse of the temperature with the same four interatomic potentials.

Nonetheless, it is observed on Figure 2.22 that the peak in heat capacity corresponds exactly to the point of maximum increase in diffusivity; as the first derivative reaches its maximum. This clearly highlights the collective behaviour of oxygen and the supposed sub-melting of oxygen sublattice at the Bredig temperature.

In addition, hyperstoichiometric results of calculations of both oxygen diffusivity and heat capacity with the SNAP-NC are displayed in Figure 2.23. A noticeable decrease in both the intensity of the heat capacity peak and the transition temperature is observed at higher stoichiometry.

The use of the SNAP potential has been tremendously important in this work to highlight the correlation between the lattice parameter and the Bredig transition. Ad-

ditionally, despite being completely different interatomic potentials - one fitted to experimental data and the other to *ab initio* calculations - they yield very similar results in terms of comparing heat capacity with oxygen diffusivity. This is an important achievement, and a paper based on these results covering an in-depth study is being written for publication in the coming months.

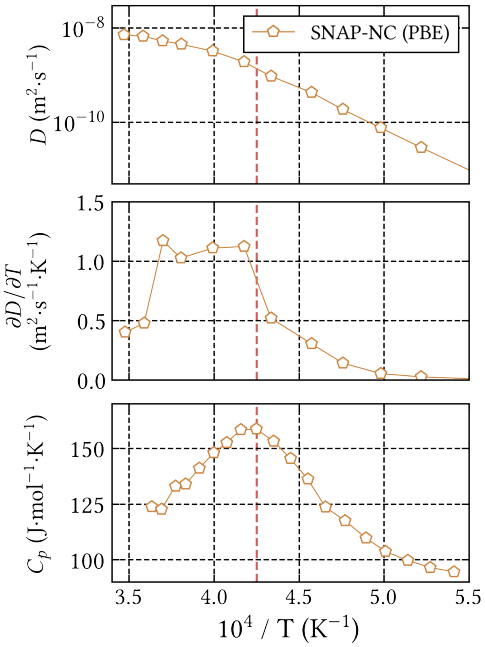

Figure 2.22 – Oxygen diffusivity, its first derivative w.r.t temperature and heat capacity of stoichiometric UO_2; computed with SNAP-NC.

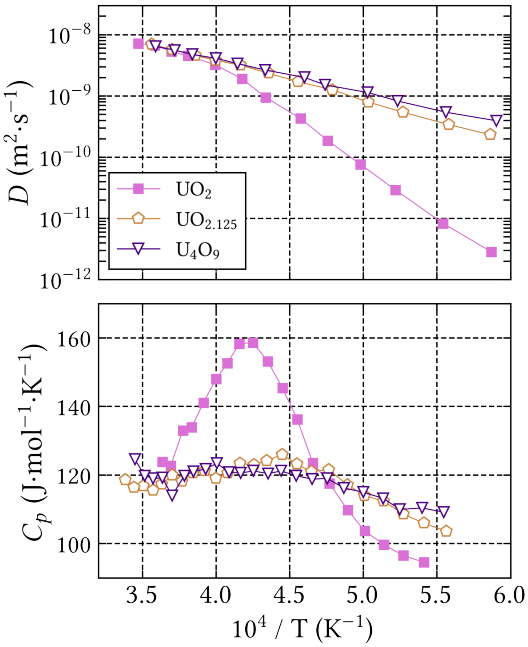

Figure 2.23 – Oxygen diffusivity and heat capacity for stoichiometric (UO_2), hyper-stoichiometric ($UO_{2.215}$) and U_4O_9; computed with SNAP-NC.

2.6.2. Cationic auto-diffusion in UO_2

Cationic self-diffusion has multiple effects on nuclear fuel materials. For uranium dioxide (UO_2), it is a key mechanism in creep, i.e. a slow and time-dependent deformation of materials under constant stress that affects the structural integrity of fuel pellets and cladding, especially at high temperatures, typical of reactor environments. Furthermore, self-diffusion rates influence grain growth and phase transformations, leading to microstructural evolution during operation, which in turn affects thermal conductivity, mechanical properties, and fission gas release. In mixed oxide fuels (U,Pu)O_2, the self-diffusion of uranium and plutonium atoms affects the homogeneity of the Pu distribution during the manufacturing processes. Local variations in plutonium concentration can lead to localised hotspots, impacting the fuel's performance and safety. In operating conditions, U and Pu atoms can migrate as a result of irradiation, leading to inhomogeneities. Thus, the study of cationic self-diffusion in UO_2, and, by extend, to PuO_2 and (U,Pu)O_2 through multi-scale numerical methods is crucial for

understanding and improving the performance of nuclear fuel materials.

The proposed methodology involves the linkage of three methods: the activation-relaxation technique (ART) method [286], to explore the PES and discover migration mechanisms, the NEB method [287], to evaluate the migration energies of those mechanisms, and finally the kinetic cluster expansion (KineCluE) code [288], to compute the transport coefficients of chemical species from migration energies. The Figure 2.24 displays a schematic representation of such a linkage.

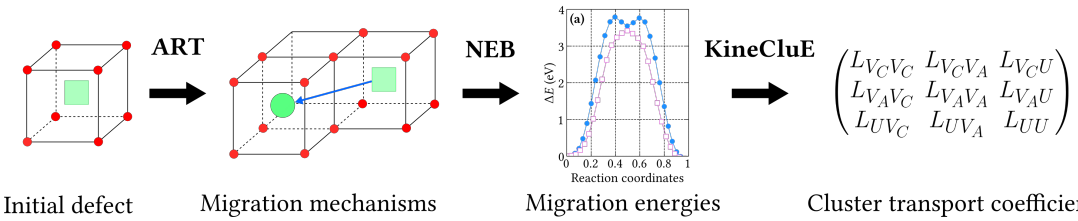

Figure 2.24 – Illustration of the methodology involving the linkage of ART, NEB and KineCluE.

In this context, the SNAP developed in Chapter 2 has been used by Petra Ospital to compute the migration energies of three mechanisms previously identified and compared to the CRG potential. Those mechanisms are:

- The migration of an isolated cationic vacancy along the ⟨110⟩ direction (Figure 2.25-a).
- The migration of a bi-vacancy (cationic-anionic), where the cationic vacancy migrates along the ⟨110⟩ and the anionic vacancy migrates successively in the ⟨010⟩ and ⟨100⟩ directions such that the final defects remain unchanged (Figure 2.25-b).
- The migration of a BSD-3 where the cationic vacancy migrates along the ⟨110⟩ direction and anionic vacancies along the ⟨100⟩ and ⟨010⟩ directions, the final configuration remaining a BSD-3 (Figure 2.25-c).

Results, displayed in Figure 2.26, show that SNAP exhibits lower migration energies than CRG. These differences, ranging from 0.5 to 1 eV, are significant and one could expect a strong influence on the diffusion coefficients. Additionally, for the transition path of the isolated vacancy, CRG exhibits a metastable state at the midpoint of the reaction path state which is not observed with SNAP. Even if SNAP shows reasonably good results on the formation of BSD (see Chapter 2), it has been trained neither on formation energies of isolated vacancy and bi-vacancy defects nor on migration energies. Thus, presented results were obtained with the SNAP being in extrapolation and should be considered with care. Nevertheless, the use of MLIPs can be really beneficial, allowing higher accuracy with respect to DFT+U calculations than SEIPs while keeping an acceptable computational cost. Thus, permitting for a systematic study of migration mechanisms. In this particular case, we emphasise that MLIPs trained specifically for defect calculations (formation and migration energies) should be preferred to a 'global'

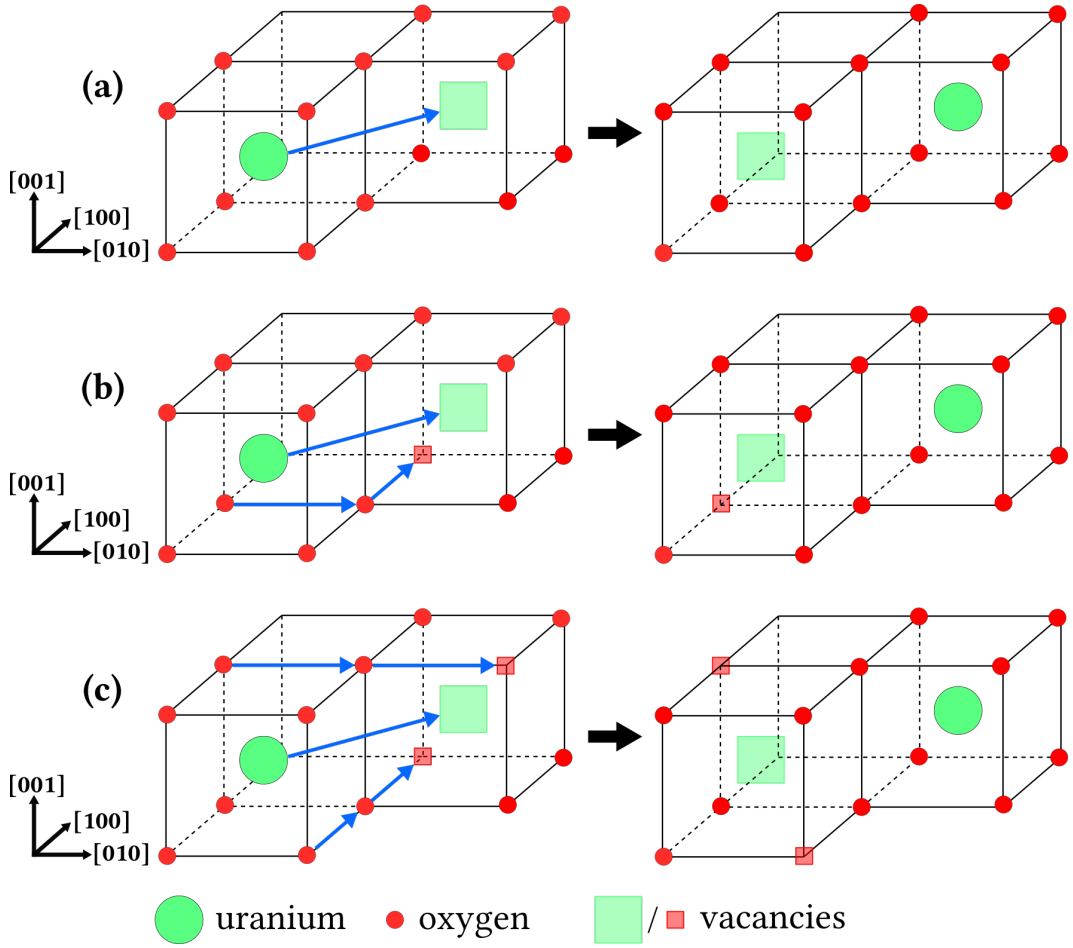

Figure 2.25 – Illustration of the migration mechanisms for the (a) isolated cationic vacancy; (b) bi-vacancy; (c) BSD-3.

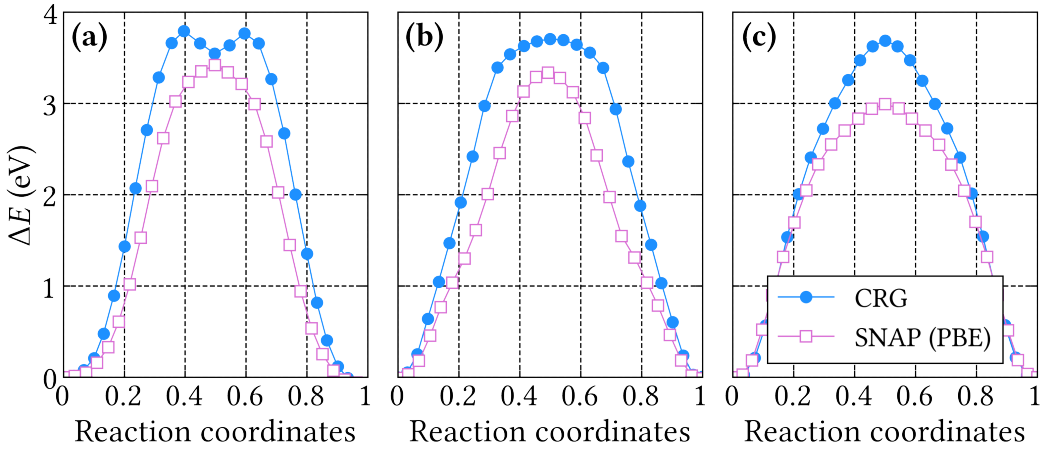

Figure 2.26 – Migration energy path for the (a) isolated cationic vacancy; (b) bi-vacancy; (c) BSD-3.

one, balancing the accuracy-transferability trade-off in favour of accuracy. From the opposite point of view, a DFT+U evaluation of defects migration mechanisms identified by the ART method would be an efficient way to extend training sets on which MLIPs are trained to adequately describe defects migration events in large-scale MD simulations. My contribution to the collaboration was mainly the development of the SNAP model and supporting Petra Ospital in its use for NEB calculations.

2.7. Conclusion

The initial phase of the chapter was focused on developing and validating two machine learning interatomic potentials for uranium dioxide using the SNAP and HDNNP methodologies. We used active learning methods alongside state-of-the-art DFT+U calculations to generate diverse and representative ensembles of atomic configurations to train these potentials. Despite the complexity of the reference DFT+U calculations, both potentials showed good agreement with a wide range of *ab initio* and experimental metrics.

We investigated the temperature dependence of the potentials, specifically by examining the evolution of elastic constants, thermal expansion, and heat capacity. Comparisons with existing experimental data demonstrated reasonable agreement. Moreover, our potentials successfully reproduced the superionic transition (Bredig transition) around 2500 K, which remains a topic of theoretical and experimental investigations [51, 52].

Our SNAP potential was leveraged to relax stacking fault configurations, enabling their subsequent evaluation using DFT+U. Notably, this represents the first DFT+U computation of stacking fault energy surfaces. The latters significantly contribute to the understanding of the plastic behaviour of UO_2, including the evaluation of dislocation nucleation stresses, and are fundamental to the field of nuclear fuels. In the final part of this chapter, we presented two applications of the developed potentials, conducted in collaboration with other students. The first study examined oxygen diffusivity in hyperstoichiometric UO_{2+x}, for which a specific SNAP was developed without long-range coulombic interactions. This work highlighted a possible correlation between the material's density and the collective motion of oxygen associated with the Bredig transition. We also demonstrated the use of SNAP in NEB calculations as part of the ART workflow, showcasing the results of the point defect migration energies, which exhibited several differences compared to the CRG potential.

Chapter 3.

Mechanical response of UO_2 single crystal at the atomic scale

La vie, c'est pas un cookie.

– Pauline Richard

Contents

3.1. Toward a new DFT recipe . . . 88
3.2. A new database, a new potential . . . 92
3.3. Assessment of the SNAP-PBEsol . . . 94
3.4. Application: UO_2 mechanical response at the atomic scale . . . 105
3.4.1. Method . . . 105
3.4.2. UO_2 single crystal at 300K . . . 109
3.4.3. Effect of strain-rate on the flow surface . . . 114
3.4.4. Effect of temperature . . . 116
3.4.5. Effect of irradiation at ambient temperature . . . 122
3.4.6. Irradiation and temperature effects altogether . . . 126
3.5. Conclusion . . . 130

Despite the promising results obtained with the MLIPs developed in the previous chapter, some problems persisted and were raised through the numerous discussions we had with our potentials' users, as well as with co-workers who perform experimental measurements. In particular, the predicted density is underestimated by about 5% at 300 K up to 9% at 2500 K. This was seen as a major limitation, hampering the possibility of making comparisons with available experimental data. The problem is well identified and related to the GGA-PBE exchange-correlation functional, known to overestimate the lattice parameter. As MLIPs only reflect their training dataset, the same overestimation was anticipated.

Nevertheless, material density is not an impact-free property and it is legitimate to question the reliability of the predicted results obtained with these potentials in

atomic-scale simulations. Therefore, in this chapter, we attempt to reconcile DFT approximations with experimental observations to train MLIPs that consistently align with both *ab initio* methods and experimental data. The newly developed SNAP-PBEsol will then be used, at the end of this chapter, to study the mechanical response of UO_2 single crystal at the atomic scale.

3.1. Toward a new DFT recipe

The first step toward the improvement of the agreement between densities predicted by DFT calculations and experimental observations was to change the exchange-correlation functional. Indeed, GGA-PBE is known to underestimate binding energies and thus overestimate the lattice parameter. This overestimation is exacerbated within the DFT+U formalism, as the Hubbard correction term corresponds to a repulsive Coulombic interaction between strongly correlated electrons (see Chapter 1). We choose the PBEsol functional, which has the same functional form as PBE but with parameters tailored to give more accurate results for low temperature solids and surfaces [112]. The exchange enhancement function used for PBEsol is closer to LDA, giving stronger binding energies than PBE, and thus predicting smaller volumes. The use of PBEsol functional within the DFT+U formalism for the description of actinide oxides has already been discussed in the literature and indeed allows for a predicted density closer to the experimental one [61, 62, 289].

In Chapter 2, a longitudinal 1**k** AFM order was used (Figure 3.1) which is the most common setup encountered in the literature. However, such approximation results in a material that is not cubic anymore. We also realised that it was inducing an anisotropic response to deformation in terms of stress. This induced anisotropy has a rather small impact on the prediction of energies, and is therefore often ignored. In the context of MLIPs training, such inconsistency in the database could have a negative influence, degrading the fitting procedure. Indeed, our MLIPs formalism is blind to the magnetic configuration and is therefore unable to understand the physical origin of this anisotropy. A possible solution suggested in the literature [61, 63] is the use of a 3**k** magnetic ordering to retrieve the cubic structure of the material. To confirm those results, we performed a systematic study of different magnetic 1**k** (Figure 3.1) and 3**k** (Figure 3.2) orderings. The DFT+U parameters used were kept the same as in Chapter 2, except for the exchange-correlation functional. A complete relaxation of the lattice vectors was allowed. A particular point is that for 3**k** magnetic orders, we were unable to properly apply the OMC procedure, so we took the decision to omit it for all calculations (including 1**k** orders). To overcome the problem of metastable states, SOC was introduced in the calculations. As suggested by investigation of Dudarev *et al.* [246] and Laskowski *et al.* [290], while accounting for SOC, the OMC procedure does not allow to find lower energy states compared to a calculation without constraint on occupation matrices. Eventually, tests were performed with lowered values of $U = 3.5$ eV and $J = 0.54$ eV. Results are summarised in Table 3.1.

The lowest energy is observed for the degenerate 1**k**-b and 1**k**-c magnetic configura-

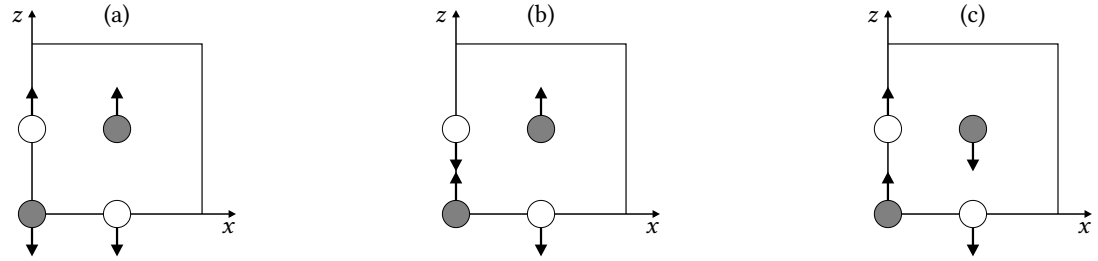

Figure 3.1 – Schematic representation of 1**k** magnetic orderings. Circles represents uranium atoms at $y = 0$ (grey) and $y = 0.5$ (white) positions. Oxygen atoms are omitted for clarity.

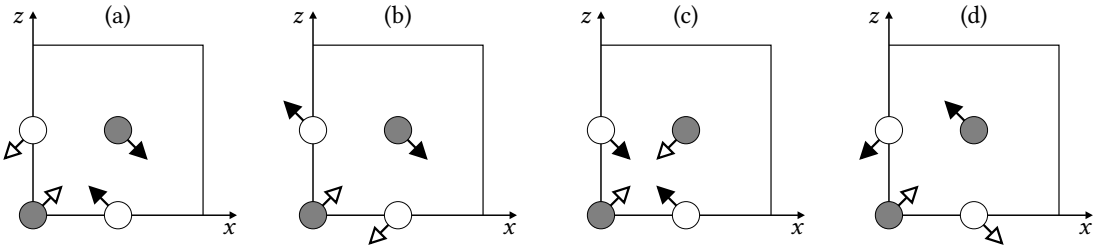

Figure 3.2 – Schematic representation of 3**k** magnetic orderings. The circles represent the uranium atoms at $y = 0$ (grey) and $y = 0.5$ (white) positions. Oxygen atoms are omitted for clarity. Open and plain arrows point toward the y and $-y$ directions, respectively.

Table 3.1 – Comparisons between the different magnetic orderings in terms of relative energy, lattice parameters and band gap.

	Exp.	AFM 1**k**			AFM 3**k**			
		a	b	c	a	b	c	d
$\Delta E/UO_2$ (meV)	-	9.4	0.0	0.0	7.4	4.9	14.9	4.7
a (Å)	5.47	5.46	5.46	5.46	5.46	5.46	5.46	5.47
b (Å)	5.47	5.46	5.46	5.46	5.46	5.46	5.46	5.46
c (Å)	5.47	5.47	5.47	5.47	5.46	5.46	5.46	5.46
α (°)	90.0	90.0	90.0	90.0	90.0	90.0	90.0	90.0
β (°)	90.0	90.0	90.0	90.0	90.0	90.0	90.0	90.0
γ (°)	90.0	90.0	90.0	90.0	90.0	90.0	90.0	89.6
Band gap (eV)	2.0 - 2.5	1.9	2.0	2.1	2.0	2.1	1.9	2.1
O distortion	?	no	no	no	yes	yes	no	yes

tions, which are however not cubic as expected. For the 3**k** ordering, the most stable configuration is the 3**k**-b, which however exhibits a distortion of the oxygen sublattice. In the literature, this is associated either with a Jahn-Teller effect or with a $pa\bar{3}$ phase. Recent studies suggest that this $pa\bar{3}$ phase might be the ground state of UO_2, but remain

inconclusive [54]. As so, we identified the 3**k**-c order as the only one that satisfies our needs, i.e. leading to a cubic structure with no oxygen distortion, and decided to use it for subsequent calculations even though it is not the most stable energetically.

Systematic investigation of the U and J parameters

Retaining the 3**k**-c magnetic order, we investigate the influence of the U and J parameters, as is commonly done in this type of study. We performed calculations using a uniform grid of U and J values, with $U \in [2;5]$ eV every 0.5 eV and $J \in [0;1]$ eV every 0.2 eV. For each pair (U, J), we first computed the equilibrium volume by fitting a Vinet equation of state to a series of 10 points within a volumetric deformation range $[-5\%; 5\%]$. From the equilibrium volume, we extracted the lattice parameter (Figure 3.3-a) and performed an additional ground state calculations to determine the band gap (Figure 3.3-b). Finally, the elastic constants were computed following the methodology described in Chapter 2. The dependence of the elastic properties (C_{11}, C_{12} and C_{44}) on U and J is displayed in Figure 3.4.

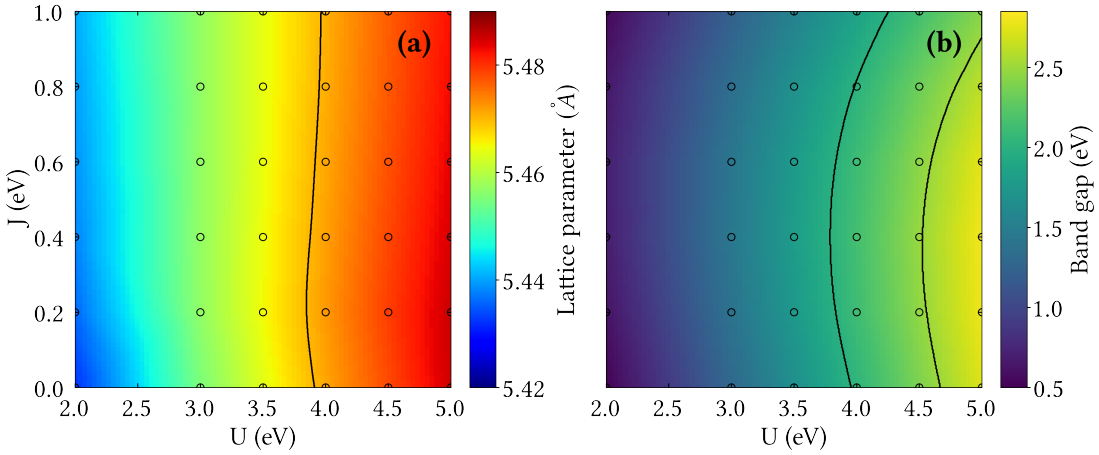

Figure 3.3 – Evolution with respect to U and J of (a) lattice parameter; (b) band gap computed with the PBEsol functional with non-linear 3**k**-c magnetic order and SOC. In (a) the solid black line corresponds to the experimental value $a_0 = 5.47$ Å. For (b) solid black lines indicate lower (2.0 eV) and upper bound (2.5 eV) of experimental band gap.

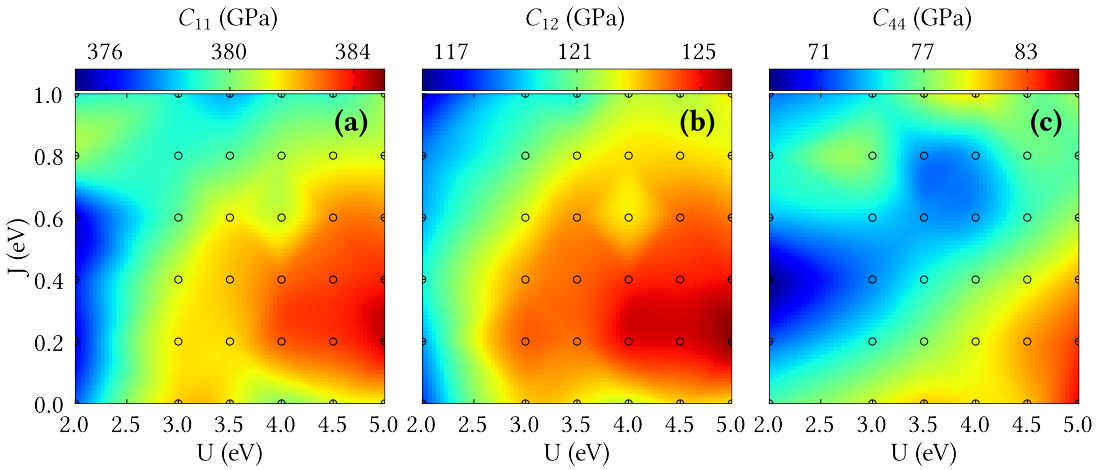

Figure 3.4 – Evolution with respect to U and J of (a) C_{11}; (b) C_{12}; (c) C_{44} elastic constants computed with the PBEsol functional with non-linear 3**k**-c magnetic order and SOC.

Regarding the influence of U and J on the lattice parameters, U has the most significant impact, while J appears to have very little influence. This is particularly highlighted by the solid line in Figure 3.3, representing a constant value of $a_0 = 5.47$ Å, which is almost vertical. For the band gap, J shows minimal influence, although variations in U indicate that lower and higher values of U tend to shift the band gap, keeping it within the experimental range.

To choose the optimal pair of (U, J) parameters, we considered the intersection of the lattice parameter line with the lower bound of the band gap. This occurs at two points: ($U = 3.94$ eV, $J = 0.76$ eV) and ($U = 3.85$ eV, $J = 0.15$ eV), both pairs produce similar results. To discriminate between these candidates, we used the results obtained from the elastic properties. Ultimately, we found that the best parameters were $U = 4.0$ eV and $J = 0.8$ eV (after rounding up) as the higher J value produced better results for C_{44}. These results are close to the values ($U = 4.5$ eV, $J = 0.54$ eV) from Kotani *et al.* [291] and are consistent with the findings of Pegg *et al.* [61, 62], who considered a $U_{\text{eff}} = U - J = 3.35$ eV, which is close to our obtained $U_{\text{eff}} = 4.0 - 0.8 = 3.2$ eV. We emphasise that parameters U and J should theoretically not be used as fitting parameters. Those parameters are intrinsic to the materials and should be obtained from experiments [243] or computed from *ab initio* methods [292–295]. Nevertheless, our purpose here was to produce a coherent database that aligns well with experimental observations in a reasonable time without reconsidering all the underlying theoretical aspects of DFT+U when applied to actinide oxides. The best we could do in a reasonable time was tuning the DFT+U parameters to fit our needs.

3.2. A new database, a new potential

With the new DFT+U setup, we built a new database. The latter is very similar to the one presented in Chapter 2 but with little modifications listed below:

- Polymorphs have been removed. We observed that they were increasing the errors towards other groups of configurations. Furthermore, we did not know how to properly perform the computations with the new DFT+U setup to maintain consistency among the database. Especially concerning the magnetism.
- We were unable to properly relax the γ-surface due to computational cost and convergence issues. Therefore, the configurations correspond to unrelaxed γ-surface.
- We deem it pertinent to incorporate homogeneous deformation paths, with the aim of conducting mechanical simulations under high deformation regimes.
- In order to address the atypical elastic behaviour observed at low temperatures, we enhance the dataset by incorporating configurations of deformed cells thermalised in NVT within the range of 300 to 2000 K.
- We added configurations corresponding to BSD-1/2/3 defects in temperature between 300 and 2000 K.
- Any configuration above 2200 K has been removed as they were leading to convergence issues within the new DFT+U setup.

For the configurations inherited from the previous GGA-PBE database, we rescale the volume according to the ratio between PBE+U prediction and PBEsol+U prediction and recalculate energy, forces, and stress by single-point calculations. All calculations were performed with the `ABINIT` packages with the PAW formalism, using the PBEsol functional along non-colinear 3**k** order accounting for SOC. The Table 3.2 summarised the new training dataset.

From this new database, we trained a SNAP, following the same methodology as in Chapter 2 but modifying the functional form. Observing good agreement with DFT+U predictions (within the new setup) and experimental observations, we decided to include the short-range contribution of the CRG potential (EAM and pair functions). We also opted to exclude long-range Coulombic interactions and removed the ZBL contribution, as it was redundant with the short-range repulsion of CRG (see Chapter 1). Ultimately, the potential takes the form:

$$E_p = E_{\mathrm{CRG}}^{\mathrm{pairs}} + E_{\mathrm{CRG}}^{\mathrm{EAM}} + E_{\mathrm{ML}} \tag{3.1}$$

The removal of long-range Coulombic interactions was motivated by the cost of the numerical methods required for their evaluation in large-scale simulations (`pppm` or Ewald summations) and to allow charged simulation boxes. The effect of charge

Table 3.2 – Training set v2.0

group label	N Config.	At/cell	N data	k-mesh
$fm\bar{3}m$	101	12	4343	$4 \times 4 \times 4$
Elastic	171	12	7353	$4 \times 4 \times 4$
Hot bulk (300 to 2200 K)	522	96	153990	$2 \times 2 \times 2$
Hot deformed (300 to 2000 K)	229	96	67555	$2 \times 2 \times 2$
Defects 1 (0 K)	89	96, 144	34940	$2 \times 2 \times 2$
Defects 2 (300 to 2000 K)	375	96, 144	124692	$2 \times 2 \times 2$
shear deformation paths	138	12	5934	$4 \times 4 \times 4$
unrelaxed γ-surfaces	209	96, 144	71015	$2 \times 2 \times 2$
Total	1936	-	481552	-

variation is therefore only locally encompassed within the short-range contribution of the ML potential (r_{cut} = 5.28 Å), which then becomes a pure short-range potential. The CRG contribution has a cutoff of 10Å, allowing to account for 'mid-range' interactions.

As mentioned above, the Ewald summation method incurs very high computational costs. Removing the long-range Coulombic interactions provides a significant gain in computational efficiency. This is illustrated in Figure 3.5, which shows the performance rate (in simulation time per day) as a function of the number of atoms in the supercell for the new SNAP-PBEsol and CRG. For a small number of atoms (approximately 100k), both potentials perform equally well, though SNAP-PBEsol exhibits much better scaling with respect to the number of computational nodes (128 MPI x 1 thread). However, for larger cell sizes (768K and more), with the same number of nodes, SNAP-PBEsol systematically demonstrates a higher performance rate of about one order of magnitude. Nevertheless, these results should be interpreted with care. We only tested the Ewald summation method and it is expected that the `pppm` method performs much better for very large systems. A complete assessment of these methods will be part of future investigations.

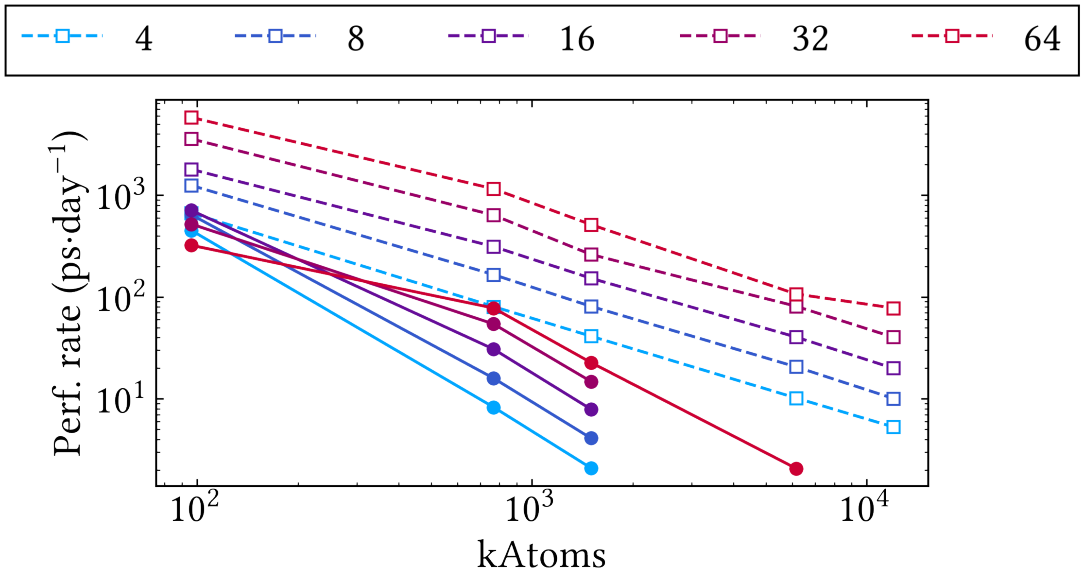

Figure 3.5 – Comparison benchmark between CRG (solid lines and plain dots) and SNAP-PBEsol (dashed lines and open squares) potentials. The colour coding corresponds to the number of computational nodes. Each node consisting in 128 `MPI` × 1 `THREAD`.

3.3. Assessment of the SNAP-PBEsol

Similarly to Chapter 2, we assessed the performance of the potential before its application. The assessment process being almost identical, we restrict ourselves here to the presentation of a limited set of relevant properties for the application presented at the end of the chapter, i.e. the mechanical response of UO_2 single crystal. Unless specified, all the properties presented in the following paragraphs were obtained with the same methodology as in Chapter 2.

Numerical error

We first evaluate the numerical error with respect to reference DFT data. Due to the linear form of the SNAP, no overfitting is expected and so we did not isolate a part of the dataset for testing purposes. Thus, all the dataset has been used for training and the errors summarised in the Table 3.3 correspond to the error on the total dataset. Corresponding correlation plots are displayed in Figure 3.6.

Table 3.3 – Errors for SNAP-PBEsol potential

		E (MAE) (meV/atom)	F (MAE) (meV/Å)	W (MAE) (GPa)	E(RMSE) (meV/atom)	F (RMSE) (meV/Å)	W (RMSE) (GPa)
SNAP	$fm\bar{3}m$	1.27	0.11	0.08	1.47	0.21	0.16
	elastic	1.55	9.33	0.23	2.42	46.87	0.51
	Hot bulk (300 to 2200 K)	5.76	283.16	0.34	7.36	393.82	0.49
	Hot deformed (300 to 2000 K)	5.30	269.24	0.32	6.82	368.59	0.44
	Defects 1 (0 K)	3.42	119.09	0.30	4.48	204.04	0.41
	Defects 2 (300 to 2000 K)	6.32	343.94	0.43	8.15	464.94	0.58
	shear deformation path	6.62	186.42	2.45	9.06	384.72	3.82
	unrelaxed γ-surfaces	2.74	189.84	1.03	3.58	337.99	2.01
	Total	4.87	265.75	0.56	6.73	389.96	1.30

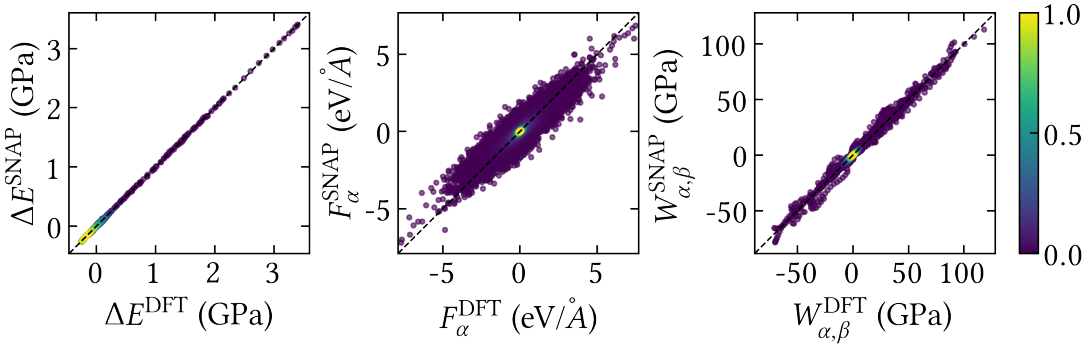

Figure 3.6 – Parity plot for energy, forces and stresses between DFT values (x-axis) and predicted values by the SNAP-PBEsol (y-axis). Point are coloured by the density value estim

Equation of state

The choice was made not to include the polymorphic phases of UO_2 in the training dataset for the new potential. This was motivated by the complexity of properly simulating those phases with the new DFT+U setup, in particular the treatment of magnetism. Nevertheless, we computed the equation of state (energy-volume, pressure-volume) at 0 K for the UO_2 polymorphs ($fm\bar{3}m$, *pnma*, *pbcn* and $P4_2mnm$) with the SNAP-PBEsol to ensure that the fluorite ($fm\bar{3}m$) phase was the most stable at 0 GPa. Results are reported on Figure 3.7. We also show that the SNAP-PBEsol properly handle volumetric deformation in the range $\{-30\%; 30\%\}$ in perfect agreement with DFT+U calculations.

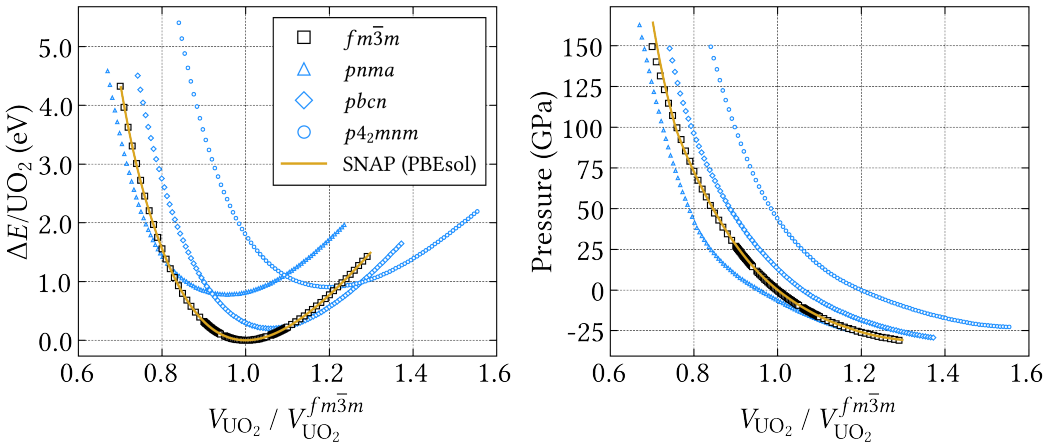

Figure 3.7 – Equation of state at 0 K of four different UO_2 polymorphs: $fm\bar{3}m$, *pnma*, *pbcn* and $P4_2mnm$. The white square correspond to the DFT+U (PBEsol + 3**k** +SOC) results, whereas the SNAP-PBEsol results are either displayed as yellow line for the $fm\bar{3}m$ phase or in blue symbol for other polymorphs not included in the training set.

Thermodynamic properties

One of the main issues with the preceding potentials was the under-estimation of the material density as well as a higher thermal expansion. Results for the new SNAP-PBEsol are displayed in Figures 3.8 and 3.9. It can be seen from Figure 3.8-a that the SNAP-PBEsol perfectly matches the recommended experimental density up to 2400 K with an error less than 1% in the range 300-2500 K (Figure 3.8-b). The same observation is achieved for thermal expansion, which is in very good agreement with Fink *et al.* experimental recommendations [53] up to 2400 K. Around 2500 K the potential deviates both in density and thermal expansion. The first explanation is that the potential falls into the extrapolation regime. Indeed, due to the particular difficulties to converge calculations of high-temperature configurations with the DFT-PBEsol setup, the highest temperature encountered in the training set is 2200 K (see Section 3.2). The other issue is the PBEsol functional itself; although it is suitable for static to low-temperature calculations, it was never intended to describe high temperatures. Nevertheless, we were satisfied in regard to our needs in terms of physical application that are not likely to ever go above 2200 K. We emphasise that those results, especially concerning the density, are a significant improvement compared to previous potentials.

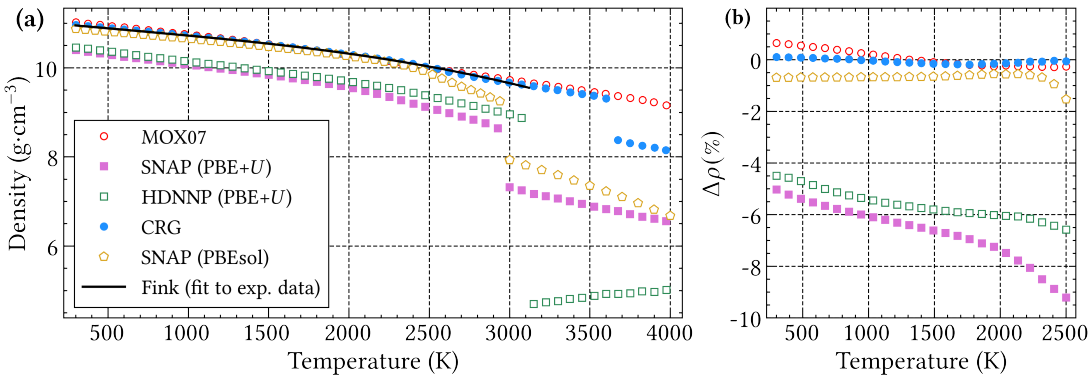

Figure 3.8 – (a) Evolution of the density with respect to temperature. The black line display the experimental recommendation from Fink *et al.* [53]. (b) Relative variation of the density with respect to experimental recommendation [53].

Another noticeable result is that even without proper inclusion of the superionic transition in the database unlike potentials from Chapter 2, we do observe the characteristic peak in the C_p associated to the Bredig transition. The onset of the transition with the SNAP-PBEsol is in good agreement with experimental recommendations and other potentials. Although, it exhibits the largest absolute value among all tested potentials. While the reason for this increase in the peak's value remains unclear, we rule out the possibility that this might be related to PBEsol. Instead, we suggest that it could be linked to the absence of long-range Coulombic interactions that are expected to stabilise the oxygen sub-lattice in this temperature regime. This assumption seems to be confirmed by results presented in Chapter 2, where a SNAP, trained on the PBE dataset but without long-range Coulombic interactions, exhibits a similar behaviour. Finally, as for previous potentials, the Bredig peak overlaps with the fusion peak, and melting is expected sooner than CRG or MOX-07. We also remark in Figure 3.8 that the density drop associated with melting occurs almost at the same temperature for the three MLIPs regardless of the formalism behind their respective *ab initio* training set. However, above melting they exhibit different behaviour, with SNAP-PBEsol presenting a stronger linear decrease than SNAP. In any case, those results fall outside the recommended range of 0 to 2400 K for the SNAP-PBEsol.

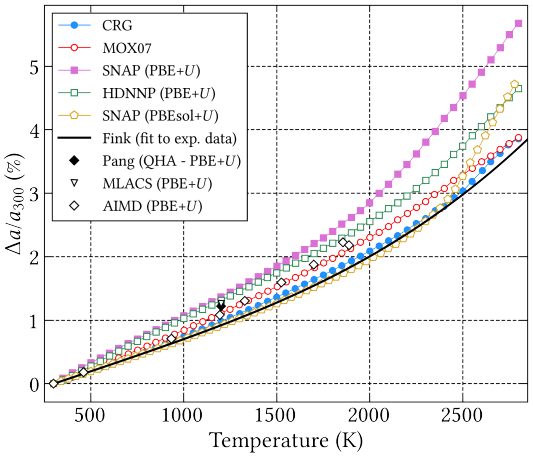

Figure 3.9 – Evolution of the ratio $\Delta a/a_{300}$ with respect to temperature. The black line displays the experimental recommendation from Martin [272]. The black diamond was extracted from the *ab initio* work of Pang *et al.* [199]. Open diamonds correspond to AIMD results extracted from [273]. Open triangles are results obtained by the MLACS method [274].

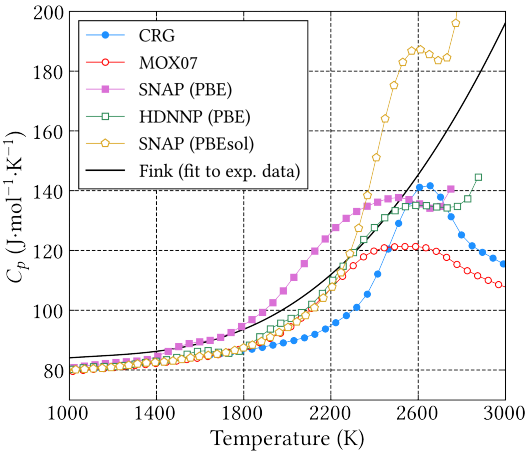

Figure 3.10 – Evolution of the specific heat-capacity, C_p, with respect to temperature. The black line display the experimental recommendation from Fink [53].

Thermo-elasticity

The elastic properties at 0 K are summarised in Table 3.4, where results obtained by SNAP-PBEsol are in very good agreement with respective DFT+U values, except for the universal anisotropy index which is heavily overestimated, but much closer to the experimental value of Brandt *et al.* [278]. The evolution of the elastic tensor with respect to temperature was obtained following the same methodology as in Chapter 2 for the range 300 to 2400 K. Results are presented in Figure 3.11. Overall, SNAP-PBEsol exhibits similar trends as previous MLIPs for C_{11} with a linear decrease up to 2000 K where a stronger decrease is observed at the onset of the Bredig transition. For C_{12}, the results for SNAP-PBEsol exhibit a better overall agreement with CRG compared to MLIPs-PBE, correcting in particular the rapid softening observed with HDNNP and the constant value of SNAP in the range 300 to 800 K. As for C_{12}, an accentuated decrease is observed starting from 2000 K. For C_{44}, the results are comparable to HDNNP with non-flat curves below 1000 K as for SNAP.

Concerning the evolution of elastic moduli with temperature (displayed Figure 3.12), SNAP-PBEsol exhibits a generally good agreement with respect to the available comparison data. They also seem to better catch the low temperature regime that was not properly described by previous MLIPs (especially SNAP) as mentioned in Chapter 2.

[1] at 298.15K

Table 3.4 – Elastic constant, bulk modulus (K), shear modulus (G), Young modulus (E), Poisson ratio (ν) and universal anisotropy (A^U) from experiments, SNAP-PBEsol, and PBEsol+3**k** +SOC

	C_{11} (GPa)	C_{12} (GPa)	C_{12} (GPa)	B (GPa)	G (GPa)	E (GPa)	ν -	A^U -
Brandt *et al.* [278]	400	125	59	217	83	222	0.33	0.91
Wachtman *et al.* [279][1]	396	121	64	213	87	231	0.32	0.74
PBEsol+3**k** +SOC	380	125	72	210	90	238	0.31	0.40
SNAP-PBEsol	381	119	55	207	78	209	0.33	0.96

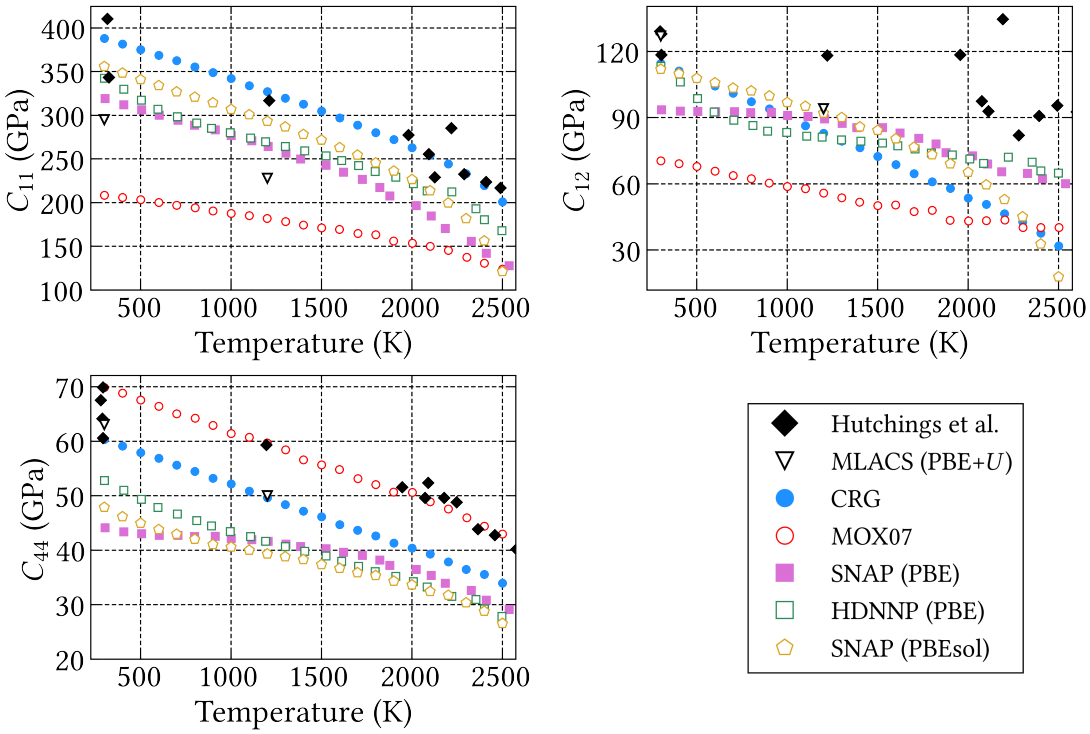

Figure 3.11 – Evolution of elastic constants (C_{11}, C_{12} and C_{44}) with respect to temperature, for five potentials (CRG in filled blue circles, MOX-07 in open red circles, SNAP in purple squares, HDNNP in open green squares and SNAP-PBEsol in open orange pentagons). The black diamonds display the existing experimental data, extracted from [281]. The open black triangles refer to *ab initio* values obtained through the MLACS method [26, 274].

Finally, we reported the evolution of the Poisson ratio and universal anisotropy index with respect to temperature in Figure 3.13. For the Poisson ratio, the evolution is very similar to SNAP up to 2000 K. Above 2000 K, the latter keep increasing, while the former exhibit a strong drop between 2000 and 2500 K followed by an increase above 2500 K. This behaviour for the Poisson ratio is shared by CRG at the same temperature but

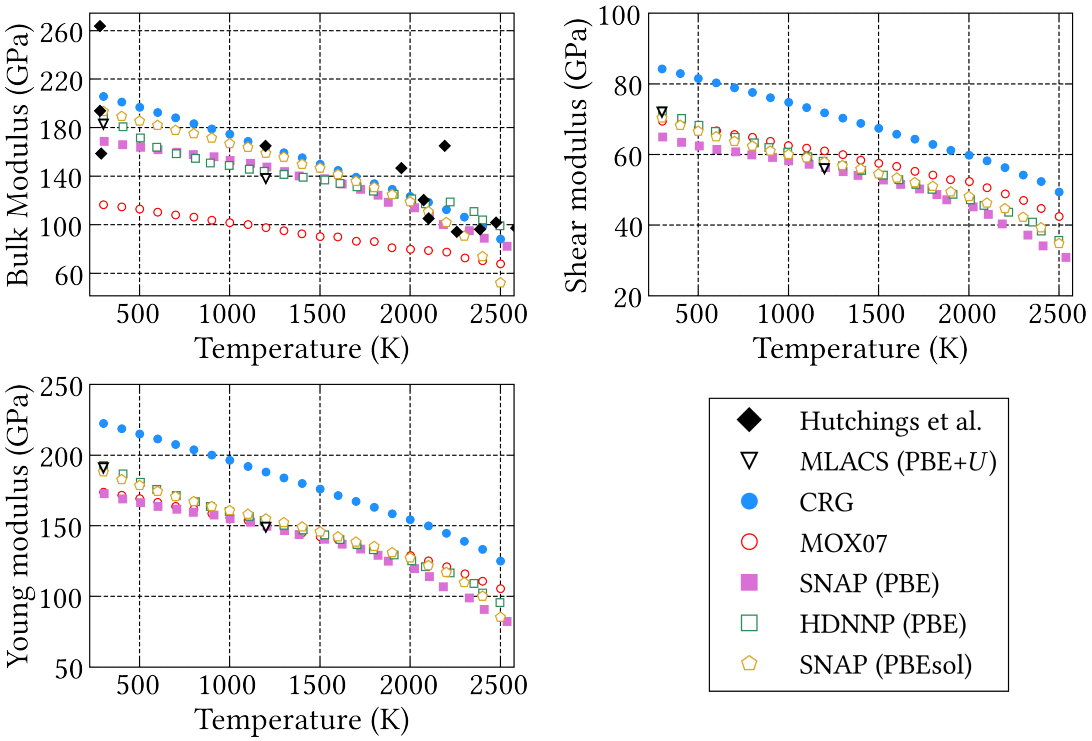

Figure 3.12 – Evolution of bulk, shear and Young moduli with respect to temperature, for five potentials (CRG in filled blue circles, MOX-07 in open red circles, SNAP in purple squares, HDNNP in open green squares and SNAP-PBEsol in open orange pentagons). The black diamonds display the existing experimental data, extracted from [281]. The open black triangles refer to *ab initio* values obtained through the MLACS method [26, 274].

with a less pronounced drop. For the universal anisotropy index, SNAP-PBEsol exhibits a rather constant value, ranging from 1.2 to 1.0 between 0 to 2000 K, then sharply drops at the Bredig transition as for CRG and HDNNP. In the case of SNAP-PBEsol, A^U drops almost to zero, translating a strong isotropization of the elastic response with temperature. In Section 3.4, we will show a similar behaviour of the single crystal plastic repsonse.

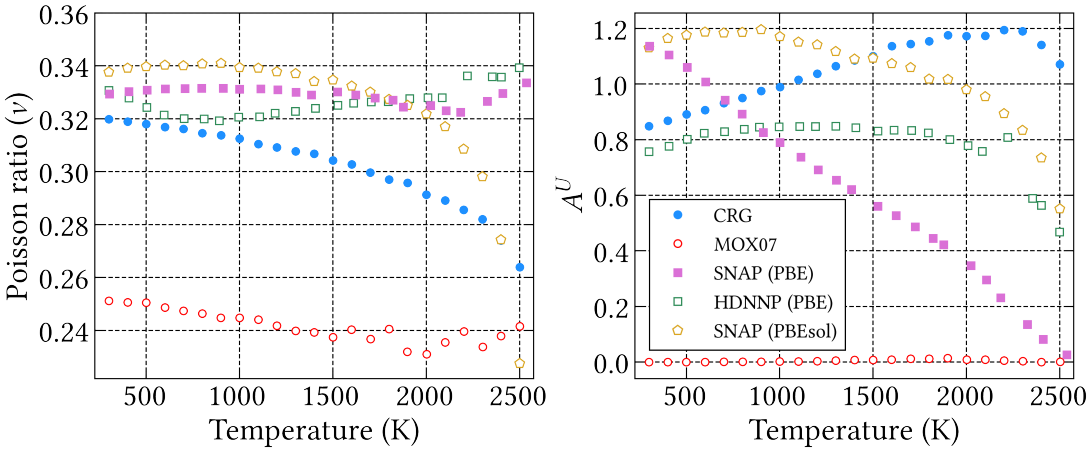

Figure 3.13 – Evolution of the Poisson ration ν, and universal anisotropy index A^U with respect to temperature.

Overall, SNAP-PBEsol shows only slight improvements over the previous potential in terms of thermo-elasticity but still demonstrates good agreement in evaluating the thermo-elastic properties of the material.

Stacking fault surfaces

The generalised stacking fault energy surfaces were computed following the same methodology as in Chapter 2. However, computational complexity prevented it from properly relaxing the PBEsol+3**k** +SOC surfaces, even with the workaround presented in Chapter 2, and are therefore not presented. The surfaces obtained with SNAP-PBEsol are displayed in Figure 3.14, to be compared to Figure 2.18 in Chapter 2, whereas the extracted MEP are displayed in Figure 3.15. For all three planes no phenomenological differences were observed; the {100} and {110} planes comparing very well to PBE+U results. For the {111} slip plane, while the overall shape of the surface agrees with PBE+U results, the energy barrier along the MEP (Figure 3.15) is lowered by about 0.7 J/m^2. This diminution in the energy barrier is to be considered carefully, as the energies for the {111} and {110} slip planes become very close with SNAP-PBEsol, suggesting a competition between the two slip system during gliding processes. This could play an important role in describing the plasticity in UO_2 in terms of dislocation mobility or activated slip planes at the onset of a deformation. Further investigation of these consequences is required and will be subject of future work. Nevertheless, despite the complexity of the γ-surface calculations using the PBEsol+3**k** +SOC setup and the associated convergence challenges encountered, we consider the results to be satisfactory.

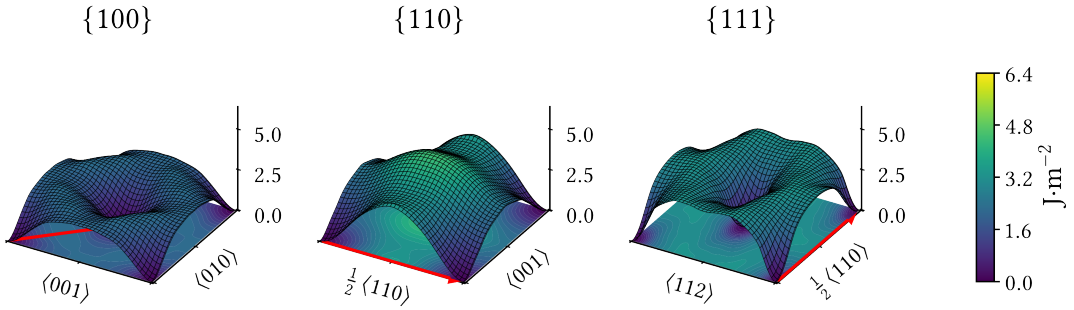

Figure 3.14 – Generalised stacking fault energy surfaces (γ-surfaces) for the {100}, {110} and {111} slip planes in UO_2 computed with the SNAP-PBEsol. For each plane, the Burgers vector $1/2\langle 110\rangle$ is represented by a red arrow. For ease of comparison, all γ-surfaces are plotted on the same energy scale.

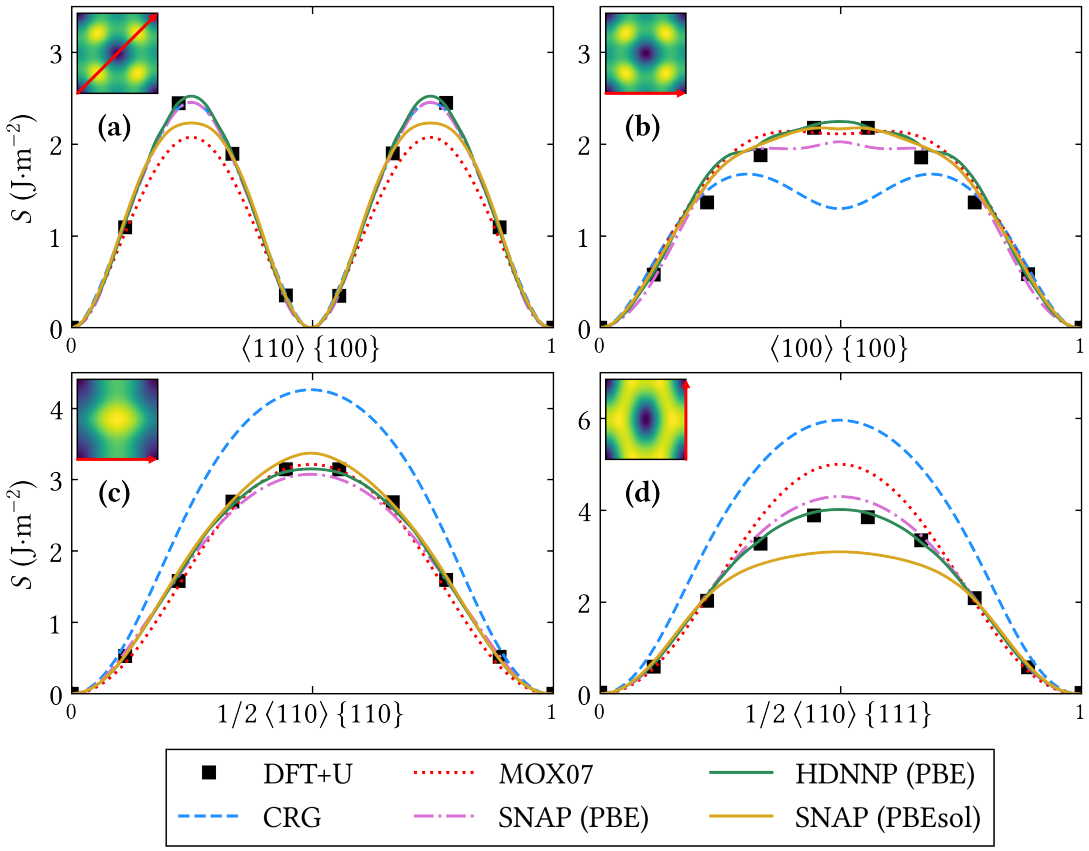

Figure 3.15 – (a) $\langle 110\rangle\{100\}$; (b) $\langle 100\rangle\{100\}$; (c) $1/2\langle 110\rangle\{110\}$; (d) $1/2\langle 110\rangle\{100\}$ γ-lines in UO_2.

Free surface energies

Free surfaces are of particular importance in UO_2 as they are directly involved in the cracking process, frequently encountered during in-reactor lifetime of the pellets, but

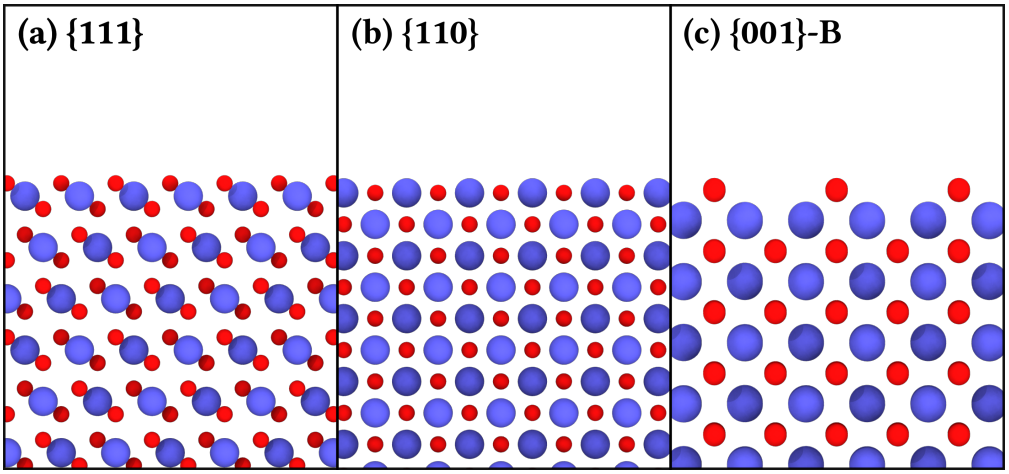

Figure 3.16 – Side view of (a) stoichiometric {111}; (b) stoichiometric {110}; (c) neutral {001}-B surface terminations in UO_2. For the {001} the B correspond to one of the two possible termination of oxygen atoms [303].

also for their role in the formation process of fission noble gas (Xe and Kr) bubbles. At the micrometer length scale [296, 297], faceted-shaped voids were observed, therefore, during a bubble's formation, the void morphology and stability is likely to be driven by the free surface energies. Those intra- and inter-granular fission gas bubbles degrade the mechanical properties of UO_2 [21, 298] leading to fuel swelling and are therefore extensively studied [33, 149, 150, 187, 299–302]. Additionally, expected applications with the new SNAP-PBEsol potential are large scales MD simulations of micro-pillar or nano-indentation. Both of these applications demand accurate description of free surfaces to ensure realistic and reliable simulation outcomes.

As we did not include free surfaces in the training database (mainly due to the computational complexity of the DFT setup), we assessed the potential by computing the free surface energies for three surfaces often encountered in UO_2. Those are the stoichiometric {111} (Figure 3.16-a), stoichiometric {110} (Figure 3.16-b) and the neural {001}-B (Figure 3.16-c) surfaces. Side views for the three surfaces are displayed in Figure 3.16. For the {001} surface, there are two possible terminations denoted A and B [303]. Only the B-terminated surface has been investigated.

Slab configurations were constructed with the studied free surfaces oriented orthogonal to the z-axis. The supercell dimensions for the three considered surfaces are: (a) $53.58 \times 30.94 \times 75.78$ Å (9216 atoms), (b) $30.94 \times 21.88 \times 61.87$ Å (3072 atoms), and $21.86 \times 21.86 \times 43.79$ Å (1536 atoms). Since the SNAP-PBEsol potential does not account for long-range Coulombic interactions, separating the two free surfaces by at least the potential interaction range (11 Å) is sufficient to achieve convergence of the slab energy. The surface energy, which represents the excess energy per unit area due to the presence of a surface at equilibrium, is calculated as follows:

$$E_{\text{surf}} = \frac{1}{2A_{\text{surf}}}\left(E_{\text{slab}} - N_{\text{UO}_2}^{\text{slab}} E_{\text{UO}_2}^{\text{bulk}}\right) \tag{3.2}$$

Where A_{surf} is the surface area. The surface energy is divided by a factor of 2 as a consequence of the slab configuration containing two free surfaces. Results are summarised in Table 3.5. We observe a reasonable agreement of the surface energy values predicted with other comparison data, in particular with PBE+U data, that exhibit an overall lowering of all the considered surface energies. Importantly we do conserve the relative stability between considered surfaces $E_{\{111\}} < E_{\{110\}} < E_{\{001\}-B}$. It is noteworthy that these results align well, despite being in the extrapolation regime, which is a pleasant surprise. This is an important result, as this enables the study of cavities and fission gas bubbles with the potential.

Table 3.5 – Surface energies from the present work and from several other studies. A and B correspond to the different possible terminations of oxygen atoms of the {001} surface [303].

		{111} $J{\cdot}m^{-2}$	{110} $J{\cdot}m^{-2}$	{001}-A $J{\cdot}m^{-2}$	{001}-B $J{\cdot}m^{-2}$
Bottin *et al.* [304]	PBE+U	0.73	1.16	1.46	-
Galvin *et al.* [299]	CRG	1.07	1.65	2.00	2.25
Sattonnay *et al.* [187]	SMTB-Q	1.07	1.72	2.03	2.48
Boyarchenkov *et al.* [301]	MOX-07	1.14	-	1.60	-
This work	SNAP-PBEsol	0.68	1.00	-	1.70

3.4. Application: UO_2 mechanical response at the atomic scale

The understanding of plastic activity and mechanical behaviour at the atomic scale of UO_2 single crystal is important if one wants to build constitutive laws that can be leveraged at larger time and space scales, which are not reachable by atomistic calculations. As mentioned in Section 2.5.5, uranium dioxide exhibits anisotropic elastic behaviour. In addition, it was experimentally observed that the activation of slip systems in UO_2 was dependent on the loading direction [305], spreading the anisotropy to plastic activity as well. Therefore, the different mechanisms of irreversible deformation are expected to depend on the loading direction, even at the atomic scale. In order to systematically explore all possible deformation mechanisms, we follow a methodology proposed by Lafourcade *et al.* [306] to compute the critical shear stress flow surface which represents the orientation dependence of the macroscopic stress at the onset of the first irreversible deformation mechanism, that is, under defect nucleation conditions.

In this Section all the simulations were performed on pristine UO_2 (i.e. without any initial defects). We are perfectly aware that, under reactor conditions (even at ambient temperature), nuclear fuels are subjected to intense stress and irradiation conditions and contain a large amount of defects, in particular a non-zero dislocation density. Such initial defect population is known to lower the material's flow stress and prevent nucleation processes. Nevertheless, we estimated that a comprehensive study on perfect single crystal behaviour remains a prerequisite to more in-depth studies. The Section 3.4.5 will be dedicated to the influence of radiation damage on the mechanical response of UO_2 single crystal. This first application also represents a good opportunity to highlight the capability of the developed SNAP to handle large-scale molecular dynamics simulations involving multiple physical phenomena under extreme conditions far from equilibrium.

3.4.1. Method

The critical von Mises shear stress $\sigma_{\mathrm{vM}}^{\mathrm{max}}$ corresponds to the stress required for the nucleation of the first plastic defect and / or the activation of an irreversible deformation mechanism. It is directly extracted from strain-stress curves, as illustrated in Figure 3.17, where the macroscopic stress σ_{vM} is defined following the von Mises formulation,

$$\sigma_{\mathrm{vM}} = \left(\frac{1}{2}\left[\left(\sigma_{\mathrm{xx}} - \sigma_{\mathrm{yy}}\right)^2 + \left(\sigma_{\mathrm{xx}} - \sigma_{\mathrm{zz}}\right)^2 + \left(\sigma_{\mathrm{yy}} - \sigma_{\mathrm{zz}}\right)^2 + 6\left(\sigma_{\mathrm{xy}}^2 + \sigma_{\mathrm{xz}}^2 + \sigma_{\mathrm{yz}}^2\right)\right]\right)^{\frac{1}{2}} \tag{3.3}$$

with $\boldsymbol{\sigma}$ the usual symmetric stress tensor extracted from MD simulations. The shear strain ϵ,

$$\epsilon = \left(E_{\mathrm{xy}}^2 + E_{\mathrm{xz}}^2 + E_{\mathrm{yz}}^2 + \frac{1}{6}\left[\left(E_{\mathrm{xx}} - E_{\mathrm{yy}}\right)^2 + \left(E_{\mathrm{xx}} - E_{\mathrm{zz}}\right)^2 + \left(E_{\mathrm{yy}} - E_{\mathrm{zz}}\right)^2\right]\right)^{\frac{1}{2}} \tag{3.4}$$

is obtained from the Green-Lagrange strain tensor $\boldsymbol{E}$,

$$\boldsymbol{E} = \frac{1}{2}\left(\boldsymbol{F}^{\mathsf{T}}\boldsymbol{F} - \boldsymbol{I}\right) \tag{3.5}$$

with $\boldsymbol{F}$ the deformation gradient tensor and $\boldsymbol{I}$ the 2nd order identity tensor. If one considers a reference configuration with a frame matrix $\boldsymbol{H_0}$ with columns defined as the periodic directions of the simulation cells (e.g. diagonal for orthorhombic cells), the total deformation gradient tensor transforms this reference frame into the current frame through $\boldsymbol{H} = \boldsymbol{F}\boldsymbol{H_0}$. This formulation will be explained in detail later, for the deformation paths formalism used in the present work. Although it is not the only available definition for strain, it is still a good measure for macroscopic shear deformations along arbitrary directions, which proves appropriate in the present case.

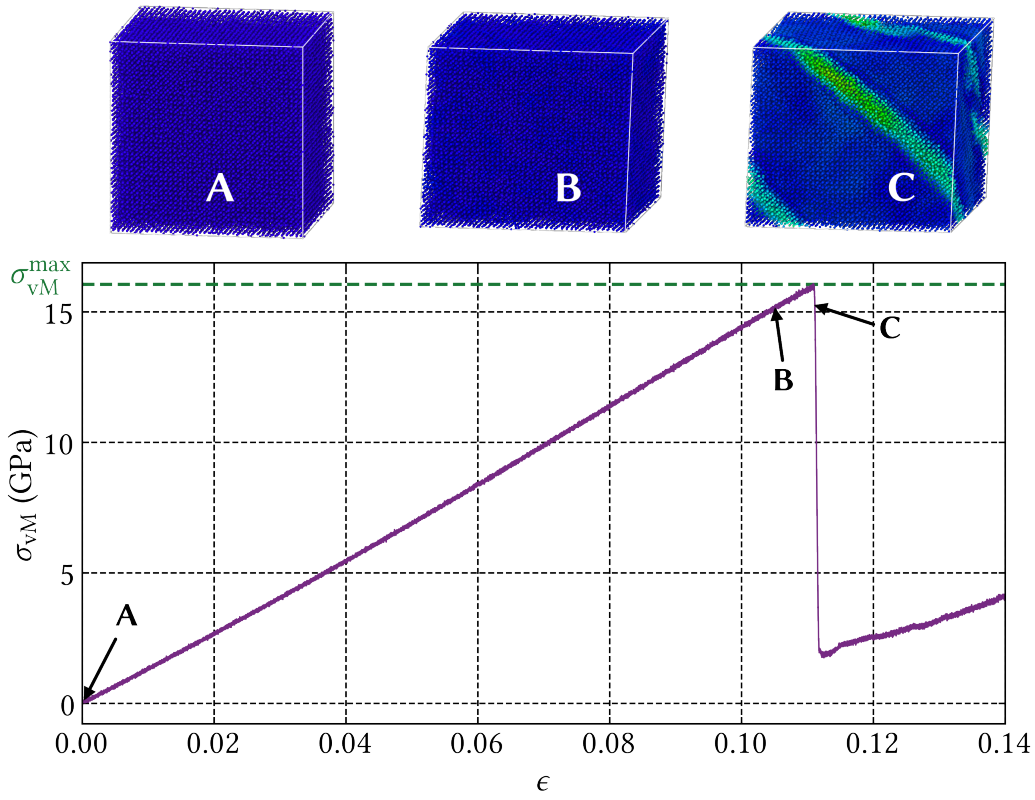

Figure 3.17 – Illustration of a stress-strain curve where the strain ϵ and the macroscopic stress are given by eq. (3.3) and (3.4). The simulation boxes represented above correspond to snapshots taken at states A, B and C. Only uranium atoms are represented and coloured with respect to their local atomic shear strain.

In addition, it can prove useful to compute the deformation gradient tensor at the atomic scale, i.e. per atom. Locally, this tensor represents the gradient of the best

interpolation field of displacements of neighbouring atoms, relative to a central atom α:

$$\boldsymbol{F}_\alpha = \left(\sum_{\beta \in \mathcal{V}(\alpha)} \boldsymbol{x}^{\alpha\beta} \otimes \boldsymbol{X}^{\alpha\beta} \right) \cdot \left(\sum_{\beta \in \mathcal{V}(\alpha)} \boldsymbol{X}^{\alpha\beta} \otimes \boldsymbol{X}^{\alpha\beta} \right)^{-1} \tag{3.6}$$

where β denotes the neighbouring atoms and $\boldsymbol{X}^{\alpha\beta}$, $\boldsymbol{x}^{\alpha\beta}$ refer to the vectors between atoms α and β in the reference and current states, respectively. This definition of local atomic deformation is the one implemented in the `ovito` software.

Flow stress surfaces are built by locating the critical shear stress of each loading direction, mapping a unit sphere around the pristine UO_2 single crystal. The directions of deformation are defined by two vectors $\boldsymbol{\eta}$ and $\boldsymbol{\kappa}$, which, respectively, represent the shear direction and the vector normal to the sheared plane. By construction, $\boldsymbol{\eta}$ and $\boldsymbol{\kappa}$ are orthogonal, and related to the angles $\theta \in [0, \pi]$ and $\phi \in [0, 2\pi]$ by

$$\boldsymbol{\eta} = \begin{bmatrix} \sin\theta\cos\phi \\ \sin\theta\sin\phi \\ \cos\theta \end{bmatrix} \qquad \boldsymbol{\kappa} = \begin{bmatrix} \cos\theta\cos\phi \\ \cos\theta\sin\phi \\ -\sin\theta \end{bmatrix}, \tag{3.7}$$

as illustrated in Figure 3.18. One could introduce a third angle, $\chi \in [0, 2\pi]$, which corresponds to the inclination of the plane defined by $(\boldsymbol{\eta}, \boldsymbol{\kappa})$ with respect to the z-axis. We chose to fix $\chi = 0$, implying that the vector $\vec{e_z}$ is always included in the $(\boldsymbol{\eta}, \boldsymbol{\kappa})$ plane. This is justified, as the z-axis is a rotational symmetry axis for UO_2 mechanical properties.

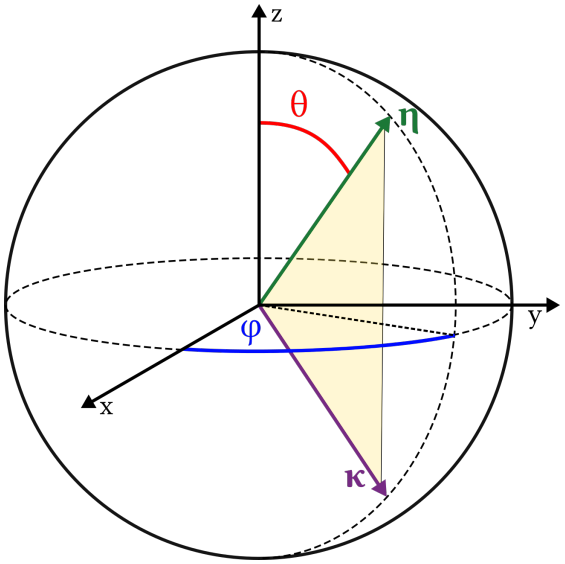

Figure 3.18 – Representation of the unit sphere mapping every loading directions. The vector $\boldsymbol{\eta}$ represents the shear direction and $\boldsymbol{\kappa}$ the normal to the shear plane.

During molecular dynamics simulations, the lattice vectors of the simulation cell

define the frame tensor $\boldsymbol{H}$ that evolves with time such that,

$$\boldsymbol{H}(t) = \boldsymbol{F}(t)\boldsymbol{H}_0 \tag{3.8}$$

where $\boldsymbol{H}_0$ corresponds to the frame tensor of the crystal in the reference configuration (i.e. before any applied deformation) and $\boldsymbol{F}(t)$ is the deformation gradient tensor previously defined. In order to apply pure shear deformations at a constant strain-rate along arbitrary directions of the 3D space, $\boldsymbol{F}(t)$ is defined as follows

$$\boldsymbol{F}(t+\delta t) = \boldsymbol{F}(t) + \delta t\dot{\gamma}\boldsymbol{F}(t)\boldsymbol{\eta}\otimes\boldsymbol{\kappa} \tag{3.9}$$

with $\boldsymbol{\eta}\otimes\boldsymbol{\kappa}$ the dyadic product ($[\boldsymbol{\eta}\otimes\boldsymbol{\kappa}]_{ij} = \eta_i\kappa_j$). This formulation of the deformation gradient tensor ensures that the deformation is applied at a constant strain-rate $\dot{\gamma}$ for an isochoric pure shear deformation in the direction defined by the vectors $\boldsymbol{\eta}$ and $\boldsymbol{\kappa}$. When dealing with triclinic simulation cells, an important constraint is that LAMMPS requires the frame tensor $\boldsymbol{H}$ to be defined as an upper triangular matrix

$$\boldsymbol{H} = \begin{pmatrix}\boldsymbol{a} & \boldsymbol{b} & \boldsymbol{c}\end{pmatrix} = \begin{pmatrix} l_x & xy & xz \\ 0 & l_y & yz \\ 0 & 0 & l_z \end{pmatrix} \tag{3.10}$$

where the diagonal components l_x, l_y and l_z, correspond to the box length along the x, y and z axis, while off-diagonal components, xy, xz and yz (referred to as "tilt factors") characterise the amount of displacement applied to the edges of an orthogonal box faces. Inevitably, such constraints are violated by the formulation of Eqs. (3.8) and (3.9), since for specific deformation directions they might induce large rotations of the simulation box. Therefore, $\boldsymbol{H}(t)$ is rotated as follows

$$\tilde{\boldsymbol{H}}(t) = \boldsymbol{Q}(t)\boldsymbol{H}(t) \tag{3.11}$$

where $\boldsymbol{Q}(t)$ is a rigid rotation matrix that preserve the axes of periodicity. The matrix $\boldsymbol{Q}(t)$ is built so that $\boldsymbol{a}$ is aligned with the x-axis and $\boldsymbol{b}$ lies in the xy-plane. We also imposed $\tilde{\boldsymbol{H}}(0) = \boldsymbol{H}_0$, the non-deformed initial box.

It is important to note that the true time evolution of the frame tensor $\boldsymbol{H}(t)$ is entirely generated before applying rigid-body rotation through $\boldsymbol{Q}(t)$. Then and only then, the new time evolution of the frame tensor $\tilde{\boldsymbol{H}}(t)$ can be used to calculate the time evolution of the 6 independent parameters (l_x, l_y, l_z, xy, xz and yz) that define the simulation box and correspond to the applied deformation. The `fix deform` as implemented in LAMMPS was used by providing analytical functions that describe the parameters variation $\Delta L(t)$ with respect to time and their respective variation rate $\mathrm{d}\Delta L(t)/\mathrm{d}t$. The analytical functions for $\Delta L(t)$ are chosen as 3rd order polynomials of the form

$$\Delta L(t) = At + Bt^2 + Ct^3 + D \tag{3.12}$$

where L is any of the 6 parameters. Polynomial coefficients (A, B, C) are fitted to

the analytical evolution of $\tilde{\boldsymbol{H}}(t)$ calculated by Eqs. (3.8), (3.9) and (3.11). The rate of change $\mathrm{d}\Delta L/\mathrm{d}(t)$ is trivially derived from (3.12). A comparison between polynomial fitting, analytical parameters, and the results of a LAMMPS simulation are displayed in Figure 3.19. Note that in Eq. (3.12), D is not fitted nor fixed to 0 but rather used as an offset during the restart of a simulation allowing for a continuous deformation.

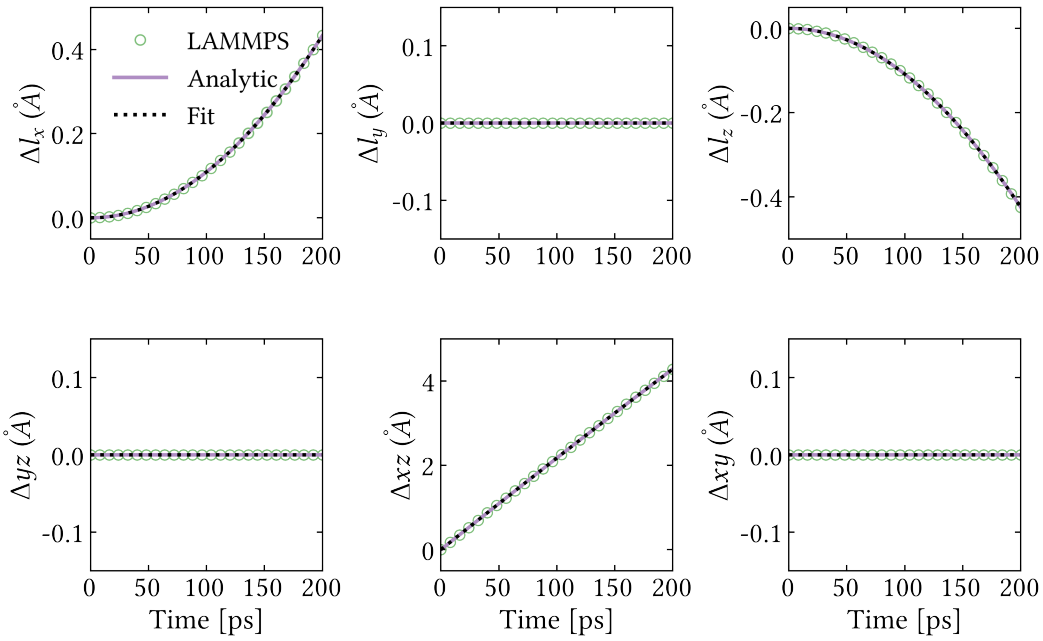

Figure 3.19 – Time evolution of the variation in l_x, l_y, l_z, xy, xz and yz, for fixed $\dot{\gamma} = 10^9\mathrm{s}^{-1}$ with $\theta = 0°$ and $\phi = 0°$. The initial simulation parameters are $lx = ly = lz = 21.87$Å and $xy = xz = yz = 0$Å. The plain purple line represents the analytical calculation of $\tilde{\boldsymbol{H}}(t)$ components, the black dotted line the 3rd-order polynomial fits and the open green dot the results extracted from the corresponding LAMMPS MD simulation.

3.4.2. UO_2 single crystal at 300K

We start by studying the case of pristine UO_2 at 300K. MD simulations were conducted using the LAMMPS code with the SNAP-PBEsol potential developed in the previous sections. Angles $\theta, \phi \in [0, \pi/2]$ are taken every $\pi/16$, so a total of 100 MD trajectories were needed to span $1/8^{\text{th}}$ of the unit sphere. The full sphere (i.e. $\theta \in [0, \pi], \phi \in [0, 2\pi]$) is then reconstructed using the crystal symmetry operations. First, a 20×20×20 supercell (corresponding to 96k atoms) is equilibrated in the NVT ensemble with equilibrium volume extracted from NPT simulations (see Section 3.3) at 300 K. The thermalised supercell is then used as initial conditions for subsequent MD simulations with deformations. For each loading direction, the simulation cell is dynamically strained at each timestep through the application of $\boldsymbol{F}(t)$ corresponding to a constant strain-rate of $\dot{\gamma} = 10^8\mathrm{s}^{-1}$. The maximum von Mises stress is automatically extracted

from each simulation, and the entire 3D flow stress surface is eventually reconstructed. Results are displayed in Figure 3.20.

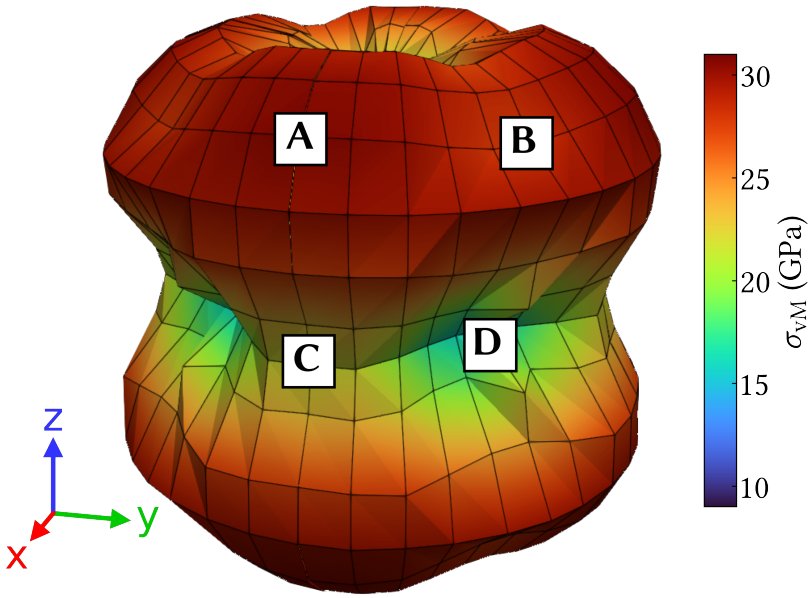

Figure 3.20 – Critical shear stress flow surface of UO_2 at 300K obtained for $\dot{\gamma} = 10^8 s^{-1}$. Label A, B, C or D corresponds to particular directions selected for a more careful examination of the activated mechanism.

The absolute value of the critical shear stress shown in Figure 3.20 ranges from 15 GPa to 30 GPa. This is several orders of magnitude larger than the expected experimental values for the same type of experiments. Three factors could explain the overestimation of the critical stress. First, the box size was kept relatively small for computational efficiency, but is known to have an effect on the calculated stress value. Indeed, the present case represents a configuration in which the flow stress surface is in fact a direct measure of the critical stress at nucleation of deformation mechanisms. The larger the sample, the lower the stress at nucleation. Lafourcade et al. [306] reported a decrease of about 20% of the critical stress at nucleation by increasing the size of the simulation box by a factor of 64 for a molecular crystal. Second, the value of the strain-rate $\dot{\gamma} = 10^8 s^{-1}$, is several orders of magnitude larger than experimental values usually achieved in quasi-static conditions, i.e. at a strain-rate lower than $10^3 s^{-1}$. In the same study, Lafourcade et al. observed that critical stresses were lowered by about 10% by decreasing the strain-rate by 1 order of magnitude (from $10^8 s^{-1}$ to $10^7 s^{-1}$). The influence of the strain-rate for the present case is the subject of the Section 3.4.3. Finally, as mentioned earlier, the material is a pristine single crystal free of initial defects. Pristine samples do not possess any defects that could help accommodate the deformation they are subjected to. In the presence of dislocations or point defects, applying a macroscopic deformation to the sample would not trigger nucleation processes but rather defect mobility through

dislocation mediated-plasticity or diffusion for example. In the present case, what is measured is in fact the stress at nucleation for a given strain-rate which is inevitably higher than what is measured in quasi-static mechanical loading. Section 3.4.5 will be dedicated to the influence of pre-existing radiation defects in the materials on the flow stress surface. However, it is strongly believed that the present framework can prove useful to discover deformation mechanisms in materials for which the behaviour at extreme conditions remains largely unexplored or inadequately understood.

For the present conditions, i.e. a pristine single crystal under high-rate deformation, the flow stress surface appears irregular in terms of critical stress, which appears direction dependent. A more detailed examination of the system during multiple simulations reveals that these differences are associated with the activation of different deformation mechanisms. In particular, four directions labelled **A**, **B**, **C** and **D** on Figure 3.20 are selected to illustrate the diversity of UO_2 behaviours, for which associated mechanisms are depicted in Figure 3.21 and described in the following paragraphs.

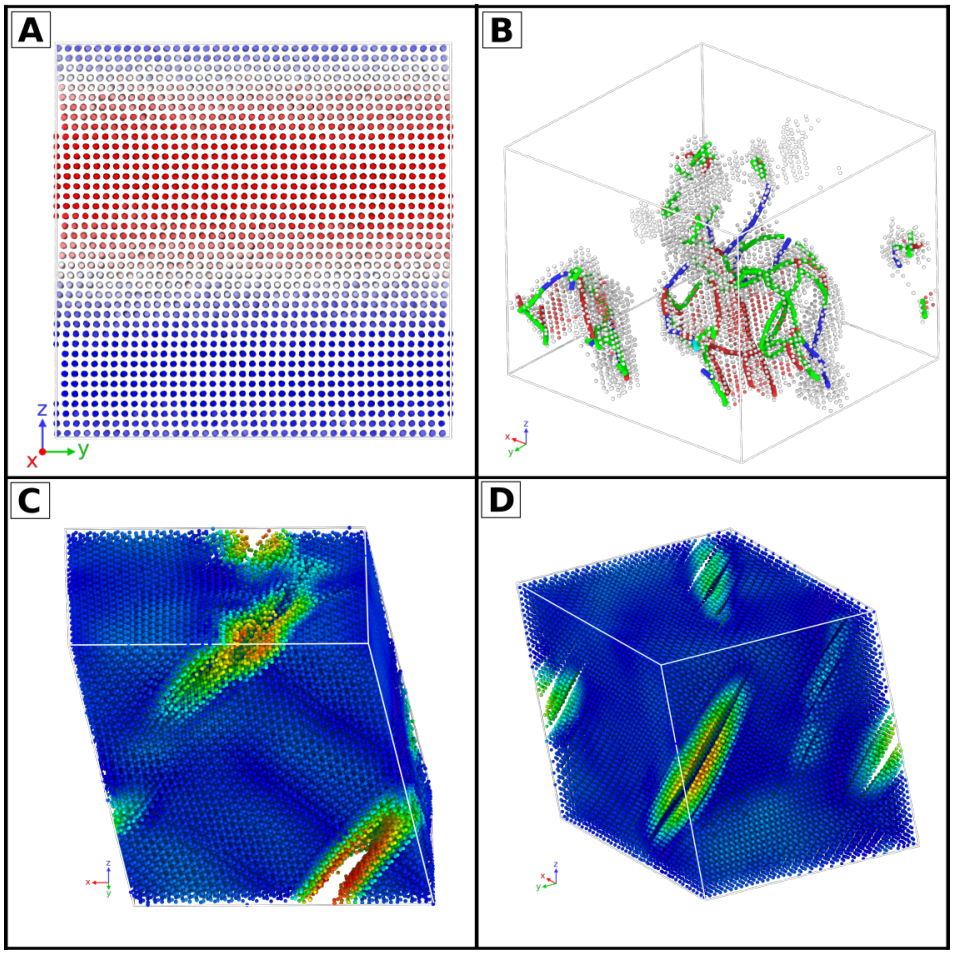

Figure 3.21 – Nucleated plasticity defects for particular direction (A, B, C and D) of the flow surface (Figure 3.20).

A - Elastic instability

In the direction exhibiting the highest critical stress ($\phi = 0, \theta = \pi/4$), the deformation is initially accommodated by a crystal distortion along the y axis that looks similar to a buckled configuration. This is highlighted in Figure 3.21-A where atoms are coloured by their displacement vectors along y with respect to the unperturbed configuration. Such a macroscopic distortion, where no local defects are observed, is characteristic of elastic instabilities in materials. The first small drop in the stress-strain curve (see Figure 3.22) corresponds to the onset of this elastic instability. After the first drop, the stress remains rather high and exhibits small oscillations that may be attributed to the propagation of elastic waves in the material through periodic boundary conditions. The dynamic of the buckling process is controlled by the growth of the buckled domains, and generally depends on the strain-rate [306]. The lower the strain-rate, the longer the time for the buckling mechanism to relax. Depending on the buckling pattern with respect to the boundary conditions, the final pattern can contain one wavelength as shown in Figure 3.21-A. Eventually, if the deformation exceeds the maximum value that can be accommodated by the buckling mechanism, another deformation mechanism will take over, as it occurs at larger strain through a second stress drop in Figure 3.22.

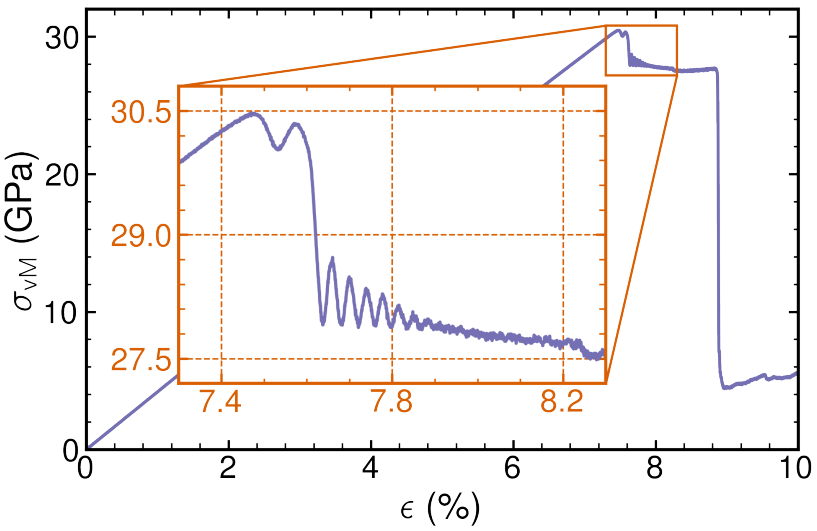

Figure 3.22 – Stress-strain curves corresponding to the **A** direction (Figure 3.20) at the onset of the plastic deformation.

Few to none literature has been found on such elastic instabilities in UO_2 or other ceramic materials. Nevertheless, such unusual mechanisms have been observed and documented for highly anisotropic materials such as molecular crystals [306], dense anisotropic carbon-based materials [307] or layered crystalline solids [308, 309]. What all these materials have in common is a large elastic anisotropy. Although the elastic anisotropy of UO_2 single crystal is not as large as for these materials, it is, to the best of our knowledge, the first time such a deformation mechanism has been observed at the atomic scale. In addition, the present observation of such an unusual mechanism

could indicate a path toward the discovery of new deformation mechanisms in UO_2 or other anisotropic ceramic materials.

B - Dislocation nucleation

For the deformation path along the **B** direction ($\phi = \pi/4$, $\theta = \pi/4$), the strain is accommodated by the nucleation of several dislocations. As depicted in Figure 3.21, at the onset of plastic deformation, several interacting dislocations of different types are nucleated. These dislocations were extracted using the dislocation extraction algorithm (DXA) as implemented in the `ovito` software. Due to the rather small size of the simulation box and the time interval between outputs, it is possible that the observed dislocations have already travelled across the supercell a few times due to periodic boundary conditions. In this case, it is not obvious nor easy to identify which slip systems were activated at the onset of the deformation. Indeed, as soon as dislocations nucleate in the sample, the dislocation density is very large due to the sample's size. In addition, the applied high strain-rate implies that dislocations have a high velocity which can lead to some chaotic behaviour of the dislocations interactions. Future work will be dedicated to the study of larger samples at a lower strain-rate.

C/D - Cracking

Finally, the directions **C** ($\phi = 0$, $\theta = 0$) and **D** ($\phi = \pi/4$, $\theta = 0$) correspond to the directions with the lowest critical stress. In those cases, nucleation and propagation of fractures is observed throughout the sample. Characteristic of brittle materials, this behaviour is expected for UO_2 which is a ceramic and experimentally exhibits a brittle behaviour at ambient temperature [43]. In addition, the high strain-rate can exacerbate such mechanisms, making UO_2 single crystal mechanical response consistent with what is expected at this temperature.

In order to better characterise the cracking processes and in particular to extract their common features in terms of orientation, the `ovito` software has been employed to compute the normal vector to the crack plane. First, a surface mesh using the alpha-shape method was built to identify the N_s atoms at the inner surface of the crack on which the gyration tensor $\boldsymbol{S}$ was computed as follows,

$$S_{\alpha,\beta} = \frac{1}{N_s} \sum_{i=1}^{N_s} \left(R_\alpha^{(i)} - R_\alpha^0\right)\left(R_\beta^{(i)} - R_\beta^0\right) \tag{3.13}$$

with $\boldsymbol{R}^0$ the position of the centre of mass

$$R_\alpha^0 = \frac{1}{N_s} \sum_{i=1}^{N_s} R_\alpha^{(i)}. \tag{3.14}$$

The normal vector to the crack plane $\boldsymbol{n}$ is eventually obtained as the eigenvector associated with the lowest eigenvalue of $\boldsymbol{S}$. Figure 3.23 depicts the extracted cracks and

the respective plane for both direction **C** and **D**. Through this method, we identified $\boldsymbol{n}_C = [101]$ for direction **C** and and $\boldsymbol{n}_D = [111]$ for direction **D**. The results agree with a negative value of the resolved stress applied to the planes in the direction of their respective normal (see Figure 3.23). The formulation of the resolved stress is as follow,

$$\tau_\alpha = \det(\boldsymbol{F})\left(\boldsymbol{F}^T \sigma \boldsymbol{F}^{-T}\right) : (\boldsymbol{n_\alpha} \otimes \boldsymbol{n_\alpha}) \tag{3.15}$$

where $\boldsymbol{F}$ and $\boldsymbol{\sigma}$ are the macroscopic deformation gradient and macroscopic stress tensors respectively, $\boldsymbol{n}$ is the normal to the considered plane and : the tensor double contraction. The negative value indicates a tensile load applied in the direction orthogonal to the atomic plane considered, promoting a mode I cracking process.

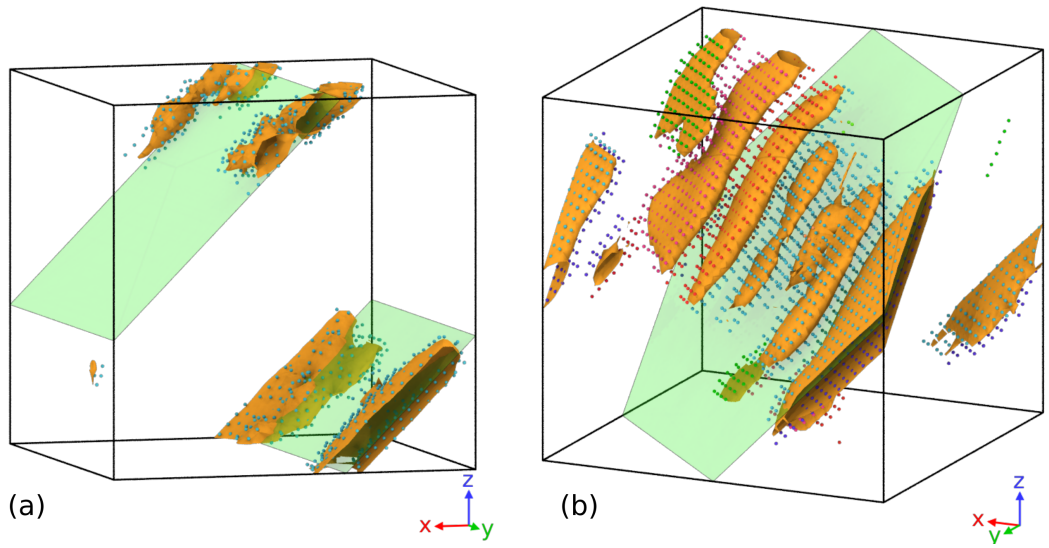

Figure 3.23 – Nucleated fractures for particular direction. (a) and (b) display the fractures observed for loading along **C** and **D** directions of the flow surface (Figure 3.20). Identified fracture planes are of {101} and {111} types respectively. Dots represent atoms located on the fracture inner surface, orange meshes represent the surfaces identified with the alpha shape method and green planes the identified fracture planes.

3.4.3. Effect of strain-rate on the flow surface

In the previous section, a strain-rate $\dot{\gamma} = 10^8 s^{-1}$ was used. Before continuing we investigate the influence of the strain-rate on the simulation results. We used the same methodology as before except that due to symmetry, we span the $1/32^{th}$ of the unit sphere with $\theta, \phi \in [0, \pi/4]$ every $\pi/20$, reducing the required number of MD runs to 25. The 2D projection of the 3D sphere with varying strain-rate is presented in Figure 3.24. Due to the simulation time being excessive with decreasing strain-rates, we limit ourselves to strain-rates greater than $\dot{\gamma} = 2.5 \times 10^7 s^{-1}$.

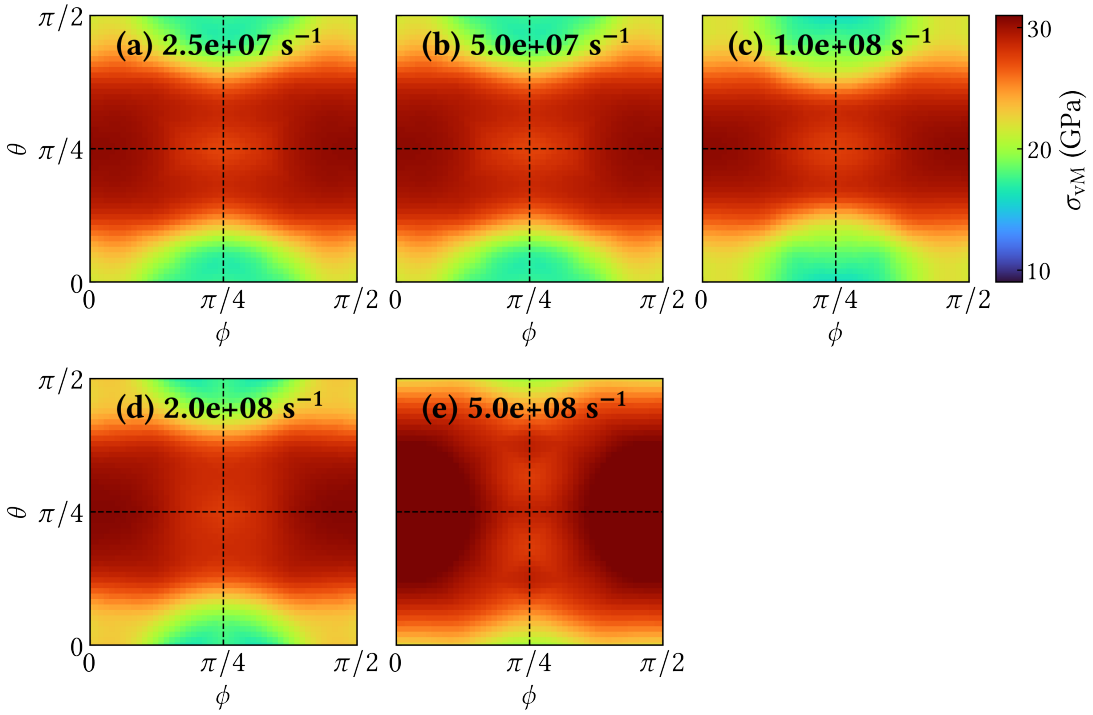

Figure 3.24 – 2D projections of the 3D flow stress surface for different strain-rates. The color scale for the von Mises critical stress is common to all projections. (c) corresponds to the 2D projection of Figure 3.20 averaged by symmetry.

A qualitative agreement between the flow stress surfaces is obtained, especially in terms of shape, i.e. the directional dependence of the stress at nucleation of the first deformation mechanism. This indicates that the strain-rate does not impact the phenomenology of the irreversible deformation processes. Concerning the values of the critical shear stress, except for $\dot{\gamma} = 5 \times 10^8 s^{-1}$ which exhibits a higher stress threshold, no significant effect is observed from $2.5 \times 10^7 s^{-1}$ up to $2.0 \times 10^8 s^{-1}$. To further assess the influence of the strain-rate, we extracted, from Figure 3.24, the critical shear stress in the same particular directions as in Section 3.4.2. Results are presented in Figure 3.25. As expected, the strongest deviations are observed for $5.0 \times 10^8 s^{-1}$, while the lower strain-rate simulations exhibit close threshold values and no significant differences. Additional simulations were performed at a higher temperature of 1600 K in order to determine whether the strain-rate effect was temperature dependent. Flow stress surfaces were computed for 3 strain-rate values $\dot{\gamma} = [2.5 \times 10^7 s^{-1}, 5.0 \times 10^7 s^{-1}, 1.0 \times 10^8 s^{-1}]$ and the resulting 2D projections are provided in the Appendix B. No significant differences were observed for the different strain-rates at 1600 K either, indicating that the use of $\dot{\gamma} = 10^8 s^{-1}$ is a reasonable choice for the previous and subsequent sections.

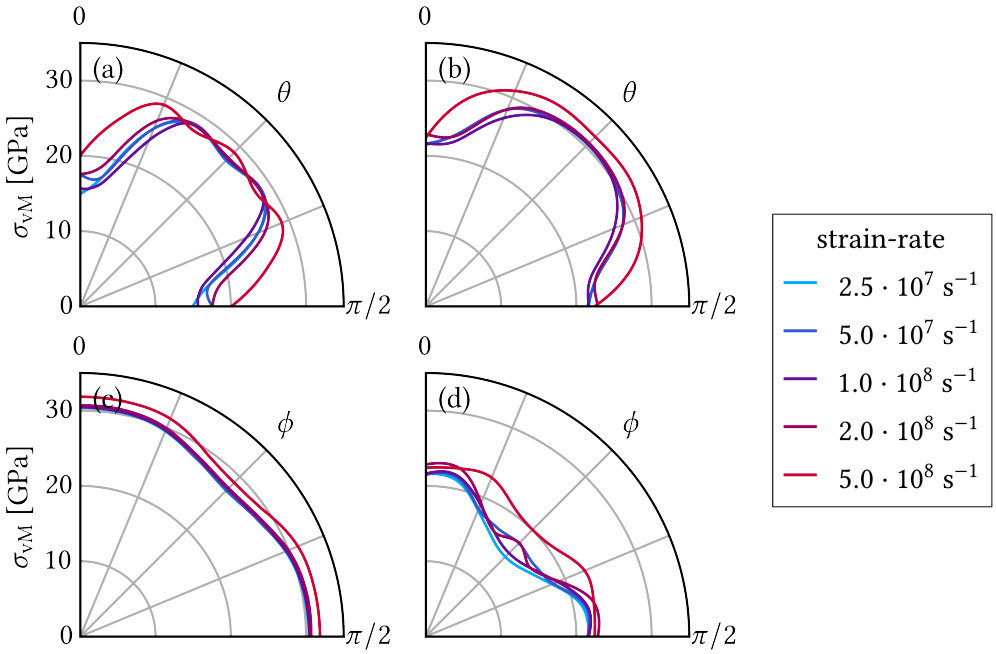

Figure 3.25 – 2D slices of the 3D flow stress surfaces in different planes for the multiple considered strain-rates. (a) $\phi = \pi/4, \theta \in [0, \pi/2]$ (b) $\phi = 0, \theta \in [0, \pi/2]$; (c) $\phi \in [0, \pi/2], \theta = \pi/4$; (d) $\phi \in [0, \pi/2], \theta = 0$.

It is important to note that a strain-rate of $10^8 s^{-1}$ stays several orders of magnitude higher than experimental or engineering strain-rates that are about $10^{-4} s^{-1}$, i.e. under quasi-static conditions. The high strain-rate regime could, however, be attained experimentally using shock waves, but is not the topic of this manuscript. We reach here the glass ceiling of MD, as approaching real strain-rates would require simulation times that are beyond the reach of current simulation capabilities. Indeed, for $10^8 s^{-1}$, the simulated time has already to be of the order of nanoseconds, and for $2.5 \times 10^7 s^{-1}$ the first nucleation event appears after around a dozen nanoseconds. To put this in perspective, even on modern supercomputer architectures, our developed SNAP can perform simulations at rates up to ten nanoseconds per day (and more realistically, few nanoseconds per day).

3.4.4. Effect of temperature

We now investigate the effect of temperature on the critical shear stress of UO_2 single crystal. For this purpose, we employed the same methodology with $\theta, \phi \in [0, \pi/4]$ every $\pi/20$, spanning the $1/32^{th}$ of the unit sphere with 25 MD simulations. Supercells of 20×20×20 conventional cells (as in 3.4.2) were equilibrated in the NVT ensemble at 900, 1200, 1600 and 2000 K at their respective equilibrium volume and used as initial conditions. The corresponding surfaces are displayed in Figure 3.26. As the points located on the 3D flow stress surface are proportionally scaled by the critical stress value, this information is redundant with the colour used. However, both represent

a good guide for the reader's eye and help to understand the strong influence that temperature has on the flow surface.

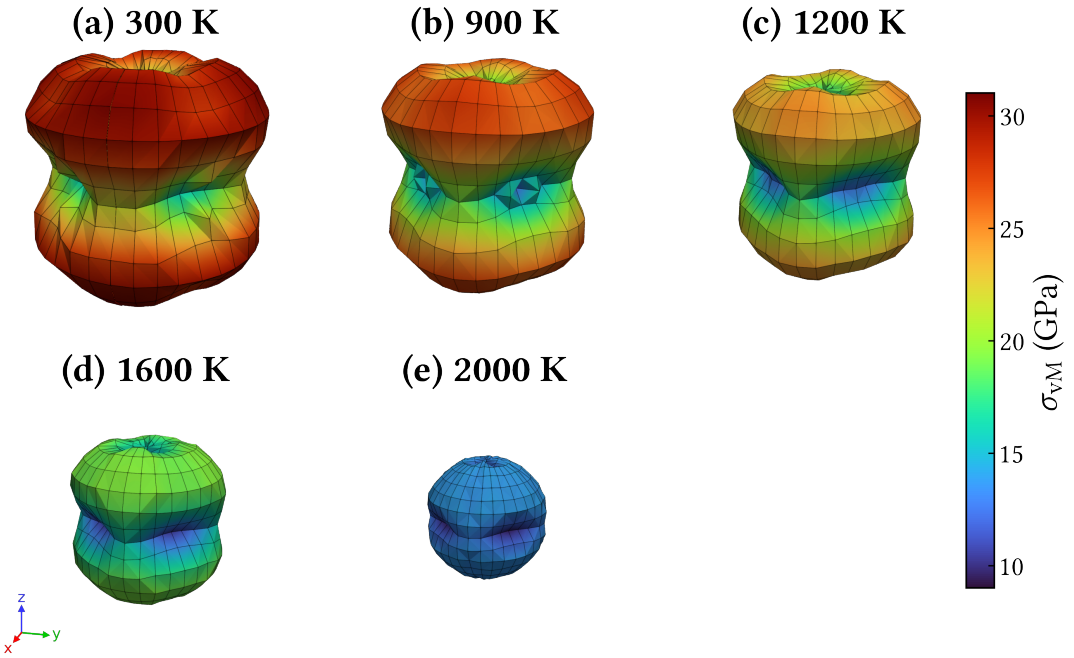

Figure 3.26 – 3D flow stress surfaces at various temperatures between 300K and 2000K. The same color scale is used for all representations.

The first striking result is a strong decrease of the critical stress with respect to temperature. Table 3.6 summarises the minimum and maximum values for each temperature. The maximum critical stress goes from 30.6 GPa at 300 K to 13.9 GPa at 2000 K, traducing a 55% decrease. We also observed that certain directions exhibit a larger diminution of the threshold stress than others, which is illustrated in Figure 3.27 where the difference in critical stress between 300 K and 2000 K is presented for the entire surface. The maximum diminution being mainly observed around $\theta = \pi/4$. This non-homogeneous decrease of the critical stress indicates that the mechanical response at 2000 K does not have the same directional dependence which is discussed hereafter.

The critical stress surfaces become more isotropic with increasing temperature. It can be directly observed in Figure 3.26 where the flow surface becomes more regular and close to a sphere with increasing temperature. In addition, this phenomenon is illustrated in Figure 3.28, where slices correspond to particular directions are presented.

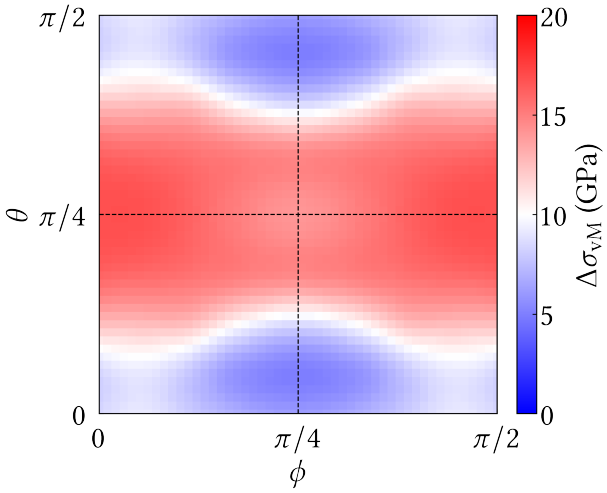

Figure 3.27 – Variation in critical shear stress between 300 K and 2000 K for every loading directions.

Table 3.6 – Minimum and maximum critical shear stress for each temperature.

T (K)	σ_{max} (GPa)	σ_{min} (GPa)
300	15.4	30.6
900	11.9	27.8
1200	11.1	24.8
1600	10.4	19.5
2000	9.5	13.9

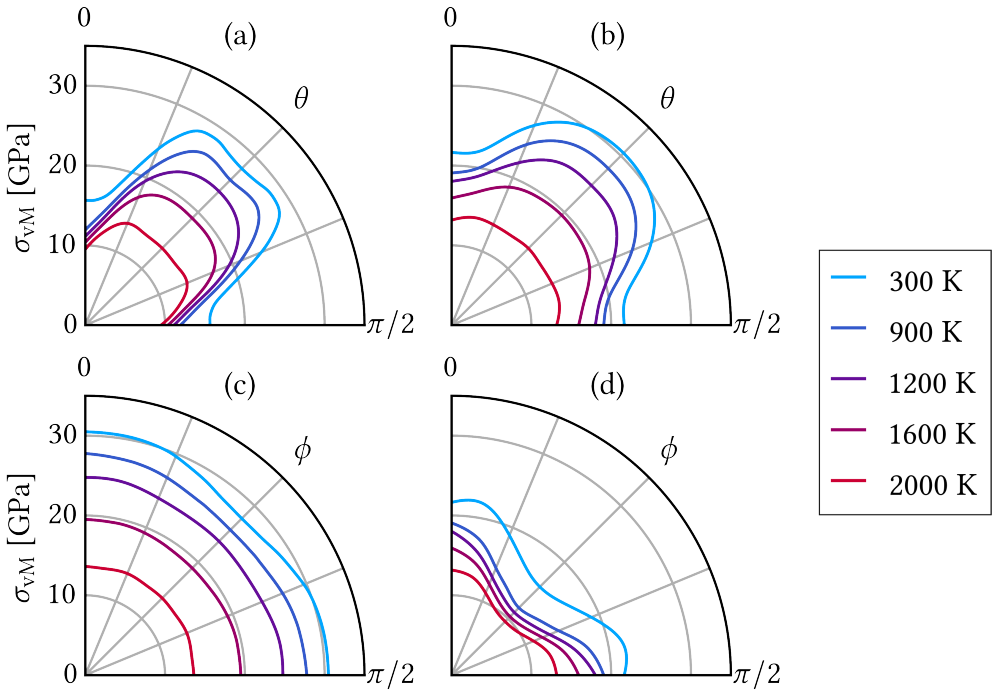

Figure 3.28 – 2D slices of the 3D flow stress surfaces in different planes for different temperatures. (a) $\phi = \pi/4, \theta \in [0, \pi/2]$ (b) $\phi = 0, \theta \in [0, \pi/2]$; (c) $\phi \in [0, \pi/2], \theta = \pi/4$; (d) $\phi \in [0, \pi/2], \theta = 0$.

In order to understand and relate the isotropisation process to the other properties of the material, the natural choice when dealing with mechanical response is to check the elastic properties. To this end, we computed the directional Young and Shear

modulii and projected them in the same directions as for Figure 3.28 for varying temperatures. Results are presented in Figures 3.29 and 3.30. The directional dependence of elastic modulii is derived from elasticity theory and computed from the stiffness tensor (additional details are provided in Appendix A). The latter was obtained in Section 3.3, following the same methodology as described in Section 2.5.5. One can notice the similarity between the shapes of critical flow stresses and shear modulus, which is not a surprise as pure shear deformations are imposed. The variation of shear modulus lets appear a slight isotropisation that roughly corresponds to the one observed for critical stresses, suggesting that the process is related but not solely driven by the elastic properties of the materials. Indeed, while a decrease of approximately 55% was observed for the maximum critical stress between 300 K and 2000 K, the average shear modulus of UO_2 decreases from 70 GPa to 48 GPa, equivalent to a 32% decrease.

In addition to providing parallel comparisons with flow stress surfaces, Figures 3.29 and 3.30 give a good indication on UO_2 elastic anisotropy. Indeed, the universal anisotropy index [310] A^U drops from 1.13 to 0.98. Although the flow stress surface is subject to a strong isotropisation, this is also the case for elasticity, but is less pronounced. However, while the value of A^U decreases, the elastic anisotropy is still high at 2000 K since a perfect isotropy would require A^U=0. Finally, the presence of this non negligible elastic anisotropy is consistent with the elastic instabilities observed for some directions on the flow stress surface.

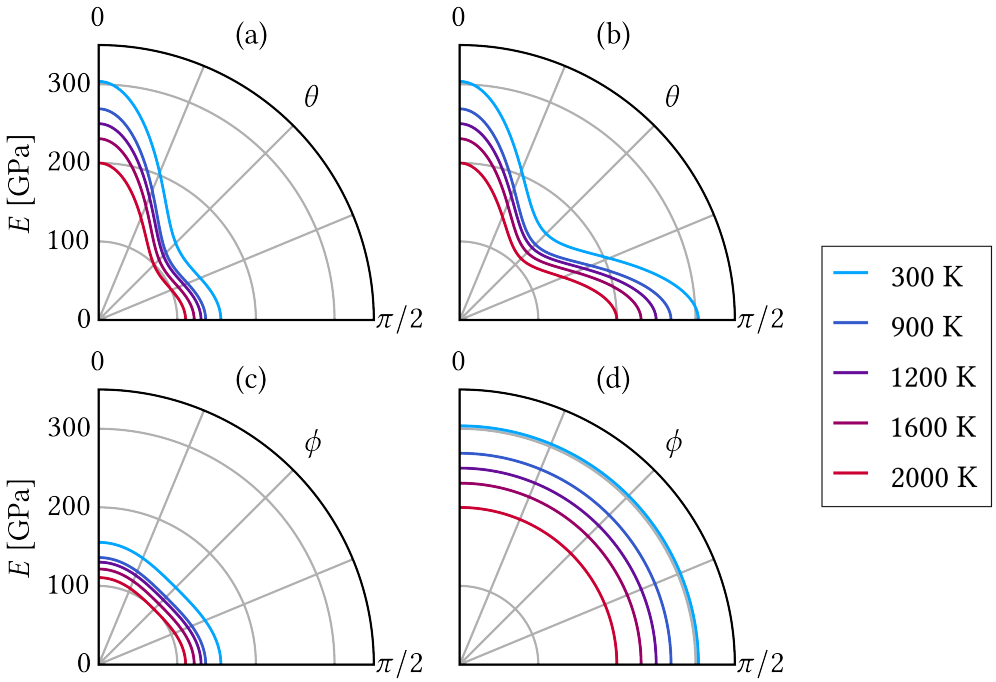

Figure 3.29 – 2D slices of the directional Young modulus at different temperatures. Projections are performed in similar planes as for Figure 3.28. (a) $\phi = \pi/4, \theta \in [0, \pi/2]$ (b) $\phi = 0, \theta \in [0, \pi/2]$; (c) $\phi \in [0, \pi/2], \theta = \pi/4$; (d) $\phi \in [0, \pi/2], \theta = 0$.

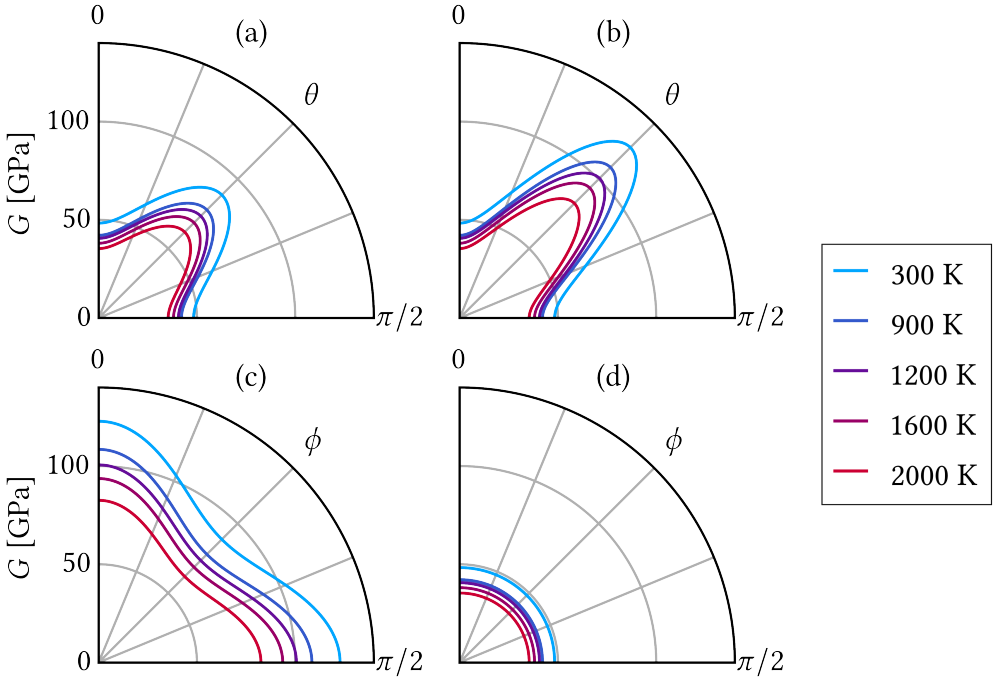

Figure 3.30 – 2D slices of the directional Shear modulus at different temperatures. Projections are performed in similar planes as for Figure 3.28. (a) $\phi = \pi/4, \theta \in [0, \pi/2]$ (b) $\phi = 0, \theta \in [0, \pi/2]$; (c) $\phi \in [0, \pi/2], \theta = \pi/4$; (d) $\phi \in [0, \pi/2], \theta = 0$.

Effect of temperature on deformation mechanisms

Both temperature and strain-rate have an obvious influence on the critical stress at nucleation for UO_2 under pure directional shear. Regardless of the temperature or strain-rate, it was observed that a dependence on the loading direction was present with different deformation mechanisms activated along different directions. As mentioned, directions **A**, **B** and **C**/**D** were subjected to elastic instabilities, dislocation-mediated plasticity, and crack nucleation, respectively.

In the present section, we focus on the **C** direction, where crack nucleation and propagation throughout the sample was systematically observed. For that direction, the microstructures right after the critical stress is reached are analysed. The analysis is automated for deformations performed at a constant strain-rate of $10^8 s^{-1}$ and temperatures of 300 K, 900 K, 1200 K, 1600 K and 2000 K. The resulting microstructures for each temperature are reported in Figure 3.31 where the orange mesh and blue lines represent the fracture surfaces and dislocations, respectively, obtained by the alpha-shape and DXA methods from the `ovito` software. One obvious result is that dislocation lines appear only for the cases at 1600 K and 2000 K, indicating a transition in terms of the activated deformation mechanism for that direction. One can see that for lower temperatures, only cracks are present, always located in the same fracture plane, which is consistent with the similar deformation path used. However, a mixed behaviour is

observed at 1600 K where both cracks and plastic signatures are observed, indicating, for example, a dislocation nucleation process from free surfaces. Finally, the higher temperature case indicated a disappearance of [111] fracture planes. Instead, a small amount of orange defect mesh is located around dislocation lines, which can also be the signature of a loss of crystallinity due to the high dislocation density and high strain-rate used in this work.

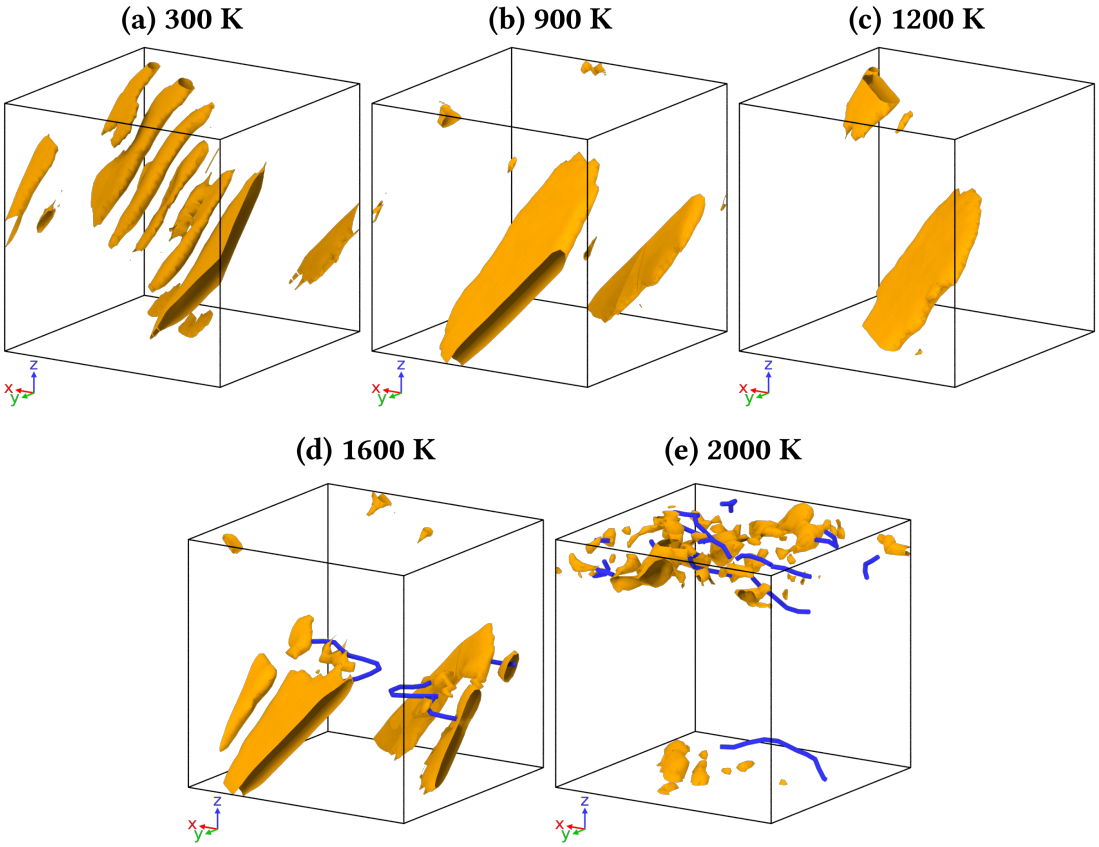

Figure 3.31 – Evolution of the nucleated plastic defect with respect to temperature for the **C** direction. Orange meshes represent identified surfaces and blue lines correspond to $1/2\langle 110\rangle$ dislocations.

In conclusion, we show that the UO_2 single crystal is subject to a fragile to ductile transition, even given the high strain-rate of $10^8 s^{-1}$ considered in this work. Although these first observations are made on small UO_2 samples, further work could be dedicated to a similar study on larger samples, to avoid cascade events and plastic localisation that could induce bias in observed behaviour due to size effects and periodic boundary conditions. In addition, larger samples containing initial defects would be more representative of the real material. The next section explores an initial attempt, focusing on irradiated UO_2 single crystals.

3.4.5. Effect of irradiation at ambient temperature

In previous subsections, simulations were performed on pristine UO_2. To better approximate the real material and understand the influence of the irradiated microstructure on the mechanical response of UO_2 single crystal, we employed the same methodology as previously described but with initial supercells that are more representative of the early stages of the irradiation process in UO_2.

Irradiated 40×40×40 supercells (corresponding to 768k atoms) containing non-zero damage density (point defects and dislocations) were gratefully provided by Chartier *et al.* [59]. The configurations were obtained using the Frenkel pairs accumulation (FPA) methodology [311, 312] to replicate ballistic damages. The method consists in randomly picking uranium atoms that are then displaced to new random positions, creating Frenkel pairs, at regularly-spaced time intervals. Each displacement is followed by an equilibration at the working temperature allowing for damage annealing process by recombination of Frenkel pairs [313]. This approach has the advantage of bypassing the accumulation of displacement cascades [314, 315] by directly generating their end states, namely point defects, and has been demonstrated to be highly effective in simulating irradiation damage in various oxides [316, 317] and graphite [318]. Chartier *et al.* [59] performed the calculations using the Morelon empirical potential [29], creating 800 uranium Frenkel pairs every 2 ps. This corresponds to a dose rate of

$$K_0 = \frac{800 \cdot 2 \times 10^{-12}}{768000/3} = 1.5625 \times 10^9 \,\mathrm{dpU \cdot s^{-1}} \tag{3.16}$$

Note that because only uranium defects are created, the damage is expressed in displacement per uranium (dpU). From the provided simulation boxes, we only had access to the iteration step of the MD simulation ($\mathrm{MD_{step}}$) and because in [59] the simulation timestep was not given, we assumed a timestep $\Delta t = 0.5$ fs and calculated the dose (in dpU) as

$$\begin{aligned} \mathrm{dose} &= \mathrm{MD_{step}} \cdot \Delta t \cdot K_0 \\ &= \mathrm{MD_{step}} \cdot 0.5 \times 10^{15} \cdot 1.5625 \times 10^9 \end{aligned} \tag{3.17}$$

leading to a satisfactory agreement with the original publication.

Radiation damage in the material mainly manifests in the form of point defects (interstitials and vacancies), which are direct results of the FPA method, and dislocations, emerging from the recombination of those defects. The simulation boxes were analysed using the `ovito` software in which the point defect concentrations were derived from a Voronoï analysis. Dislocation densities for three types of dislocation (namely $1/3\langle 111\rangle$, $1/3\langle 110\rangle$ and $1/6\langle 112\rangle$) were determined using DXA. The accumulation of radiation defects with respect to dose is presented in Figure 3.32.

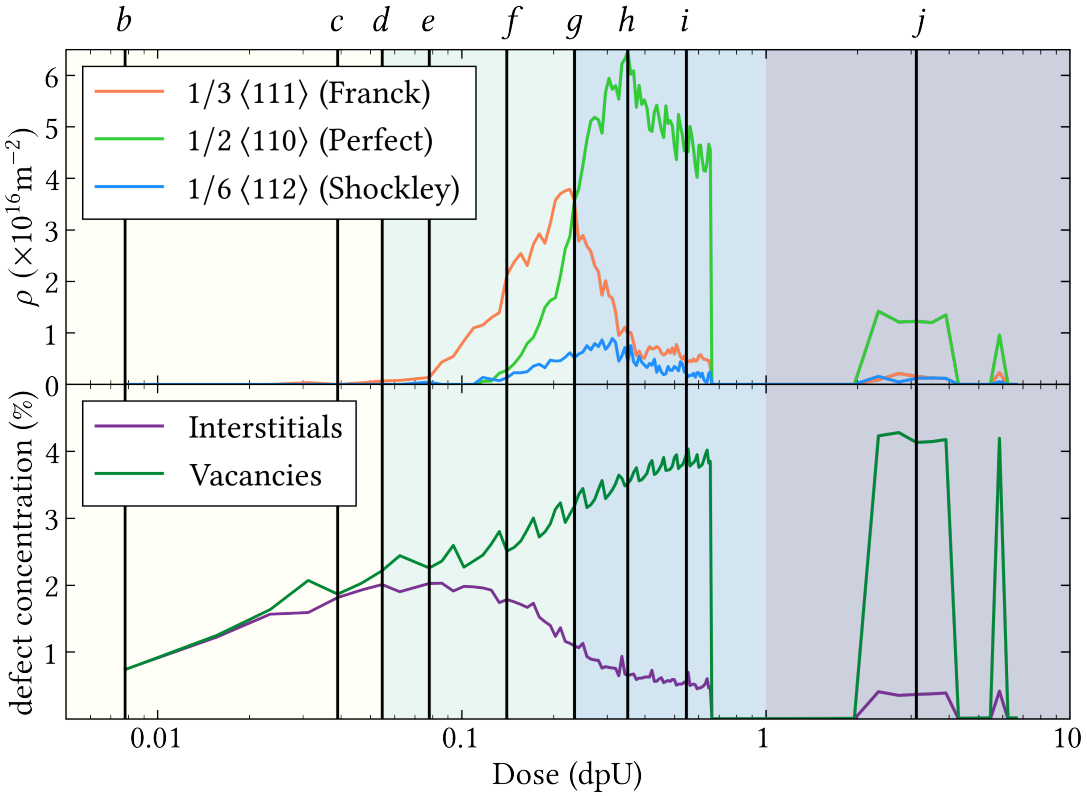

Figure 3.32 – Evolution of dislocation density (top) and defects concentration (bottom) as a function of the irradiation dose in dpU. Vertical black line mark the sampled configuration of subsequent MD simulations with deformations.

According to [59] the accumulation of radiation defects in the material can be split into four stages (represented by the background colouration in Figure 3.32). The first stage is characterised by the accumulation of interstitials and vacancies in the same concentration, corresponding to a recombination regime [55], then both concentrations diverge. This marks the beginning of the second stage, where the vacancy concentration continues to increase while the interstitial concentration decreases. This decrease is associated with interstitial clustering that leads to the nucleation of Franck dislocation loops (Figure 3.32-top). Those dislocations are unstable above nanometer size [319] and thus transform into perfect loops during a third stage. The transformation mechanism is reported as $1/6\langle 112\rangle + 1/3\langle 111\rangle \rightarrow 1/2\langle 110\rangle$ [320] in agreement with the nucleation of Shockley partials, which coincides with the increase in perfect loops and the decrease in Frank loops. The final stage corresponds to the conversion of perfect loops into lines. For further details, we redirect the reader to the original publication [59].

Throughout this trajectory, 9 configurations were extracted, marked as thicker black lines in Figure 3.32 and labelled from *b* to *j* (*a* being reserved for the pristine material), each corresponding to a particular stage of the irradiation process. Each configuration was then equilibrated for 50 ps in the *NVT* ensemble at 300 K to be used as initial conditions for subsequent deformation simulations using the methodology described

in Section 3.4.1 with $\theta, \phi \in [0, \pi/4]$ every $\pi/20$ spanning $1/32^{\text{th}}$ of the unit sphere with 25 MD simulations.

Figure 3.33 displays the von Mises stress as a function of the strain for pristine UO_2 (Figure 3.33-*a*) and each selected snapshot (Figures 3.33-*b* to *j*) for all loading directions, at ambient temperature (300 K). To serve as a guide for the reader's eye, the curves are coloured according to the maximum value reached by the von Mises stress in the range $\epsilon \in [0, 0.15]$.

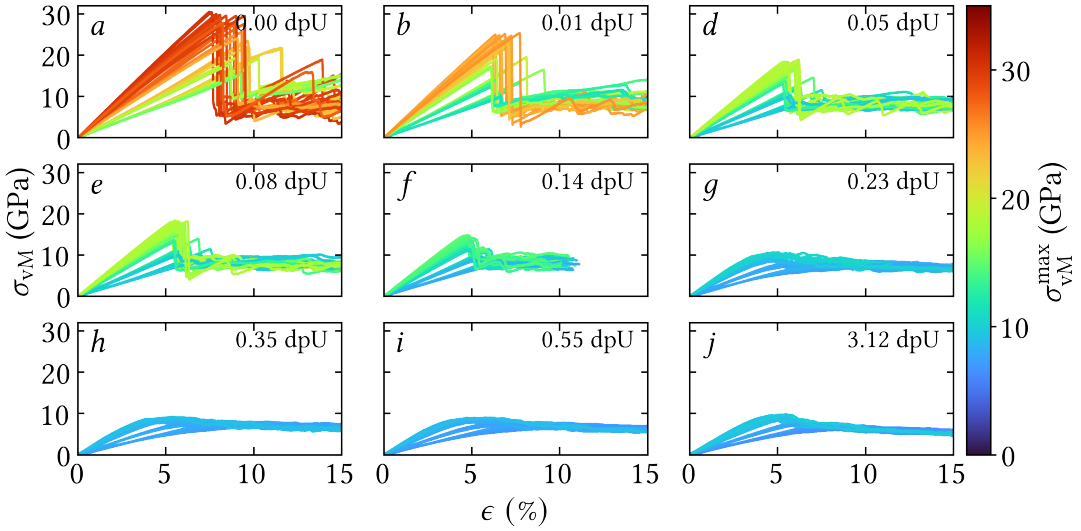

Figure 3.33 – Stress-strain curves for every loading direction with initial configuration *a* to *j* at 300 K. The corresponding radiation dose is given in the top-right corner. The curves are coloured according to the maximum value of the von Mises stress, σ_{vM}^{max} in the range $\epsilon \in [0, 0.15]$.

We first notice an important overall decrease in the critical stresses with respect to the irradiation dose. The initial defects population helps to accommodate the deformation the UO_2 samples are subjected to and therefore lower the material's flow stress. We also observed that, starting from 0.23 dpU (Figure 3.32-g), curves' shape do not exhibit a clear drop in stress which would be associated to a decrease of plastic defects nucleation processes. This is rather due to the pre-existing radiation defects that hinder nucleation process and instead accommodate the deformation through dislocation mobility or diffusion. As the dose increases, nucleation of plastic defects is no longer necessary because the initial population is probably sufficient to accommodate the deformation as is. Nonetheless, this complicates the determination of the critical flow stress as was the case in preceding sections. Indeed, the more defects the microstructure contains, the closer the critical stress is to a real flow stress. On the other hand, the less defects the microstructure contains, the closer the critical stress is to a nucleation critical stress. Therefore, we chose not to represent the 3D flow surfaces as a more elaborate analysis would have to be developed. However, considering steady-state stress as a large strain would probably be a good candidate.

In order to investigate the decrease in the maximum stress value, in Figure 3.34, the evolution of the maximum von Mises stress in the same directions as in Sections 3.4.2 and 3.4.4 with respect to the irradiation dose. We observe that the diminution is directional dependent. Indeed, for directions **A** and **B** the absolute value of critical stress ranges from around 30 GPa at 0 dpU to 9 GPa at 0.35 dpU. On the other hand, directions **C** and **D** exhibit lower variations. In relative value, in all directions the decrease ranges from 70% for the direction **A** to 50% for direction **D**. Similarly to temperature effects in the pristine material, the strongest diminution is observed for direction corresponding to $\theta = \pi/4$ (**A** and **B**). We also observed a slight bump for all directions, with a maximum around 0.08 dpU, which corresponds to the beginning of the Frank loop growth (see 3.32-top).

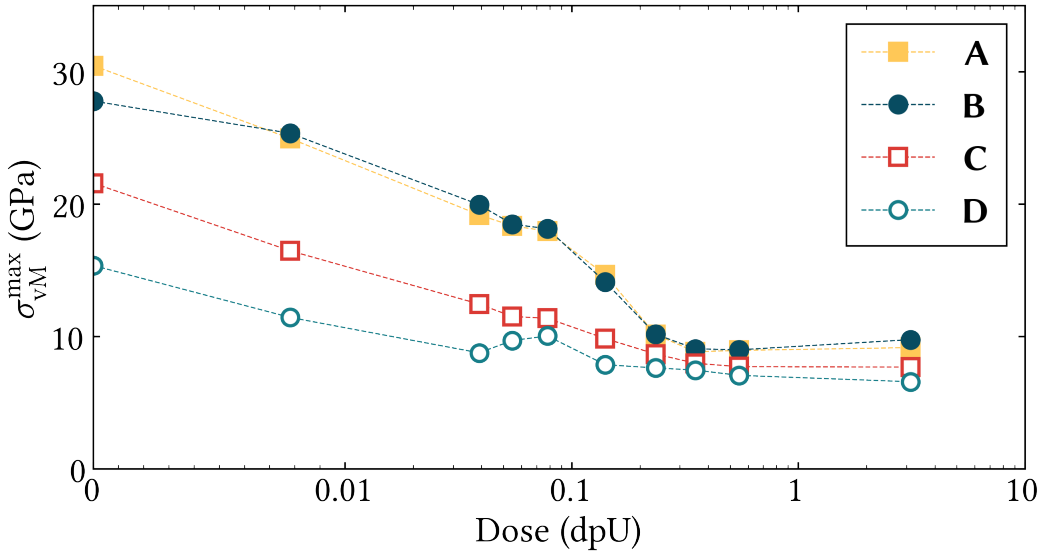

Figure 3.34 – Evolution of the maximum von Mises stress, σ_{vM}^{max} in the range $\epsilon \in [0, 0.15]$, with respect to the dose in dpU for direction **A**, **B**, **C** and **D** (see Figure 3.20. The x-axis is displayed in `symlog` representation.

Furthermore, a progressive isotropisation of the material is observed in both Figures 3.33 and 3.34, with the mechanical response of the materials at high strain-rate being nearly isotropic around 0.35 dpU (Figure 3.34-h) corresponding to the maximum of the perfect loops dislocation density (see Figure 3.32). As mentioned, the mechanical response of the material being mainly driven by the mobility of pre-existing dislocations, the quasi-isotropic behaviour might be explained by a homogeneous distribution of the perfect loops inside the material. In the presence of nucleation processes, i.e. at a very low irradiation dose, propagation of dislocations and / or other processes evolve along highly localised directions, hindering the ability of other defects to evolve in other directions in the crystals. This has for effect a large dependence on the materials' response to the loading direction. At moderate to high irradiation doses, the initial defects population is non-negligible and the mobility of defects in various directions of

the crystal structure is allowed. Thus, the mechanical response is less attached to the loading direction.

3.4.6. Irradiation and temperature effects altogether

Eventually, we were interested in the effect of the temperature associated with radiation damage. The same methodology was employed, with the selected irradiated configurations being equilibrated in the *NVT* ensemble for 50 ps at 900, 1200, 1600 and 2000 K (same temperature as Section 3.4.4). This procedure allows us to get insights into the coupled effects of both irradiation and temperature on the mechanical response of UO_2 single crystals.

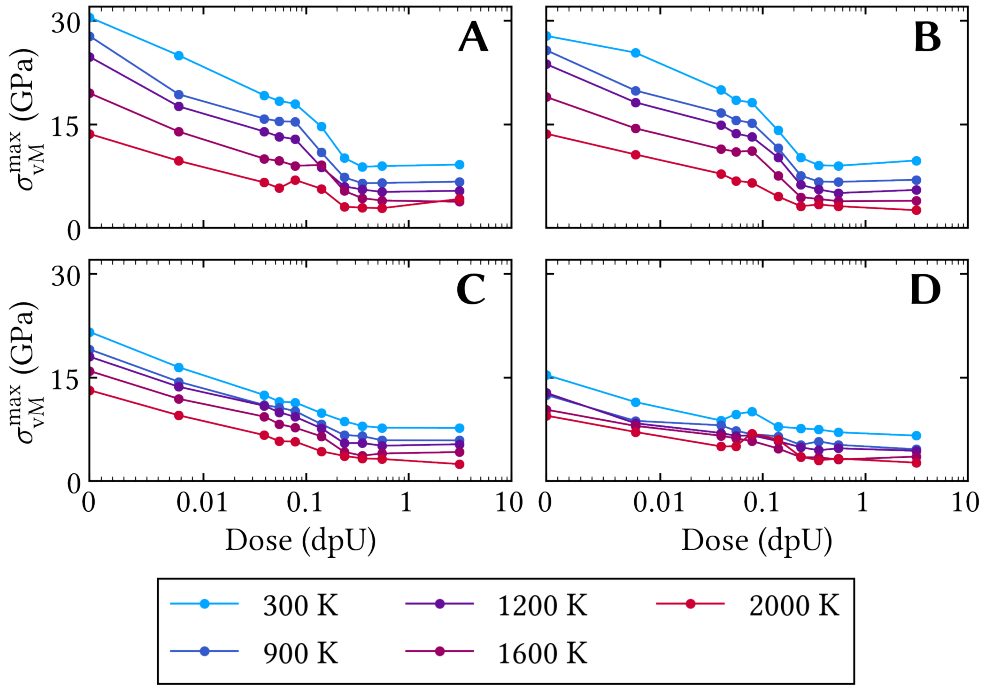

Figure 3.35 – Evolution of the maximum von Mises stress, σ_{vM}^{max} in the range $\epsilon \in [0, 0.15]$, with respect to the dose in dpU for direction **A**, **B**, **C** and **D** (see Figure 3.20 as function of temperature.

We present in Figure 3.35 the variation of the critical stress σ_{vM}^{max} with respect to the irradiation dose for the four deformation directions previously considered. These critical stress values were extracted from stress vs. strain curves at different temperatures and irradiation doses displayed in Figures 3.36, 3.37, 3.38 and 3.39, that are similar to 3.33. These figures contain a lot of information as they render for the temperature, deformation direction, and irradiation dose effects at the same time. However, the information is condensed in Figure 3.35 where we can directly and easily discuss the effect of different conditions on the flow stress of UO_2 irradiated samples for 4 specific directions of deformation.

One common effect for all samples is that the temperature at which the material is strained lowers the critical stress for a fixed value of dpU. For directions **A** and **B**, the decrease is more pronounced at lower dpU while for directions **C** and **D** the decrease due to temperature appears constant with dpU.

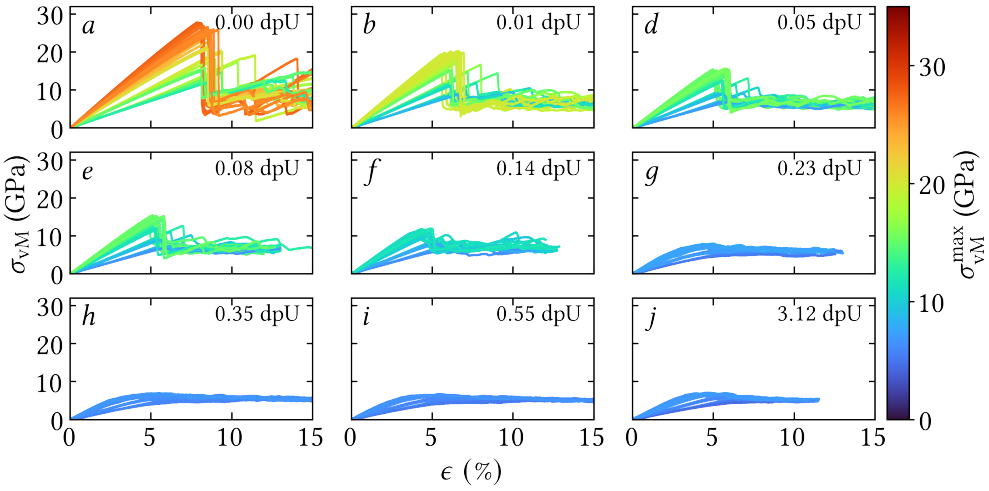

Figure 3.36 – Stress-strain curves for every loading direction with initial configuration *a* to *j* at 900 K. The corresponding radiation dose is given in the top-right corner. The curves are coloured according to the maximum value of the von Mises stress, σ_{vM}^{max} in the range $\epsilon \in [0, 0.15]$.

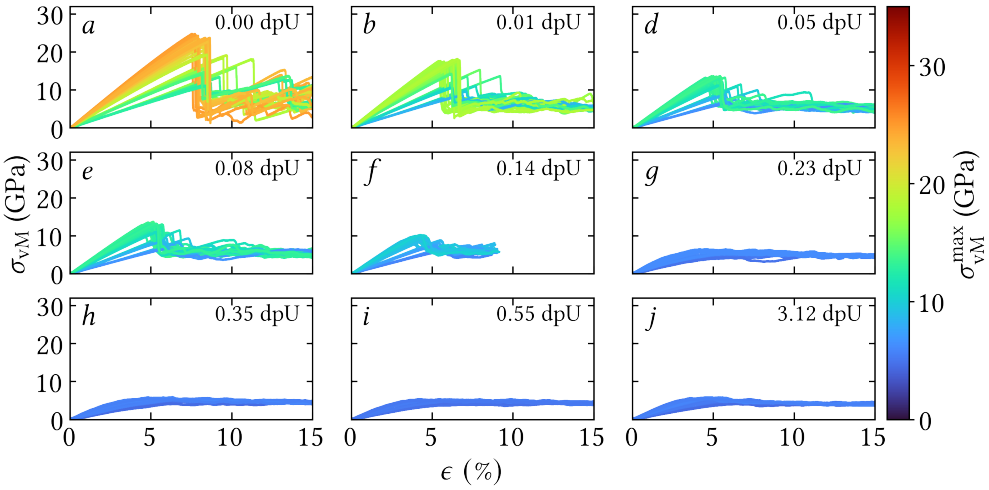

Figure 3.37 – Stress-strain curves for every loading direction with initial configuration *a* to *j* at 1200 K. The corresponding radiation dose is given in the top-right corner. The curves are coloured according to the maximum value of the von Mises stress, σ_{vM}^{max} in the range $\epsilon \in [0, 0.15]$.

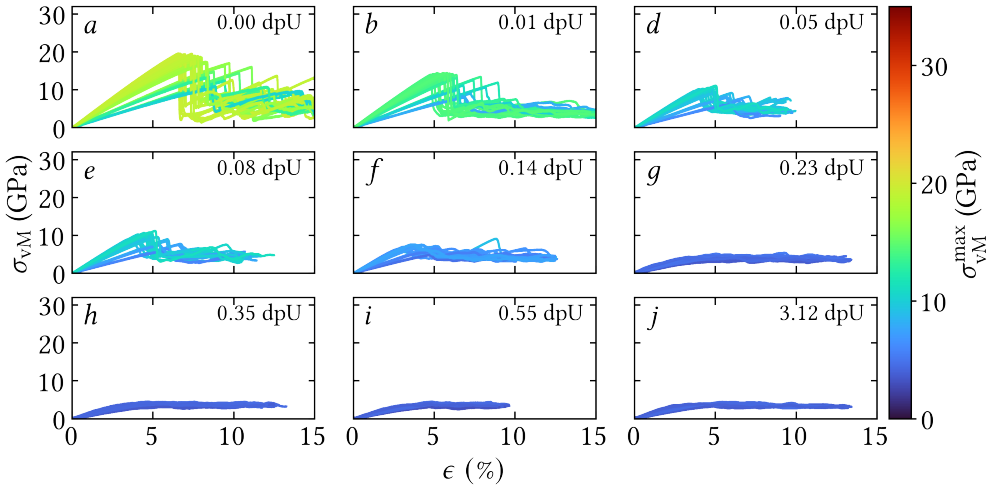

Figure 3.38 – Stress-strain curves for every loading direction with initial configuration *a* to *j* at 1600 K. The corresponding radiation dose is given in the top-right corner. The curves are coloured according to the maximum value of the von Mises stress, $\sigma_{\mathrm{vM}}^{\mathrm{max}}$ in the range $\epsilon \in [0, 0.15]$.

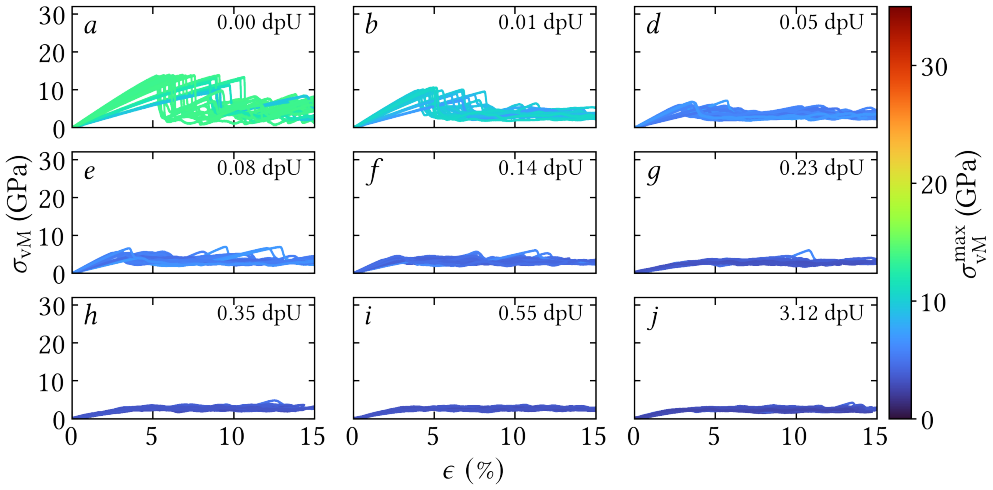

Figure 3.39 – Stress-strain curves for every loading direction with initial configuration *a* to *j* at 2000 K. The corresponding radiation dose is given in the top-right corner. The curves are coloured according to the maximum value of the von Mises stress, $\sigma_{\mathrm{vM}}^{\mathrm{max}}$ in the range $\epsilon \in [0, 0.15]$.

Looking at the effect of dpU on the critical stress, one can see that it induces a decrease of the latter for all directions, bringing their critical stresses to an approximate common value for large irradiation doses. This is in line with the isotropisation of the mechanical response at high temperature / high dose induced by both the presence of a larger number of defects that do not need to be nucleated and their mobility that is facilitated by the temperature.

In order to gather the information and allow a further analysis of these results, we provide in Figure 3.40 colour maps of the critical stress as a function of dpU and temperature for the 4 specific deformation directions. In these graphs, it is evident that temperature exerts a more pronounced influence on the directions **A** / **B** as compared to directions **C** / **D**. Although there are differences at low dpU between the different directions, independently of temperature, the critical stress for all directions converges to similar values at moderate dpU and temperatures, again indicating the homogenisation of the mechanical response.

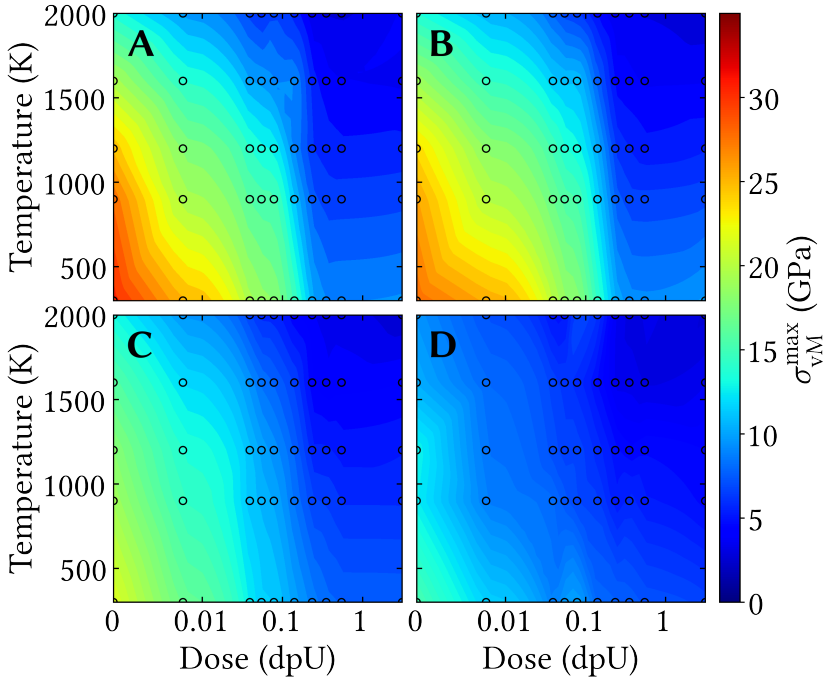

Figure 3.40 – Colour maps of the critical von Mises stress as a function of irradiation dose (dpU) for the 4 specific directions discusses in the present section. Colour maps are a result of interpolation of the discrete data represented as open circles.

Finally, in order to further condense the information, the critical von Mises stress was averaged for all deformation directions. The results are displayed in Figure 3.41 (left) as a function of irradiation dose dpU and temperature and their respective, but coupled, effects can be observed directly. Both temperature and dpU induce a decrease in flow stress, the latter being less linear when only looking at the effect of dpU only.

Although a similar flow stress can be obtained at moderate dpU, high temperature and at higher dose, low temperature, this does not imply that the deformation mechanisms and their evolution are strictly the same. Indeed, a lower dose will generate a small amount of crystal defects, but their mobility will be facilitated by the higher temperature. On the other hand, a higher dose will induce a large population of defects, but low temperature will hinder their mobility. Then, what will differentiate between the

two situations will be the mobility of the dislocations, and probably their interaction mechanisms. Such phenomena can benefit from other types of simulations, such as MD simulations at larger scale or discrete dislocation dynamics (DDD) simulations.

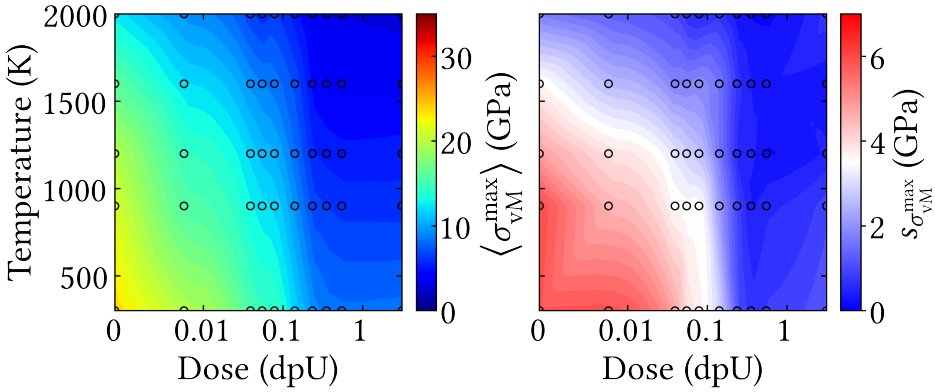

Figure 3.41 – **(left)** Colormap of the critical von Mises stress as a function of irradiation dose (dpU) average over all deformation directions. **(right)** Corresponding variance of the critical von Mises stress.

As the critical stress displayed in Figure 3.41 (left) is averaged over all orientations, the corresponding variance is displayed in Figure 3.41 (right). This is a direct measure of the isotropic character of UO_2 mechanical response to pure shear. Indeed, a perfectly isotropic material would display a very low variance, while an anisotropic one would exhibit strong fluctuations in the directional flow stress directly translated by a large variance. Here, the variance is high at low doses and low temperatures, which is in line with the observations discussed in the preceding sections. High variance is associated with low defects' density and a higher variety of deformation mechanisms in addition to nucleation processes. The low variance, on the other hand, comes from the higher initial density of defects due to high irradiation doses, as well as from their easy mobility due to higher temperature. In fine, the variance of the critical von Mises stress represents a good homogenisation tool for studying the directional dependence of a materials' response at high strain-rate, as demonstrated in the present work.

3.5. Conclusion

In this chapter, our objective was to reconcile DFT approximations with experimental observations. We chose to use the PBEsol functional along with non-collinear 3**k** magnetic order, which allowed us to correctly predict the isotropic fluorite structure of the material, with a density closely matching experimental data. To stabilise the associated magnetic configurations, it was necessary to consider SOC. In addition, the inclusion of spin-orbit coupling made it possible to dispense with the electronic OMC procedure. Using this new DFT setup, we developed a new SNAP that, upon validation,

exhibits a very good agreement with the experimental density up to 2500 K and thus corrects aspects of previous potentials.

This new potential was then used to investigate the thermomechanical properties of the material by computing the orientational dependence of the macroscopic stress at the onset of the first irreversible deformation mechanism, i.e. the critical shear stress flow surface. The results highlighted the anisotropic behaviour of UO_2 at ambient temperature both in terms of stress thresholds and deformation mechanism. We observed at least 3 mechanisms: buckling, cracking, and dislocation nucleation.

The influence of temperature on the flow surface was also investigated, revealing a significant reduction in critical shear stresses as well as isotropization of the material. Additionally, we observed a transition from a brittle behaviour at 300 K to a more ductile-like behaviour at higher temperatures. This brittle-ductile transition, which has been observed experimentally for UO_2, underscores the predictive capacity of our SNAP-PBEsol framework.

Finally, we examined the influence of pre-existing irradiation defects (point defects and dislocations) at the onset of deformation. Specifically, we observed that a non-zero initial dislocation density significantly lowers critical stresses and homogenises the plastic response. These preliminary results highlight the diverse and complex mechanical behaviour of uranium dioxide, while also demonstrating the capability of the developed potentials to handle large-scale molecular dynamics simulations involving multiple physical phenomena.

Conclusions and perspectives

It is good to have an end to journey toward; but it is the journey that matters, in the end.

– Ernest Hemingway

Actinide oxides represent a complex subject of investigation due to the particular nature of these materials. The aim of this work was to explore the feasibility of applying machine learning methods to describe these materials at the atomic scale, and in particular uranium dioxide, the most widely used nuclear fuel in the world.

The first part of this work was dedicated to the development and validation of two machine learning interatomic potentials for uranium dioxide using the SNAP and the HDNNP methodologies. Active learning methods were paired with state-of-the-art DFT+U calculations to generate diverse and representative ensembles of atomic configurations on which the potentials were trained. Despite the complexity of the reference DFT+U calculations, both potentials exhibit good agreement with a large and selective set of *ab initio* and experimental metrics. The temperature dependence of the potentials was investigated, specifically regarding the evolution of elastic constants, thermal expansion, and heat capacity. Comparison with existing experimental data shows reasonable agreement. Additionally, our potentials successfully reproduce the superionic transition (Bredig transition) around 2500 K, despite the relatively small 96-atom configurations used in the training set. This transition, associated with increased mobility of the oxygen sublattice, has been theoretically an experimentally discussed and is still the object of intense investigations [51, 52]. Finally, we leveraged our SNAP potential to relax stacking fault configuration, allowing their subsequent evaluation using DFT+U. The stacking fault energy surfaces computed with this approach could contribute significantly to understanding the plastic behaviour of UO_2, including the evaluation of dislocation nucleation stresses. These results are fundamental to the field of nuclear fuels. Indeed, they enable to probe the validity and accuracy of MLIPs and SEIPs to simulate dislocation mobility and stability in UO_2, which is crucial in the context of irradiated nuclear fuels. In the final part of this chapter we briefly presented two different applications of the developed potentials, performed in collaboration with other students. The first was the study of oxygen diffusivity in hyperstoichiometric UO_{2+x}, for which a specific SNAP was developed without long-range Coulombic interactions. The work highlighted the possible correlation between the material volume and the collective motion of oxygen atoms associated with the Bredig transition. We also

presented the use of the SNAP in NEB calculations as part of the ART workflow and the results obtained for the migration energies of point defects, exhibiting several differences with the CRG potential.

Despite the very promising results obtained in the first part, a number of questions remained uncleared, in particular the underestimated density predicted by our MLIPs, hampering the comparisons to experimental predictions. Although the problem was well identified and related to the GGA-PBE exchange-correlation functional, of which the potentials are only intended to be a reflection, numerous discussions raised the question of how much confidence can be placed in the predicted results with these potentials for atomic-scale fuel simulations. Therefore, in a second part, we looked at reconciling the DFT approximations with experimental observations. We chose to use the PBEsol functional, which allowed us to improve the agreement between our predictions and the experimental density. In order to correctly reproduce the isotropic fluorite structure of the material, we also chose to use a non-collinear 3**k** magnetic order. To this end, it was necessary to consider SOC in the calculations in order to stabilise the associated magnetic configurations.It is noteworthy, as previously highlighted in the literature, that this approach also eliminates the necessity for the electronic occupation matrices control procedure. This new DFT setup was then used as the basis for the development and validation of a new SNAP which exhibits a very good agreement with the experimental density up to 2500 K, and therefore corrects some of the main concerns raised for the previous potentials.

Confident in this new potential, we investigated the thermomechanical properties of the material by computing the critical shear stress flow surface, which represents the orientation dependence of the macroscopic stress at the onset of the first irreversible deformation mechanism. The results obtained highlight the anisotropic behaviour of UO_2 a 300 K in terms of stress thresholds but also in the type of mechanism that occurs to accommodate the deformations. We observed at least 3 mechanisms: buckling, cracking, and dislocation nucleation. The influence of temperature was investigated, revealing both a strong decrease in critical shear stresses and an isotropization of the material. We also observed a transition between brittle behaviour at 300 K, to a more ductile-like behaviour at higher temperature. This brittle-ductile transition, experimentally observed for UO_2, comforts the prediction capability of our SNAP-PBEsol framework. We finally considered the influence of pre-existing irradiation defects at the onset of the deformation. In particular, we observed that non-zero initial dislocation density strongly participates in lowering critical stresses and to the homogenisation of the plastic response. Those preliminary results, which highlight the diverse and complex mechanical behaviour of uranium dioxide, also provided a good opportunity to demonstrate the capability of the developed potentials to handle large-scale molecular dynamic simulations involving multiple physical phenomena.

The work achieved in this manuscript opens the way to numerous perspectives for the study of nuclear fuel materials. Here, we focused on uranium dioxide and have shown that it is now possible to perform accurate materials predictions that are consistent

with *ab initio* predictions and experimental results.

Future investigations will aim at extending our developed potentials to more complex fuel materials by extending the training set to include additional species such as plutonium, americium, or fission products such as xenon. This extension would enable the simulation of a crucial topic for pressurised water reactors and fast neutron reactors: the fission gas evolution and released in MOX fuels. The main difficulties associated with the development of MLIP including additional species would be, as always, the construction of a diverse and representative database of atomic configurations. When considering additional chemical species in a material one should also consider the additional degree of freedom related to the compositions, which largely increase the domain of the configuration space that would be required to sample. In that sense, mixed oxides share common features with high-entropy alloys, for which several methods are developed to further improve the sampling of the configuration space. Active learning methods mentioned in chapter 2 could be really beneficial, but other approaches based on generative models are also at the cutting edge to sample representative configurations from high-dimensional spaces [321].

An other perspective, would be to investigate the impact of augmented physical descriptions, such as magnetic spins or charge fluctuations, within the classical model. Recent studies have combined MLIPs with magneto-elastic Hamiltonian [322–324], which could be used to investigate the piezomagnetic properties of UO_2 [325–327] or the influence of the Néel transition on its thermal conductivity at low temperature [328].

The superposition of MLIPs with variable charge models [187, 329, 330] could enable advanced atomistic studies of phenomena crucial to nuclear fuel applications, such as accurate simulations of nonstoichiometric materials.

Eventually, the preliminary study of thermomechanical behaviour at the onset of irreversible deformation presented in chapter 2 could be used as a starting point for further in-depth studies. In this work, we mainly presented nucleation of plastic defects, but in the real material the motion of pre-existing defects is certainly the main mechanism to accommodate the deformations. Nevertheless, these large-scale MD results could also be used as ingredients to build meso-scale constitutive laws for the material under conditions that are nearly impossible to achieve within experimental studies.

Bibliography

1. Noirot, J., Lamontagne, J., Nakae, N. *et al.* Heterogeneous UO2 fuel irradiated up to a high burn-up: Investigation of the HBS and of fission product releases. *Journal of Nuclear Materials* **442,** 309–319 (Nov. 2013) (cit. on pp. ix, 1).
2. Noirot, J. *Les combustibles nucléaires* tech. rep. (2008), 25–28 (cit. on pp. ix, 1).
3. Noirot, J., Desgranges, L. & Lamontagne, J. Detailed characterisations of high burn-up structures in oxide fuels. *Journal of Nuclear Materials* **372,** 318–339 (Jan. 2008) (cit. on pp. ix, 1).
4. Lucuta, P. G., Matzke, H. & Hastings, I. J. A pragmatic approach to modelling thermal conductivity of irradiated UO2 fuel: Review and recommendations. *Journal of Nuclear Materials* **232,** 166–180 (Sept. 1996) (cit. on pp. ix, 1).
5. Cappia, F., Pizzocri, D., Marchetti, M. *et al.* Microhardness and Young's modulus of high burn-up UO2 fuel. *Journal of Nuclear Materials* **479,** 447–454 (Oct. 2016) (cit. on pp. ix, 1).
6. Henry, R., Zacharie-Aubrun, I., Blay, T. *et al.* Irradiation effects on the fracture properties of UO2 fuels studied by micro-mechanical testing. *Journal of Nuclear Materials* **536,** 152179 (Aug. 2020) (cit. on pp. ix, 1).
7. Götzmann, O., Hofmann, P. & Thümmler, F. Attack upon the cladding of oxide fuel pins by fuel and fission products. *Journal of Nuclear Materials* **52,** 33–50 (Aug. 1974) (cit. on pp. ix, 2).
8. Sidky, P. S. Iodine stress corrosion cracking of Zircaloy reactor cladding: iodine chemistry (a review). *Journal of Nuclear Materials* **256,** 1–17 (July 1998) (cit. on p. ix).
9. Cox, B. Pellet-clad interaction (PCI) failures of zirconium alloy fuel cladding — A review. *Journal of Nuclear Materials* **172,** 249–292 (Aug. 1990) (cit. on pp. ix, 2).
10. Desgranges, L., Riglet-Martial, C., Aubrun, I. *et al.* Evidence of tellurium iodide compounds in a power-ramped irradiated UO2 fuel rod. *Journal of Nuclear Materials* **437,** 409–414 (June 2013) (cit. on p. ix).
11. Introïni, C., Ramière, I., Sercombe, J. *et al.* ALCYONE: the fuel performance code of the PLEIADES platform dedicated to PWR fuel rods behavior. *Annals of Nuclear Energy* **207,** 110711 (Nov. 2024) (cit. on pp. x, 2).
12. Lainet, M., Michel, B., Dumas, J.-C. *et al.* GERMINAL, a fuel performance code of the PLEIADES platform to simulate the in-pile behaviour of mixed oxide fuel pins for sodium-cooled fast reactors. *Journal of Nuclear Materials* **516,** 30–53 (Apr. 2019) (cit. on pp. x, 2).

13. Bernaud, S., Ramière, I., Latu, G. *et al.* PLEIADES: A numerical framework dedicated to the multiphysics and multiscale nuclear fuel behavior simulation. *Annals of Nuclear Energy* **205,** 110577 (Sept. 2024) (cit. on pp. x, 2).
14. Anisimov, V. I., Zaanen, J. & Andersen, O. K. Band theory and Mott insulators: Hubbard U instead of Stoner I. *Phys. Rev. B* **44,** 943–954 (July 1991) (cit. on pp. x, 4, 18).
15. Liechtenstein, A. I., Anisimov, V. I. & Zaanen, J. Density-functional theory and strong interactions: Orbital ordering in Mott-Hubbard insulators. *Phys. Rev. B* **52,** R5467–R5470 (Aug. 1995) (cit. on pp. x, 4, 18, 50).
16. Dudarev, S. L., Botton, G. A., Savrasov, S. Y. *et al.* Electron-energy-loss spectra and the structural stability of nickel oxide: An LSDA+U study. *Phys. Rev. B* **57,** 1505–1509 (Jan. 1998) (cit. on pp. x, 4, 18).
17. Dorado, B., Andersson, D. A., Stanek, C. R. *et al.* First-principles calculations of uranium diffusion in uranium dioxide. *Phys. Rev. B* **86,** 035110 (July 2012) (cit. on pp. x, xi, 4).
18. Jomard, G., Amadon, B., Bottin, F. *et al.* Structural, thermodynamic, and electronic properties of plutonium oxides from first principles. *Phys. Rev. B* **78,** 075125 (Aug. 2008) (cit. on pp. x, 4, 19, 20, 50).
19. Dorado, B. & Garcia, P. First-principles DFT+U modeling of actinide-based alloys: Application to paramagnetic phases of UO_2 and (U,Pu) mixed oxides. *Phys. Rev. B* **87,** 195139 (May 2013) (cit. on pp. xi, 4, 20, 50, 51).
20. Vathonne, E., Wiktor, J., Freyss, M. *et al.* DFT + U investigation of charged point defects and clusters in UO2. *J. Phys.: Condens. Matter* **26,** 325501 (July 2014) (cit. on pp. xi, 4, 51).
21. Andersson, D. A., Garcia, P., Liu, X. .-. *et al.* Atomistic modeling of intrinsic and radiation-enhanced fission gas (Xe) diffusion in $UO_{2\pm x}$: Implications for nuclear fuel performance modeling. *Journal of Nuclear Materials* **451,** 225–242 (Aug. 2014) (cit. on pp. xi, 4, 103).
22. Maillard, S., Andersson, D., Freyss, M. *et al.* Assessment of atomistic data for predicting the phase diagram and defect thermodynamics. The example of non-stoichiometric uranium dioxide. *Journal of Nuclear Materials* **569,** 153864 (Oct. 2022) (cit. on pp. xi, 4).
23. Dorado, B., Freyss, M., Amadon, B. *et al.* Advances in first-principles modelling of point defects in UO2: f electron correlations and the issue of local energy minima. *J. Phys.: Condens. Matter* **25,** 333201 (July 2013) (cit. on pp. xi, 4).
24. Burr, P. A. & Cooper, M. W. D. Importance of elastic finite-size effects: Neutral defects in ionic compounds. *Phys. Rev. B* **96,** 094107 (Sept. 2017) (cit. on pp. xi, xii, 4, 5, 75).
25. Bathellier, D., Messina, L., Freyss, M. *et al.* Effect of cationic chemical disorder on defect formation energies in uranium–plutonium mixed oxides. *Journal of Applied Physics* **132,** 175103 (Nov. 2022) (cit. on pp. xi, 4, 5).

26. Castellano, A., Bottin, F., Bouchet, J. *et al. Ab* initio canonical sampling based on variational inference. *Phys. Rev. B* **106,** L161110 (Oct. 2022) (cit. on pp. xi, 5, 58, 73, 74, 99, 100).
27. Buckingham, R. A. & Lennard-Jones, J. E. The classical equation of state of gaseous helium, neon and argon. *Proceedings of the Royal Society of London. Series A. Mathematical and Physical Sciences* **168,** 264–283 (Jan. 1997) (cit. on pp. xii, 5, 22).
28. Potashnikov, S. I., Boyarchenkov, A. S., Nekrasov, K. A. *et al.* High-precision molecular dynamics simulation of UO2–PuO2: Pair potentials comparison in UO2. *Journal of Nuclear Materials* **419,** 217–225 (Dec. 2011) (cit. on pp. xii, 5, 25).
29. Morelon, N.-D., Ghaleb, D., Delaye, J.-M. *et al.* A new empirical potential for simulating the formation of defects and their mobility in uranium dioxide. *Philosophical Magazine* **83,** 1533–1555 (Jan. 2003) (cit. on pp. xii, 5, 25, 122).
30. Basak, C. B., Sengupta, A. K. & Kamath, H. S. Classical molecular dynamics simulation of UO2 to predict thermophysical properties. *Journal of Alloys and Compounds* **360,** 210–216 (Oct. 2003) (cit. on pp. xii, 5).
31. Basak, C. B. & Kolokol, A. S. A Novel Pseudo-Ion Approach in Classical MD Simulation: A Case Study on (U0.8Pu0.2)O2 Mixed Oxide. *Journal of the American Ceramic Society* **95,** 1435–1439 (2012) (cit. on pp. xii, 5, 25).
32. Yakub, E., Ronchi, C. & Staicu, D. Molecular dynamics simulation of premelting and melting phase transitions in stoichiometric uranium dioxide. *The Journal of Chemical Physics* **127,** 094508 (Sept. 2007) (cit. on pp. xii, 5).
33. Murphy, S. T., Chartier, A., Van Brutzel, L. *et al.* Free energy of Xe incorporation at point defects and in nanovoids and bubbles in UO_2. *Phys. Rev. B* **85,** 144102 (Apr. 2012) (cit. on pp. xii, 5, 103).
34. Van Brutzel, L. & Rarivomanantsoa, M. Molecular dynamics simulation study of primary damage in UO2 produced by cascade overlaps. *Journal of Nuclear Materials* **358,** 209–216 (Nov. 2006) (cit. on pp. xii, 5, 21).
35. Fossati, P., Van Brutzel, L. & Devincre, B. Molecular dynamics simulation of dislocations in uranium dioxide. *Journal of Nuclear Materials* **443,** 359–365 (Nov. 2013) (cit. on pp. xii, 5, 75).
36. Brutzel, L. V. & Vincent-Aublant, E. Grain boundary influence on displacement cascades in UO2: A molecular dynamics study. *Journal of Nuclear Materials* **377,** 522–527 (July 2008) (cit. on pp. xii, 5).
37. Daw, M. S. & Baskes, M. I. Embedded-atom method: Derivation and application to impurities, surfaces, and other defects in metals. *Phys. Rev. B* **29,** 6443–6453 (June 1984) (cit. on pp. xii, 5, 23, 54).
38. Cooper, M. W. D., Rushton, M. J. D. & Grimes, R. W. A many-body potential approach to modelling the thermomechanical properties of actinide oxides. *J. Phys.: Condens. Matter* **26,** 105401 (Feb. 2014) (cit. on pp. xii, 5, 25).

39. Govers, K., Lemehov, S., Hou, M. *et al.* Comparison of interatomic potentials for UO2. Part I: Static calculations. *Journal of Nuclear Materials* **366,** 161–177 (June 2007) (cit. on pp. xii, 5, 26).

40. Zhang, Y., Millett, P. C., Tonks, M. R. *et al.* Molecular dynamics simulations of intergranular fracture in UO2 with nine empirical interatomic potentials. *Journal of Nuclear Materials* **452,** 296–303 (Sept. 2014) (cit. on pp. xii, 5).

41. Bathellier, D., Lainet, M., Freyss, M. *et al.* A new heat capacity law for UO2, PuO2 and (U,Pu)O2 derived from molecular dynamics simulations and useable in fuel performance codes. *Journal of Nuclear Materials* **549,** 152877 (June 2021) (cit. on pp. xii, 5).

42. Bourasseau, E., Onofri, C., Ksibi, A. *et al.* Atomic structure of grain boundaries in UO2 Bicrystals: A coupled high resolution transmission electron Microscopy/Atomistic simulation approach. *Scripta Materialia* **206,** 114191 (Jan. 2022) (cit. on pp. xii, 3, 5, 21).

43. Balboa, H., Van Brutzel, L., Chartier, A. *et al.* Assessment of empirical potential for MOX nuclear fuels and thermomechanical properties. *Journal of Nuclear Materials* **495,** 67–77 (Nov. 2017) (cit. on pp. xii, 26, 27, 75, 113).

44. Torres, E., CheikNjifon, I., Kaloni, T. P. *et al.* A comparative analysis of the phonon properties in UO2 using the Boltzmann transport equation coupled with DFT + U and empirical potentials. *Computational Materials Science* **177,** 109594 (May 2020) (cit. on pp. xii, 5, 26).

45. Jin, M., Khafizov, M., Jiang, C. *et al.* Assessment of empirical interatomic potential to predict thermal conductivity in ThO2 and UO2. *J. Phys.: Condens. Matter* **33,** 275402 (May 2021) (cit. on pp. xii, 5, 26, 28, 66, 67).

46. Brutzel, L. V., Fossati, P. & Chartier, A. Molecular dynamics simulations of microstructural evolution of irradiated (U,Pu)O2<math><msub is="true"><mrow is="true"></mrow><mn is="true">2</mn></msub></math> studied via simulated XRD patterns. *Journal of Nuclear Materials* **567,** 153834 (Aug. 2022) (cit. on pp. xii, 5).

47. Skelton, R. & Walker, A. M. Peierls-Nabarro modeling of dislocations in UO2. *Journal of Nuclear Materials* **495,** 202–210 (Nov. 2017) (cit. on pp. xii, 5, 26, 75, 77).

48. Zuo, Y., Chen, C., Li, X. *et al.* Performance and Cost Assessment of Machine Learning Interatomic Potentials. *J. Phys. Chem. A* **124,** 731–745 (Jan. 2020) (cit. on pp. xiii, 6, 30, 53, 54).

49. Yang, X., Tiwari, J. & Feng, T. Reduced anharmonic phonon scattering cross-section slows the decrease of thermal conductivity with temperature. *Materials Today Physics* **24,** 100689 (May 2022) (cit. on pp. xiii, 6, 51).

50. Kobayashi, K., Okumura, M., Nakamura, H. *et al.* Machine learning molecular dynamics simulations toward exploration of high-temperature properties of nuclear fuel materials: case study of thorium dioxide. *Sci Rep* **12,** 9808 (June 2022) (cit. on pp. xiii, 6).

51. Fossati, P. C. M., Chartier, A. & Boulle, A. Structural Aspects of the Superionic Transition in AX2 Compounds With the Fluorite Structure. *Front. Chem.* **9** (Oct. 2021) (cit. on pp. xiii, 85, 133).
52. Hiernaut, J. P., Hyland, G. J. & Ronchi, C. Premelting transition in uranium dioxide. *Int J Thermophys* **14,** 609–612 (May 1993) (cit. on pp. xiii, 26, 69, 85, 133).
53. Fink, J. K. Thermophysical properties of uranium dioxide. *Journal of Nuclear Materials* **279,** 1–18 (Mar. 2000) (cit. on pp. xiv, 68, 69, 96–98).
54. Desgranges, L. & Baldinozzi, G. *How to Figure Out Local Order Against Average Order in UO2?* in *TMS 2023 Annual Meeting & Exhibition* (Mar. 2023) (cit. on pp. 2, 90).
55. Sizmann, R. The effect of radiation upon diffusion in metals. *Journal of Nuclear Materials* **69-70,** 386–412 (Feb. 1978) (cit. on pp. 2, 123).
56. Sonoda, T., Kinoshita, M., Ray, I. L. F. *et al.* Transmission electron microscopy observation on irradiation-induced microstructural evolution in high burn-up UO2 disk fuel. *Nuclear Instruments and Methods in Physics Research Section B: Beam Interactions with Materials and Atoms* **191,** 622–628 (May 2002) (cit. on pp. 2, 4).
57. Nogita, K., Hayashi, K., Une, K. *et al.* Depth profiles of damage accumulation in UO2 and (U,Gd)O2 pellets irradiated with 100 MeV iodine ions. *Journal of Nuclear Materials* **273,** 302–309 (Aug. 1999) (cit. on p. 3).
58. Bengtsson, S. *IAEA-TECDOC* tech. rep. 1036 (1998), 177 (cit. on p. 3).
59. Chartier, A., Onofri, C., Van Brutzel, L. *et al.* Early stages of irradiation induced dislocations in urania. *Applied Physics Letters* **109,** 181902 (Nov. 2016) (cit. on pp. 3, 21, 122, 123).
60. Cooper, M. W. D. Ceramic nuclear fuel performance and the role of atomic scale simulations. *Journal of Nuclear Materials* **561,** 153531 (Apr. 2022) (cit. on p. 3).
61. Pegg, J. T., Aparicio-Anglès, X., Storr, M. *et al.* DFT+U study of the structures and properties of the actinide dioxides. *Journal of Nuclear Materials* **492,** 269–278 (Aug. 2017) (cit. on pp. 6, 20, 88, 91).
62. Pegg, J. T., Shields, A. E., Storr, M. T. *et al.* Magnetic structure of UO ₂ and NpO ₂ by first-principle methods. *Phys. Chem. Chem. Phys.* **21,** 760–771 (2019) (cit. on pp. 6, 20, 88, 91).
63. Zhou, S., Ma, H., Xiao, E. *et al.* Capturing the ground state of uranium dioxide from first principles: Crystal distortion, magnetic structure, and phonons. *Phys. Rev. B* **106,** 125134 (Sept. 2022) (cit. on pp. 6, 20, 52, 88).
64. Lafourcade, P. *Multiscale Modeling of the Mechanical Behavior of an Energetic Material: TATB* PhD thesis () (cit. on p. 7).

65. Lafourcade, P., Maillet, J.-B., Bruzy, N. *et al.* Molecular dynamics informed calibration of crystal plasticity critical shear stresses for the mesoscopic mechanical modeling of 1,3,5-triamino-2,4,6-trinitrobenzene (TATB) single crystal. *Journal of Applied Physics* **135,** 075901 (Feb. 2024) (cit. on pp. 7, 21).

66. Gear, C. W. *THE NUMERICAL INTEGRATION OF ORDINARY DIFFERENTIAL EQUATIONS OF VARIOUS ORDERS* tech. rep. ANL-7126 (Argonne National Lab., Ill., Jan. 1966) (cit. on p. 11).

67. Butcher, J. C. *Runge–Kutta Methods for Ordinary Differential Equations* in *Numerical Analysis and Optimization* (eds Al-Baali, M., Grandinetti, L. & Purnama, A.) (Springer International Publishing, Cham, 2015), 37–58 (cit. on p. 11).

68. Butcher, J. C. A history of Runge-Kutta methods. *Applied Numerical Mathematics* **20,** 247–260 (Mar. 1996) (cit. on p. 11).

69. Runge, C. Ueber die numerische Auflösung von Differentialgleichungen. *Math. Ann.* **46,** 167–178 (June 1895) (cit. on p. 11).

70. Verlet, L. Computer "Experiments" on Classical Fluids. I. Thermodynamical Properties of Lennard-Jones Molecules. *Phys. Rev.* **159,** 98–103 (July 1967) (cit. on p. 11).

71. Fraige, F. Y. & Langston, P. A. Integration schemes and damping algorithms in distinct element models. *Advanced Powder Technology* **15,** 227–245 (Jan. 2004) (cit. on p. 11).

72. Verlet, L. Computer "Experiments" on Classical Fluids. II. Equilibrium Correlation Functions. *Phys. Rev.* **165,** 201–214 (Jan. 1968) (cit. on p. 11).

73. Andersen, H. C. Molecular dynamics simulations at constant pressure and/or temperature. *The Journal of Chemical Physics* **72,** 2384–2393 (Feb. 1980) (cit. on p. 12).

74. Berendsen, H. J. C., Postma, J. P. M., van Gunsteren, W. F. *et al.* Molecular dynamics with coupling to an external bath. *The Journal of Chemical Physics* **81,** 3684–3690 (Oct. 1984) (cit. on p. 12).

75. Bussi, G., Donadio, D. & Parrinello, M. Canonical sampling through velocity rescaling. *J Chem Phys* **126,** 014101 (Jan. 2007) (cit. on p. 12).

76. Van Gunsteren, W. F. & Berendsen, H. J. C. A Leap-frog Algorithm for Stochastic Dynamics. *Molecular Simulation* **1,** 173–185 (Mar. 1988) (cit. on p. 12).

77. Schneider, T. & Stoll, E. Molecular-dynamics study of a three-dimensional one-component model for distortive phase transitions. *Phys. Rev. B* **17,** 1302–1322 (Feb. 1978) (cit. on p. 12).

78. Nosé, S. A unified formulation of the constant temperature molecular dynamics methods. *The Journal of Chemical Physics* **81,** 511–519 (July 1984) (cit. on p. 12).

79. Hoover, W. G. Canonical dynamics: Equilibrium phase-space distributions. *Phys. Rev. A* **31,** 1695–1697 (Mar. 1985) (cit. on p. 12).

80. Parrinello, M. & Rahman, A. Polymorphic transitions in single crystals: A new molecular dynamics method. *Journal of Applied Physics* **52,** 7182–7190 (Dec. 1981) (cit. on p. 12).

81. Basconi, J. E. & Shirts, M. R. Effects of Temperature Control Algorithms on Transport Properties and Kinetics in Molecular Dynamics Simulations. *J. Chem. Theory Comput.* **9,** 2887–2899 (July 2013) (cit. on p. 12).

82. Ke, Q., Gong, X., Liao, S. *et al.* Effects of thermostats/barostats on physical properties of liquids by molecular dynamics simulations. *Journal of Molecular Liquids* **365,** 120116 (Nov. 2022) (cit. on p. 12).

83. Thompson, A. P., Aktulga, H. M., Berger, R. *et al.* LAMMPS - a flexible simulation tool for particle-based materials modeling at the atomic, meso, and continuum scales. *Computer Physics Communications* **271,** 108171 (Feb. 2022) (cit. on pp. 12, 24, 54, 55, 58).

84. Schrödinger, E. An Undulatory Theory of the Mechanics of Atoms and Molecules. *Phys. Rev.* **28,** 1049–1070 (Dec. 1926) (cit. on p. 12).

85. Born, M. & Oppenheimer, R. Zur Quantentheorie der Molekeln. *Annalen der Physik* **389,** 457–484 (1927) (cit. on p. 13).

86. Hartree, D. R. & Hartree, W. Self-consistent field, with exchange, for beryllium. *Proceedings of the Royal Society of London. Series A - Mathematical and Physical Sciences* **150,** 9–33 (Jan. 1997) (cit. on p. 14).

87. Fock, V. Näherungsmethode zur Lösung des quantenmechanischen Mehrkörperproblems. *Z. Physik* **61,** 126–148 (Jan. 1930) (cit. on p. 14).

88. Møller, C. & Plesset, M. S. Note on an Approximation Treatment for Many-Electron Systems. *Phys. Rev.* **46,** 618–622 (Oct. 1934) (cit. on p. 14).

89. Raghavachari, K., Trucks, G. W., Pople, J. A. *et al.* A fifth-order perturbation comparison of electron correlation theories. *Chemical Physics Letters* **157,** 479–483 (May 1989) (cit. on p. 14).

90. Slater, J. C. The Theory of Complex Spectra. *Phys. Rev.* **34,** 1293–1322 (Nov. 1929) (cit. on p. 14).

91. Echenique, P. & Alonso, J. L. A mathematical and computational review of Hartree–Fock SCF methods in quantum chemistry. *Molecular Physics* **105,** 3057–3098 (Dec. 2007) (cit. on p. 14).

92. Hohenberg, P. & Kohn, W. Inhomogeneous Electron Gas. *Phys. Rev.* **136,** B864–B871 (Nov. 1964) (cit. on p. 14).

93. Kohn, W. & Sham, L. J. Self-Consistent Equations Including Exchange and Correlation Effects. *Phys. Rev.* **140,** A1133–A1138 (Nov. 1965) (cit. on pp. 15, 17).

94. Langreth, D. C. & Mehl, M. J. Beyond the local-density approximation in calculations of ground-state electronic properties. *Phys. Rev. B* **28,** 1809–1834 (Aug. 1983) (cit. on p. 17).

95. Becke, A. D. Density-functional exchange-energy approximation with correct asymptotic behavior. *Phys. Rev. A* **38,** 3098–3100 (Sept. 1988) (cit. on p. 17).

96. Barth, U. v. & Hedin, L. A local exchange-correlation potential for the spin polarized case. i. *J. Phys. C: Solid State Phys.* **5,** 1629 (July 1972) (cit. on p. 17).

97. Rajagopal, A. K. & Callaway, J. Inhomogeneous Electron Gas. *Phys. Rev. B* **7,** 1912–1919 (Mar. 1973) (cit. on p. 17).

98. Perdew, J. P. & Zunger, A. Self-interaction correction to density-functional approximations for many-electron systems. *Phys. Rev. B* **23,** 5048–5079 (May 1981) (cit. on pp. 17, 18).

99. Herman, F., Van Dyke, J. P. & Ortenburger, I. B. Improved Statistical Exchange Approximation for Inhomogeneous Many-Electron Systems. *Phys. Rev. Lett.* **22,** 807–811 (Apr. 1969) (cit. on p. 17).

100. Herman, F., Ortenburger, I. B. & Van Dyke, J. P. A method for improving the physical realism of first-principles band structure calculations. *International Journal of Quantum Chemistry* **4,** 827–846 (1969) (cit. on p. 17).

101. Perdew, J. P., Chevary, J. A., Vosko, S. H. *et al.* Atoms, molecules, solids, and surfaces: Applications of the generalized gradient approximation for exchange and correlation. *Phys. Rev. B* **46,** 6671–6687 (Sept. 1992) (cit. on p. 17).

102. Perdew, J. P., Chevary, J. A., Vosko, S. H. *et al.* Erratum: Atoms, molecules, solids, and surfaces: Applications of the generalized gradient approximation for exchange and correlation. *Phys. Rev. B* **48,** 4978–4978 (Aug. 1993) (cit. on p. 17).

103. Armiento, R. & Mattsson, A. E. Functional designed to include surface effects in self-consistent density functional theory. *Phys. Rev. B* **72,** 085108 (Aug. 2005) (cit. on p. 17).

104. Mattsson, A. E., Armiento, R., Paier, J. *et al.* The AM05 density functional applied to solids. *The Journal of Chemical Physics* **128,** 084714 (Feb. 2008) (cit. on p. 17).

105. Becke, A. D. Density functional calculations of molecular bond energies. *The Journal of Chemical Physics* **84,** 4524–4529 (Apr. 1986) (cit. on p. 17).

106. Tsuneda, T., Suzumura, T. & Hirao, K. A reexamination of exchange energy functionals. *The Journal of Chemical Physics* **111,** 5656–5667 (Oct. 1999) (cit. on p. 17).

107. Hamprecht, F. A., Cohen, A. J., Tozer, D. J. *et al.* Development and assessment of new exchange-correlation functionals. *The Journal of Chemical Physics* **109,** 6264–6271 (Oct. 1998) (cit. on p. 17).

108. Hammer, B., Hansen, L. B. & Nørskov, J. K. Improved adsorption energetics within density-functional theory using revised Perdew-Burke-Ernzerhof functionals. *Phys. Rev. B* **59,** 7413–7421 (Mar. 1999) (cit. on p. 17).

109. Zhang, Y. & Yang, W. Comment on "Generalized Gradient Approximation Made Simple". *Phys. Rev. Lett.* **80,** 890–890 (Jan. 1998) (cit. on p. 17).

110. Perdew, J. P. & Wang, Y. Accurate and simple analytic representation of the electron-gas correlation energy. *Phys. Rev. B* **45,** 13244–13249 (June 1992) (cit. on p. 17).

111. Perdew, J. P., Burke, K. & Ernzerhof, M. Generalized gradient approximation made simple. *Phys. Rev. Lett.* **77,** 3865–3868 (Oct. 1996) (cit. on pp. 17, 50).

112. Perdew, J. P., Ruzsinszky, A., Csonka, G. I. *et al.* Restoring the Density-Gradient Expansion for Exchange in Solids and Surfaces. *Phys. Rev. Lett.* **100,** 136406 (Apr. 2008) (cit. on pp. 17, 88).

113. Schoenes, J. Optical properties and electronic structure of UO2. *Journal of Applied Physics* **49,** 1463–1465 (Mar. 1978) (cit. on p. 17).

114. McNeilly, C. E. The electrical properties of plutonium oxides. *Journal of Nuclear Materials* **11,** 53–58 (Jan. 1964) (cit. on p. 17).

115. Butterfield, M. T., Durakiewicz, T., Guziewicz, E. *et al.* Photoemission of surface oxides and hydrides of delta plutonium. *Surface Science* **571,** 74–82 (Nov. 2004) (cit. on p. 17).

116. Becke, A. D. A new mixing of Hartree–Fock and local density-functional theories. *The Journal of Chemical Physics* **98,** 1372–1377 (Jan. 1993) (cit. on p. 17).

117. Adamo, C. & Barone, V. Toward reliable density functional methods without adjustable parameters: The PBE0 model. *The Journal of Chemical Physics* **110,** 6158–6170 (Apr. 1999) (cit. on p. 17).

118. Heyd, J., Scuseria, G. E. & Ernzerhof, M. Hybrid functionals based on a screened Coulomb potential. *The Journal of Chemical Physics* **118,** 8207–8215 (May 2003) (cit. on p. 17).

119. Heyd, J., Scuseria, G. E. & Ernzerhof, M. Erratum: "Hybrid functionals based on a screened Coulomb potential" [J. Chem. Phys. 118, 8207 (2003)]. *The Journal of Chemical Physics* **124,** 219906 (June 2006) (cit. on p. 17).

120. Georges, A., Kotliar, G., Krauth, W. *et al.* Dynamical mean-field theory of strongly correlated fermion systems and the limit of infinite dimensions. *Rev. Mod. Phys.* **68,** 13–125 (Jan. 1996) (cit. on p. 18).

121. Kotliar, G., Savrasov, S. Y., Haule, K. *et al.* Electronic structure calculations with dynamical mean-field theory. *Rev. Mod. Phys.* **78,** 865–951 (Aug. 2006) (cit. on p. 18).

122. Anisimov, V. I. & Gunnarsson, O. Density-functional calculation of effective Coulomb interactions in metals. *Phys. Rev. B* **43,** 7570–7574 (Apr. 1991) (cit. on p. 18).

123. Anisimov, V. I., Poteryaev, A. I., Korotin, M. A. *et al.* First-principles calculations of the electronic structure and spectra of strongly correlated systems: dynamical mean-field theory. *J. Phys.: Condens. Matter* **9,** 7359 (Sept. 1997) (cit. on p. 18).

124. Gebhardt, J. & Elsässer, C. DFT with corrections for an efficient and accurate description of strong electron correlations in NiO. *J. Phys.: Condens. Matter* **35,** 205901 (Mar. 2023) (cit. on p. 18).

125. DelloStritto, M. J., Kaplan, A. D., Perdew, J. P. *et al.* Predicting the properties of NiO with density functional theory: Impact of exchange and correlation approximations and validation of the r2SCAN functional. *APL Materials* **11,** 060702 (June 2023) (cit. on p. 18).

126. Hosseini, S. V., Abbasnejad, M. & Mohammadizadeh, M. R. Ab initio study of Raman modes and thermodynamic properties of TinO2n-1. *Journal of Applied Physics* **133,** 175103 (May 2023) (cit. on p. 18).

127. Zhang, S., Vo, H. & Galli, G. Predicting the Onset of Metal-Insulator Transitions in Transition Metal Oxideds-A First Step in Designing Neuromorphic Devices. *Chem. Mater.* **33,** 3187–3195 (May 2021) (cit. on p. 18).

128. Zhou, J.-J., Park, J., Timrov, I. *et al.* Ab Initio Electron-Phonon Interactions in Correlated Electron Systems. *Phys. Rev. Lett.* **127,** 126404 (Sept. 2021) (cit. on p. 18).

129. Sale, M., Xia, Q., Avdeev, M. *et al.* Crystal and Magnetic Structures of Melilite-Type Ba2MnSi2O7. *Inorg. Chem.* **58,** 4164–4172 (Apr. 2019) (cit. on p. 18).

130. Czyżyk, M. T. & Sawatzky, G. A. Local-density functional and on-site correlations: The electronic structure of La_2CuO_4 and $LaCuO_3$. *Phys. Rev. B* **49,** 14211–14228 (May 1994) (cit. on p. 18).

131. *The* `ABINIT` *code is a common project of the Catholic University of Louvain (Belgium), Corning Incorporated, CEA (France) and other collaborators (URL http://www.abinit.org).* (cit. on pp. 18, 50).

132. Romero, A. H., Allan, D. C., Amadon, B. *et al.* ABINIT: Overview and focus on selected capabilities. *The Journal of Chemical Physics* **152,** 124102 (Mar. 2020) (cit. on pp. 18, 50).

133. Gonze, X., Amadon, B., Antonius, G. *et al.* The Abinitproject: Impact, environment and recent developments. *Computer Physics Communications* **248,** 107042 (Mar. 2020) (cit. on pp. 18, 50).

134. Meredig, B., Thompson, A., Hansen, H. A. *et al.* Method for locating low-energy solutions within DFT + U. *Phys. Rev. B* **82,** 195128 (Nov. 2010) (cit. on p. 19).

135. Geng, H. Y., Chen, Y., Kaneta, Y. *et al.* Interplay of defect cluster and the stability of xenon in uranium dioxide from density functional calculations. *Phys. Rev. B* **82,** 094106 (Sept. 2010) (cit. on p. 19).

136. Amadon, B., Jollet, F. & Torrent, M. γ and β cerium: LDA + U calculations of ground-state parameters. *Phys. Rev. B* **77,** 155104 (Apr. 2008) (cit. on p. 19).

137. Dorado, B. *Etude des propriétés de transport atomique dans le dioxyde d'uranium par le calcul de structure électronique : influence des fortes corrélations* These de doctorat (Aix-Marseille 2, Sept. 2010) (cit. on pp. 19, 20, 50).

138. Talla Noutack, M. S., Geneste, G., Jomard, G. *et al.* First-principles investigation of the bulk properties of americium dioxide and sesquioxides. *Phys. Rev. Mater.* **3,** 035001 (Mar. 2019) (cit. on pp. 19, 20).

139. Ratcliff, L. E., Genovese, L., Park, H. *et al.* Exploring metastable states in UO2 using hybrid functionals and dynamical mean field theory. *J. Phys.: Condens. Matter* **34,** 094003 (Dec. 2021) (cit. on p. 19).

140. Teli, N. A. & Sirajuddeen, M. M. S. Investigation of half-metallic ferromagnetism in hafnium and tantalum doped NiO for spintronic applications: A DFT study. *Current Applied Physics* **19,** 357–362 (Apr. 2019) (cit. on p. 20).

141. Miwa, K. Prediction of Raman spectra with DFT+U method. *Phys. Rev. B* **97,** 075143 (Feb. 2018) (cit. on p. 20).

142. Waller, O., Piekarz, P., Bosak, A. *et al.* Lattice dynamics of neodymium: Influence of $4f$ electron correlations. *Phys. Rev. B* **94,** 014303 (July 2016) (cit. on p. 20).

143. Xu, Z., Joshi, Y. V., Raman, S. *et al.* Accurate electronic and chemical properties of 3d transition metal oxides using a calculated linear response U and a DFT + U(V) method. *J. Chem. Phys.* **142** (Apr. 2015) (cit. on p. 20).

144. Willett-Gies, T. I., Nelson, C. M., Abdallah, L. S. *et al.* Two-phonon absorption in LiF and NiO from infrared ellipsometry. *Journal of Vacuum Science & Technology A* **33,** 061202 (July 2015) (cit. on p. 20).

145. Wang, Y., Zhang, L. A., Shang, S. *et al.* Accurate calculations of phonon dispersion in CaF_2 and CeO_2. *Phys. Rev. B* **88,** 024304 (July 2013) (cit. on p. 20).

146. Himmetoglu, B., Katukuri, V. M. & Cococcioni, M. Origin of magnetic interactions and their influence on the structural properties of Ni2MnGa and related compounds. *J. Phys.: Condens. Matter* **24,** 185501 (Apr. 2012) (cit. on p. 20).

147. Car, R. & Parrinello, M. Unified Approach for Molecular Dynamics and Density-Functional Theory. *Phys. Rev. Lett.* **55,** 2471–2474 (Nov. 1985) (cit. on p. 20).

148. Govers, K., Lemehov, S., Hou, M. *et al.* Molecular dynamics simulation of helium and oxygen diffusion in $UO_2 \pm x$. *Journal of Nuclear Materials* **395,** 131–139 (Dec. 2009) (cit. on p. 21).

149. Govers, K., Bishop, C. L., Parfitt, D. C. *et al.* Molecular dynamics study of Xe bubble re-solution in UO2. *Journal of Nuclear Materials* **420,** 282–290 (Jan. 2012) (cit. on pp. 21, 103).

150. Liu, X. .-. & Andersson, D. A. Molecular dynamics study of fission gas bubble nucleation in UO2. *Journal of Nuclear Materials* **462,** 8–14 (July 2015) (cit. on pp. 21, 103).

151. Beigbeder, T., Bourasseau, E. & Rushton, M. Thermophysical properties of liquid (U, Zr)O2 by molecular dynamics. *Molecular Simulation* **47,** 1502–1508 (Dec. 2021) (cit. on p. 21).

152. Tchipev, N., Seckler, S., Heinen, M. *et al.* TweTriS: Twenty trillion-atom simulation (Jan. 2019) (cit. on p. 21).

153. Germann, T. C. & Kadau, K. Trillion-atom molecular dynamics becomes a reality. *Int. J. Mod. Phys. C* **19,** 1315–1319 (Sept. 2008) (cit. on p. 21).

154. Li, S., Wu, B., Zhang, Y. *et al. Massively Scaling the Metal Microscopic Damage Simulation on Sunway TaihuLight Supercomputer* in *Proceedings of the 47th International Conference on Parallel Processing* (Association for Computing Machinery, New York, NY, USA, Aug. 2018), 1–11 (cit. on p. 21).

155. Shaw, D. E., Adams, P. J., Azaria, A. *et al. Anton 3: twenty microseconds of molecular dynamics simulation before lunch* in *Proceedings of the International Conference for High Performance Computing, Networking, Storage and Analysis* (Association for Computing Machinery, New York, NY, USA, Nov. 2021), 1–11 (cit. on p. 21).

156. Jones, J. E. & Chapman, S. On the determination of molecular fields. —II. From the equation of state of a gas. *Proceedings of the Royal Society of London. Series A, Containing Papers of a Mathematical and Physical Character* **106,** 463–477 (Jan. 1997) (cit. on p. 21).

157. Abrahamson, A. A. Born-Mayer-Type Interatomic Potential for Neutral Ground-State Atoms with $Z = 2$ to $Z = 105$. *Phys. Rev.* **178,** 76–79 (Feb. 1969) (cit. on p. 22).

158. Morse, P. M. Diatomic Molecules According to the Wave Mechanics. II. Vibrational Levels. *Phys. Rev.* **34,** 57–64 (July 1929) (cit. on p. 22).

159. Ziegler, J. F. & Biersack, J. P. in *Treatise on Heavy-Ion Science: Volume 6: Astrophysics, Chemistry, and Condensed Matter* (ed Bromley, D. A.) 93–129 (Springer US, Boston, MA, 1985) (cit. on pp. 22, 52).

160. Baskes, M. I. Application of the Embedded-Atom Method to Covalent Materials: A Semiempirical Potential for Silicon. *Phys. Rev. Lett.* **59,** 2666–2669 (Dec. 1987) (cit. on p. 23).

161. Baskes, M. I. Modified embedded-atom potentials for cubic materials and impurities. *Phys. Rev. B* **46,** 2727–2742 (Aug. 1992) (cit. on pp. 23, 54).

162. Baskes, M. I., Srinivasan, S. G., Valone, S. M. *et al.* Multistate modified embedded atom method. *Phys. Rev. B* **75,** 094113 (Mar. 2007) (cit. on p. 23).

163. Tersoff, J. New empirical approach for the structure and energy of covalent systems. *Phys. Rev. B* **37,** 6991–7000 (Apr. 1988) (cit. on p. 23).

164. Axilrod, B. M. & Teller, E. Interaction of the van der Waals Type Between Three Atoms. *The Journal of Chemical Physics* **11,** 299–300 (June 1943) (cit. on p. 23).

165. Muto, Y. Force between nonpolar molecules. *J. Phys. Math. Soc. Jpn* **17,** 629–631 (1943) (cit. on p. 23).

166. Moriarty, J. A. Angular forces and melting in bcc transition metals: A case study of molybdenum. *Phys. Rev. B* **49,** 12431–12445 (May 1994) (cit. on p. 23).

167. Moriarty, J. A. Density-functional formulation of the generalized pseudopotential theory. III. Transition-metal interatomic potentials. *Phys. Rev. B* **38,** 3199–3231 (Aug. 1988) (cit. on p. 23).

168. Moriarty, J. A., Benedict, L. X., Glosli, J. N. *et al.* Robust quantum-based interatomic potentials for multiscale modeling in transition metals. *Journal of Materials Research* **21,** 563–573 (Mar. 2006) (cit. on p. 23).

169. Carrard, T., Prat, R., Latu, G. *et al. ExaNBody: A HPC Framework for N-Body Applications* in *Euro-Par 2023: Parallel Processing Workshops* (eds Zeinalipour, D., Blanco Heras, D., Pallis, G. *et al.*) (Springer Nature Switzerland, Cham, 2024), 342–354 (cit. on p. 24).

170. André, R. F., Meyniel, L. & Carenco, S. Nickel carbide (Ni3C) nanoparticles for catalytic hydrogenation of model compounds in solvent. *Catal. Sci. Technol.* **12,** 4572–4583 (July 2022) (cit. on p. 24).

171. Portehault, D., Delacroix, S., Gouget, G. *et al.* Beyond the Compositional Threshold of Nanoparticle-Based Materials. *Acc. Chem. Res.* **51,** 930–939 (Apr. 2018) (cit. on p. 24).

172. Matar, S. F. First-principles investigations of the electronic and magnetic structures and the bonding properties of uranium nitride fluoride (UNF). *Zeitschrift für Naturforschung B* **72,** 725–730 (Oct. 2017) (cit. on p. 24).

173. Hockney, R. W. & Eastwood, J. W. *Computer simulation using particles* (Jan. 1988) (cit. on p. 24).

174. Pollock, E. L. & Glosli, J. Comments on P3M, FMM, and the Ewald method for large periodic Coulombic systems. *Computer Physics Communications* **95,** 93–110 (June 1996) (cit. on p. 24).

175. Wolf, D., Keblinski, P., Phillpot, S. R. *et al.* Exact method for the simulation of Coulombic systems by spherically truncated, pairwise r-1 summation. *The Journal of Chemical Physics* **110,** 8254–8282 (May 1999) (cit. on p. 24).

176. Fennell, C. J. & Gezelter, J. D. Is the Ewald summation still necessary? Pairwise alternatives to the accepted standard for long-range electrostatics. *J Chem Phys* **124,** 234104 (June 2006) (cit. on p. 24).

177. Dick, B. G. & Overhauser, A. W. Theory of the Dielectric Constants of Alkali Halide Crystals. *Phys. Rev.* **112,** 90–103 (Oct. 1958) (cit. on p. 25).

178. Lindan, P. J. D. & Gillan, M. J. The dynamical simulation of superionic UO2 using shell-model potentials. *Philosophical Magazine B* **69,** 535–548 (Mar. 1994) (cit. on p. 25).

179. Rappe, A. K. & Goddard, W. A. I. Charge equilibration for molecular dynamics simulations. *J. Phys. Chem.* **95,** 3358–3363 (Apr. 1991) (cit. on p. 25).

180. Nakano, A. Parallel multilevel preconditioned conjugate-gradient approach to variable-charge molecular dynamics. *Computer Physics Communications* **104,** 59–69 (Aug. 1997) (cit. on p. 25).

181. Aktulga, H. M., Fogarty, J. C., Pandit, S. A. *et al.* Parallel reactive molecular dynamics: Numerical methods and algorithmic techniques. *Parallel Computing* **38,** 245–259 (Apr. 2012) (cit. on p. 25).

182. Chenoweth, K., van Duin, A. C. T. & Goddard, W. A. ReaxFF Reactive Force Field for Molecular Dynamics Simulations of Hydrocarbon Oxidation. *J. Phys. Chem. A* **112,** 1040–1053 (Feb. 2008) (cit. on p. 25).

183. Phillpot, S. R., Antony, A. C., Shi, L. *et al.* Charge Optimized Many Body (COMB) potentials for simulation of nuclear fuel and clad. *Computational Materials Science* **148,** 231–241 (June 2018) (cit. on pp. 25, 27).

184. Li, Y. A universal COMB potential for the whole composition range of the uranium-oxygen system. *Journal of Nuclear Materials* **513,** 102–119 (Jan. 2019) (cit. on p. 25).

185. Li, Y., Liang, T., Sinnott, S. B. *et al.* A charge-optimized many-body potential for the U–UO2–O2 system. *J. Phys.: Condens. Matter* **25,** 505401 (Nov. 2013) (cit. on pp. 25, 27).

186. Mbongo, D., Tétot, R., Ducher, R. *et al.* Improved SMTB-Q model applied to oxygen migration and pressure phase transitions in UO2. *J. Phys.: Condens. Matter* **32,** 095701 (Nov. 2019) (cit. on pp. 25, 27).

187. Sattonnay, G. & Tétot, R. Bulk, surface and point defect properties in UO2 from a tight-binding variable-charge model. *J. Phys.: Condens. Matter* **25,** 125403 (Feb. 2013) (cit. on pp. 25, 103, 104, 135).

188. Yamada, K., Kurosaki, K., Uno, M. *et al.* Evaluation of thermal properties of mixed oxide fuel by molecular dynamics. *Journal of Alloys and Compounds* **307,** 1–9 (July 2000) (cit. on p. 25).

189. Arima, T., Yamasaki, S., Inagaki, Y. *et al.* Evaluation of thermal conductivity of hypostoichiometric (U, Pu)O2-x solid solution by molecular dynamics simulation at temperatures up to 2000 K. *Journal of Alloys and Compounds* **415,** 43–50 (May 2006) (cit. on p. 25).

190. Potashnikov, S. I., Boyarchenkov, A. S., Nekrasov, K. A. *et al.* High-precision molecular dynamics simulation of UO2–PuO2: Anion self-diffusion in UO2. *Journal of Nuclear Materials* **433,** 215–226 (Feb. 2013) (cit. on p. 25).

191. Tiwary, P., van de Walle, A., Jeon, B. *et al.* Interatomic potentials for mixed oxide and advanced nuclear fuels. *Phys. Rev. B* **83,** 094104 (Mar. 2011) (cit. on p. 25).

192. Yakub, E., Ronchi, C. & Iosilevski, I. Thermodynamic model of solid non-stoichiometric uranium dioxide. *J. Phys.: Condens. Matter* **18,** 1227 (Jan. 2006) (cit. on pp. 25, 53).

193. Axe, J. D. Long-Wave Lattice Dynamics of the Fluorite Structure. *Phys. Rev.* **139,** A1215–A1220 (Aug. 1965) (cit. on p. 26).

194. Takoukam-Takoundjou, C., Bourasseau, E., Rushton, M. J. D. *et al.* Optimization of a new interatomic potential to investigate the thermodynamic properties of hypo-stoichiometric mixed oxide fuel U1-yPuyO2-x. *J. Phys.: Condens. Matter* **32,** 505702 (Sept. 2020) (cit. on p. 26).

195. Labonne, B., Orlat, S. & Bertolus, M. Development of an interatomic potential for mixed uranium-americium oxides and application to the determination of the structural and thermodynamic properties of (U,Am)O2 with americium contents below 50%. *Journal of Nuclear Materials* **579,** 154390 (June 2023) (cit. on p. 26).

196. Porto, G., Bouchet, J., Bathellier, D. *et al.* Thermodynamic and thermoelastic properties of hypostoichiometric MOX fuels with molecular dynamics simulations. *Journal of Nuclear Materials* **598,** 155163 (Sept. 2024) (cit. on p. 26).

197. Govers, K., Lemehov, S., Hou, M. *et al.* Comparison of interatomic potentials for UO2. *Journal of Nuclear Materials* **376,** 66–77 (May 2008) (cit. on p. 26).

198. Pang, J. W. L., Chernatynskiy, A., Larson, B. C. *et al.* Phonon density of states and anharmonicity of UO_2. *Phys. Rev. B* **89,** 115132 (Mar. 2014) (cit. on pp. 26, 28, 66).

199. Pang, J. W. L., Buyers, W. J. L., Chernatynskiy, A. *et al.* Phonon Lifetime Investigation of Anharmonicity and Thermal Conductivity of UO_2 by Neutron Scattering and Theory. *Phys. Rev. Lett.* **110,** 157401 (Apr. 2013) (cit. on pp. 26, 66–68, 98).

200. White, J. T. & Nelson, A. T. Thermal conductivity of UO2+x and U4O9-y. *Journal of Nuclear Materials* **443,** 342–350 (Nov. 2013) (cit. on p. 28).

201. Gofryk, K., Du, S., Stanek, C. R. *et al.* Anisotropic thermal conductivity in uranium dioxide. *Nat Commun* **5,** 4551 (Aug. 2014) (cit. on p. 28).

202. Huang, R., Sun, Y., Yang, Z. *et al.* A novel ReaxFF multi-scale method for analyzing the fracture behavior of the CeO2. *Computational Materials Science* **219,** 112002 (Feb. 2023) (cit. on p. 27).

203. Streitz, F. H. & Mintmire, J. W. Electrostatic potentials for metal-oxide surfaces and interfaces. *Phys. Rev. B* **50,** 11996–12003 (Oct. 1994) (cit. on p. 27).

204. Fossati, P. C. M., Van Brutzel, L., Chartier, A. *et al.* Simulation of uranium dioxide polymorphs and their phase transitions. *Phys. Rev. B* **88,** 214112 (Dec. 2013) (cit. on p. 27).

205. Soulié, A. *Etude à l'échelle atomique de la plasticité et de la sur-stœchiométrie dans le dioxyde d'uranium* PhD thesis (Université Paris Saclay (COmUE), Oct. 2018) (cit. on p. 28).

206. Barbour, O. *Étude à l'échelle atomique du diagramme de phases de l'oxyde d'uranium entre UO_2 et U_4O_9 à l'aide d'une méthode Monte Carlo des Chemins* PhD thesis (Université Paris-Saclay, Nov. 2022) (cit. on p. 28).

207. Salles, N. *Etude des différents polymorphes de l'alumine et des phases transitoires apparaissant lors des premiers stades d'oxydation de l'aluminium : simulation à l'échelle atomique par un modèle à charges variables en liaisons fortes* PhD thesis (Université de Bourgogne, Sept. 2014) (cit. on p. 28).

208. Onat, B., Ortner, C. & Kermode, J. R. Sensitivity and dimensionality of atomic environment representations used for machine learning interatomic potentials. *The Journal of Chemical Physics* **153,** 144106 (Oct. 2020) (cit. on pp. 30, 32).

209. Himanen, L., Jäger, M. O. J., Morooka, E. V. *et al.* DScribe: Library of descriptors for machine learning in materials science. *Computer Physics Communications* **247,** 106949 (Feb. 2020) (cit. on p. 30).

210. Rupp, M., Tkatchenko, A., Müller, K.-R. *et al.* Fast and Accurate Modeling of Molecular Atomization Energies with Machine Learning. *Phys. Rev. Lett.* **108,** 058301 (Jan. 2012) (cit. on p. 30).

211. Schütt, K. T., Glawe, H., Brockherde, F. *et al.* How to represent crystal structures for machine learning: Towards fast prediction of electronic properties. *Phys. Rev. B* **89,** 205118 (May 2014) (cit. on p. 30).

212. Moussa, J. E. Comment on "Fast and Accurate Modeling of Molecular Atomization Energies with Machine Learning". *Phys. Rev. Lett.* **109,** 059801 (Aug. 2012) (cit. on p. 31).

213. Behler, J. & Parrinello, M. Generalized Neural-Network Representation of High-Dimensional Potential-Energy Surfaces. *Phys. Rev. Lett.* **98,** 146401 (Apr. 2007) (cit. on pp. 31, 39).

214. Behler, J. Atom-centered symmetry functions for constructing high-dimensional neural network potentials. *The Journal of Chemical Physics* **134,** 074106 (Feb. 2011) (cit. on pp. 31, 39, 47).

215. Shapeev, A. V. Moment Tensor Potentials: A Class of Systematically Improvable Interatomic Potentials. *Multiscale Model. Simul.* **14,** 1153–1173 (Jan. 2016) (cit. on p. 31).

216. Bartók, A. P., Payne, M. C., Kondor, R. *et al.* Gaussian Approximation Potentials: The Accuracy of Quantum Mechanics, without the Electrons. *Phys. Rev. Lett.* **104,** 136403 (Apr. 2010) (cit. on pp. 31, 33, 34).

217. Bartók, A. P., Kondor, R. & Csányi, G. On representing chemical environments. *Phys. Rev. B* **87,** 184115 (May 2013) (cit. on pp. 31, 34).

218. Khorshidi, A. & Peterson, A. A. Amp: A modular approach to machine learning in atomistic simulations. *Computer Physics Communications* **207,** 310–324 (Oct. 2016) (cit. on p. 31).

219. Pun, G. P. P., Batra, R., Ramprasad, R. *et al.* Physically informed artificial neural networks for atomistic modeling of materials. *Nat Commun* **10,** 2339 (May 2019) (cit. on pp. 33, 42).

220. Mishin, Y. Machine-learning interatomic potentials for materials science. *Acta Materialia* **214,** 116980 (Aug. 2021) (cit. on p. 33).

221. Thompson, A. P., Swiler, L. P., Trott, C. R. *et al.* Spectral neighbor analysis method for automated generation of quantum-accurate interatomic potentials. *Journal of Computational Physics* **285,** 316–330 (Mar. 2015) (cit. on pp. 33, 35, 37, 54).

222. Wood, M. A. & Thompson, A. P. Extending the accuracy of the SNAP interatomic potential form. *The Journal of Chemical Physics* **148,** 241721 (Mar. 2018) (cit. on p. 33).

223. Singraber, A., Behler, J. & Dellago, C. Library-Based LAMMPS Implementation of High-Dimensional Neural Network Potentials. *J. Chem. Theory Comput.* **15,** 1827–1840 (Mar. 2019) (cit. on pp. 39, 44, 57).

224. Singraber, A., Morawietz, T., Behler, J. *et al.* Parallel Multistream Training of High-Dimensional Neural Network Potentials. *J. Chem. Theory Comput.* **15,** 3075–3092 (May 2019) (cit. on pp. 39, 44, 46, 58).

225. Gastegger, M., Schwiedrzik, L., Bittermann, M. *et al.* wACSF—Weighted atom-centered symmetry functions as descriptors in machine learning potentials. *The Journal of Chemical Physics* **148,** 241709 (Mar. 2018) (cit. on pp. 41, 42).

226. Imbalzano, G., Anelli, A., Giofré, D. *et al.* Automatic selection of atomic fingerprints and reference configurations for machine-learning potentials. *The Journal of Chemical Physics* **148,** 241730 (Apr. 2018) (cit. on pp. 41, 55, 56).

227. Mahoney, M. W. & Drineas, P. CUR matrix decompositions for improved data analysis. *Proceedings of the National Academy of Sciences* **106,** 697–702 (Jan. 2009) (cit. on pp. 41, 56).

228. Bircher, M. P., Singraber, A. & Dellago, C. *Improved Description of Atomic Environments using Low-cost Polynomial Functions with Compact Support* Feb. 2021. arXiv: 2010.14414 [cond-mat, physics:physics] (cit. on p. 42).

229. Pun, G. P. P., Yamakov, V., Hickman, J. *et al.* Development of a general-purpose machine-learning interatomic potential for aluminum by the physically informed neural network method. *Phys. Rev. Mater.* **4,** 113807 (Nov. 2020) (cit. on p. 42).

230. Lin, Y.-S., Pun, G. P. P. & Mishin, Y. Development of a physically-informed neural network interatomic potential for tantalum. *Computational Materials Science* **205,** 111180 (Apr. 2022) (cit. on p. 42).

231. Kingma, D. P. & Ba, J. *Adam: A Method for Stochastic Optimization* Jan. 2017. arXiv: 1412.6980 [cs] (cit. on p. 43).

232. Kalman, R. E. A New Approach to Linear Filtering and Prediction Problems. *Journal of Basic Engineering* **82,** 35–45 (Mar. 1960) (cit. on pp. 44, 58).

233. Kalman, R. E. & Bucy, R. S. New Results in Linear Filtering and Prediction Theory. *Journal of Basic Engineering* **83,** 95–108 (Mar. 1961) (cit. on pp. 44, 58).

234. Julier, S. & Uhlmann, J. Unscented filtering and nonlinear estimation. *Proceedings of the IEEE* **92,** 401–422 (Mar. 2004) (cit. on p. 44).

235. Singhal, S. & Wu, L. *Training Multilayer Perceptrons with the Extended Kalman Algorithm* in *Advances in Neural Information Processing Systems* **1** (Morgan-Kaufmann, 1988) (cit. on pp. 44, 57).

236. Welch, G. & Bishop, G. *An introduction to the kalman filter.* (1995) (cit. on p. 44).

237. Puskorius & Feldkamp. *Decoupled extended Kalman filter training of feedforward layered networks | Semantic Scholar* in () (cit. on p. 46).

238. Feldkamp & Puskorius. *Training controllers for robustness: multi-stream DEKF | Semantic Scholar* in () (cit. on p. 46).

239. Pukrittayakamee, A., Malshe, M., Hagan, M. *et al.* Simultaneous fitting of a potential-energy surface and its corresponding force fields using feedforward neural networks. *The Journal of Chemical Physics* **130,** 134101 (Apr. 2009) (cit. on p. 47).

240. Dubois, E. T., Tranchida, J., Bouchet, J. *et al.* Atomistic simulations of nuclear fuel UO_2 with machine learning interatomic potentials. *Phys. Rev. Mater.* **8,** 025402 (Feb. 2024) (cit. on p. 50).

241. Blöchl, P. E. Projector augmented-wave method. *Phys. Rev. B* **50,** 17953–17979 (Dec. 1994) (cit. on p. 50).

242. Torrent, M., Jollet, F., Bottin, F. *et al.* Implementation of the projector augmented-wave method in the ABINIT code: Application to the study of iron under pressure. *Computational Materials Science* **42,** 337–351 (Apr. 2008) (cit. on p. 50).

243. Kotani, A. & Yamazaki, T. Systematic analysis of core photoemission spectra for actinide di-oxides and rare-earth sesqui-oxides. *Progress of Theoretical Physics Supplement* **108,** 117–131 (Feb. 1992) (cit. on pp. 50, 91).

244. Njifon, I. C., Bertolus, M., Hayn, R. *et al.* Electronic Structure Investigation of the Bulk Properties of Uranium–Plutonium Mixed Oxides (U, Pu)O2. *Inorg. Chem.* **57,** 10974–10983 (Sept. 2018) (cit. on p. 51).

245. Wang, J., Ewing, R. C. & Becker, U. Electronic structure and stability of hyper-stoichiometric UO_{2+x} under pressure. *Phys. Rev. B* **88,** 024109 (July 2013) (cit. on p. 51).

246. Dudarev, S. L., Liu, P., Andersson, D. A. *et al.* Parametrization of LSDA + U for noncollinear magnetic configurations: Multipolar magnetism in UO_2. *Phys. Rev. Mater.* **3,** 083802 (Aug. 2019) (cit. on pp. 51, 88).

247. Monkhorst, H. J. & Pack, J. D. Special points for Brillouin-zone integrations. *Phys. Rev. B* **13,** 5188–5192 (June 1976) (cit. on p. 52).

248. Harris, C. R., Millman, K. J., van der Walt, S. J. *et al.* Array programming with NumPy. *Nature* **585,** 357–362 (Sept. 2020) (cit. on p. 54).

249. Adams, B. M., Bohnhoff, W. J., Dalbey, K. R. *et al. Dakota, A Multilevel Parallel Object-Oriented Framework for Design Optimization, Parameter Estimation, Uncertainty Quantification, and Sensitivity Analysis: Version 6.13 User's Manual* tech. rep. SAND2020-12495 (Sandia National Lab. (SNL-NM), Albuquerque, NM (United States), Nov. 2020) (cit. on pp. 54, 55).

250. Hamilton, B. W., Yoo, P., Sakano, M. N. *et al.* High-pressure and temperature neural network reactive force field for energetic materials. *The Journal of Chemical Physics* **158,** 144117 (Apr. 2023) (cit. on p. 54).

251. Artrith, N. & Behler, J. High-dimensional neural network potentials for metal surfaces: A prototype study for copper. *Phys. Rev. B* **85,** 045439 (Jan. 2012) (cit. on pp. 59, 60).

252. Sivaraman, G., Krishnamoorthy, A. N., Baur, M. *et al.* Machine-learned interatomic potentials by active learning: amorphous and liquid hafnium dioxide. *npj Comput Mater* **6,** 1–8 (July 2020) (cit. on p. 59).

253. Jinnouchi, R., Miwa, K., Karsai, F. *et al.* On-the-Fly Active Learning of Interatomic Potentials for Large-Scale Atomistic Simulations. *J. Phys. Chem. Lett.* **11,** 6946–6955 (Sept. 2020) (cit. on p. 59).

254. Li, Z., Kermode, J. R. & De Vita, A. Molecular Dynamics with On-the-Fly Machine Learning of Quantum-Mechanical Forces. *Phys. Rev. Lett.* **114,** 096405 (Mar. 2015) (cit. on p. 59).

255. Podryabinkin, E. V. & Shapeev, A. V. Active learning of linearly parametrized interatomic potentials. *Computational Materials Science* **140,** 171–180 (Dec. 2017) (cit. on p. 59).

256. Podryabinkin, E., Garifullin, K., Shapeev, A. *et al. MLIP-3: Active learning on atomic environments with Moment Tensor Potentials* Aug. 2023. arXiv: 2304.13144 [physics] (cit. on p. 59).

257. Jacobsen, T. L., Jørgensen, M. S. & Hammer, B. On-the-Fly Machine Learning of Atomic Potential in Density Functional Theory Structure Optimization. *Phys. Rev. Lett.* **120,** 026102 (Jan. 2018) (cit. on p. 59).

258. Smith, J. S., Nebgen, B., Lubbers, N. *et al.* Less is more: Sampling chemical space with active learning. *The Journal of Chemical Physics* **148,** 241733 (May 2018) (cit. on p. 59).

259. Bernstein, N., Csányi, G. & Deringer, V. L. De novo exploration and self-guided learning of potential-energy surfaces. *npj Comput Mater* **5,** 1–9 (Oct. 2019) (cit. on p. 59).

260. Zhang, L., Lin, D.-Y., Wang, H. *et al.* Active learning of uniformly accurate interatomic potentials for materials simulation. *Phys. Rev. Mater.* **3,** 023804 (Feb. 2019) (cit. on p. 59).

261. Vandermause, J., Torrisi, S. B., Batzner, S. *et al.* On-the-fly active learning of interpretable Bayesian force fields for atomistic rare events. *npj Comput Mater* **6,** 1–11 (Mar. 2020) (cit. on p. 59).

262. Freund, Y., Seung, H. S., Shamir, E. *et al.* Selective Sampling Using the Query by Committee Algorithm. *Machine Learning* **28,** 133–168 (Aug. 1997) (cit. on p. 60).

263. Schran, C., Brezina, K. & Marsalek, O. Committee neural network potentials control generalization errors and enable active learning. *The Journal of Chemical Physics* **153,** 104105 (Sept. 2020) (cit. on p. 60).

264. Kee, S., del Castillo, E. & Runger, G. Query-by-committee improvement with diversity and density in batch active learning. *Information Sciences* **454-455,** 401–418 (July 2018) (cit. on pp. 61, 62).

265. Patra, S. & Bruzzone, L. A cluster-assumption based batch mode active learning technique. *Pattern Recognition Letters* **33,** 1042–1048 (July 2012) (cit. on p. 61).

266. Hu, L., Lu, S. & Wang, X. A new and informative active learning approach for support vector machine. *Information Sciences* **244,** 142–160 (Sept. 2013) (cit. on p. 61).

267. Hu, R., Mac Namee, B. & Delany, S. J. Active learning for text classification with reusability. *Expert Systems with Applications* **45,** 438–449 (Mar. 2016) (cit. on p. 61).

268. Cardoso, T. N. C., Silva, R. M., Canuto, S. *et al.* Ranked batch-mode active learning. *Information Sciences* **379,** 313–337 (Feb. 2017) (cit. on p. 61).

269. Bochkarev, A., Lysogorskiy, Y., Menon, S. *et al.* Efficient parametrization of the atomic cluster expansion. *Phys. Rev. Mater.* **6,** 013804 (Jan. 2022) (cit. on p. 62).

270. Bottin, F., Bieder, J. & Bouchet, J. a-TDEP: Temperature Dependent Effective Potential for Abinit – Lattice dynamic properties including anharmonicity. *Computer Physics Communications* **254,** 107301 (Sept. 2020) (cit. on p. 66).

271. Dolling, G., Cowley, R. A. & Woods, A. D. B. THE CRYSTAL DYNAMICS OF URANIUM DIOXIDE. *Can. J. Phys.* **43,** 1397–1413 (Aug. 1965) (cit. on p. 67).

272. Martin, D. G. The thermal expansion of solid UO2 and (U, Pu) mixed oxides — a review and recommendations. *Journal of Nuclear Materials* **152,** 94–101 (May 1988) (cit. on pp. 68, 98).

273. Cheik Njifon, I. *Modélisation des modifications structurales, électroniques et thermodynamiques induites par les défauts ponctuels dans les oxydes mixtes à base d'actinides (U,Pu)O2* thesis (Aix-Marseille, Nov. 2018) (cit. on pp. 68, 98).

274. Castellano, A. *Étude des effets de la température sur les combustibles nucléaires par une approche ab initio* PhD thesis (Sorbonne Université, Jan. 2022) (cit. on pp. 68, 73, 74, 98–100).

275. Szpunar, B., Szpunar, J. A. & Sim, K.-S. Theoretical investigation of structural and thermo-mechanical properties of thoria. *Journal of Physics and Chemistry of Solids* **90,** 114–120 (Mar. 2016) (cit. on p. 69).

276. Wu, Z. & Cohen, R. E. More accurate generalized gradient approximation for solids. *Phys. Rev. B* **73,** 235116 (June 2006) (cit. on p. 69).

277. Nakamura, H. & Machida, M. High-temperature properties of thorium dioxide: A first-principles molecular dynamics study. *Journal of Nuclear Materials* **478,** 56–60 (Sept. 2016) (cit. on p. 69).

278. Brandt, O. G. & Walker, C. T. Ultrasonic Attenuation and Elastic Constants for Uranium Dioxide. *Phys. Rev.* **170,** 528–541 (June 1968) (cit. on pp. 71, 98, 99).

279. Wachtman, J. B., Wheat, M. L., Anderson, H. J. *et al.* Elastic constants of single crystal UO2 at 25° C. *Journal of Nuclear Materials* **16,** 39–41 (May 1965) (cit. on pp. 71, 99).

280. Clavier, G. & Thompson, A. P. Computation of the thermal elastic constants for arbitrary manybody potentials in LAMMPS using the stress-fluctuation formalism. *Computer Physics Communications* **286,** 108674 (May 2023) (cit. on p. 71).

281. Hutchings, M. T. High-temperature studies of UO2 and ThO2 using neutron scattering techniques. *J. Chem. Soc., Faraday Trans. 2* **83,** 1083–1103 (Jan. 1987) (cit. on pp. 73, 74, 99, 100).

282. Dorado, B., Jomard, G., Freyss, M. *et al.* Stability of oxygen point defects in UO_2 by first-principles DFT + U calculations: Occupation matrix control and Jahn-Teller distortion. *Phys. Rev. B* **82,** 035114 (July 2010) (cit. on p. 75).

283. Soulié, A., Crocombette, J.-P., Kraych, A. *et al.* Atomistically-informed thermal glide model for edge dislocations in uranium dioxide. *Acta Materialia* **150,** 248–261 (May 2018) (cit. on pp. 75, 77).

284. Ashbee, K. H. G. & Yust, C. S. A mechanism for the ease of slip in UO2+x. *Journal of Nuclear Materials* **110,** 246–250 (Oct. 1982) (cit. on p. 75).

285. Keller, R. J., Mitchell, T. E. & Heuer, A. H. Plastic deformation in nonstoichiometric UO2 + x single crystals—II. Deformation at high temperatures. *Acta Metallurgica* **36,** 1073–1083 (Apr. 1988) (cit. on p. 75).

286. Barkema, G. T. & Mousseau, N. Event-Based Relaxation of Continuous Disordered Systems. *Phys. Rev. Lett.* **77,** 4358–4361 (Nov. 1996) (cit. on p. 83).

287. J?nsson, H., Mills, G. & Jacobsen, K. W. in *Classical and Quantum Dynamics in Condensed Phase Simulations* 385–404 (WORLD SCIENTIFIC, June 1998) (cit. on p. 83).

288. Schuler, T., Messina, L. & Nastar, M. KineCluE: A kinetic cluster expansion code to compute transport coefficients beyond the dilute limit. *Computational Materials Science* **172,** 109191 (Feb. 2020) (cit. on p. 83).

289. Chen, J.-L. & Kaltsoyannis, N. DFT + U Study of Uranium Dioxide and Plutonium Dioxide with Occupation Matrix Control. *J. Phys. Chem. C* **126,** 11426–11435 (July 2022) (cit. on p. 88).

290. Laskowski, R., Madsen, G. K. H., Blaha, P. *et al.* Magnetic structure and electric-field gradients of uranium dioxide: An ab initio study. *Phys. Rev. B* **69,** 140408 (Apr. 2004) (cit. on p. 88).

291. Kotani, A. & Yamazaki, T. Systematic Analysis of Core Photoemission Spectra for Actinide Di-Oxides and Rare-Earth Sesqui-Oxides. *Progress of Theoretical Physics Supplement* **108,** 117–131 (Feb. 1992) (cit. on p. 91).

292. Outerovitch, R. & Amadon, B. Electronic interaction U_{pp} on oxygen p orbitals in oxides: Role of correlated orbitals on the example of UO_2 and TiO_2. *Phys. Rev. B* **107,** 235126 (June 2023) (cit. on p. 91).

293. Outerovitch, R. *Études des interactions électroniques effectives dans les solides fortement corrélés* These de doctorat (université Paris-Saclay, Dec. 2022) (cit. on p. 91).

294. Aryasetiawan, F., Imada, M., Georges, A. *et al.* Frequency-dependent local interactions and low-energy effective models from electronic structure calculations. *Phys. Rev. B* **70,** 195104 (Nov. 2004) (cit. on p. 91).

295. Aryasetiawan, F., Karlsson, K., Jepsen, O. *et al.* Calculations of Hubbard U from first-principles. *Phys. Rev. B* **74,** 125106 (Sept. 2006) (cit. on p. 91).

296. Moore, K. T. X-ray and electron microscopy of actinide materials. *Micron* **41,** 336–358 (June 2010) (cit. on p. 103).

297. Castell, M. R. Wulff shape of microscopic voids in UO_2 crystals. *Phys. Rev. B* **68,** 235411 (Dec. 2003) (cit. on p. 103).

298. Rondinella, V. V. & Wiss, T. The high burn-up structure in nuclear fuel. *Materials Today* **13,** 24–32 (Dec. 2010) (cit. on p. 103).

299. Galvin, C. O. T., Rushton, M. J. D., Cooper, M. W. D. *et al.* The predicted shapes of voids and Xe bubbles in UO_2. *Journal of Nuclear Materials* **543,** 152622 (Jan. 2021) (cit. on pp. 103, 104).

300. Bottin, F., Geneste, G. & Jomard, G. Thermodynamic stability of the UO_2 surfaces: Interplay between over-stoichiometry and polarity compensation. *Phys. Rev. B* **93,** 115438 (Mar. 2016) (cit. on p. 103).

301. Boyarchenkov, A. S., Potashnikov, S. I., Nekrasov, K. A. *et al.* Molecular dynamics simulation of UO2 nanocrystals surface. *Journal of Nuclear Materials* **421,** 1–8 (Feb. 2012) (cit. on pp. 103, 104).

302. Chartier, A., Van Brutzel, L. & Freyss, M. Atomistic study of stability of xenon nanoclusters in uranium oxide. *Phys. Rev. B* **81,** 174111 (May 2010) (cit. on p. 103).

303. Abramowski, M., Grimes, R. W. & Owens, S. Morphology of UO2. *Journal of Nuclear Materials* **275,** 12–18 (Oct. 1999) (cit. on pp. 103, 104).

304. Bottin, F., Geneste, G. & Jomard, G. Thermodynamic stability of the UO 2 surfaces: Interplay between over-stoichiometry and polarity compensation. *Phys. Rev. B* **93,** 115438 (Mar. 2016) (cit. on p. 104).

305. Sawbridge, P. T. & Sykes, E. C. Dislocation glide in UO2 single crystals at 1600°K. *The Philosophical Magazine: A Journal of Theoretical Experimental and Applied Physics* **24,** 33–53 (July 1971) (cit. on p. 105).

306. Lafourcade, P., Denoual, C. & Maillet, J.-B. Irreversible Deformation Mechanisms for 1,3,5-Triamino-2,4,6-Trinitrobenzene Single Crystal through Molecular Dynamics Simulations. *J. Phys. Chem. C* **122,** 14954–14964 (July 2018) (cit. on pp. 105, 110, 112).

307. Leyssale, J.-M., Couégnat, G., Jouannigot, S. *et al.* Mechanisms of elastic softening in highly anisotropic carbons under in-plane compression/indentation. *Carbon* **197,** 425–434 (Sept. 2022) (cit. on p. 112).

308. Lafourcade, P., Denoual, C. & Maillet, J.-B. Elastic instability in graphite single crystal under dynamic triaxial compression: Effect of strain-rate on the resulting microstructure. *Journal of Applied Physics* **128,** 045101 (July 2020) (cit. on p. 112).

309. Gruber, J., Plummer, G. & Tucker, G. J. Bending the rules: Strain accommodation in layered crystalline solids through nanoscale buckling over dislocations. *Journal of the Mechanics and Physics of Solids* **182,** 105450 (Jan. 2024) (cit. on p. 112).

310. Ranganathan, S. I. & Ostoja-Starzewski, M. Universal Elastic Anisotropy Index. *Phys. Rev. Lett.* **101,** 055504 (Aug. 2008) (cit. on pp. 119, 163).

311. Crocombette, J.-P., Chartier, A. & Weber, W. J. Atomistic simulation of amorphization thermokinetics in lanthanum pyrozirconate. *Applied Physics Letters* **88,** 051912 (Jan. 2006) (cit. on p. 122).

312. Chartier, A., Meis, C., Crocombette, J.-P. *et al.* Molecular Dynamic Simulation of Disorder Induced Amorphization in Pyrochlore. *Phys. Rev. Lett.* **94,** 025505 (Jan. 2005) (cit. on p. 122).

313. Van Brutzel, L., Chartier, A. & Crocombette, J. P. Basic mechanisms of Frenkel pair recombinations in UO_2 fluorite structure calculated by molecular dynamics simulations. *Phys. Rev. B* **78,** 024111 (July 2008) (cit. on p. 122).

314. Martin, G., Garcia, P., Sabathier, C. *et al.* Irradiation-induced heterogeneous nucleation in uranium dioxide. *Physics Letters A* **374,** 3038–3041 (July 2010) (cit. on p. 122).

315. Devanathan, R., Brutzel, L. V., Chartier, A. *et al.* Modeling and simulation of nuclear fuel materials. *Energy Environ. Sci.* **3,** 1406–1426 (Sept. 2010) (cit. on p. 122).

316. Chartier, A., Catillon, G. & Crocombette, J.-P. Key Role of the Cation Interstitial Structure in the Radiation Resistance of Pyrochlores. *Phys. Rev. Lett.* **102,** 155503 (Apr. 2009) (cit. on p. 122).

317. Catillon, G. & Chartier, A. Pressure and temperature phase diagram of Gd2Ti2O7 under irradiation. *Journal of Applied Physics* **116,** 193502 (Nov. 2014) (cit. on p. 122).

318. Chartier, A., Van Brutzel, L., Pannier, B. *et al.* Atomic scale mechanisms for the amorphisation of irradiated graphite. *Carbon* **91,** 395–407 (Sept. 2015) (cit. on p. 122).

319. Le Prioux, A., Fossati, P., Maillard, S. *et al.* Empirical potential simulations of interstitial dislocation loops in uranium dioxide. *Journal of Nuclear Materials* **479,** 576–584 (Oct. 2016) (cit. on p. 123).

320. Baufeld, B., Baither, D., Messerschmidt, U. *et al.* In Situ Study on the Generation of Radiation Damage in Cubic-Zirconia in the High-Voltage Electron Microscope. *Journal of the American Ceramic Society* **76,** 3163–3166 (1993) (cit. on p. 123).

321. Karcz, M. J., Messina, L., Kawasaki, E. *et al.* Semi-supervised generative approach to chemical disorder: application to point-defect formation in uranium–plutonium mixed oxides. *Phys. Chem. Chem. Phys.* **25,** 23069–23080 (Aug. 2023) (cit. on p. 135).

322. Nikolov, S., Wood, M. A., Cangi, A. *et al.* Data-driven magneto-elastic predictions with scalable classical spin-lattice dynamics. *npj Comput Mater* **7,** 1–12 (Sept. 2021) (cit. on p. 135).

323. Nikolov, S., Nieves, P., Thompson, A. P. *et al.* Temperature dependence of magnetic anisotropy and magnetoelasticity from classical spin-lattice calculations. *Phys. Rev. B* **107,** 094426 (Mar. 2023) (cit. on p. 135).

324. Drautz, R. Atomic cluster expansion of scalar, vectorial, and tensorial properties including magnetism and charge transfer. *Phys. Rev. B* **102,** 024104 (July 2020) (cit. on p. 135).

325. Caciuffo, R., Santini, P., Carretta, S. *et al.* Multipolar, magnetic, and vibrational lattice dynamics in the low-temperature phase of uranium dioxide. *Phys. Rev. B* **84,** 104409 (Sept. 2011) (cit. on p. 135).

326. Jaime, M., Saul, A., Salamon, M. *et al.* Piezomagnetism and magnetoelastic memory in uranium dioxide. *Nat Commun* **8,** 99 (July 2017) (cit. on p. 135).

327. Antonio, D. J., Weiss, J. T., Shanks, K. S. *et al.* Piezomagnetic switching and complex phase equilibria in uranium dioxide. *Commun Mater* **2,** 1–6 (Feb. 2021) (cit. on p. 135).

328. Gofryk, K., Du, S., Stanek, C. R. *et al.* Anisotropic thermal conductivity in uranium dioxide. *Nat Commun* **5,** 4551 (Aug. 2014) (cit. on p. 135).

329. Goff, J., Zhang, Y., Negre, C. *et al.* Shadow Molecular Dynamics and Atomic Cluster Expansions for Flexible Charge Models. *J. Chem. Theory Comput.* **19,** 4255–4272 (July 2023) (cit. on p. 135).

330. Novikov, I. S. & Shapeev, A. V. Improving accuracy of interatomic potentials: more physics or more data? A case study of silica. *Materials Today Communications* **18,** 74–80 (Mar. 2019) (cit. on p. 135).

331. Zener, C. Contributions to the Theory of Beta-Phase Alloys. *Phys. Rev.* **71,** 846–851 (June 1947) (cit. on p. 163).

Appendix A.

Elasticity in solids

Elasticity theory

The elasticity theory linearly relates stress to strain. The stress describes the surface forces acting on a volume element in a continuum. The strain describes the state of deformation of a solid body. Both stress and strain can be represented by a 2nd order tensor with 6 independent coordinates. They are respectively denoted $\boldsymbol{\sigma}$ and $\boldsymbol{\epsilon}$.

The stress is related to strain by the *stiffness* tensor, $\boldsymbol{C}$, as:

$$\sigma_{ij} = C_{ijkl}\epsilon_{kl} \tag{A.1}$$

Similarly, the strain is related to stress by the *compliance* tensor, $\boldsymbol{S}$, defined as the inverse of the stiffness tensor.

$$\epsilon_{ij} = S_{ijkl}\sigma_{ij} \tag{A.2}$$

Both stiffness and compliance are 4th order tensors defined in a 3D vector space. Due to translational and rotational symmetries, the number of independent coordinates of 4th order tensors reduces to 21 from 81 (3^4) in the least symmetric cases. Furthermore, the cumbersome 2nd and 4th order tensor are commonly replaced by vectors and matrices in a 6 dimensional space by using the scheme introduced by Voigt. This is justified because only six components are required to describe stress and strain.

Tensor notation	11	22	33	23,32	31,13	12,21
Voigt's notation	1	2	3	4	5	6

If the transformation applies directly for stress and stiffness, it requires corrective coefficients for strain:

$$\epsilon_{ij} = \begin{cases} \epsilon_p & \text{for } i = j \\ \frac{1}{2}\epsilon_p & \text{for } i \neq j \end{cases} \tag{A.3}$$

and compliance:

$$S_{ijkl} = \omega_{pq} S_{pq} \tag{A.4}$$

with

$$\omega_{pq} = \begin{cases} 1 & \text{if } p \text{ and } q \text{ are } 1, 2, 3 \text{ only,} \\ \frac{1}{2} & \text{if either } p \text{ or } q \text{ is } 4, 5, 6, \\ \frac{1}{4} & \text{if } p \text{ and } q \text{ are } 4, 5, 6 \text{ only} \end{cases} \tag{A.5}$$

which can be summarize by the following formula:

$$\omega_{pq} = \frac{1}{(1 + \lfloor p/3 \rfloor) \times (1 + \lfloor q/3 \rfloor)} \tag{A.6}$$

Averaging schemes

For ease of use, elastic properties of anisotropic material are often replaced by those of an "equivalent" isotropic material. This is especially important to describe material consisting of grains of random orientation. There are three main averaging schemes: Voigt, Reuss and Hill.

1. Voigt scheme relies on the stiffness matrix (assuming uniform strain). The bulk modulus K_V and shear modulus G_V (sub-scripted with a V for Voigt) are given by:

$$K_V = \frac{A + 2B}{3} \tag{A.7}$$

$$G_V = \frac{A - B + 3C}{5} \tag{A.8}$$

where:

$$A = \frac{1}{3}\sum_{i=1}^{3} C_{ii}, \qquad B = \frac{1}{3}\sum_{\substack{i,j=1,\\ i<j}}^{3} C_{ij}, \qquad C = \frac{1}{3}\sum_{i=4}^{6} C_{ii} \tag{A.9}$$

2. Reuss averaging scheme, denoted by the R sub-script, is based on the compliance matrix and writes:

$$K_R = \frac{1}{3a + 6b} \tag{A.10}$$

$$G_R = \frac{1}{4a - 4b + 3c} \tag{A.11}$$

where:

$$a = \frac{1}{3}\sum_{i=1}^{3} S_{ii}, \qquad b = \frac{1}{3}\sum_{\substack{i,j=1,\\ i<j}}^{3} S_{ij}, \qquad c = \frac{1}{3}\sum_{i=4}^{6} S_{ii} \tag{A.12}$$

3. The Hill average is the arithmetic average of the Voigt and Reuss values.

In any cases, the Young's modulus E and the Poisson's ratio ν are given by:

$$E = \left(\frac{1}{3G} + \frac{1}{9K}\right)^{-1} \tag{A.13}$$

$$\nu = \frac{1}{2}\left(1 - \frac{3G}{3K + G}\right) \tag{A.14}$$

The universal anisotropy index A^U [310] can be used to characterized the anisotropy of the material. It writes:

$$A^U = \boldsymbol{C}^V : \boldsymbol{S}^R - 6 \tag{A.15}$$

where $\boldsymbol{C}^V$ and $\boldsymbol{S}^R$ are the Voigt and Reuss estimates of the stiffness and compliances tensors. They are expressed in terms of shear modulus bulk modulus as follow:

$$\boldsymbol{C}^V = 2G_V\boldsymbol{K} + 3K_V\boldsymbol{J} \tag{A.16}$$

$$\boldsymbol{S}^R = (2G_R)^{-1}\boldsymbol{K} + (3K_R)^{-1}\boldsymbol{J} \tag{A.17}$$

with $\boldsymbol{J}$ and $\boldsymbol{K}$ the spherical and deviatoric parts of the unit 4th order tensor. Contracting (A.16) and (A.17) universal anisotropy index A^U can eventually be written in terms of shear and bulk moduli:

$$A^U = 5\frac{G_V}{G_R} + \frac{K_V}{K_R} - 6 \geq 0 \tag{A.18}$$

A^U is identically zero for isotropic crystal. It is a universal measure to quantify single crystals elastic anisotropy, accounting for both shear and bulk contribution, and can be interpreted as a generalization of the Zener anisotropy index [331].

Tensor rotation and Euler's angles

A 4th order tensor rotates in a new basis set following:

$$T'_{\alpha\beta\gamma\delta} = r_{\alpha i}r_{\beta j}r_{\gamma k}r_{\delta l}T_{ijkl} \tag{A.19}$$

where Einstein's summation rule is adopted and $r_{\alpha i}$ are the components of the rotation matrix.

A direction in cartesian space is defined by a point on a unit sphere. It is fully characterized by angles $\theta \in [0, \pi]$ and $\phi \in [0, 2\pi]$. The resulting unit vector, $\vec{a}$, is the first unit vector in the new basis set and has for coordinates:

$$\vec{a} = \begin{pmatrix} \sin\theta\cos\phi \\ \sin\theta\sin\phi \\ \cos\theta \end{pmatrix} \tag{A.20}$$

Some elastic properties (e.g. shear modulus or Poisson's ratio) requires a second unit vector, $\vec{b}$, orthogonal to $\vec{a}$ and characterised by a third angle $\chi \in [0, 2\pi]$.

$$\vec{b} = \begin{pmatrix} \cos\theta\cos\phi\cos\chi - \sin\phi\sin\chi \\ \cos\theta\sin\phi\cos\chi + \cos\phi\sin\chi \\ -\sin\theta\cos\chi \end{pmatrix} \tag{A.21}$$

By definition, the components of the first two colmns of the rotation matrix are the coordinates of $\vec{a}$ and $\vec{b}$. This is enough to obtain all the components of the fourth order

tensor in the subvectorial space defined by directions 1 and 2. For instance:

$$S'_{12} = S'_{1122} = r_{1i}r_{1j}r_{2k}r_{2l}S_{ijkl} = a_i a_j b_k b_l S_{ijkl} \tag{A.22}$$

$$S'_{66} = S'_{1212} = r_{1i}r_{2j}r_{1k}r_{2l}S_{ijkl} = a_i b_j a_k b_l S_{ijkl} \tag{A.23}$$

By scanning θ, ϕ and χ over the unit sphere, it is possible to access all the components without the third unit vector.

Directional dependency of elastic properties

The Young's modulus and the linear compressibility can also be expressed in terms of the compliance matrix. The Young's modulus is obtained using a purely normal stress in (A.2) in its vector form and is given by:

$$E(\theta, \phi) = \frac{1}{S'_{11}(\theta, \phi)} = \frac{1}{a_i a_j a_k a_l S_{ijkl}} \tag{A.24}$$

The linear compressibility is obtained by applying isotropic stress (corresponding to pressure p) so that $\epsilon_{ij} = -pS_{ijkk}$. Considering that the extension to direction a is $\epsilon_{ij}a_i a_j$ therefore:

$$\beta(\theta, \phi) = a_i a_j S_{ijkk} \tag{A.25}$$

Shear modulus and Poisson's ratio depends on the two direction a and b (respectively the direction of the stress applied and the direction of mesurement). The shear modulus is obtained by applying a pure shear stress in (A.2) and results in:

$$G(\theta, \phi, \chi) = \frac{1}{4S'_{66}(\theta, \phi, \chi)} = \frac{1}{4a_i b_j a_k b_l S_{ijkl}} \tag{A.26}$$

Poisson's ratio is given by:

$$\nu(\theta, \phi, \chi) = -\frac{S'_{12}(\theta, \phi, \chi)}{S'_{11}(\theta, \phi)} = -\frac{a_i a_j b_k b_l S_{ijkl}}{a_i a_j a_k a_l S_{ijkl}} \tag{A.27}$$

Both Young's modulus and linear compressiblity representations are strainforward as they only depends on one direction. On the other hand, shear modulus and Poisson's ratio depend on 2 directions and cannot be directly represented in a 3D space. A convenient representation is to plot for each direction (ϕ, θ) the minimum and maximum value for varying $\chi \in [0, 2\pi]$:

$$f(\theta, \phi) = \min_{\chi} F(\theta, \phi, \chi) \tag{A.28}$$

$$g(\theta, \phi) = \max_{\chi} F(\theta, \phi, \chi) \tag{A.29}$$

where F is G or ν.

Appendix B.

Mechanical study: Supplementary materials

B.1. Effect of strain rate at 1600 K

This section presents additional results for the investigation of the strain rate effect on the critical shear stress flow surfaces. The methodology employed is the same as in Section 3.4.3 but with a initial temperature of 1600 K. Based on the results at 300 K, only 3 strain rate were tested here. Results are displayed Figures B.1 and B.2. We observed no significant differences between the three tested strain rates.

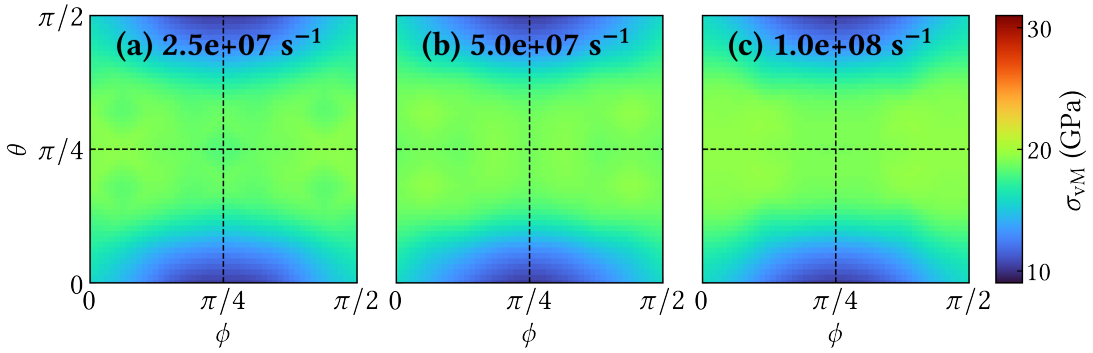

Figure B.1 – 2D projections of the 3D flow stress surface for different strain-rates at 1600 k. The color scale for the von Mises critical stress is common to all projections. (c) corresponds to the 2D projection of figure 3.26-d averaged by symmetry.

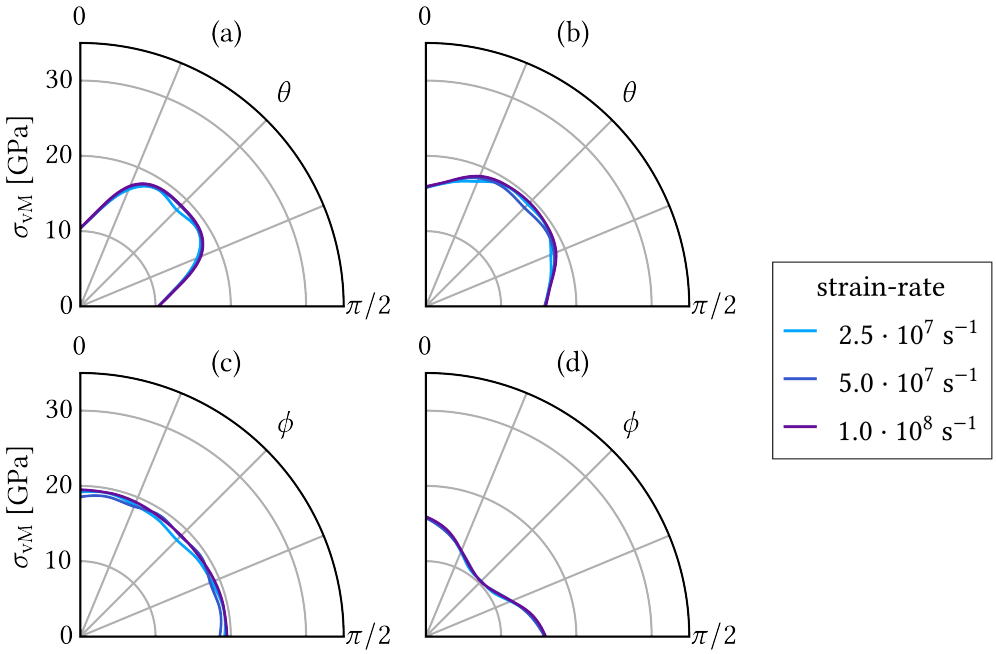

Figure B.2 – 2D slices of the 3D flow stress surfaces at 1600 K (fig. 3.26-d) in different planes for the multiple considered strain-rates. (a) $\phi = \pi/4, \theta \in [0, \pi/2]$ (b) $\phi = 0, \theta \in [0, \pi/2]$; (c) $\phi \in [0, \pi/2], \theta = \pi/4$; (d) $\phi \in [0, \pi/2], \theta = 0$.